Sapienza University of Rome

Doctorate of Philosophy in Electronic Engineering
XXXIII Cycle

Noninvasive electric and magnetic stimulation of the brain: numerical modeling and dosimetrical assessment

Candidate

Micol Colella

ID Number 1526041

Thesis Advisor

Prof. Micaela Liberti

Thesis Co-Advisors

Prof. Francesca Apollonio

Prof. Domenico Caputo

Prof. Gaetano Scarano

A.Y. 2020/2021

SAPIENZA
UNIVERSITÀ DI ROMA

SAPIENZA UNIVERSITY OF ROME

DOCTORATE OF PHILOSOPHY IN ELECTRONIC ENGINEERING
XXXIII CYCLE

Noninvasive electric and magnetic stimulation of the brain: numerical modeling and dosimetrical assessment

Candidate

Micol Colella

ID Number 1526041

Thesis Committee

Prof. Micaela Liberti (Thesis Advisor)
Prof. Francesca Apollonio
Prof. Domenico Caputo
Prof. Gaetano Scarano (Thesis Co-Advisors)

Reviewers

Dr. L. M. Angelone
Prof. T. Samaras

A.Y. 2020/2021

Noninvasive electric and magnetic stimulation of the brain: numerical modeling and dosimetrical assessment

Ph.D. Thesis - Sapienza University of Rome

© 2021 Micol Colella. All rights reserved.

Thesis submitted in partial fulfillment of the requirements for the degree of Doctor of Philosophy in Electronic Engineering.

This thesis has been typeset by LaTeX.
Version: May 17, 2021.

Author's address:
Micol Colella
Sapienza - University of Rome
Via Eudossiana 25, 00184 Rome, Italy
e-mail: micol.colella@uniroma1.it
web-site:

Contents

Abstract **1**

Introduction and thesis outline **3**

I Magnetic and Electric fields applied to noninvasive brain stimulation: the fundamental role of numerical dosimetry **7**

1 Non-invasive brain stimulation - NIBS **9**

1.1 Overview of invasive and noninvasive brain stimulation techniques . . . 13

1.2 Transcranial direct current stimulation: physical principle, device and applications . . . 18

1.3 Transcranial Magnetic Stimulation: Physical principle, device and applications . . . 29

2 Numerical modeling and electromagnetic (EM) computational dosimetry of NIBS techniques **43**

2.1 The importance of simulating NIBS techniques . . . 43

2.2 An overview of the main computational methods . . . 45

2.3 Modeling the stimulator . . . 52

2.4 Modeling the human head . . . 55

3 Effect of Skin Conductivity on the Electric Field Induced by Transcranial Stimulation Techniques in Different Head Model **61**

3.1 Abstract 61
3.2 Introduction 62
3.3 Models and methods 66
3.4 Results 74
3.5 Discussion 77
3.6 Conclusions 79
3.7 Appendix 1: Reducing the anatomical complexity of the MIDA model . 80
3.8 Appendix 2:A simplified multilayered model of the skin to estimate the average σ_s in Duke and MIDA 81

4 Combining TMS, MRI and computational dosimetry: The effective navigated (En-)TMS 85
4.1 The effective navigated (En-)TMS: A novel approach for EM-dosimetry 85
4.2 Custom EM-code: Solution approach 88
4.3 Custom EM-code: Simulation set-up 95
4.4 Custom EM-code: Comparison between the isotropic and anisotropic brain model 96
4.5 A strategy for a real time solution 99
4.6 Discussion and future work 102

II Computational dosimetry on innovative devices and applications: the effects of low intensity pulsed magnetic fields 105

5 Exposure to low intensity, low frequency magnetic fields 107
5.1 Overview of the effects of ELF-MF exposure 107
5.2 Studies on humans 112

6 Patient Semi-specific Computational Modeling Applied to Neuroprotective Treatments in Acute Ischemic Stroke 119
6.1 Abstract 119
6.2 Introduction 120
6.3 Methods 123
6.4 Results 130
6.5 Discussion and conclusions 135

6.6 Appendix 1: Analysis on the best approximating frequency 139
6.7 Appendix 2: Variability assessment 142

7 The I-NIC project: A multicentric, randomized, double blind, placebo controlled study to assess LF PEMFs efficacy in ischemic patients 147
7.1 Introduction 147
7.2 Study protocol 149
7.3 Neuroradiological evaluation of the lesions and extraction of the 3D model 150
7.4 Dosimetrical analysis 155
7.5 Conclusions 161

III Computational dosimetry on innovative devices and applications: noninvasive magnetic stimulation with miniaturized coils 163

8 Electric field focality: a limitation in today's coils 165
8.1 Importance of a focal TMS 165
8.2 Solutions to augment TMS focality 167

9 A novel micro-technology device for focal noninvasive neural tissue stimulation 171
9.1 Abstract 171
9.2 Introduction 172
9.3 The m-Coil and the f-NIMS system 173
9.4 Stimulation experiments with the f-NIMS system 179
9.5 Electromagnetic modeling of the m-Coil and neuronal dynamics simulations 181
9.6 Discussions and conclusions 187
9.7 Appendix 188

10 Numerical investigation of different miniaturized coil designs 193
10.1 Abstract 193
10.2 Introduction 194
10.3 Models and Methods 195
10.4 Results 197

10.5 Discussion and conclusions 201

Conclusions **204**

Bibliography **217**

List of Figures

1.1 LeRoy's set up to stimulate the optic nerves in a blind subject. 10

1.2 D'Arsonval demonstrating magnetic stimulation on himself. 11

1.3 Demonstration of TMS application with the first prototype developed by Barker and Jalinus in 1985. 12

1.4 Schematization of existing stimulation techniques (Figure adapted from (Knotkova et al., 2019)). TMS and tDCS are higlighted in blue as they are the main topic of the thesis. Other invasive electrical stimulation techniques that are not mentioned in the text are: optical nerve stimulation (ONS), trigeminal nerve stimulation (TNS), vestibular prosthetics, direct peripheral nerve stimulation (DPNS) 14

1.5 Example of pad electrodes montage: (A) M1-SO montage. (B) Bifrontal montage (Figure adapted from (Borges et al., 2019)) 22

1.6 Example of supporting cap for HD-tDCS with 64 electrodes. Red and blue dots show anodal 4×1 ring configuration. Image adapted from `https://soterixmedical.com/research/hd-tdcs/accessories/hd-cap`. 23

1.7 Typical commercial TMS coil: (A) Circular coil, (B) Figure-8 coil, (C) Double-cone coil. Image adapted from `https://www.magstim.com`. . . . 34

2.1 2D representation of the Cartesian grid of the lumped electrical elements network. 50

2.2 Example of a commercial TMS figure-8 coil (PN9925-00, MagStimEden Prairie, MN) model and application: (a) The model, consisting in a current wire wound in the shape of an eight.
(b) B-field distribution computed on the plane parallel to the coil, at 5 mm distance from it. (c) B-field distribution computed on the plane perpendicular to the coil and crossing its center. (d) Example of coil location over the MIDA head model and B-field streamlines. (e) E-field distribution computed on the surface of the grey matter. 53

2.3 Example of tDCS pad electrodes model and application: (a) The electrodes model consists in two rectangular pads of 5 cm x 7 cm of Perfect Electric Conductor (PEC), placed over a saline soaked sponge. Each electrode is fed at its center by a metallic contact (cyan cylinder). (b) Example of electrodes placement over the MIDA head model and E-field streamlines. (e) E-field distribution computed on the surface of the grey matter. 54

2.4 The MIDA model (Iacono et al., 2015). A sagittal cut shows the different head structured included. 57

2.5 An example of patient specific model, generated from the dataset available from `https://simnibs.github.io/simnibs/build/html/dataset.html`. 58

3.1 Positioning of the tDCS electrodes (panels a and b) and the TMS coil (panels c and d) in correspondence of the primary motor area (M1) of MIDA (panels a and c) and Duke (panels b and d). 71

3.2 Normalized probability distribution of E-field intensity ($|E|$) induced by tDCS inside the grey matter (left) and the withe matter (right) for the two models: MIDA (upper row) and Duke (bottom row) and for different skin conductivities (σ): 0.0002 S/m (blue), 0.08 S/m (yellow), 0.17 S/m (cyan), and 0.465 S/m (magenta). In each panel the inset reports the 99_{th} percentile (E_{99}), considered as an accurate estimate of the maximum value, and the mean value (E_{mean}). 74

3.3 SMAPE distribution on the sagittal plane passing through the center of the cathode, calculated in tDCS stimulation, for the two models: MIDA (upper row) and Duke (bottom row), comparing σ=0.08 S/m with σ=0.0002 S/m (first column), σ=0.17 S/m with σ=0.0002 S/m (second column), and σ=0.465 S/m with σ=0.0002 S/m (third column). 75

3.4 SMAPE distribution on the sagittal plane crossing the left hemisphere at 1 mm from the center of the head, calculated in TMS stimulation, for the two models: MIDA (upper row) and Duke (bottom row), comparing σ_s=0.08 S/m with σ_s=0.0002 S/m (first column), σ_s=0.17 S/m with σ_s=0.0002 S/m (second column), and σ_s=0.465 S/m with σ_s=0.0002 S/m (third column)). 77

3.5 Coronal view of the two models MIDA and Duke taken at the center of the head. Nominal skin thickness is 1.5 mm for both models. All tissues common to both the models are listed in the legend. 80

3.6 E-field intensity distribution over the sagittal plane crossing the cathode: comparison between full detail MIDA model and reduced MIDA model. 81

3.7 Multilayered skin model inside two metallic parallel plates ($20mm \times 20mm$). Overall thickness is 1.5 mm, individual thicknesses and electric conductivity for each layer are: stratum corneum - 14 μm; σ=0.0002 S/m, cellular epidermis - 61 μm; σ=0.009 S/m, dermis - 1 mm; σ=0.526 S/m, and SAT – 0.425; σ=0.0417 S/m. 82

4.1 Flowchart summarizing the overall strategy adopted to perform E-field calculation (Scheme adapted from (Paffi et al., 2015b)) 89

4.2 Sketch showing the rototranslation operation of coil and brain domains. 91

4.3 Fractional anisotropy map over the three coordinate planes: Coronal and sagittal planes crossing the center of the head, and axial plane crossing the center of the forehead. The solid lines mark the contour of the grey and the white matter 92

4.4 Direction cosines map along the three cartesian directions. Red panel: cos$x$ over the three coordinate planes (coronal, sagittal, axial). Green panel: cos$y$ over the three coordinate planes (coronal, sagittal, axial). Blue panel: cos$z$ over the three coordinate planes (coronal, sagittal, axial) 93

4.5 Conductivity tensor: distribution maps of σ_{xx}, σ_{yy} and σ_{zz} over the coronal plane that crosses the center of the head 96

4.6 Comparison between the induced E-field computed on the anisotropic and isotropic brain. (a) $|E|$ distribution on the surface of the anisotropic brain cortex. (b) $|E|$ distribution on the surface of the isotropic brain cortex. (c) Distribution of the SMAPE between (a) and (b). 97

4.7 Analysis of the induced E-field components. (a) σ_{xx} values on the surface of the cortex. (b) $|E_x|$ distribution on the surface of the anisotropic brain cortex. (c) $|E_x|$ distribution on the surface of the isotropic brain cortex. (d) Distribution of the SMAPE between (b) and (c). (e) σ_{yy} values on the surface of the cortex. (f) $|E_y|$ distribution on the surface of the anisotropic brain cortex. (g) $|E_y|$ distribution on the surface of the isotropic brain cortex. (h) Distribution of the SMAPE between (f) and (g).(i) σ_{zz} values on the surface of the cortex. (l) $|E_z|$ distribution on the surface of the anisotropic brain cortex. (m) $|E_z|$ distribution on the surface of the isotropic brain cortex. (n) Distribution of the SMAPE between (l) and (m). 98

4.8 E-field and SMAPE distribution on the sagittal plane that crosses the coil center. (a)Results for the anisotropic brain. (b)Results for the isotropic brain. (c)SMAPE between (a) and (b). The area below the coil delimited by the dashed lines in expanded in the top row. 99

4.9 The methodology implemented for a real-time solution: the portion of brain below the center of the coil is selected and considered surrounded by a domain of CSF. 100

4.10 Comparison between the off-line and the real time solution: (Blue panel) Comparison on the coronal plane at y=127 mm for the isotropic brain. (Orange panel) Comparison on the coronal plane at y=126 mm for the anisotropic brain. 101

5.1 CNP signal pattern (Figure from (Camera et al., 2015)) 115

5.2 I-ONE signal in time, frequency, power spectrum, adapted from (Paffi et al., 2016). 116

6.1 Sketch of workflow, (a)step 1: solenoid model (experimentally validated), (b) step 2: semi-specific model based on reconstructed ischemic volume for each patient, (c) step 3: dosimetric evaluations. 124

6.2 Stimulation model. (a) Pulsed signal in frequency domain; simulated $\|\mathbf{B}\|$ (c) and measured $\|\mathbf{B}\|$ (d) on the plane of the coil. Measurements are conducted with the Gaussmeter/Teslameter Model DG-50, from the company Laboratorio Elettrofisico. 125

6.3 Final semi-specific patient models: all patients are shown on xz-plane. The shortest distance between the ischemia and the coil is defined as d_{min}.128

6.4 (a) Planes relative to the coil used to observe pre-treatment and post-treatment ischemic slices. (b) Example of volume selection: here the threshold is set for B to 1.7 mT. Inside the blue smaller circle: the volume of ischemia exposed to a B field equal or greater than 1.7 mT is represented in white; how that partial volume has changed after the treatment is shown in cyan. 129

6.5 Streamline view of **B** field along the frontal plane (f-plane in the coil based coordinate) for the three patients shows direction of the B field inside the head. In green: pre-treatment ischemic volume; in cyan: post-treatment ischemic volume. Blue inset shows the spatial gradient of $\|\mathbf{B}\|$ which the ischemia is exposed to during the treatment. 130

6.6 a) Time course of $\|\mathbf{B}\|$ field for all patients in the voxel of the pre-treatment ischemic volume that experiences the lowest B. All the three patients undergo to at least 1 mT; b) Time course of induced **J** for all patients in the voxel of the pre-treatment ischemic volume that experiences the highest value of **J**. 131

6.7 $\|\mathbf{B}\|$ field distribution of *patient AA* on the planes parallel to the coil. Analysis is carried out at different distances d from the coil. For each distance, the edges of the slice of ischemia before (pre, in light green) and after (post, in cyan) the treatment are given, in order to compare the dimensions. 132

6.8 Distribution of $\|\mathbf{B}\|$ on the plane parallel to the coil, for patient AA. Analysis is carried out at different distances 'd' from the coil. For each distance, the edges of the slice of ischemia before (pre, in light green) and after (post, in cyan) the treatment are given, in order to compare the dimensions. 134
6.9 Distribution of $\|\mathbf{B}\|$ on the frontal plane orthogonal to the coil (f-plane), for patient AA. Analysis is carried out at different distances 'f' from the coil. For each distance, the edges of the slice of ischemia before (pre, in light green) and after (post, in cyan) the treatment are given, in order to compare the dimensions. 135
6.10 Scatter plot of the percentage quantity "ratio" with respect to increasing values of lower bound B field thresholds. Data for the three patients are pooled together, resulting in a decaying exponential function. Ratio is defined as the percentage of $\text{Volume}_{post}/\text{Volume}_{pre}$, where:
Volume_{pre}= Ischemic pre-treatment volume that was exposed to B intensity greater than or equal to a certain threshold during the treatment.
Volume_{post} = Ischemic post-treatment volume that is present in a region of the brain that was exposed to a B intensity greater than or equal to a certain threshold, during the treatment. 137
6.11 Spectrogram of the current density signal. On top the time course is reported. On the side the spectrum. 140
6.12 Plot of the mean SMAPE over the frequency. 141
6.13 Coil misplacement. Left panel: reference position of the coil. Right panel: representation of the coil shifts by 1 cm along the transversal (top) and longitudinal (bottom) direction. $\|\mathbf{B}\|$ distribution on the surface of the coil is reported. 142
6.14 Histograms showing frequency of occurrence of $\|\mathbf{B}\|$ inside the ischemic volume when placing the coil in different positions over the head. . . . 143
6.15 The semi-specific head model built-up with ViP Glenn (left panel), MIDA (central panel) and ViP Duke (right panel). $\|\mathbf{B}\|$ on the surface of the ischemic lesion is reported for all the three models. 144
6.16 Histograms showing frequency of occurrence of $\|\mathbf{B}\|$ inside the ischemic volume when placed in three different human head models, i.e. Duke, Glenn and MIDA. 145

7.1 Flow-chart of the I-NIC study 149
7.2 Results of segmentation using the thresholding method: comparison between two different values of Thr_{min}. 151
7.3 Examples of segmentation. Top: Segmentation from an active patient recruited at Nuovo Ospedale Civile S.Agostino Estense, Modena. In red is the segmentation of hypointense areas. Bottom: Segmentation from a placebo patient recruited at Nuovo Ospedale Civile S.Agostino Estense, Modena. In red is the segmentation of hypointense areas. 152
7.4 Example of intracranial hemorrhage score. (a) Patient with score 0.(b) Patient with score 1.(c) Patient with score 2. 154
7.5 Semi-specific model for two recruited patients. Top panel: Active patient Modena 8. Bottom panel: Placebo patient Modena 1. In green and in cyan are the pre- and post-treatment lesions respectively. In grey the chronic ischemic volume affected by a hypointense signal level is reported. The stimulating coil is modeled as a current wire placed over the head. 156
7.6 B field distribution on the surface of the ischemic lesions that are characterized by a volume above 10 cm^3 157
7.7 Patient Modena 8: B field distribution on planes parallel to the coil and at different distances d. For each distance, contours of slices of ischemia before (pre,in light green) and after (post hyperintense in cyan and post hypointense in red) the treatment are given, in order to compare the dimensions. 158
7.8 Patient Modena 1: B field distribution on planes parallel to the coil and at different distances d. For each distance, contours of slices of ischemia before (pre,in light green) and after (post hyperintense in cyan and post hypointense in red) the treatment are given, in order to compare the dimensions. 158
7.9 Boxplot of the ratio between post-treatment and pre-treatment volumes as a function of B-field intensities, for active (red) and placebo (blue) patients. In the boxplot, top and bottom line of the box are the 1st and 3rd quartile respectively, inside line is the mean value. The vertical lines (or whiskers) show maximum and minimum value of the distribution. . . 160

8.1 Figure taken and adapted from (Deng et al., 2013; Gomez et al., 2018): Optimal trade-off between focality $S_{1/2}$, and depth, $d_{1/2}$ for the 50 coil studied in (Deng et al., 2013), see the reference for identification of the specific coils corresponding to the numbers. 168

9.1 Comparison between the m-Coil and a commercial figure-8 coil. Purple inset shows the dimensions of a single m-Coil. 174

9.2 Block diagram of the f-NIMS system 175

9.3 Electrical characterization. (A) Frequency response of the m-Coil on the range from 20 Hz to 120 MHz. (B) Magnitude and phase of the impedance Zs and (C) Series resistance Rs and inductance Ls in the frequency range 20 Hz – 100 kHz. 177

9.4 Output of the f-NIMS system measured from the positive channel (v+) at experimental conditions: (A)Voltage pulse, (B)Current pulse. 178

9.5 Recorded sensory nerve action potentials (SNAPs): (A) Position of stimulating electrodes to detect the radial nerve. (B-C) Position of the m-Coil and recording electrodes during the stimulation 179

9.6 Recorded sensory nerve action potentials (SNAPs): (A)-(B) Electric stimulation and m-Coil stimulation on the same subject: recording from snuff (black trace) and from the thumb (red trace). (C) m-Coil stimulation: different recordings from the snuff of the same subject. (D) m-Coil stimulation: recording from the Snuff of different subjects. 180

9.7 Numerical comparison between the m-Coil and the standard Figure-8 TMS coil. (A).The m-coil model and MagStim figure-8 (PN9925-00) model. (B) Electric field intensity distribution generated by the m-Coil at 1.9 kHz (top) and by the figure-8 coil at 3 kHz (bottom) on a slab of dielectric material (σ=0.3 S/m). 182

9.8 Electric field intensity distribution generated by the m-Coil (top) and by the figure-8 coil (bottom) in the section of cortex highlighted in cyan. 183

9.9 Modeling the experiments: position of the m-Coil over the wrist of one subject (left). Position of the m-Coil model over the wrist of the neurofunctionalized model Yoon-Sun, position of the stimulation area and recording site are shown as well. 184

9.10 Distribution of $\mid E \mid$. Left: $\mid E \mid$ on the surface of nerve and muscles (cyan inset shows detail below the coil). Center and Right: $\mid E \mid$ on two cross-sectional planes of the arm - sagittal (Right) and transversal (Center) - that pass through the center of the m-Coil. 185
9.11 Lilac sub panel shows the action potential computed for the suprathreshold stimulation at the recording site. Blue sub-panel panel shows (Top) distribution of $\mid E \mid$ on the surface of the nerve. Two spheres represent the center of the coil and the position of the first action potential (AP), as computed from neuron. Distance between the two is 7.5 mm. (Bottom) Activating function (AF) along the nerve fiber. Distance between center of the coil and position of first AP, as estimated by the activating function is 7 mm. 186
9.12 (A) Z-component of the B field (B_z) generated by the physical m-Coil when fed at 20 A (left) and position of the m-Coil during the experiments. (B) Simulated Z-component of the B-field (B_z) generated by the m-Coil model fed at 20 A (right). 188
9.13 Box plot representation of the distribution of Δ_{max} (maximum variation with respect to the m-Coil position) computed over the 20 superficial fibers available in the model(red splines). Top and bottom line of the box are the 1st and 3rd quartile respectively, the x represents the mean value. The vertical lines (or whiskers) show maximum and minimum value. Inner points and outliers are also reported.Arrows show direction of longitudinal shifting (Blue), transversal shifting (orange), tilting (grey) and lifting (yellow). 190
9.14 Sagittal and coronal view of the two anatomical models Jeduk and Yoon-Sun. Blue splines represent the deep branch of the radial nerve. Red splines represent the superficial branch of the radial nerve. Grey spheres show location of numerically estimated stimulation site. 191
9.15 Variability study over changes in the conductivity. The box plot represents the distribution of Δ_{max} (maximum variation) computed over the 20 superficial fibers available in the model. Top and bottom line of the box are the 1st and 3rd quartile respectively, the x represents the mean value. The vertical lines (or whiskers) show maximum and minimum value. 192

10.1 Four figure-8 m-Coils models: m-Coil models and placement over the right arm of the neurofunctionalized model Yoon-Sun, and the point where the two figure-8 m-Coils touch was precisely above the nerve trajectory in the wrist area. 197
10.2 Vector view of the **B** field generated by each m-Coil model. Arrows show direction, orientation and intensity of **B**. Intensities of **B** are represented by a color bar in a logarithmic scale with 0 dB referenced to 40 mT, which is the maximum | **B** | induced on the surface of the skin by the air core figure-of-eight m-Coil (Panel c) when fed with 1 A. 198
10.3 Direction, orientation, and intensity of the E field induced in the arm of the Yoon-Sun model on the longitudinal plane of the arm that crosses the center of the stimulating coil. A vector view of the E field is superimposed on the intensities distribution map. 199
10.4 The tangential (left) and normal (right) components of the E field-induced along the nerve by the 2-layered circular m-Coil, the 4-layered circular m-Coil, and figure-8 m-Coil. 200

List of Tables

3.1 Values of skin conductivity (σ_s) (1st column) and related reference (2nd column) used in numerical studies (3rd column) dealing with different kinds of exposure (4th column) and frequencies (5th column). 67

3.2 Estimated overall σ_s considering the reference values of thickness and conductivity given in (Tsai et al., 2019) (SC = Stratum corneum). . . . 83

3.3 Estimated overall σ_s considering the lower extremity value of thickness for stratum corneum (SC), epidermis and dermis and reference values for conductivity, as given in (Tsai et al., 2019). 83

3.4 Estimated overall σ_s considering the upper extremity value of thickness for stratum corneum (SC), epidermis and dermis and reference values for conductivity, as given in (Tsai et al., 2019). 83

3.5 Estimated overall σ_s considering the reference value of thickness for stratum corneum (SC), epidermis and dermis and lower std deviation for conductivity of epidermis and dermis, as given in (Tsai et al., 2019). . . 84

3.6 Estimated overall σ_s considering the reference value of thickness for stratum corneum (SC), epidermis and dermis and upper std deviation for conductivity of epidermis and dermis, as given in (Tsai et al., 2019). . . 84

6.1 Ratio between post-treatment and pre-treatment ischemic volume regions, selected based on the different ranges of exposure they experience. The slash symbol shows that neither pre-treatment nor post-treatment ischemia is present in that specific region. 136

6.2 Ratio between post treatment and pre treatment ischemic region of volumes, selected based on the different ranges of exposure they experience. The slash symbol shows that neither pre treatment nor post treatment ischemia is present in that specific region. 136

7.1 Results of the neuroradiological evaluation. (*) Indicates presence of hypointense areas of which it was not possible to determine the entity, due to the absence of T_2* and T_1 sequences. 155
7.2 Ratio between post-treatment and pre-treatment ischemic volume regions, selected based on the different ranges of exposure they experience. 159

9.1 Comparison between the f-NIMS system and a Standard TMS system. . 176
9.2 Electric conductivity of the simulated tissues: values considered in the variability study. 191

Abstract

The use of electromagnetic (EM) fields for medical applications has extensively grown over the past decades, to the point that the novel term "Electroceuticals" was coined to identify the potentialities of EM fields as an option over drug treatments ("Pharmaceuticals"). A particular branch of electroceuticals are the noninvasive brain stimulation (NIBS) techniques, examples of which are transcranial magnetic stimulation (TMS) and transcranial direct current stimulation (tDCS), that have been extensively studied for the treatment of several psychiatric disorders and neurological diseases. These techniques exert their therapeutic effect by means of an electric field, either induced by a pulsed magnetic field, or generated by injected currents, respectively. Nonetheless, the field of brain stimulation is constantly growing, and increasing efforts are applied to develop novel techniques or to ameliorate existing ones. A fundamental tool that supports the growth and expansion of noninvasive brain stimulation advances in the medical field is the use of numerical dosimetry, that provide an important insight to the mechanisms of action behind brain stimulation by correlating the physiological outcome with the induced EM quantities. Furthermore, it can help optimizing existing techniques to improve the treatment efficacy, as in the case of neuronavigated stimulation, or assessing innovative approaches. In this regard, an accurate modeling, that considers the stimulation device as well as the subject's head, becomes of paramount importance together with understanding all the parameters that can affect the estimation of the induced EM quantities. In this thesis numerical dosimetry of standard and innovative brain stimulation techniques is conducted. Concerning standard techniques, such as tDCS and TMS, the aim is to investigate the influence of tissue properties on the EM solution, moreover an alternative EM dosimetry custom code for neuronavigated TMS is proposed. A new methodology is also proposed to assess the therapeutic efficacy of a novel treatment that apply low frequency pulsed magnetic fields to treat patients with acute cerebral ischemic stroke. Finally, aiming to overcome TMS low spatial selectivity, a prototype of miniaturized coil was developed and characterized both experimentally and numerically to demonstrate its ability to elicit stimulation of neural tissues on healthy subjects.

Introduction and thesis outline

Over the past decades the use of electromagnetic (EM) fields in medicine has broadly expanded and continues to affirm itself each year with the development of new technologies and devices, to the point that the new terminology "*Electroceuticals*" was specifically coined in 2013 by the bioelectronics research group at GSK (London), headed by Kristoffer Famm (Famm et al., 2013), to identify the family of techniques that apply EM fields as an alternative to standard pharmaceutical treatments. In contrast with standard systemic pharmacotherapy, electroceuticals are potentially able to restore the healthy balance of the body in a more selective and organ-specific way, since their "active ingredient" is the electric pulse, which is the phenomenon that any living organism puts into play to transfer information across different body compartments and to regulate its physiological functions. Electrical impulses flow through the networks of cells that compose the nervous system, i.e. neurons and nerves, which, therefore, become the sensitive target for electroceutical therapy, that consists in applying a stimulation to restore a broken communication pattern or to alter physiological activities triggered by a pathological status, by enhancing them or inhibiting them. The electroceutical devices developed until now, either approved for use in clinics or still under investigation in research, provide the stimulation to specific nerves or brain areas invasively, by implanted stimulators, or noninvasively, by stimulators placed in contact with the surface of the skin. As the nervous system, whether is the central or the peripheral, is very compact and made of independent circuits that often run close to one another, both invasive and noninvasive treatments cause an unavoidable and unwanted stimulation of non-targeted cells that makes it non trivial to interpret the clinical outcome and may determine the onset of side effects. Thus, as for any pharmacological treatment, in

which characterizing the relationship between the drug dose and its consequent effect is a fundamental step to control the clinical benefits, also for electroceuticals there are aspects that must be assessed to guarantee a successful therapy. First, it is necessary to localize all the areas that are interested by the stimulation; secondly, the EM quantities induced in the biological tissues must be quantified and correlated to the physiological outcomes. Such analysis can be conducted experimentally, by using proper exposure systems and instruments that allow to measure the effects of the EM field, and how it varies with changes in the stimulation parameters. This is known as experimental dosimetry, which, however, is not always trivial to carry out.

Therefore, the use of computational dosimetry, which consists in reproducing the experiments *in-silico*, is assuming an increasing importance to understand the biological effects induced by stimulation with EM fields, since it guarantees a greater degree of reproducibility over experiments and allows to study quantities that would be more difficult to be accounted for experimentally. Furthermore, computational study can be performed in a multiphysics approach. This allows to combine the EM quantities induced by the stimulation, with biophysical models, that reproduce the physiological activity of neuronal cells. This being said, there are some critical aspects concerning the computational dosimetry as well. In order to obtain reliable results, an accurate dosimetrical model must be considered and should properly reproduce the characteristics of the stimulator as well as those of the stimulated body part, since they both influence the distribution of the EM quantities responsible for the physiological effects observed experimentally. Therefore, an inaccurate modeling could lead to a misinterpretation of the experimental outcomes. The work conducted during this thesis focused on carrying out the numerical dosimetry for noninvasive brain stimulation (NIBS) techniques, with the aim to investigate different aspects that are still open questions in the research field. It moved from two well known applications, i.e. transcranial magnetic stimulation (TMS) and transcranial direct current stimulation (tDCS), to eventually investigate innovative aspects of magnetic stimulation. TMS and tDCS are extensively studied in literature, but the parameters to be set to conduct an accurate EM dosimetry haven't been standardized yet. Particularly critical is the level of detail needed to describe the head model as well as the EM properties to be assigned to each tissue, and particularly to the layer of skin.

This aspect is investigated in Part I of the thesis. After reporting an overview of the main applications of TMS and tDCS, and a description of the different methodologies

applied nowadays to study such techniques numerically, the section presents the work performed to understand how tissue characteristics affect the estimation of the electric field for both techniques, with particular attention to TMS, for which a novel code for the EM dosimetry was developed, as part of the En-TMS project (POR FESR LAZIO 2014 – 2020), carried out in collaboration with Sentech S.r.l., InfoSolution S.p.a., and the department of Physiology and Farmacology "Vittorio Erspamer", at University of Rome "La Sapienza". Focusing on TMS, it is well known that its mechanism of action accounts for two different effects: an acute effect exerted by the stimulation and a long term effect caused by the neuromodulation that acts at the level of the neurotransmitters. This last effect can be the only one to be exerted when TMS is applied at low intensities and low frequencies, either in continuous wave (LF-EMF) or pulsed wave (LF-PEMF). In Part II, an overview of the biological effects of LF-EMF is reported, followed by the description of a new dosimetrical methodology proposed to conduct the dosimetrical analysis on a novel PEMF therapy, that is currently under investigation as an alternative therapy for the treatment of acute ischemic stroke in a multicentric, randomized, double-blind, placebo controlled study conducted in collaboration with IGEA Clinical Biophysics S.p.a.

Finally, despite its great potential and numerous applications, TMS is strongly limited by its poor spatial resolution, which prevent from a selective stimulation of specific brain areas. Therefore a great effort has been applied in literature to augment TMS focality and several strategies have been proposed over the years. In Part III, a novel miniaturized coil for noninvasive magnetic stimulation is presented. The work reported in this section was carried out in collaboration with the Athinoula A. Martinos Center, where the coil was designed and developed, and the Beth Israel Deaconess Medical Center, were it was tested on the peripheral nervous system of healthy volunteers. The numerical model of the coil was developed to conduct the computational dosimetry of the experiments in a multiphysics approach, to investigate and assess all the parameters that would affect the stimulation outcome.

Part I

Magnetic and Electric fields applied to noninvasive brain stimulation: the fundamental role of numerical dosimetry

Chapter 1

Non-invasive brain stimulation - NIBS

"Imagine a day when electrical impulses are a mainstay of medical treatment. Your clinician will administer electroceuticals that target individual nerve fibres or specific brain circuits to treat an array of conditions. These will modulate the neural impulses that control the body, repair lost function and reinstate a healthy balance."(Famm et al., 2013). As futuristic as this statement may seem, the use of electricity as a therapeutic tool dates back to the age of the Roman Empire. As a matter of fact, in 46 AD, Scribonius Largus, physician of Emperor Claudius, reported in his book *Compositiones Medicamentorum* the use of torpedo fish to treat headaches and gouts (Cambiaghi and Parent, 2018). Presumably, the electrical shocks released by the torpedo fish would strike the peripheral skin receptors, or affect spinal or brain structures, leading to a transient period of pain relief. Such applications of torpedo fish were a very early means of transcutaneous electrical nerve stimulation (TENS) for therapeutic purposes (Pascual-Leone and Wagner, 2007). In spite of the fact that this procedure had been used across different ages and civilization, it was with the Industrial Revolution in the 18th century that the effects of electricity on human and animal tissues were studied in a biomedical perspective (Cambiaghi and Parent, 2018). Already in 1755, French physician Charles LeRoy unknowingly demonstrated the excitability of the optic nerves during an attempt to restore the sight of a blind patient, by means of electric wires wound around the patient's head (Fig. 1.1) (Pascual-Leone and Wagner, 2007; Lewis and Rosenfeld, 2015).

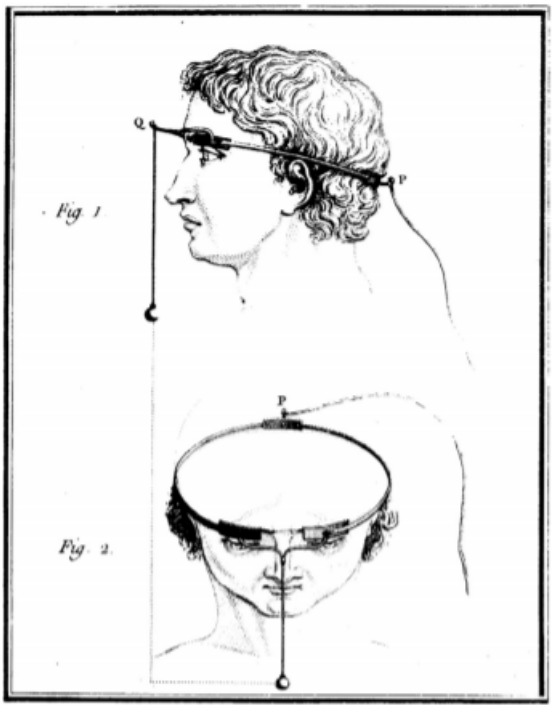

Figure 1.1: LeRoy's set up to stimulate the optic nerves in a blind subject.

Thirty years later, in 1787 Luigi Galvani demonstrated electrical excitability of muscles and nerves, experimenting on frogs' legs (Cambiaghi and Parent, 2018), and in the early 1800s, Galvani's nephew, Giovanni Aldini, applied electrical stimulation to the human cerebral cortex, for the first time, showing facial muscle contractions caused by direct activation of the facial nerves (Zago et al., 2008). Moreover he applied weak transcranial direct-currents (DC) to treat individuals suffering from melancholia, a depression like syndrome (Parent, 2004). The interest in such revolutionary medical approach and the enthusiasm related to its beneficial effects grew rapidly over the 18th century, as openly declared by the words of Eusebio Sguario, that described how research on electricity was oriented towards healing medical conditions, just after understanding its effect on human bodies:
"Ciò che ricercano gli uomini dalle scienze non essendo solamente il dilettevole, quanto l'utile [...]: appena si conobbe, che tanto era il potere che aveva l'elettricità sui corpi umani, che subito si ricerco s'ella avrebbe potuto mai per buona ventura apportar qualche sollievo ai mancamenti della salute. Nessun pensiero era più facile a cader

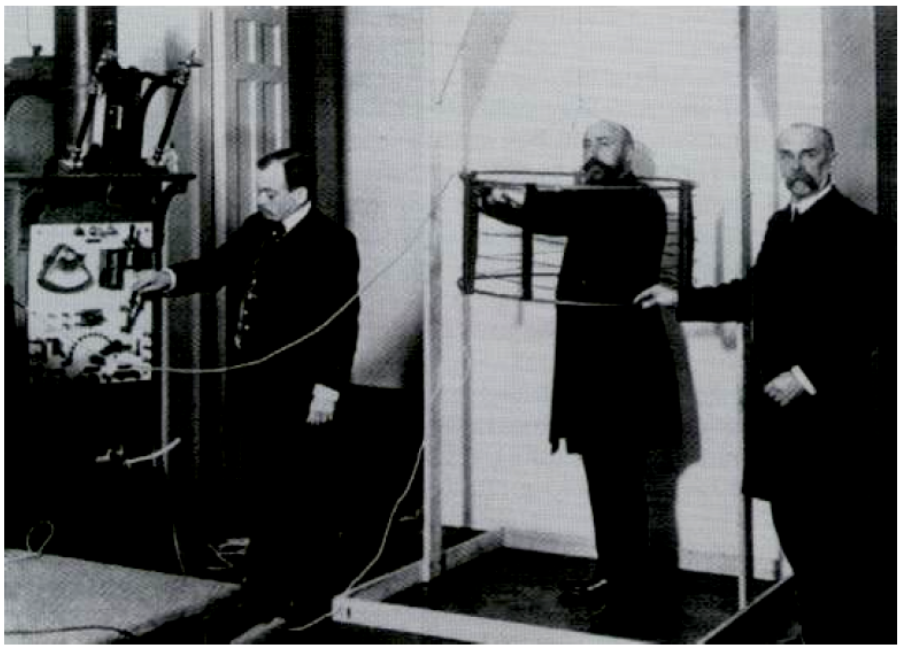

Figure 1.2: D'Arsonval demonstrating magnetic stimulation on himself.

in mente di questo".
(Translation from (Cambiaghi and Parent, 2018): What people look for in science is not only pleasure, but usefulness [...]: as soon as the power of electricity on human bodies was known, research was initiated to see if it could be used to bring relief to the failures of health. No thought was easier to conceive than that one...). Several physicians continued to experiment DC for the treatment of mental disorders during the 19th century and the early part of the 20th century, but the variation of procedures, unclear descriptions and few qualitative details led to variable and sometimes inconclusive results, thus the use of DC stimulation was abandoned until the 1960's (Sarmiento et al., 2016), when numerous researchers started to experiment weak (0.25 μA/mm^2 - 20 μA/mm^2) DC applied directly to the exposed cortex of animals, showing alterations in the level of neural excitability (Pascual-Leone and Wagner, 2007; Sarmiento et al., 2016). Eventually, in 1998, Priori and his colleagues investigated the influence of DC in the brain by testing its effects on cerebral cortex excitability, thus promoting the usage of DC and laying the ground for modern tDCS (transcranial Direct Current Stimulation) (Priori et al., 1998; Sarmiento et al., 2016).

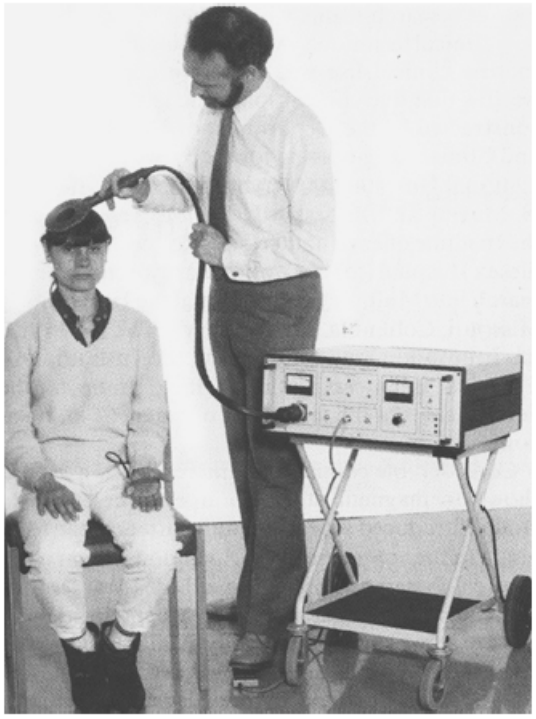

Figure 1.3: Demonstration of TMS application with the first prototype developed by Barker and Jalinus in 1985.

While the use of electric stimulation in medicine has ancient roots, magnetic stimulation was first studied at the end of the 19th century as an implication of Faraday's Law. The first to report the effect of magnetic stimulation was the physicist Jaques-Arsène d'Arsonval in his paper "Apparatus for Measuring Alternating Currents of All Frequencies" where he found that "*an intensity of 110 V, 30 A with a frequency of 42 cycles per second, gives rise to, when one places the head into the coil, phosphenes and vertigo*" (Fig. 1.2) (Pascual-Leone and Wagner, 2007; Reif-Acherman, 2017). Other physicits, among which was Thompson in 1910, indipendetly reported similar results of visual excitation of the retina (Thompson, 1910). It was between the 1960 and the 1980 that the ability of a time varying magnetic field to elicit muscular contractions was demonstrated and intensively studied on animals and humans (Geddes, 1991). Particularly, in 1976, Barker and co-workers developed the first stimulator capable of generating peak fields of 2.2 T with a rise time of approximately 100 μs and studied the possibility to achieve velocity-selective nerve stimulation (Barker et al., 1979; Geddes,

1991). Since at that time, the generation of motor evoked potentials was becoming of increasing interest, in 1985 Barker and Jalinus demonstrated that their magnetic stimulator, placed over appropriate regions of the motor cortex, could elicit movements of the hand or the leg, without causing distress or pain (Barker et al., 1985) (see Fig. 1.3). Given its ability to noninvasively stimulate the brain with minimal discomfort for the subject, the interest in magnetic stimulation continued to grow, and although it originated as a diagnostic and investigational tool, it moved fast towards the therapeutic applications in neurology, psychiatry and rehabilitation(Horvath et al., 2011).

1.1 Overview of invasive and noninvasive brain stimulation techniques

Two centuries of research and discoveries on how electricity and magnetism interact with the human body, and particularly with the central nervous system, led to the development of modern electroceuticals, a new category of therapeutic agents whose targets are the neuronal circuits, which are the main and preferential communication pathway between organs (Mishra, 2017). In fact, the language of our body is made of electrical impulses that travel along the neuronal fibers and reach specific target sites, such as nervous terminations or neurotransmitters, therefore the use of electroceuticals potentially allows for a direct intervention that would reestablish a healthy balance in the body, when lost, in a much more selective and organ specific way over standard systemic pharmacotherapy (Famm et al., 2013; Mishra, 2017; Horn et al., 2019). Several electroceuticals therapies are currently FDA approved for the treatment of different conditions, such as obesity, treated by stimulation of the ventral and dorsal gastric branches of the vagus nerve, or urinary incontinence, treated by stimulation of the third sacral nerve root (Horn et al., 2019). These applications testify the growing relevance of electroceuticals in the medical field. The target of the electroceuticals can be cardiac, thoracic, as well as abdnominal, but a particular class of devices aims to treat neurological diseases and psychiatric disorders, and go under the name of brain stimulation (BS) techniques, a set of technologies that is able to interact with the brain activity in a way to induce controlled and controllable manipulations of the neuronal activity. Modern BS covers a wide range of applications, and the techniques often overlap in terms of the physiological mechanism they induce. A scheme of the existing

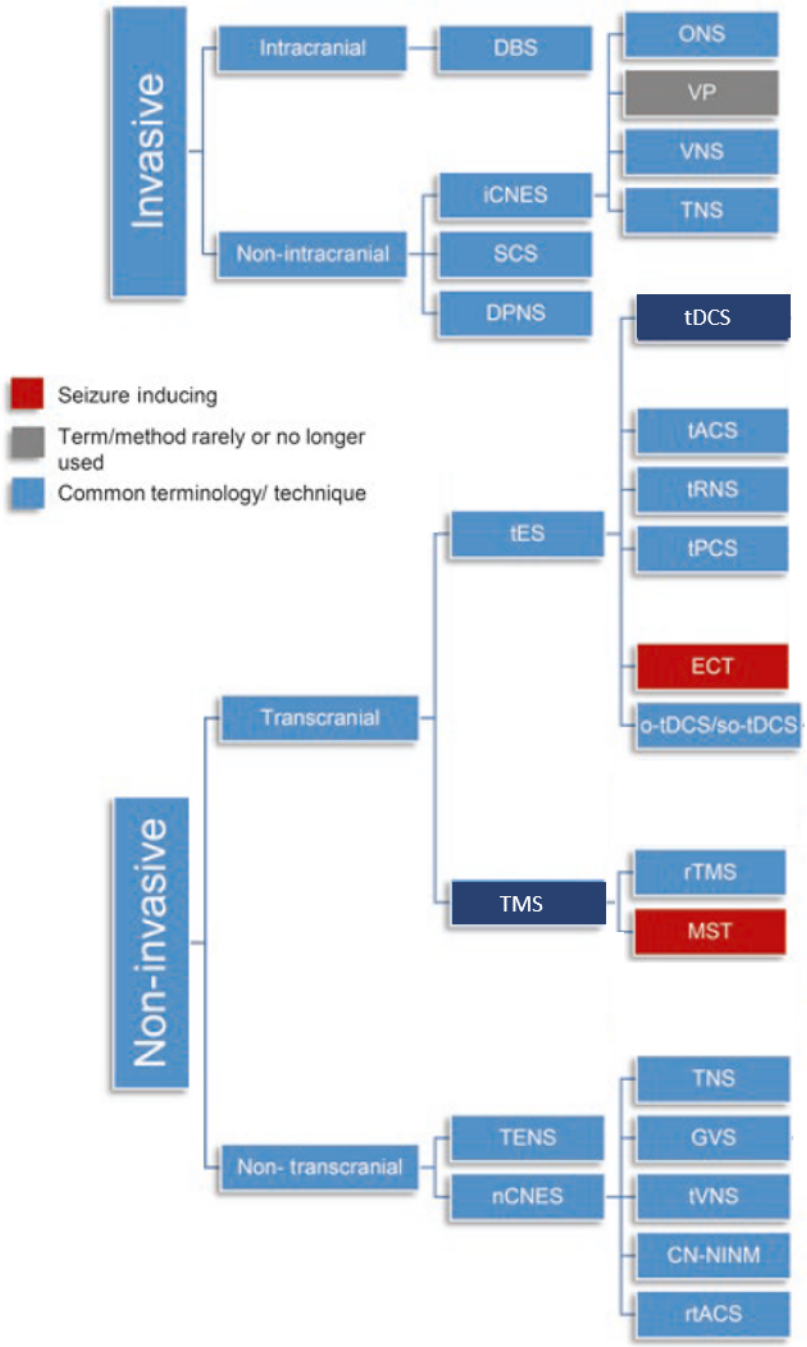

Figure 1.4: Schematization of existing stimulation techniques (Figure adapted from (Knotkova et al., 2019)). TMS and tDCS are higlighted in blue as they are the main topic of the thesis. Other invasive electrical stimulation techniques that are not mentioned in the text are: optical nerve stimulation (ONS), trigeminal nerve stimulation (TNS), vestibular prosthetics, direct peripheral nerve stimulation (DPNS)

stimulation techniques is reported in Fig. 1.4 (Knotkova et al., 2019).

Invasive techniques

It is now frequent in the clinical practice to use implanted devices that directly acts on specific brain areas or nerves to gain the therapeutic effect. The electric stimulus is administered through electrodes and generated by a neurostimulator. A commonly used device for intracranial stimulation is the deep brain stimulator (DBS), which is FDA and CE-approved for the treatment of epilepsy and motor dysfunctions such as Parkinson's disease (PD), essential tremor (ET), or dystonia (Lozano et al., 2019). Therefore, the target areas for DBS are the basal ganglia, which are the brain regions associated with the control of voluntary motor movements. Particularly, the subthalamic nucleus as well as the globus pallidus (GP) are possible targets for PD (Odekerken et al., 2016; Lozano et al., 2019), although GP is more established to treat dystonia (Moro et al., 2017). Thalamic ventral intermediate nucleus stimulation is frequently applied for ET (Cury et al., 2017; Lozano et al., 2019). As with all the brain stimulation techniques, the mechanism of action of DBS is still under investigation, nonetheless it is thought to disrupt the pathological brain circuit activity at the network and ionic level, thus generating the improvements in symptoms (McIntyre and Anderson, 2016; Ashkan et al., 2017; Lozano et al., 2019).

Conversely to DBS, several other stimulation techniques are defined as extra-cranial, since they target extra-cranial structures such as cranial nerves, spinal cord tracts or peripheral nerves. An example of cranial nerve electrical stimulation (CNES) is the vagus nerve stimulation (VNS), which target the left vagus nerve, one of the two nerves that run from the brainstem through the neck and down to each side of the chest and abdomen. The VNS has been originally used by physicians to treat epilepsy for patients that did not respond to anti-seizure drugs (Wright et al., 2017; Johnson and Wilson, 2018), but is currently explored for the treatment of several other conditions, due to its anti-inflammatory properties (Johnson and Wilson, 2018; Horn et al., 2019), as previously mentioned. Most commonly, the pulse used in VNS for epilepsy treatment is a current pulse in the range of 1.50 mA - 2.25 mA, 250 μs wide, delivered at a frequency of 20 Hz (Wheless et al., 2018). As for all the stimulation techniques, the mechanism of action underlying the antiepileptic effect of VNS is not fully understood, but scientific evidence shows that it likely involves the brainstem nuclei, which contain noradrenergic and serotonergic neurons that exert antiepileptic effects (Panebianco et al., 2015). Another invasive extracranial stimulation technique is the spinal cord stimulation (SCS), which is applied to treat chronic neuropathic pain, by means of

stimulating leads placed into the epidural space, that are fed by a programmable pulse generator, surgically implanted subcutaneously (Kreis and Fishman, 2009). SCS is considered to neutralize the overexcitability of wide dynamic range neurons, which are responsible for the response to painful stimuli and cause an abnormal transmission of pain sensation to the brain when they receive excessive nociceptive inputs (Dones and Levi, 2018).

Noninvasive techniques

Whenever the stimulation is given across the scalp, rather than with stimulators surgically implanted inside specific brain areas, it is said to be noninvasive (NIBS). Similarly to invasive BS, NIBS techniques can induce an alteration of the brain activity and neuronal connections, and cause changes in brain plasticity, consequently inducing changes in cognitive, behavioral, and emotional processes, therefore making NIBS not only a powerful therapeutic tool, but an efficient neuro-investigative and diagnostic tool, as well. Additionally, given their ability to induce long-term effects, considerable effort has been made over the years also in demonstrating their potential in the treatment of a variety of neurological disorders, such as Parkinson's disease, tinnitus, epilepsy or chronic pain, and psychiatric diseases, among which are depression, obsessive-compulsive disorder, and schizophrenia, thus becoming possible alternatives to the pharmacological treatments. Therapeutic role of NIBS has been also demonstrated for poststroke rehabilitation of aphasia or of hand function (Klomjai et al., 2015; Biou et al., 2019).

Existing NIBS techniques include electric and magnetic stimulation as well as the emerging technique of focus ultrasound stimulation (FUS), that uses acoustic pulses to induce changes in cortical excitability with a millimetric resolution (Polanía et al., 2018). In this thesis, only electric and magnetic stimulation is investigated. The main electric and magnetic NIBS techniques are reported in Fig. 1.4 and can be divided into two major groups, on the basis of the physical principle involved: transcranial magnetic stimulation (TMS), that is based on the electromagnetic induction, and transcranial electric stimulation (TES) that applies currents to the scalp, by means of superficial electrodes. In turns, both techniques can be further divided depending on the intensity of the stimulating current, that can be equal to or above the stimulation threshold, therefore inducing a neurostimulatory and neuromodulatory effect, or it can be below the stimulation threshold, thus inducing only a neuromodulatory effect. When applied at high current intensities, TES is commonly known as Electroconvulsive Therapy or ECT. This is a seizure inducing technique that applies high intensity pulsed currents

through the scalp. It is mostly used for the treatment of drug resistant depression, although it is painful and requires anaesthesia (Yrondi et al., 2018). Therefore, many researchers moved towards investigating possible beneficial effects of low intensity stimulation. When low current intensities are applied, TES is defined as tES. The most well known tES technique is transcranial direct current stimulation, or tDCS, which consists in delivering low-intensity (0.5 mA – 2 mA) direct currents through two or more electrodes applied on the surface of the scalp and that will be extensively described in Section 1.2. Other variations of tDCS consist in delivering currents at higher frequencies, with the aim to directly interact with the EEG brain waves. Among these, is transcranial alternating current stimulation (tACS), which delivers through the scalp a sinusoidal low intensity current at frequencies in the EEG spectrum, therefore synchronizing with the ongoing rhythmic activity of the human brain, and determining behavioural effects (Antal and Paulus, 2013; Herrmann et al., 2013; Tavakoli and Yun, 2017). So far, tACS is currently employed as a neuro-invastigative tool and it is studied as a possible treatment for neurological and psychiatric disorders caused by abnormal oscillatory patterns, such as Parkinson's, disease or schizophrenia, as it would facilitate the restore of normal oscillations (Antal and Paulus, 2013). Nevertheless, a tACS methodology has not yet been standardized (Tavakoli and Yun, 2017).
Possible alternatives to tACS are transcranial random noise stimulation (tRNS) and transcranial pulsed current stimulation (tPCS). The first consists in applying a current that alternates at random frequencies (normally distributed between 0.1 Hz and 640 Hz), with amplitudes within a specific range in the mA (Reed and Cohen Kadosh, 2018). tRNS is a relatively recent stimulation technique and its mechanisms of action are still under investigation, but its effects are thought to be similar to those of tACS, with the advantage of being less epileptogenic (Terney et al., 2008). For what concerns tPCS, it is a neuromodulatory paradigm that consists in interrupting tDCS in order to take advantage of two extra parameters, "pulse duration (PD)" and "inter-pulse interval (IPI)", which may affect the cortico-spinal excitability (Jaberzadeh et al., 2014). Its mechanisms of action and effects are still under investigation. Nonetheless, studies have reported that weak electrical pulsed currents can induce changes in the brain activity of healthy subjects (Jaberzadeh et al., 2014; Morales-Quezada et al., 2014), particularly a modulation of the inter-hemispheric coherence was noticed, with a net increment for the theta and beta waves, which suggests a state of network synchrony among neuronal populations (Morales-Quezada et al., 2014). Noninvasive electrical

stimulation can also target cranial nerves (nCNES), such as the vagus nerve (tVNS) or the trigeminal nerve (TNS), the galvanic vestibular stimulation (GVS), or peripheral nerves, with the transcutaneous electrical nerve stimulation (TENS), Fig. 1.4. For what concerns transcranial magnetic stimulation, it was applied from the beginning at intensities above the stimulation threshold in order to propose it as an effective and less painful substitute to high intensity ES. Standard TMS consists in sending to the cortex high-intensity magnetic pulses of different shapes and with different protocols and will be described in detail in section 1.3. An alternative to TMS is magnetic seizure therapy (MST), which consists in sending to the cortex a train of high intensity magnetic pulses at a frequency > 60 Hz. Such frequency allows to induce seizures in the brain (Lisanby et al., 2003). MST is currently studied as a possible substitute of the electroconvulsive therapy (ECT), in the treatment of drug resistant depression (Kayser et al., 2015; Daskalakis et al., 2020).
Magnetic fields can interact with the nervous system at lower frequency and intensity as well. The effect of extremely low frequency magnetic field (ELF-MF) was at first investigated in the field of protectionism to guarantee a safe exposure to both the general public and the workers, particularly from power lines, that would cause perception of magnetophosphenes (Ziegelberger et al., 2020). Nevertheless, in-vivo and in-vitro studies conducted over the years, showed how ELF-MF exposure could also alter brain activity, modifying several neuronal functions, such as motor control, cognitive activities, sleep and mood, and influencing biochemical reactions involved in analgesic, as well as neuroprotective effects (Di Lazzaro et al., 2013).
In the following Sections, 1.2 and 1.3, a detailed description of tDCS and TMS mechanism of actions and application protocols are reported, while a detailed description of ELF-MF effects and possible therapeutic applications is reported in Section 5.1 of Part II.

1.2 Transcranial direct current stimulation: physical principle, device and applications

Transcranial direct current stimulation (tDCS) is a noninvasive brain stimulation technique that uses a low-intensity (0.5 mA – 2 mA) direct current flowing between two or more metallic electrodes placed on the scalp and connected to a stimulation de-

vice (Nitsche et al., 2008; Nitsche and Paulus, 2001; Priori et al., 1998). Such current is capable of modulating excitability of neurons, by modifying their transmembrane potentials and bringing them closer to, or further from, their firing threshold, without eliciting any depolarization, or hyperpolarization (Reed and Cohen Kadosh, 2018). Therefore tDCS is considered a purely neuromodulatory technique, since the currents injected to the scalp generate an E-field whose intensity is not able to elicit action potentials, but can influence the spontaneous activity of the neurons, such as the level of excitability or the firing rate in response to additional inputs (Fregni et al., 2015). In fact, when a neuronal membrane is depolarized by the DC current, meaning that its potential gets closer to the firing threshold, less afferent activity is required to induce an action potential, whereas if it is hyperpolarized, neuronal excitability, and therefore spontaneous activity, is reduced (Stagg et al., 2018). It should be noted that at the level of one single neuron, simultaneous depolarization and hyperpolarization occurs, as was shown in-vitro on rat hippocampal by Bikson and co-workers (Bikson et al., 2004). This means that orientation of the neuron with respect to the stimulating electric field generated by tDCS is critical and a larger efficacy of stimulation would take place when the injected current meets the long axis of a neuron, as larger and more distant membrane compartments would be homogeneously polarized (Stagg et al., 2018). Nevertheless, this shifts in single neurons membrane potentials are relatively low (0.2 mV to 0.5 mV) with respect to the resting potential of about -70 mV (Radman et al., 2009), therefore the effectiveness of tDCS stimulation derives more from amplification, caused by respective alterations of action potential generation in larger neuronal networks. This mechanism is known as the acute effect of tDCS, meaning the one triggered by the injected currents but that does not outlast the stimulation. Acute effects of tDCS explain how tDCS delivered to the motor cortex of healthy subjects modulates excitability of the area underlying the electrode, as revealed by changes in the amplitude of motor evoked potentials (MEP) (Lefaucheur et al., 2017; Stagg et al., 2018; Bikson et al., 2019). Such modulation can go either in the direction of an increase in MEP amplitude, as well as towards a decrease. This would depend on the polarity of the so-called active electrode, which is the one placed over the target area. When the active electrode is the anode (i.e. anodal tDCS or a-tDCS), a depolarization effect is achieved on neurons and M1 excitability is increased, whereas in cathodal (c-) tDCS, neurons are hyperpolarized, resulting in a net reduction of M1 excitability (Da Silva et al., 2011; Fregni et al., 2020). Therefore, a-tDCS is considered to have an excitatory

effect on brain activity, while c-tDCS has an inhibitory effect. For both tDCS types of stimulation, a return, or reference, electrode is required to allow the current flow and it is usually placed contralaterally over a neutral area, such as the supraorbital (SO), although this strongly depends on the electrode shape and application, therefore other electrode placements (or montages) have been investigated over the years, as reported in Sections 1.2.1 and 1.2.2. Several studies conducted over the years have shown the ability of tDCS to alter oscillatory cortical activity in brain areas other than M1, particularly in the prefrontal cortex (PFC) regions, where tDCS-induced neuromodulation meaningfully affects cognitive and emotional processes (Chase et al., 2020). Moreover, evidence from pharmacological studies showed that no synaptic changes occur during the acute effect of tDCS, which appears to be driven solely by membrane potential alterations (Nitsche et al., 2003; Stagg et al., 2018). Sustained tDCS stimulation, in the order of minutes, results in physiological alterations that can last several hours after the end of stimulation, namely after (or longterm) effects. The mechanisms for the after-effects are still not completely understood, but they are presumed to be related to synaptic plasticity (Jamil and Nitsche, 2017). Animal studies conducted in the late 60s revealed that stimulating anesthetized rats with a direct current for 5 minutes or longer would result in prolonged increase or decrease of spontaneous firing activity, depending on the stimulation polarity (Bindman et al., 1964; Jamil and Nitsche, 2017). Further studies demonstrated that these effects were not purely electrical, but would also depend on protein synthesis, particularly on N-methyl D-aspartate (NMDA) receptors (Islam et al., 1995a,b; Jamil and Nitsche, 2017). Although transferring findings from animal models to human is not straightforward in tDCS applications, pharmacological studies showed that tDCS long term effects in humans involve glutamatergic processes, especially regarding NMDA receptors (Jamil and Nitsche, 2017; Stagg et al., 2018; Fregni et al., 2020), as shown by Nitsche and colleagues in the early 2000, with the blockade of NMDA receptors that would prevent tDCS-induced excitability alterations, in both anodal and cathodal tDCS, whereas NMDA receptor agonists enhance increases in anodal tDCS-induced excitability (Nitsche et al., 2003, 2004; Stagg et al., 2018). Additionally, it has been shown that tDCS acts by decreasing γ-aminobutyric acid (GABA) concentrations (Stagg et al., 2009). Although further investigation is needed to understand long-term tDCS effects, these first findings lead to possibility of using tDCS as a therapeutic tool. In fact, these neuromodulators can alter plasticity in non-linear and complex ways, which is relevant in neurological or psychiatric diseases

where these neuromodulators are often out of balance (Jamil and Nitsche, 2017; Fregni et al., 2020).

1.2.1 tDCS electrodes typologies

The electrodes used during tDCS treatment consists of a conductive material, such as metal or conductive rubber, placed in contact with an electrolitic solution, that can be a conductive gel (more frequently used in small circular electrodes) or soaked sponges (more frequently used in bigger rectangular electrodes), and that works as a buffer between the electrode itself and the surface of the skin. The chosen material have to guarantee a good conductivity as well as non-corrosive nature and bioinertness (Solomons and Shanmugasundaram, 2020). Moreover, the design and preparation of tDCS electrodes are central to tolerability over the subject head and aim at reducing the adverse event of cutaneous sensations, such as perception of warmth, itching, and tingling, or erythema (Fertonani et al., 2015; Aparício et al., 2016; Bikson et al., 2016; Khadka et al., 2019), which not only cause a discomfort for the subject but compromise blinding of experiments, and affect performance, specially in cognitive studies (Nitsche and Paulus, 2011). For instance, an optimal thickness of sponge should be about 5 mm, since a thicker sponge layer would increase edge effects in the current distribution, whereas a thinner sponge would increases the tingling sensation (Solomons and Shanmugasundaram, 2020). Sponge hydration must be accurately balanced, as well. In fact, in case of over-saturated sponges, saline might leak from the sponge, covering an area of the scalp outside the surface area of the electrode and delivering the current through a wider area (Woods et al., 2016). This would create an amorphous current distribution that is not reproducible within or between subjects. Therefore, it is important that a good contact between the complex electrode/saline and the scalp is achieved only under the electrode. Electrode size and shape influences the current density distribution on the surface of the scalp as well, and therefore their design and size should be chosen so to optimize the electric field distribution on the target area and to keep a current density below the thresholds for skin and neural damage, to avoid onset of side effects (Solomons and Shanmugasundaram, 2020). Another central consideration that affects efficacy of tDCS, is determining where to place the electrodes over the head (i.e. montage). Even though the rationale behind it consists in placing active electrodes over the area to be stimulated and a return electrode in a neutral

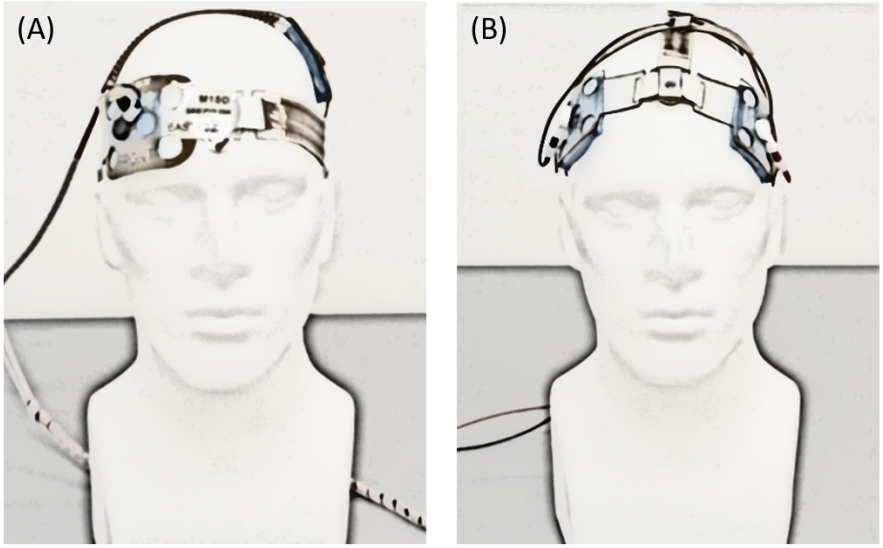

Figure 1.5: Example of pad electrodes montage: (A) M1-SO montage. (B) Bifrontal montage (Figure adapted from (Borges et al., 2019))

position. Many studies over the years have shown that different montages around the same target area can lead to different experimental outcomes (Nitsche and Paulus, 2001; Mahmoudi et al., 2011; Wörsching et al., 2018; Da Silva et al., 2019; Patel and Madhavan, 2019), as they induce different current distributions that would cause a stimulation of the whole brain or a more selective stimulation of particular lobes of the brain (Bhattacharjee et al., 2019; Minhas et al., 2011; Kessler et al., 2012; Woods et al., 2016).

Pad electrodes

Since the beginning of tDCS applications (Priori et al., 1998; Nitsche and Paulus, 2001; Hummel et al., 2005), the use of two rectangular or square shaped electrodes, called pad electrodes, with typical dimensions of 7 cm $\times$ 5 cm, or 5 cm $\times$ 5 cm, has been very frequent, and it is still considered, nowadays. For instance, in (Fleming et al., 2017), they investigated the impact of electrode arrangement on the efficacy of tDCS in post-stroke patients, with two carbon electrodes encased in 25 cm2 saline-soaked sponges, and in (Foerster et al., 2018), they explored the effect of different angle-orientations of tDCS electrodes applied over the upper limb motor cortex (M1) on motor cortex excitability in healthy volunteers, with 35 cm^2 saline-soaked sponge electrodes. Positioning of the electrode with respect to the sponge can be varied, in some

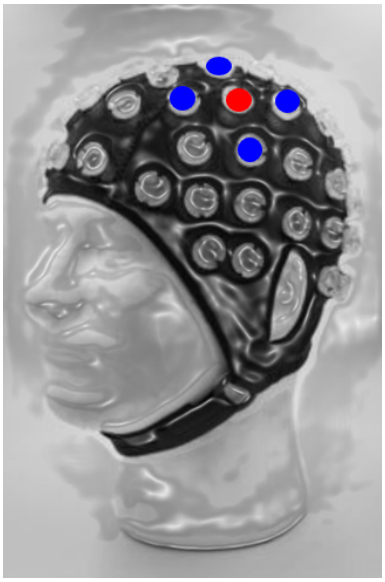

Figure 1.6: Example of supporting cap for HD-tDCS with 64 electrodes. Red and blue dots show anodal 4×1 ring configuration. Image adapted from `https://soterixmedical.com/research/hd-tdcs/accessories/hd-cap`.

configurations it is embedded inside a rectangular sponge pocket, with the electrode being smaller than the sponge, whereas in others the electrode is placed behind the rectangular sponge, and an insulating rubber encases the metal and sponge, except on the skin contact side (Khadka et al., 2019). Example of two typical pad electrode montages is reported in Fig. 1.5 A recent innovation was proposed in (Khadka et al., 2018) with the dry electrode that excludes the use of any saline or other electrolytes, or any electrode preparation steps except the connection to the stimulator. Authors showed an improvement in toleribility, whereas the onset of erythema and adverse-events were comparable to that of state-of-the-art sponge electrodes (Khadka et al., 2018). Due to their size, pad electrodes stimulate large regions of the brain, and therefore they are characterized by a poor focality (Datta et al., 2009; Bastani and Jaberzadeh, 2013; Solomons and Shanmugasundaram, 2020). A first solution proposed to enhance focality in tDCS is by reducing the size of the active electrode and increase that of the return electrode, so to minimize stimulation under it (Nitsche et al., 2007).

Another variant of electrodes montage is the so called HD-electrode strategy that uses electrodes as small as 1 cm, with a circular shape (Minhas et al., 2010). Each HD-electrode includes a cup filled with conductive gel or paste that creates the contact *HD-tDCS*

area with the skin. Suspended inside the gel is a metal ring (Khadka et al., 2019), disk or pellet made from Ag/AgCl. Given their small size, up to 64 electrodes can be simultaneously placed on the head by means of a cap headgear, according to the International 10/10 EEG system (Dmochowski et al., 2011), as shown in Fig. 1.6. A typical HD-tDCS configuration is the "4 × 1 ring" electrode montage, which consists in one active electrode placed over the target area and surrounded by 4 reference electrodes (Datta et al., 2009; Alam et al., 2016; Shen et al., 2016; Hill et al., 2017). Either experimental and computational studies compared the conventional tDCS (i.e. with rectangular electrodes) with the HD-tDCS, and showed the increased focality (Mikkonen et al., 2020; Wang et al., 2018). Nevertheless, a very recent study by Pellegrini and co-workers, investigated variability in corticospinal and cortico-cortical excitability response and showed that conventional tDCS significantly reduced intra-individual variability compared to HD-tDCS (Pellegrini et al., 2020).

1.2.2 tDCS applications and protocols

Disturbances in neuronal circuits underlie psychiatric diseases and neuronal disorders. Consequently, over the past decades there's been an increasing interest in applying tDCS to improve the symptoms associated to such type of illnesses, by altering the disrupted patterns (Kekic et al., 2016). Depending on the pathology under treatment, the therapy protocol changes in terms of type and location of the electrodes, type of stimulation (anodal or cathodal), current intensity and duration of treatment. Nevertheless, no standard exists, yet. Recently two evidence based guidlines were published for tDCS applications (Lefaucheur et al., 2017; Fregni et al., 2020). In 2016, the European Chapter of the International Federation of Clinical Neurophysiology commissioned to a group of European experts the task of gathering knowledge about the state of the art of the therapeutic use of tDCS regarding chronic pain, Parkinson's disease and other movement disorders, motor stroke, post-stroke aphasia, multiple sclerosis,epilepsy, consciousness disorders, Alzheimer's disease, tinnitus, depression, schizophrenia, and craving/addiction (Lefaucheur et al., 2017). A more recent review following similar criteria was conducted by Fregni and co-workers (Fregni et al., 2020). On the basis of (Lefaucheur et al., 2017), which considered only studies that applied repeated tDCS sessions to a sample of 10-24 patients or more than 25 patients, with a sham controlled procedure, no tDCS protocol was found to have a definite efficacy (i.e. level A rec-

ommendation) on any of the aforementioned applications. Whereas, in (Fregni et al., 2020), where studies with active group composed of a smaller number of patients were considered as well, definitely effective level A recommendation was assigned to a-tDCS over left dorsolateral prefrontal cortex (DLPFC). Level B recommendation (probable efficacy) was proposed for fibromyalgia (Fregni et al., 2020; Lefaucheur et al., 2017), a chronic pain syndrome that affects the musculoskeletal system, whereas a level C recommendation (possible efficacy) was proposed for anodal tDCS of the left M1 (or contralateral to pain side, with right orbitofrontalcathode) in chronic lower limb neuropathic pain secondary to spinal cord lesion (Lefaucheur et al., 2017) and migrain pain (Fregni et al., 2020).

Chronic pain

Many studies have applied anodal (a-)tDCS of the primary motor cortex (M1), contralateral to the pain (for focal or lateralized pain) or the left hemisphere for more diffuse pain, with the cathode positioned over the contralateral supraorbital (SO) region, and showed potentials in the treatment of a number of different chronic pain conditions (Pinto et al., 2018; Hughes et al., 2020). Hypotheses have been moved to justify the effect, according to which a-tDCS over M1 activates inhibitory systems, thus reducing overactivation of thalamic nuclei (Pinto et al., 2018; Castillo Saavedra et al., 2014). Another montage that has been tested is anodal/cathodal tDCS over the left DLPFC, specially for fibromyalgia and migraine (Shirahige et al., 2016; Zhu et al., 2017). Typical tDCS intensities for the treatment of chronic pain is 2 mA and duration of the session is 20 minutes, as used in (Kim et al., 2013) for painful diabetic polyneuropathy or in (Volz et al., 2016) to treat chronic abdominal pain associated with inflammatory bowel disease. More recently, the same protocol was applied to evaluate efficacy and safety of M1-SO a-tDCS on clinical pain severity and mobility performance in older adults with knee osteoarthritis pain (Ahn et al., 2017). Results showed promising clinical efficacy for reduction in pain perception, albeit not consistent in all pain measurements (Ahn et al., 2017). A comparison between M1 and DLPFC a-tDCS, was conducted in a sham controlled study by Brockardt and colleagues (Borckardt et al., 2017). In one case the anode was placed over the knee representation of M1 and cathode over the right DLPFC, in the other anode was placed over the left DLPFC and cathode over the knee representation of the sensory cortex. For both, four 20-minute sessions at 2 mA were administered, showing that a-tDCS of the prefrontal cortex was better than motor cortex stimulation at reducing post-operative opioid use (Borckardt et al., 2017). Despite the aforementioned positive results, other studies did not show any significant

difference in pain intensity reduction between active and sham condition (Attal et al., 2016; Wrigley et al., 2013).
More evidence are reported in literature in favor of a-tDCS over both M1 and DLPFC for treatment of fibromyalgia (FM) (Lefaucheur et al., 2017; Zhu et al., 2017; Fregni et al., 2020; Brighina et al., 2019; Castillo Saavedra et al., 2014). Over the years, the majority of the studies employing tDCS on FM, apply the same protocols as for the treatment of other pain conditions. i.e. anodal stimulation, 2 mA and sessions of 20 minutes (Fregni et al., 2006a; Valle et al., 2009; Roizenblatt et al., 2007; Mendonca et al., 2011; Fagerlund et al., 2015; Jales Junior et al., 2015; Mendonca et al., 2016). More recently, lower stimulation intensities have been investigated as well, such as 1 mA as in (Silva et al., 2017; Khedr et al., 2017), or 1.5 mA in (To et al., 2017) and (Yoo et al., 2018). The main difference across all the aforementioned studies is in the treatment schedules, that can be as short as 5 (Fregni et al., 2006a; Roizenblatt et al., 2007; Fagerlund et al., 2015) or 10 (Valle et al., 2009; Khedr et al., 2017) daily sessions up to one weekly session for 10 weeks (Jales Junior et al., 2015) or two weekly sessions for 4 weeks (To et al., 2017; Yoo et al., 2018). In 2006, Fregni and co-workers (Fregni et al., 2006a) were the first to show that a-tDCS over left M1, with cathode over contralateral SO, was able to ameliorate pain and life quality in FM patients, as compared to left DLPFC or sham stimulation, and the effect persisted for 3 weeks after the stimulation period. This positive effect was confirmed in (Roizenblatt et al., 2007) and, more recently in (Fagerlund et al., 2015), while in 2016, Mendoca and colleagues applied the aforementioned protocol showing positive effects on other FM related symptoms such as anxiety and mood (Mendonca et al., 2016). Positive effects on pain and life quality were obtained also in other studies that explored longer stimulation periods to induce more lasting effects, up to 2 months after the end of the stimulation (Brighina et al., 2019; Khedr et al., 2017). Significant changes in pain scores were reported in more recent studies that targeted the DLPFC (Brighina et al., 2019). In a single session study by Silva and co-workers (Silva et al., 2017), stimulation of left DLPFC at 1 mA a significant analgesic effect was observed and was attributed to an indirect inhibitory modulation of thalamic activity (Silva et al., 2017). In the trial reported in (To et al., 2017), eight tDCS sessions over bilateral DLPFC significantly ameliorated pain scores. Possible positive effect of HD-tDCS was evalueted in a phase II open-label trial (Castillo-Saavedra et al., 2016), where they estimated that a median number of 15 sessions of HD-tDCS were required to achieve a 50% FM pain reduction.

Major depression

Additionally to being investigated as a possible target for chronic pain treatment, DLPFC have been proven to be a possible effective target also in the treatment of major depression (MDD), based on historical observation of hypometabolism of the left DLPFC, associated with right prefrontal hyperfunction, in MDD patients, together with a dysfunction of brain plasticity, characterized by an alteration of long-term potentiation and depression (Brunoni et al., 2012; Cirillo et al., 2017). Behind these findings lays the rationale of tDCS applied to major depression, which consists in positioning the anode over the left DLPFC, to increase local activity and restore normal functioning (Sathappan et al., 2019), while the cathode is either positioned over the right DLPFC or the right supraorbital or fronto-temporal area. Such different montages lead to distinct current distributions, nevertheless the influence on clinical effects remains unclear (Csifcsák et al., 2018). The antidepressant effect of anodal tDCS over the left DLPFC was first reported in (Fregni et al., 2006b) after a daily session of 10 minutes, for five alternate days. Such result was confirmed in following studies applying the same montage (anode over l-DLPC and cathode over contra-lateral SO), amplitude and session schedule (Boggio et al., 2007, 2008). Nonetheless, in 2010 Loo and co-workers (Loo et al., 2010) failed to prove superior antidepressant efficacy of the same protocol, but demonstrated a decrease in depression symptoms after 15 sessions at 2 mA, each lasting 20 minutes. More recent studies applied a-tDCS for longer sessions and higher intensities, although considering different montages (anode and cathode over left and right DLPFC, respectively) and electrode sizes, i.e. 25 cm^2 (Valiengo et al., 2017), and 20 cm^2 (Sharafi et al., 2019). Both studies showed antidepressant effect of a-tDCS exposure over sham. Several reviews and meta-analyses conducted over the years demonstrated that tDCS is modestly effective in treating depressive episodes (Bennabi and Haffen, 2018; Razza et al., 2020; Lefaucheur et al., 2017), but further well-designed, large-scale randomized control trials (RCT) are warranted (Razza et al., 2020). So far, only anodal tDCS of the left dorsolateral prefrontal cortex (DLPFC)(with right orbitofrontal cathode) received level A recommendation and solely for major depressive episode without drug resistance (Fregni et al., 2020).

Other diseases

Several others neuronal and psychiatric diseases are under investigation for treatment with tDCS, despite evidence is yet not sufficient to address an efficacy (Lefaucheur et al., 2017; Fregni et al., 2020). Among these, is schizophrenia, for which neuroimaging and neurophysiological studies have highlighted a link to a fronto-temporal dysconnectivity. Auditory-verbal hallucinations (AVH) have been related to a reduced brain activity in

the right and left DLPFCs, and a hyperactivity in the left temporo-parietal region (l-TPJ) is also often observed. Therefore, on the basis of the excitatory anodal stimulation versus inhibitory cathodal stimulation, an electrode montage with the cathode positioned over the left tempoparietal junction (l-TPJ) and anode placed over l-DLPFC, has been hypothesized to alleviate AVH (Mondino et al., 2015; Fröhlich et al., 2016; Lefaucheur et al., 2017; Fregni et al., 2020). A different electrode montage has also been investigated, consisting in the anode still over the left DLPFC, but the cathode over the right SO (Smith et al., 2015; Nienow et al., 2016). These studies showed cognitive improvements, whereas schizophrenia symptoms were not assessed. A review on the topic was recently published and stated that present evidence is not robust enough to demonstrate efficacy of tDCS on symptoms of schizophrenia, and further RCTs with larger and more homogeneous sampling should be conducted (Moffa et al., 2018).
Similarly, positive outcome after tDCS applications can be found in Parkinson's disease (PD), a neurodegenerative disease caused by a degeneration of dopamine-producing neurons within the basal ganglia that mainly affects the motor cortex. Therefore, in this case, tDCS protocols would primarily target the motor cortex M1 and the DLPFC, as brain activation patterns in these brain regions are highly involved in successful locomotion performance in people with PD (Lee et al., 2019). Several studies confirmed that anodal tDCS over both M1 and DLPFC resulted in improvements of motor functions (Verheyden et al., 2013; Lattari et al., 2017). Nevertheless, these results do not provide sufficient evidence for a recommendation, because of heterogeneity of the targeted area and the outcome measures (Lefaucheur et al., 2017; De Paz et al., 2019). In stroke neurorehabilitation, tDCS has shown benefits in both motor and language rehabilitation. In fact, a cerebral stroke causes alterations of the interhemispheric interactions with an increase of neuronal activity in the unaffected hemisphere and a decrease in the affected one. Application of tDCS can re-balance the level of hemispheric excitability either inhibiting the unaffected hemisphere by cathodal tDCS or exciting the affected hemisphere by anodal tDCS (Gomez Palacio Schjetnan et al., 2013). The same model can be applied in the treatment of post-stroke aphasia, where electrodes would be applied in the Wernick's area, instead of M1 (Biou et al., 2019). Other diseases under investigations are Alzheimer's (Khedr et al., 2014; Marceglia et al., 2016; Mayo-Yáñez et al., 2018), tinnitus (Yuan et al., 2018), and multiple sclerosis (Ashrafi et al., 2020), but their efficacy still needs to be demonstrated in large, multicentric RCTs consisting of repeated sessions with prolonged follow-up (Lefaucheur et al., 2017; Yuan et al.,

2018; Ashrafi et al., 2020).

1.3 Transcranial Magnetic Stimulation: Physical principle, device and applications

Transcranial magnetic stimulation (TMS) is a neurophysiologic technique that allows for noninvasive magnetic stimulation of the human brain by means of high intensity, pulsed magnetic field sent through the scalp by a stimulating coil (Rotenberg et al., 2014). It is based on the physical principle of electromagnetic induction, according to which a time-varying magnetic field, generated by a time varying current, is able to induce an electric field in a nearby conducting medium. In fact, a TMS device consists in a capacitive high-power charge-discharge system that produces a high-intensity current pulse that flows through the stimulating coil and generates a brief pulsed magnetic field, up to several Teslas, responsible for inducing an electric field inside the cerebral tissue (Valero-Cabré et al., 2017). Depending on the intensity of the stimulation and on the position and type of stimulating coil, such induced electric field is able to depolarize superficial axons and to activate neural networks in the cortex (Lefaucheur et al., 2014). Therefore, as an opposite to tDCS, the main mechanism of action of TMS is the neurostimulation of the human brain cortex. This is certainly true when TMS is applied following the single-pulse protocol, to assess cortical reactivity, or following the paired-pulse protocol to probe intracortical inhibition and facilitation. Nontheless, when patterned trains of pulses (rTMS or theta burst stimulation TBS) are used to stimulate the brain, changes in cortical excitability and metabolism are induced that last beyond the stimulation itself (Fried et al., 2017). Therefore, rTMS and TBS are considered not only to neurostimulate but to exert a neuromodulatory mechanism, as well. TMS originated as a diagnostic and investigational device for human applications, therefore many studies have been conducted on healthy volunteers to enable physicians to interact directly with ongoing neuronal activity and understand its relevance to a given task at particular time points, as well as to understand that TMS stimulation might be able to enhance the natural ability of the brain to adapt to demage and recover lost performance (Di Lazzaro et al., 2018). Nevertheless, the mechanisms involved in this approach are quite complex and still poorly understood.
Most of the current data on TMS effects have been derived from stimulation of the pri-

mary motor cortex, M1, of healthy subjects due to the ease of obtaining motor evoked potentials (MEPs)(Lefaucheur et al., 2014).

Single Pulse In fact, a TMS pulse delivered over the precentral region with an intensity equal to or greater than the subject motor stimulation threshold (MT), can evoke a muscle response, with a size that reflects the excitability of motor corticospinal output. Particularly, through recording at spinal levels, it has been shown that TMS pulses can evoke a burst of I-waves, probably produced by an indirect (I) synaptic activation of corticospinal neurons, when threshold intensity is at MT level, whereas it elicits D-waves, caused by direct (D) excitation of the axons of corticospinal neurons in the subcortical white matter, at much higher intensities of stimulation (Di Lazzaro et al., 2018).
The D- and I-waves of a descending volley sum up at the spinal cord level to produce a motor evoked potential (MEP) in the target muscle (Hand et al., 2020). These findings where first observed in the late 90s and early 00s with the underlying hypothesis that TMS tends to activate elements that are aligned horizontally to the brain surface and that might have synapses onto the corticospinal neurons, therefore resulting in I-waves (Di Lazzaro et al., 1998, 2004). This is due to the fact that TMS induces a current that flows tangentially to the brain surface. Moreover, the response to cortical TMS stimulation is also dependent on the orientation of the coil. For instance, when the handle of the figure-8 coil is oriented parallel to the interhemispheric midline (postero-anterior direction), motor cortex TMS activates the pyramidal tract only indirectly, through the recruitment of cortical interneurons, while it can also directly activate the pyramidal tract, therefore evoking direct waves (D-waves) at spinal level, when the handle of the figure-8 coil is oriented perpendicular to the interhemispheric midline (latero-medial direction) (Lefaucheur et al., 2014; Di Lazzaro et al., 2018). It should be noted that a single TMS pulse is capable of activating any type of cortical neuron. Therefore, to have insights into the range of neurons that commonly respond to TMS,

Paired pulse a paired pulse stimulation method should be considered (Di Lazzaro et al., 2018). The paired pulse protocol consists in sending a conditioning stimulus, with amplitude either sub or suprathreshold, followed by a baseline single pulse, which is referred to as the test stimulus. It has been demonstrated in 1993 by Kujirai and colleagues (Kujirai et al., 1993), and following confirmed in (Di Lazzaro et al., 1998), that subthreshold TMS pulses can suppress the MEP response to subsequent suprathreshold pulses if the interval between the two pulses is 5 ms or less. Such effect is known as short-interval intracortical inhibition (SICI). In fact, it is thought that the first, subthreshold, pulse

activates low threshold inhibitory neurons that suppress the excitatory inputs activated by the second pulse (Di Lazzaro et al., 2018). The effects of increasing the intensity of the principal TMS pulse in the presence of a subthreshold conditioning one has been further investigated in (Weise et al., 2013) where they found that an increase in test stimulus amplitude evoked an earlier wave (D-wave), while later I-waves are still suppressed. Very recently, Kohl and co-workers showed for the first time that paired pulse protocol can be applied to the cognitive domain to influence response inhibition (Kohl et al., 2019). Pharmacological experiments show that short interval inibition is mainly mediated by gamma-aminobutyric acid–GABA–activity (Di Lazzaro et al., 2006a; Lang et al., 2006; Valero-Cabré et al., 2017). Different phenomena are revealed if the interval between the two stimuli is longer than 6 ms or if the conditioning stimulus is suprathreshold. In the first case, the MEP evoked by the second pulse in facilitated, i.e. intracortical facilitation, ICI, without changes in the amplitude or number of high-frequency I-waves (Di Lazzaro et al., 2006b; Ni et al., 2011; Zewdie and Kirton, 2016; Di Lazzaro et al., 2018). Such excitatory intracortical mechanism is mostly mediated by glutamatergic activity that was at first hypothesized to occur at spinal level (Di Lazzaro et al., 2006a, 2018). Nevertheless, a recent study by cash and co-workers on paired pulse protocol applied to the DLPFC provided clear evidence that ICF modulates neuronal activity at the cortical level (Cash et al., 2017). A paired pulse facilitation of MEPs is observed also at shorter interstimulus intervals using a conditioning stimulus slightly above the motor threshold, i.e. short-interval cortical facilitation, SICF, while a decrease in cortical excitability is observed when the second pulse is delivered at a time equal to the I-wave trough ($\sim$2 ms) (Thickbroom, 2007; Zewdie and Kirton, 2016; Di Lazzaro et al., 2018). The long-lasting changes in cortical excitability produced by these protocols are thought to be a form of phase-dependent plasticity (Cash et al., 2017; Di Lazzaro et al., 2018). Moreover, the amount of SICF is influenced by the direction of the conditioning stimulus, as demonstrated in various studies (Delvendahl et al., 2014; Cash et al., 2015). Finally, another form of paired pulsed experiment consists in sending a suprathreshold CS and TS, with an interval between the two around 100 to 200 ms, producing a long interval cortical inhibition, LICI (Di Lazzaro et al., 2018; Valero-Cabré et al., 2017). LICI can last for 100 ms or more and it is believed that it is mediated by slow inhibitory postsynaptic potential (IPSPs) mediated by the GABAB receptors (McDonnell et al., 2007; Di Lazzaro et al., 2018). The paired pulse protocol can be discharged on pairs of distinct cerebral sites to

determine presence or absence of connectivity and estimate the conduction velocities between regions (Valero-Cabré et al., 2017).

Repetitive TMS

Any combination of more than two pulses delivered with a certain time interval (frequency of 0.5–1 Hz up to 5-10Hz) is referred to as repetitive TMS (rTMS). Pascual-Leone and colleagues in 1991 were among the first to study the effects of rTMS on motor cortex excitability, by showing that a series of 20 consecutive TMS pulses delivered at a frequency greater than 2 Hz gave rise to significant MEP amplitude enhancement (Pascual-Leone et al., 1991). In the following decades several studies were conducted to assess the mechanism of action of this protocol and two primary treatment regimes were established: low-frequency rTMS, which is defined by stimulation at frequencies lower than 1 Hz, and high-frequency rTMS, which is defined by stimulation at frequencies higher than 5 Hz. Low-frequency rTMS reduces neuronal excitability, whereas high-frequency rTMS increases cortical excitability (Maeda et al., 2002; Rossi et al., 2009; Chervyakov et al., 2015; Valero-Cabré et al., 2017). Conversely to single or paired pulsed TMS, rTMS protocols, particularly when delivered in long trains and in consecutive daily sessions, have the potential to modulate functions long-lastingly, through plastic mechanisms. Three types of effects are produced by rTMS sessions. First are the online effects, which are caused by direct and measurable interference with patterns of ongoing neuronal discharge at the time of stimulation. The silent period, a phenomenon that consists in suppression of electro-myographic signals induced by TMS over the motor cortex during an ongoing voluntary hand muscle activation, well explains the online TMS effect (Valero-Cabré et al., 2017). Following the online effects, after (or offline) effects can be seen with a prolonged alteration of cortical activity for an average period of 30 minutes after stimulation (Thut and Pascual-Leone, 2010), with 60 minutes peaks (Schindler et al., 2008). Induction of long-term effects on cortical activity is also possible after repetition of stimulation sessions, administered within less than 24 hours. Such time interval allows the accrual of short-term and low intensity effects during each individual sessions of rTMS that engages cortical plasticity mechanism and generate long-lasting changes (Chervyakov et al., 2015; Valero-Cabré et al., 2017). The opportunity to induce lasting neuro-modulatory effects is what made the translation of rTMS into a meaningful therapeutic intervention tool.

The following sections report an overview of the main TMS coils typologies currently available and of the recent advancements in the therapeutic applications.

1.3.1 TMS coil typologies

The design of TMS coils is extremely critical since its shape and size directly influences the magnetic field penetration and distribution that, in turn, determine the induced E-field spread in the brainWagner et al. (2007b); Valero-Cabré et al. (2017). This can affect TMS ability to discriminate between two adjacent cortical locations and to precisely localize brain areas, therefore its spatial resolution, as well as the ability to induce weaker or higher intensities of the intracortical currents, both fundamental parameters to achieve motor, sensory or behavioral effects, hence, the site of stimulation (Valero-Cabré et al., 2017; Peterchev et al., 2015). Therefore, stimulating coils of several dimensions, shapes and geometries are currently available in the market, each one optimally designed for specific applications. The two most typical TMS coils are single circular loop coil (Fig. 1.7A) and the figure-8 coil (Fig. 1.7B), both constructed from tightly wound copper wire, properly insulated and placed in a plastic case. Circular coils typically have a diameter that ranges from 80 mm to 150 mm (Zewdie and Kirton, 2016) and are able to generate a spherical magnetic field perpendicular to the coil itself, such to induce an E-field that would have its minimum below the center of the coil and maximum below its perimeter, potentially stimulating a ring-shaped area of the brain therefore lacking in spatial selectivity (Deng et al., 2013; Peterchev et al., 2014). For this reason circular coils are rarely used to investigate TMS clinical effects, while they are still considered for investigational purposes (Guerra et al., 2020; Cantone et al., 2019). To enhance focality of the circular coil, the first figure-8 coil was proposed in 1988 (Ueno et al., 1988). It consists in copper wires continuously wound so to create two abutted circular coils, with currents flowing in opposite directions, so to sum up at the middle point. Such geometrical composition allows to maximize the E-field at the center of the coil, thus increasing the focality (Ilmoniemi et al., 1999; Paffi et al., 2018). At today, the figure-8 coil is one of the most extensively used in TMS studies with both investigational and therapeutic purposes. Thanks to its relatively higher focality over the circular one, they are particularly suitable for cortical mapping (Mirbagheri et al., 2020; Seynaeve et al., 2019). Despite the relatively enhanced focality, commercially available figure-8 coil still lack in penetration depth, therefore the E-field that such coils are able to induce remain confined over superficial cortical areas (Deng et al., 2013). Therefore, several strategies have been put into field to increase TMS stimulation depth. A first solution proposed was the double-cone (DC) coil, that consists in a figure-8 with

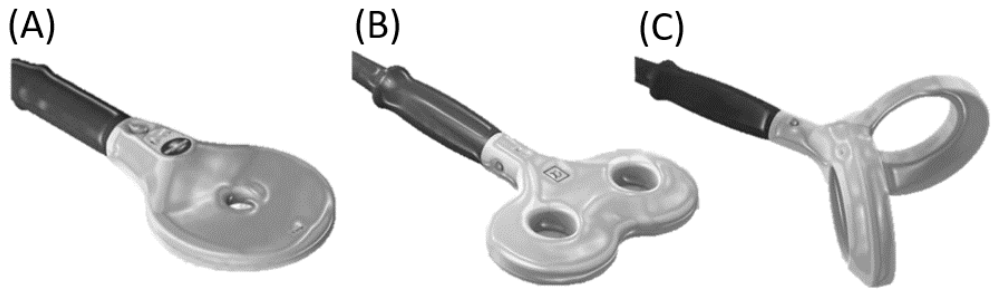

Figure 1.7: Typical commercial TMS coil: (A) Circular coil, (B) Figure-8 coil, (C) Double-cone coil. Image adapted from `https://www.magstim.com`.

the two wings bent closer together, typically forming an angle of 120° (Fig. 1.7C). Such a shape would allow to induce E-field in deeper regions, although further losing in focality (Lontis et al., 2006). Both behavioural and clinical studies suggest that the DC coil indeed modulates cingulate or medial prefrontal cortex function even if it is still under debate whether these regions are reached directly or trans-synaptically via stimulation of superficial brain areas (Schecklmann et al., 2020). Very recently, the study conducted by Schecklmann and colleagues aimed at comparing the magnetic field produced by double-cone and by figure-8 coils and, most importantly aimed at comparing their ability to stimulate superficial and deeper brain areas (Schecklmann et al., 2020). Their results demonstrated that the double-cone coil induces higher magnetic fields in deeper brain areas, with a net advantage of using the DC coil in the stimulation of the deeper leg area as compared with the more superficial hand area, were stimulation with figure-8 coil was more efficacious. A particular type of coil is the H-Coil, that aims at stimulating deeper cortical regions. Its design is more complex than that of the aforementioned two and consists of a helmet with base portion running tangential to the scalp and return portions removed from the head. Such complex design generates a summation of the electric field in specific brain regions at a depth of 4–6 cm (Fiocchi et al., 2015; Lu and Ueno, 2017). It is particularly efficient for stimulation of deep areas in the cortical-striatal-thalamic-cortical (CSTC) loop whose disfunctions are involved in onset of obsessive compulsive disorder (OCD) (Lusicic et al., 2018). Therefore, the use of H-Coil to treat OCD has been recently FDA cleared, as will be described in the following section.

1.3.2 Therapeutic applications of TMS

TMS is extensively adopted in neuroscience research to investigate intracortical, cortico-cortical, and cortico-subcortical interactions (Rotenberg et al., 2014; Lefaucheur et al., 2014; Di Lazzaro et al., 2018; Valero-Cabré et al., 2017). Moreover, depending on the protocol applied, type of coil and location of the stimulation, TMS can be effective therapeutic solution for the treatment of different neuropsychiatric conditions and a valid neuro-rehabilitation tool. Particularly, given the ability of inducing long term effects, rTMS has been extensively used for therapeutic therapeutic treatment of several psychiatric disorders and neurological diseases.

Major depression

Clinical practice have shown that rTMS may have a higher chance of success when it is administered in the year of onset of an ongoing depressive episode, to patients below the age of 65 years, and in cases known to have a limited level of resistance to treatment (Lefaucheur et al., 2020). Since it's been shown that hypoactivity of the l-DLPFC may cause symptoms of depression (De Raedt et al., 2015), one possible approach is to treat patients with HF-rTMS on the left-DLPFC, with the aim to excite the area in order to normalize any abnormal activity levels Schutter (2009); Kumar et al. (2018). Such approach have received US Food and Drug (FDA) approval in 2008, following the report of beneficial results from the study by O'Reardon and co-workers in 2007 (O'Reardon et al., 2007). Many studies continued to investigate the effect of HF rTMS on l-DLPFC reporting positive results of the real stimulation over sham (Brunoni et al., 2017; Lefaucheur et al., 2020). In 2016, Kang and co-workers exposed 24 patients (13 real, 11 sham) to 10 sessions of HF rTMS at 10 Hz and 110% of resting motor threshold (RMT) (Kang et al., 2016). They obtained a significant decrease in HDRS (Hamiltom depression rating scale) score in active patient, associated with a greater reduction of connectivity strength between bilateral DLPFC regions and left caudate, assessed with fMRI (Kang et al., 2016). A reduction in HDRS score was found in (Li et al., 2016a) with a stimulation amplitude of 100% of RMT and was associated with an increase in frontal theta power, assessed with EEG, and rostral anterior cingulate cortex metabolic activity, assessed with PET. Greater HDRS-17 score reduction can be reported when rTMS is performed twice a day rather than daily (Theleritis et al., 2017). A recent meta-analysis reported that increasing number of HF-rTMS sessions is associated with the increased efficacy of HF-rTMS in reducing depressed patients' symptom severity, and that a total number of pulses of 1200–1500 per day appear to deliver the best

antidepressant effects of HF-rTMS (Teng et al., 2017). Another possible approach that showed beneficial effects in the treatment of depression, albeit with lower statistical power than those for HF-rTMS (Lefaucheur et al., 2020) is low frequency (LF-) rTMS over the right DLPFC. Both HF-rTMS over the L-DLPFC and LF over the R-DLPFC demonstrated similar therapeutic efficacy (Cao et al., 2018), and a better tolerability was reported for LF-rTMS over HF-rTMS. Nonetheless results of sham-controlled studies conducted so far do not furnish evidence to declare LF-rTMS of the rDLPFC a protocol with definite efficacy (Lefaucheur et al., 2020). A probable antidepressant efficacy was reported for bilater rTMS in (Blumberger et al., 2016), with 600 pulses at 1 Hz on the right DLPFC followed by 1500 pulses at 10 Hz on the left DLPFC. Since the effect size of left HF-rTMS and right LF-rTMS delivered to the DLPFC is quite low (Brunoni et al., 2017), novel forms of rTMS therapy in major depression are under investigation, such as the use of H1-coils for deep HF-rTMS. In the multicenter sham-controlled study by Levkovitz and co-workers, 212 patients (101 active, 111 sham) underwent 20 sessions of deep HF-rTMS, each of 1980 pulses delivered at 18 Hz and 120% of RMT, daily for 4 weeks and then 24 additional sessions biweekly for 12 weeks, for maintenance. Results showed reduction of depression score and higher rates of remission at the end of 5-week rTMS protocol, with benefit maintained after 12-week maintenance therapy (Levkovitz et al., 2015) . This protocol was replacated in (Tavares et al., 2017), and confirmed a reduction of the depression score and a trend towards higher rate of response but not of remission, benefits were not maintained at 4-weeks follow-up. In 2018, no reduction of depression score, but higher rate of remission and response were found at the end of a 4-week deep rTMS protocol (6012 pulses in 20 sessions) in (Kaster et al., 2019). Beside the proven efficacy of HF and LF-rTMS protocols, theta burst stimulation TBS is also under investigation for treatment of depression, since it produces similar effects on cortical excitability and plastisicity than rTMS, albeit for shorter session duration (Lefaucheur et al., 2020). In 2010, two case series revealed the potential value of TBS in the treatment of depression (Chistyakov et al., 2010; Holzer and Padberg, 2010), showing reduction in depression scores, however following studies failed to prove differences in the depression score reduction between active and sham groups (Prasser et al., 2015; Chistyakov et al., 2015; Duprat et al., 2016).

Neuropathic pain A definite analgesic effect was reported in the use of HF rTMS of the primary motor cortex (M1) applied controlaterally to the pain side in patients with neuropathic pain

(Lefaucheur et al., 2014, 2020; Yang and Chang, 2020). A sham-controlled study conducted in 2015 by Khedr and co-workers assessed the efficacy of 10 daily sessions of 20 Hz HF-rTMS at 80% of RMT, over M1 in 30 patients (15 real, 15 sham) suffering from malignant neuropathic pain. Stimulation protocol consisted in 2000 pulses (10 trains every 10 seconds) with an intertrain interval of 30 seconds, delivered in a session of 6–7 minutes. Current pulses were delivered by a figure-8 coil placed over the M1 representation of the hand, on the hemisphere contralateral to the painful side; coil orientation was parallel to the interhemispheric midsagittal line. Results reported a greater reduction of pain score in the active group over the sham, although beneficial effects disappeared after 1 month, possibly related to the short duration of the session (Khedr et al., 2015; Hodaj et al., 2015). In the same year, a relatively unusual protocol was tested in (Ma et al., 2015). The protocol consisted in 10 Hz rTMS at 80% of RMT, with 300 trains of 5 seconds each, delivered every 3 seconds in sessions of 40 minutes. Results were similar to those reported in (Khedr et al., 2015), although here the average pain reduction persisted for 3 months after the treatment. Two other sham-controlled studies were performed in 2016, both obtaining a reduction of pain score compared to control condition, after exposure of the contralateral M1 to 10 Hz HF-rTMS at 80% of RMT (Attal et al., 2016) and 90% of RMT (Nurmikko et al., 2016) by a figure-8 coil. These two studies were different in terms of number of pulses, inter-train interval (3000 pulses in 3 sessions and 2000 pulses in 5 sessions, respectively) and coil orientation (antero-posterior and perpendicular to the central sulcus). Despite the clear evidence of the analgesic effect exerted by stimulating the contralateral M1, the exact location of the optimal target to be stimulated within M1 is not yet defined. Overall, two strategies are possible: either to stimulate the motor cortical representation of the painful region (Ma et al., 2015; Nurmikko et al., 2016) or to stimulate the hand motor area whatever pain location (Attal et al., 2016; Khedr et al., 2015). For instance, in a recent study by Andrè-obadia and co-workers, two different pain locations where treated (upper limb and facial) each with the coil placed over the corresponding area, and showed HF-rTMS over the hand area to be more efficacious (Andre-Obadia et al., 2018). Nonetheless, in a previous study conducted in 2015 (Lindholm et al., 2015) orofacial pain was treated with HF-rTMS protocol at 10Hz and 90% of MT, delivered by a figure-8 coil. This was a crossover study, and each patient completed three treatment sessions, including sensorimotor (S1/M1), right secondary somatosensory (S2), and sham stimulations in random order. The pain scores were significantly decreased after S2 stimulation as

compared with those after S1/M1 stimulation, suggesting that the right S2 cortex may be a new target for treating neuropathic orofacial pain (Yang and Chang, 2020). Nevertheless, the long-term results provided by repeated HF-rTMS sessions over S2 are still unknown (Lefaucheur et al., 2020). Lindohlm and co-workers justified their results with the possible different exposure of the insula (Lindholm et al., 2015). Indeed, the insula is implicated in the experience of pain (Iannetti and Mouraux, 2010), therefore different studies have proposed insular cortex stimulation. In two experimental studies, a double-cone coil was used to deliver a continous (c-)TBS train over the insular cortex (Lenoir et al., 2018) or a brief TMS train over the anterior part of the middle cingulate cortex (D'Agata et al., 2015). Both protocols resulted in a reduction of the perception of acute cutaneous pain elicited by laser or electrical stimulation (Lefaucheur et al., 2020). Conversely, insular cortex stimulation with a double-cone coil recently failed to be effective in chronic central neuropathic pain (Galhardoni et al., 2019). Other cortical areas have been investigated as an alternative to M1. In (Galhardoni et al., 2019) the cingulate cortex was exposed with an H-coil to treat chronic central neuropathic pain, although no differences in pain relieve were found between active and sham groups. The left DLPFC was exposed to 10Hz rTMS stimulation in patients with motor spinal cord injury in (Nardone et al., 2017), and resulted in a decrease in pain scores, which however did not last beyond the period of stimulation. Given the aforementioned results, focal stimulation using a figure-8 coil over M1 contralateral to pain side is so far the only relevant protocol for rTMS therapy of neuropathic pain. A particular type of chronic pain is fibromyalgia, which usually accompanied by multiple symptoms, including stiffness, fatigue, sleep disturbance, cognitive dysfunction, and depression. Several randomized controlled studies have been conducted over the years and demonstrated that rTMS can effectively reduce pain in patients with fibromyalgia (Yang and Chang, 2020). In (Medeiros et al., 2016), beneficial effect of 10 Hz-rTMS of the left M1 were found in 46 patients (23 active and 23 sham). Moreover, a recent study investigated the value of HF-rTMS delivered to the left DLPFC in fibromyalgia, showing evidence of an impact on fatigue (Fitzgibbon et al., 2018), one of fibromyalgia symptomos, 1 month after a 20 rTMS sessions over four weeks. All the aforementioned results suggest that rTMS may be a possible therapeutic option for controlling pain associated with FM (Yang and Chang, 2020). Among others, possible type of pain that received beneficial effects from either HF or LF rTMS protocol are headache, phantom pain and myofascial pain syndrome (Yang and Chang, 2020).

Post-stroke recovery

Protocols of rTMS are also the most explored therapeutic approach for post stroke motor rehabilitation. Stroke is a neurovascular disorder that causes long-term disabilities, among which are motor and speech impairments. The brain lesion caused by a stroke insult, i.e. ischemic lesion, is associated with metabolic and electrophysiological changes in the neural network, that causes a an alteration in the entire neural network within the affected area. Such destruction of neural networks stimulates a reorganization of the connections by plastic phenomena that involve the perilesional tissue in the injured hemisphere, the contralateral hemisphere, as well as the subcortical and spinal regions (Alia et al., 2017). Therefore, the rationale behind using rTMS in stroke recovery derives from the neuroplastic effects that it exerts on altered electrophysiological mechanisms, including reduced intracortical inhibition and increased transcallosal inhibition of the healthy hemisphere over the damaged side (Fisicaro et al., 2019). Therefore, the therapeutic approaches with rTMS aim at normalizing the imbalance between the affected and the unaffected hemispheres. This can be achieved with both HF and LF r-TMS. In fact, HF-rTMS on the ipsilesional hemisphere upregulates the level of cortical excitability, while by LF-rTMS on the contralesional hemisphere downregulates the effect that it exerts on the ipsilesional cortex (Hoyer and Celnik, 2011). The selection of the cortical targets is based on the pathophysiological mechanisms that are known to be involved. For instance, stronger functional connectivity between M1 and other brain areas is associated with better motor recovery (Dodd et al., 2017), therefore, patients with post-stroke motor disfunctions would be treated by stimulating ipsilateral or contralateral M1. In the evidence-based guidelines recently published by a panel of European experts on TMS, only LF-rTMS of contralesional M1, exerted in the post-acute (within one week and six months after stroke onset) stage of stroke, has been proven to have a level of definite efficacy for hand motor recovery (Lefaucheur et al., 2020). Several studies have been conducted over the years to assess the effects of contralesional LF-rTMS protocol on upper limb motor function demonstrating a clinical imporvement after the treatment. In (Du et al., 2016), 35 patients (16 active, 19 sham) received 5 sessions of LF-rTMS, at 1 Hz and intensities that ranged from 110% tp 120% of the RMT, by a figure-8 coil placed over M1. The treatment resulted in an improved motor function of the affected limbs, more marked than after ipsilesional HF-rTMS, that lasted at least 3 months after the last session (Du et al., 2016). Similar results where found in 2017 by Meng and Song (Meng and Song, 2017), who treated 20 patients (10 active, 10 sham) with 14 sessions of LF-rTMS (1 Hz, 90% RMT) over

M1. Moreover, one study showed that bihemispheric LF+HF protocol have demonstrated to be even more beneficial effect than contralesional LF-rTMS in improving upper limb motor function (Long et al., 2018). Evidence of beneficial effects was also found for HF-rTMS of ipsilateral M1 in motor stroke at the postacute stage, although with less statistical power than contralateral LF-rTMS (Li et al., 2016b; Guan et al., 2017; Sasaki et al., 2017). A possible effect of LF-rTMS over contralesional M1 to promote post-stroke recovery of hand function was found in chronic patients as well. Nonetheless data on this topic are more controversial, probably due to the absence of spontaneous recovery (Lefaucheur et al., 2020).

The same rTMS rationale can be applied to patients affected by post-stroke aphasia for which fMRI demonstrated hyperactivity of the homologous of the Broca's area in the right hemisphere that was associated with poor recovery (Crosson et al., 2007). This provided the rationale for an rTMS-mediated suppression of the right hemisphere activity, as demonstrated in several recent studies (Tsai et al., 2014; Wang et al., 2014; Yoon et al., 2015; Hu et al., 2018).

Obsessive compulsive disorder

Both LF and HF rTMS over various cortical targets such the DLPFC (right or bilaterally), the orbitofrontal cortex (OFC), the anterior cingulate cortex (ACC), or the supplementary motor area (SMA) have been investigated for the treatment of obsessive compulsive disorder (OCD). In fact, such areas are all included in the in the cortical-striatal-thalamic-cortical (CSTC) loop whose functional and anatomical abnormalities are thought to cause OCD (Lusicic et al., 2018). Therefore, many studies investigated rTMS effects on OCD treatment by exposing patients over single areas with figure-8 coil or double cone coils (Salomons et al., 2014; Jahangard et al., 2016; Arumugham et al., 2018) or by exposing the entire head with the H-coil (Carmi et al., 2018, 2019). Particularly, in (Carmi et al., 2018) the H-coil was used to stimulate a large and deep bihemispheric median prefrontal cortex region, (mPFC)-ACC, with either LF (1 Hz) and HF (20 Hz) rTMS sessions, consisting in sending 900 consecutive pulses and a 50 trains of pulses lasting 2 s each, every 20 s, respectively and both with a stimulation intensity at 100% of RMT (Carmi et al., 2018). Their results demonstrated for the first time safety, tolerability, and efficacy of multiple sessions of dTMS in the treatment of OCD and indicated that HF stimulation over the mPFC and ACC was effective in alleviation of OCD symptoms in participants who failed to receive sufficient benefit from previous treatments. Nonetheless, such clinical improvement was not observed in LF-rTMS (Carmi et al., 2018). Therefore, a following larger multicenter trial com-

pared only HF-rTMS to sham, (Carmi et al., 2019)), confirming what previously found in (Carmi et al., 2018), and received FDA clearance for the use of dTMS to treat OCD symptoms.

Parkinson's disease

Literature production and recent reviews (Yang et al., 2018; Chou et al., 2015) showed a possible therapeutic effect of HF-rTMS on motor dysfunction caused by Parkinson's disease, specially if delivered bilaterally over motor cortical regions. Nonetheless, the optimal parameters of rTMS on the functional motor improvement have yet to be established. Recently, sham controlled studies have been conducted and proved HF-rTMS to be effective in improving motor score, each exposing different area of the cortex. In 2015, Kim and colleagues exposed M1 bilaterally using a double cone coil over the leg representation (Kim et al., 2015). Protocol consisted in 5 sessions of HF (10 Hz) rTMS at 90% of RMT and reported a significant improvement of motor score and freezing of gait one week after the last session, in active patients. The same study design was applied one year later to patients with various parkinsonian symptoms and reported the same results (Chang et al., 2016), thus suggesting that using large double cone coils over the leg area might help motor score and freezing of gait, although further research is needed to make this result a specific recommendation (Lefaucheur et al., 2020). One crossover study (Yokoe et al., 2018) compared four conditions of bihemispheric HF-rTMS, consisting in 3 daily sessions at 10 Hz and 100% of RMT, using a figure-8 coil, in a series of 19 PD patients. The conditions were real stimulations over the M1 hand area, the SMA, the DLPFC, or a sham stimulation. The main finding of this study was an improvement of motor score after bilateral HF-rTMS of the M1 and SMA, but not after exposure of the DLPFC compared with the sham condition. No significant changes were observed in either the depression or apathy scores. Moreover, they reported that one patient had a mild headache during the DLPFC stimulation that spontaneously resolved (Yang et al., 2018; Yokoe et al., 2018).

Other diseases

Evidence of possible positive effects of rTMS has been reported also in patients affected by schizophrenia. In case of auditory verbal hallucinations (AVH), the most common schizophrenic positive symptom, an inhibitory action is required, therefore most studies applied LF-rTMS to the left tempo-parietal cortex (TPJ), as it is an area shown to be overactive during AVH symptoms (Jardri et al., 2011). A recent meta-analysis was published (He et al., 2017) to evaluate effects or rTMS in the treatment of both positive and negative symptoms, these last defined as an absence of normal emotions and behaviors (Boutros et al., 2014). It indicated that there may be a beneficial effect

of applying 1 Hz rTMS to the TPJ in patients with schizophrenia. However, effect size was found to be moderate and the level of evidence was relatively low, therefore conduction of future large-scale randomized controlled trials was strongly recommended before including schizophrenia in the clinical practice. Finally, as reported in the evidenced based guidelines by Lefaucheur and colleagues (Lefaucheur et al., 2020), possible efficacy also for LF-rTMS of the epileptic focus, to treat chronic epilepsy, or HF-rTMS of the left DLPFC on cigarette craving and consumption.

Chapter 2

Numerical modeling and electromagnetic (EM) computational dosimetry of NIBS techniques

2.1 The importance of simulating NIBS techniques

Non invasive brain stimulation techniques have gained enormous success over the years and are now extensively used in both clinic and research (Lefaucheur et al., 2020; Brunoni and Palm, 2019). Nonetheless, the mechanism of action that underlies the beneficial effects of the stimulation still requires to be further investigated in order to fully understand it (Chervyakov et al., 2015). Nevertheless, it is well known that such mechanism is mediated by the electromagnetic (EM) field injected by electrodes or induced by a coil inside the brain. In order to understand the relation between the EM field and the biological effects that it exerts, it is essential to know exactly how the field is distributed over the brain and its characteristics (Peterchev et al., 2013; Weise et al., 2020), that is the "dose". The concept of dose has been firstly and mainly used in pharmacology, where it indicates the chemical composition, quantity, and frequency and route of administration of a drug. The drug dose alters the chemical equilibrium of specific particles inside the body, which, in turn, determines the biological response and the clinical action (Peterchev et al., 2013). Similarly, in the context of NIBS,

the biological effect is elicited by the EM field and the desired clinical outcome will be achieved only whether the proper dose is administered. Differently from a drug, EM dose depends on a number of parameters that would make the treatment efficient or ineffective, as they influence the spatial distribution of the field over brain. Such parameters are the geometry of the stimulator, its position over the scalp, and the characteristics of the stimulating waveform, in terms of intensity and shape (Peterchev et al., 2013). A thorough understanding of the EM dose requires to know exactly what EM field distribution is generated and by which combination of the aforementioned parameters, as this would help to understand which characteristics lead to activation of which brain area (Gomez et al., 2020; Weise et al., 2020). In this sense, conducting a dosimetric analysis via experimental measurements would require difficult and, above all, invasive procedures (Huang et al., 2017), therefore the most adopted approach is the use of computational dosimetry, a fundamental tool that allows to investigate how the electromagnetic quantities interact with the brain tissues and the neuronal networks by means of numerical models. EM computational dosimetry consists in solving a discretized form of the Maxwell's equations following a specific algorithm (see section 2.2). To solve the electromagnetic (EM) problem the source (i.e. the stimulator) and the dielectric medium (i.e. human head) must be properly modeled. In this sense, there's been a wide literature production on the topic of numerical estimation of the electromagnetic field distribution induced by both TMS and tDCS inside the brain, a large portion of which focuses on combining the numerical results with mappings of the EMG responses of finger muscles (Opitz et al., 2013; Bungert et al., 2017; Mikkonen et al., 2018; Weise et al., 2020; Caulfield et al., 2020). Such combination of calculated electric field and subjects physiological response is an important step towards the localization of the cortical area responsible for the observed motor output caused by single TMS pulses applied over the primary motor cortex (Weise et al., 2020). Nonetheless, several limitations still affects these studies. Particularly, in TMS applications, the estimated optimal orientation and position of the stimulating coil would still generate an electric field distributed over large parts of the brain cortex, characterized by a wide range of neural structures, that could be driving the physiological effect, as well, and would be difficult to localize (Laakso et al., 2018b; Weise et al., 2020). Other dosimetric studies combine the computed electric field with neuronal modeling, in a multiphysics approach (Rahman et al., 2013; Gomez-Tames et al., 2020; Aberra et al., 2020) in order to directly correlate TMS or tDCS stimulation parameters with the neuronal response.

A similar approach was considered in this thesis, albeit applied to peripheral nerves, and will be discussed in Part III. Finally, dosimetric studies can be conducted to study the electric field distribution induced in brain areas of interest (Parazzini et al., 2011, 2012; Fiocchi et al., 2015, 2018c,b) or to investigate the parameters that influence estimation of the electromagnetic quantities, such as the magnetic inductance (B-)field, the electric (E-)field and the current density J, in terms of stimulator position and shape (Laakso et al., 2014; Janssen et al., 2015; Gomez-Tames et al., 2018; Foerster et al., 2018), anatomical details of the head model (Janssen et al., 2013; Parazzini et al., 2012; Laakso et al., 2015; Thomas et al., 2019), or presence of brain lesions or scalp defects (Wagner et al., 2006; Datta et al., 2010, 2011; Manoli et al., 2017). In this thesis, a dosimetric study on acute ischemic stroke patients was conducted and will be presented in Part II. Despite the deep insight that all the aforementioned studies can give in the field of noninvasive brain stimulation, these broad literature production on EM dosimetry is characterized by a high variability on both the stimulator and the patient's head model as well as in the numerical method chosen to solve the EM problem. Such differences make it difficult to address a standardized method to assess the optimal EM dose for a specific treatment, although it would be needed in order to obtain reproducible results across the different laboratories. In the following sections 2.2, 2.3 and 2.4 an overview of the main numerical methods applied and modeling strategies are reported.

2.2 An overview of the main computational methods

As mentioned in section 2.1, to study the distribution of the EM field in a complex environment, numerical algorithms must be applied to solve Maxwell's equations. In fact, Maxwell's equations are the set of differential equations that describe how the EM field, generated by a source, propagates in the space:

$$\begin{aligned} \nabla \times \mathbf{H} &= \mathbf{J} + \frac{\partial \mathbf{D}}{\partial t} \\ \nabla \times \mathbf{E} &= -\frac{\partial \mathbf{B}}{\partial t} \\ \nabla \cdot \mathbf{D} &= \rho \\ \nabla \cdot \mathbf{B} &= 0 \end{aligned} \tag{2.1}$$

Where $\mathbf{H}$ is the magnetic (H-)field, $\mathbf{E}$ is the electric (E-)field, $\mathbf{D}$ is the displacement current, $\mathbf{B}$ is the magnetic inductance and $\mathbf{J}$ is the current density. This formulation is known as the differential form of the Maxwell's equation; an integral form can be as well considered.
In the frequency domain, Eqq. 2.1 are written as in 2.2:

$$\begin{aligned} \nabla \times \mathbf{E} &= -j\omega\mathbf{B} \\ \nabla \times \mathbf{H} &= j\omega\mathbf{D} + \mathbf{J} \\ \nabla \cdot \mathbf{D} &= \rho \\ \nabla \cdot \mathbf{B} &= 0 \end{aligned} \tag{2.2}$$

where $j = \sqrt{(-1)}$ and ω is the angular frequency.

In addition to the Maxwell's equations, the constitutive relations take into account how the material behaves in presence of the EM field:

$$\begin{aligned} \mathbf{D} &= \epsilon\mathbf{E} \\ \mathbf{B} &= \mu\mathbf{H} \\ \mathbf{J} &= \sigma\mathbf{E} + \mathbf{J}_0 \end{aligned} \tag{2.3}$$

where $\epsilon := \epsilon_0\epsilon_r$ and $\mu := \mu_0\mu_r$ and ϵ_r and μ_r are the relative permittivity and permeability of the medium, while ε_0 and μ_0 are the permittivity and permeability of free space. The third equation is the EM representation of Ohm's law, where σ is the conductivity of the medium and $\mathbf{J}_0$ is an external current source. Several numerical methods exist to solve the Maxwell's equations and they are based on differential or integral equation solvers, such that they discretize the differential or integral form of Maxwell's equations. Both methods can be solved in the time or frequency domain. The algorithms make a spatial discretization of the equations in the space region that has to be analyzed and possibly a time discretization whether one operates in the time domain. Thus, the geometry of the physical systems involved in the problem is partitioned into elements of space, named cells, in which the differential equations can be computed. The spatial discretization of the domain depends on:

- domain dimension: 1D, 2D or 3D.
- element type: triangular, tetrahedral, quadrilateral, hexahedral, or a mix of more

than one type.

- element aspect ratio: isotropic or anisotropic.
- mesh density: uniform or graded mesh.
- topology: structured or unstructured mesh. A structured mesh presents a regular topology with a well known pattern; conversely, an unstructured mesh have an irregular topology where the connectivity of the grid is part of the data structure.

The entire net of elements in which the domain has been discretized is typically named "mesh" or "grid". Once the mesh is defined, the relations of the physical system within each element of the numerical space has to be found. What need to be defined then is the algorithm that is able to solve the physical problem in the discretized space for the specific characteristics chosen. Depending on the characteristic of the problem, a numerical algorithm might be more suitable than others, thus giving more accurate results. For low-frequency solutions, where the dimension of the biological body are small compared to the wavelength (i.e. up to 40 MHz for the human body), a quasi-static approximation can be introduced, thus considering a simplified version of the Maxwell's equations, where electric and magnetic fields are decoupled. In fact, in presence of a source of current, the magnetic vector potential **A** is introduced and expressed by the following integral expression derived from the Poisson's equation, for a filiform circuit:

$$A(r) = \frac{\mu_0 I}{4\pi} \int_l \frac{dl}{\|r - r'\|} \tag{2.4}$$

where I and dl are the intensity and direction of the current flowing through the source, and $\|r - r'\|$ is the distance from the observation point to the source point on the coil. Under quasi-static approximation, **B** can be written as:

$$\mathbf{B} = \nabla \times \mathbf{A}. \tag{2.5}$$

whereas, **E** can be written as:

$$\mathbf{E} = -j\omega\mathbf{A} - \nabla V \tag{2.6}$$

Thus, **E**-field is the superimposition of a primary field ($j\omega\mathbf{A}$) and a secondary field ($\nabla\phi$), being V the electric scalar potential. The primary field is due to the Faraday's

law of induction and is generated by variations in time of the applied magnetic induction. Conversely, the secondary field is due to the charge accumulation at the tissues interfaces with different complex conductivity under the action of the primary field (Roth et al., 1991; Andreuccetti and Zoppetti, 2006; Larsson, 2007). In case of absence of current sources, the vector potential **A** vanishes, and Laplace equation can be used to solve the problem:

$$\nabla \cdot (\sigma \nabla \phi) = 0 \tag{2.7}$$

The numerical work described in this thesis was performed solving Eqq. 2.4 to 2.6 to study TMS applications, and Eq. 2.7 to study tDCS applications. Depending on the work, the applied algorithms are the Finite Element Method (FEM), and the Admittance method, of which a detailed description follows.

2.2.1 The finite element method (FEM)

FEM is a computational method that solves Maxwell's differential equations in the frequency domain and is commonly used to solve complex problems described by differential equations. Several commercial simulation platforms implement this method, among which are CST Studio Suit, that is specialized for electromagnetic applications, or Comsol Multiphysics, that instead is employed in several areas of applications, such as the Electrical, the Mechanical, or the Chemical. Furthermore, the FEM method is also implemented in commercial, as well as freeware and custom made numerical software packages that are specifically built to conduct electromagnetic dosimetry on virtual human body models for medical applications. Most of the work presented in this thesis was conducted using the commercial software Sim4Life (Zurich MedTech, AG), whose low frequency electric and magnetic solvers implement the FEM method on a hesaedric structured mesh. This same software has been used in literature by other research group as well (Parazzini et al., 2015; Fiocchi et al., 2018c,b; Manoli et al., 2017). Another existing software that implements the FEM method is SimNIBS (Saturnino et al., 2019a; Gomez et al., 2020), which was tailor made for TMS and tDCS applications and has been extensively used in literature works about this topic (Opitz et al., 2014; Bungert et al., 2017; Csifcsák et al., 2018; Weise et al., 2020). Other studies implement FEM in costume made codes, as, for example, in (Laakso et al., 2015,

2018b; Mikkonen et al., 2018).
The principle of this method is to replace the entire continuous domain by a number of elementary subdomains in each of which the unknown function is represented by simple interpolation function with unknown coefficients (Zienkiewicz et al., 2005; Jin, 2014). A system of algebric equation is then obtained and solved to find the solution to the differential problem. Thus, the FEM method can be summarized in following steps:

1. Discretization of the domain: Considering a three-dimensional problem, the domain is subdivided in elementary volume of specific shapes, called elements. Most commonly the elements can be tetrahedral or cubical volumes. Each element is described by the nodes located at each corner.

2. Selection of the interpolation (or basis) function: In each element, the unknown solution is given as the sum of the basis function at each node, multiplied by an unknown coefficient. The interpolation function is usually a polynomial of first (linear) or higher order.

3. Formulation of the equation system: In order to find the unknown coefficients, the equation found in step 2 must be multiplied by the so-called weighted functions, according to the scalar product, giving a system equations matrix. The solution is given by the inversion of this matrix and can be found either in a direct or iterative way.

2.2.2 The admittance method

Considering Eq.2.6, this method allows to obtain the electric scalar potential V. The analysis domain is divided into N homogeneous cubic cells ($\Delta x \times \Delta y \times \Delta$z), centered at the point of coordinates (x, y, z), so obtaining a 3D network of lumped electrical elements, including passive components (admittances) and current generators(D'Inzeo et al., 1995; Pisa et al., 2014) (see fig. 2.1 for a simplified 2D representation) . Kirchoff's

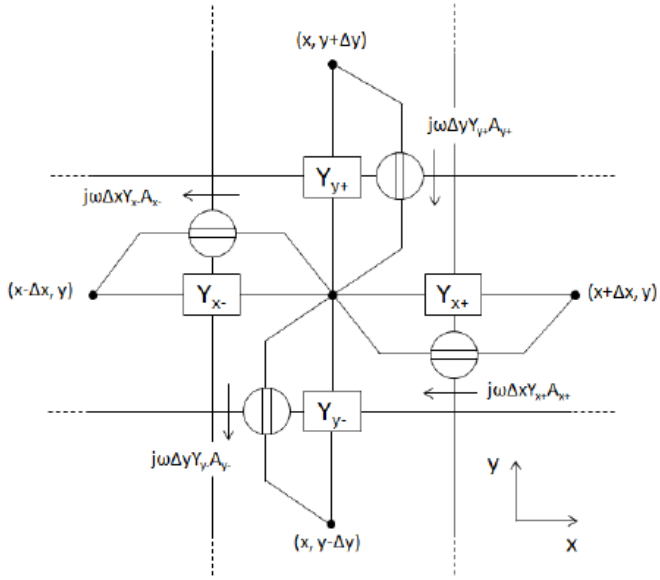

Figure 2.1: 2D representation of the Cartesian grid of the lumped electrical elements network.

law applied at each network node (x; y; z) leads to a linear system of the form:

$$V_{x,y,z} = \frac{1}{Y_{x^-} + Y_{x^+} + Y_{y^-} + Y_{y^+} + Y_{z^-} + Y_{z^+}} [Y_{x^+} V_{x+\Delta x,y,z} + Y_{x^-} V_{x-\Delta x,y,z} + \\ + Y_{y^+} V_{x,y+\Delta y,z} + Y_{y^-} V_{x,y-\Delta y,z} + Y_{z^+} V_{x,y,z+\Delta z} + Y_{z^-} V_{x,y,z-\Delta z} - Y_{x^-} \Delta x j\omega A_{x^-} + \\ + Y_{x^+} \Delta x j\omega A_{x^+} - Y_{y^-} \Delta y j\omega A_{y^-} + Y_{y^+} \Delta y j\omega A_{y^+} - Y_{z^-} \Delta z j\omega A_{z^-} + Y_{z^+} \Delta z j\omega A_{z^+}] \tag{2.8}$$

where $V_{x,y,z}$ is the unknown scalar electric potential at each network node, Y_i and A_i (i = x^-,x^+,y^-,y^+,z^-,z^+) are the admittance and the magnetic vector potential components at each surface of the cell and ω is the operating angular frequency. The magnetic vector potential **A** is calculated from Eq. 2.4, and the admittance values are calculated from the complex conductivity σ^* as:

$$Y_{x^+} = \frac{2\sigma_x^* \sigma_{x+\Delta x}^*}{\sigma_x^* + \sigma_{x+\Delta x}^*} \frac{\Delta y \Delta x}{\Delta x} \tag{2.9}$$

To solve the linear system of Eq. 2.8, the over relaxation iterative technique can be adopted (Armitage et al., 1983; D'Inzeo et al., 1995; Feng Liu et al., 2003) as it represents the best compromise among easy implementation, computer memory occupation, and speed of convergence (Saad and van der Vorst, 2000; van der Vorst, 2002; Hirata et al., 2012). This technique calculates successive estimates of the scalar vector potential from the one estimated at the previous step, to which a correction term is added, in order to accelerate convergence of the solution.

$$V_{n+1}(x, y, z) = V_n(x, y, z) + \alpha[V_{x,y,z} - V_n(x, y, z)] \tag{2.10}$$

where α is a parameter which can assume values between 1 and 2; the higher is α, the faster the solution converge, although for values too close to 2, oscillation phenomena may occur. The iterative procedure ends when the error at the n_{th} step drops below a tolerance level e:

$$\frac{\sum_{i=1}^{N} |V_i^{n+1} - V_i^n|}{\sum_{i=1}^{N} |V_i^{n+}|} < e \tag{2.11}$$

2.2.3 The boundary element method (BEM)

This method is a valid alternative to FEM method, specially when the domain has infinite extension. It formulates Maxwell's equations as boundary integral equations. Hence, it only requires discretization of the surface rather than the whole volume, reducing the complexity of the problem (Banerjee and Butterfield, 1981). Recently, an inverse BEM framework was presented in (Cobos Sánchez et al., 2018) for optimal coil designs, while a boundary element approach with fast multipole acceleration (BEM-FMM) was proposed in (Makarov et al., 2018). This method is based on the surface-charge formulation and uses the highly efficient fast multipole accelerator along with analytical computations of neighbor surface integrals for high resolution bioelectromagnetic models (Makarov et al., 2018). Recent studies compared this BEM-FMM with the FEM, simulating a canonic multisphere geometry excited by an external magnetic-dipole (Htet et al., 2019) and a realistic TMS problem (Htet et al., 2019; Gomez et al., 2020). Htet and colleagues showed that the BEM-FMM algorithm, applied to simple geometries, gave a smaller solution error for all the mesh resolutions investigated

and that it ran significantly faster for high-resolution meshes. Similarly, in the realistic model, an excellent agreement for electric field distribution across different cranium compartments was observed together with a speed improvement of three orders of magnitude when the BEM-FMM was used (Htet et al., 2019). Results on the realistic model were confirmed in (Gomez et al., 2020), although here authors highlighted that BEM is not effective at modeling highly heterogeneous media such as anisotropic tissue, for which they suggest to use the FEM.

2.3 Modeling the stimulator

Different approaches can be considered to model TMS coils and tDCS electrodes, varying from very simplified to more realistic ones. The degree of detail chosen has an influence on the estimation of the electric field generated inside the brain. In order to consider a model to be accurate, validation against experimental measurements is strongly suggested, although not always carried out. Most of the dosimetric studies on TMS adopt ideal assumption to represent the stimulating coil numerically. Specially in the earlier studies, the coil was simplistically modeled as a perfectly circular single winding current wire (Miranda et al., 2003; De Lucia et al., 2007), over which the piecewise Biot-Savart law was integrated in order to compute the magnetic vector potential **A**. Over the years different works investigated how modeling realistic coil geometries would influence the distribution and intensity of the computed E-field (Tachas et al., 2013; Petrov et al., 2017), and reported differences over 150% (Tachas et al., 2013) in the maximum E-field, with an accuracy that increased with the level of detail (Tachas et al., 2013; Petrov et al., 2017). Therefore, more recent studies consider more geometrically realistic coils (Laakso et al., 2014; Paffi et al., 2015b; Çan et al., 2019) and more complex geometries (Fiocchi et al., 2015; Lu and Ueno, 2017), albeit neglecting wire thickness. Another modeling method, particularly suitable for single or figure-8 coils, approximates the coil to a circularly shaped disk (one per lobe for the figure-8) composed of elementary magnetic dipoles. This model was firstly described in 1996 by Ravazzani and co-workers (Ravazzani et al., 1996), and has been used over the years, as in (Thielscher and Kammer, 2004), or more recently in (Gomez et al., 2020) and (Weise et al., 2020). It consists in dividing the coil area in subregions and in placing each dipole in the center of the corresponding subregion, perpendicularly to the surface.

Modeling TMS coils

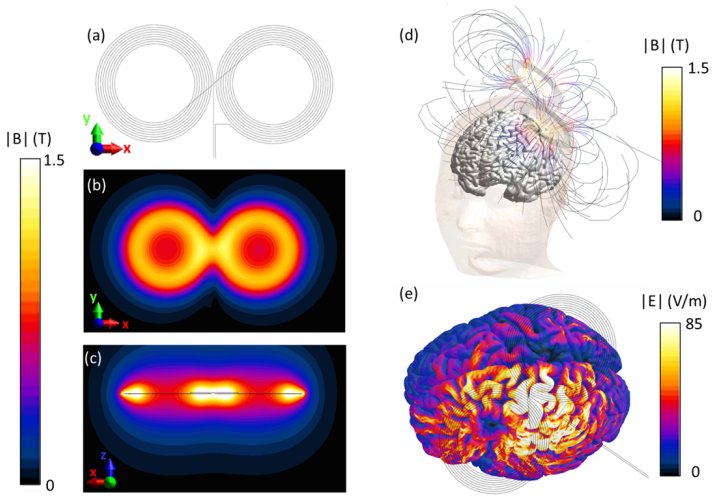

Figure 2.2: Example of a commercial TMS figure-8 coil (PN9925-00, MagStimEden Prairie, MN) model and application: (a) The model, consisting in a current wire wound in the shape of an eight.
(b) B-field distribution computed on the plane parallel to the coil, at 5 mm distance from it. (c) B-field distribution computed on the plane perpendicular to the coil and crossing its center. (d) Example of coil location over the MIDA head model and B-field streamlines. (e) E-field distribution computed on the surface of the grey matter.

The dipoles are weighted by the coil current and the areas of the subregions (Ravazzani et al., 1996; Thielscher and Kammer, 2004; Gomez et al., 2020; Weise et al., 2020). In (Gomez et al., 2020), it was demonstrated that current wire and magnetic dipole models can be equivalently accurate if a sufficiently fine discretization is considered (Gomez et al., 2020). Many studies also investigated the effect of including height and width of the current wires (Salinas et al., 2007; Petrov et al., 2017), demonstrating that considering thickness of the coil winding turns would predict the spatial distribution and magnitude of the electric field more accurately in close proximity with the surface of the coil (Salinas et al., 2007), while in further regions it would affect the induced electric field minimally , and it would not influence the predicted activation site (Petrov et al., 2017). In this thesis, a validated model of a commercial figure-8 coil (PN9925-00, MagStimEden Prairie, MN) (Paffi et al., 2015b) was considered.

The model consists in a current wire made of two co-planar windings, 9 turns each, with an internal diameter of 6 cm and an external diameter of 8.6 cm, as shown in Fig. 2.2 a. The B-field generated by this model is characterized by the typical 8-shape distribution that characterizes the figure-8 coils, with one global maximum in

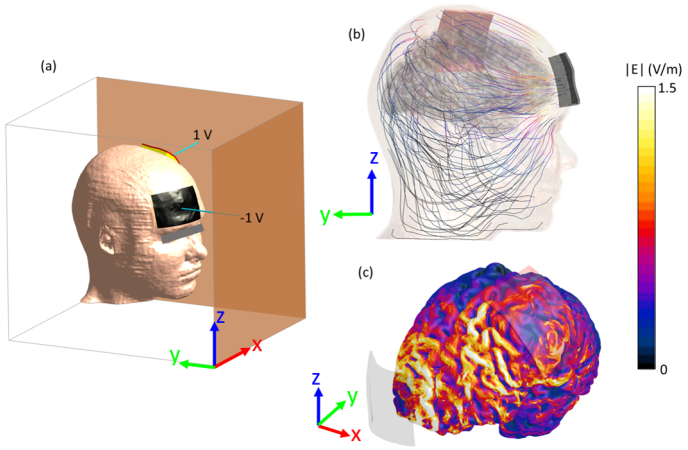

Figure 2.3: Example of tDCS pad electrodes model and application: (a) The electrodes model consists in two rectangular pads of 5 cm x 7 cm of Perfect Electric Conductor (PEC), placed over a saline soaked sponge. Each electrode is fed at its center by a metallic contact (cyan cylinder). (b) Example of electrodes placement over the MIDA head model and E-field streamlines. (e) E-field distribution computed on the surface of the grey matter.

the center, two local maxima corresponding to the two outer rims of the coil and two minima below the center of each winding (Fig. 2.2 b-c). The B-field streamlines flow perpendicularly to the surface of the coil and loop around the wires (Fig. 2.3 d). As stated in section 1.3.1, the E-field induced on the cortex by such coil has a peak in correspondence of the center of the coil and two minima at the center of the lobes (Fig. 2.2).

Modeling tDCS electrodes

The tDCS electrodes model is usually obtained by modifying the surface of the scalp of the head model, in correspondence of where electrodes are placed, since, during a tDCS treatment, the electrodes must adhere perfectly to the surface of the head. Different methods exist to model the electrodes, with different degree of detail. A first methodology consists in modeling planar current boundaries on the scalp surface (Wagner et al., 2007a), thus neglecting the presence of the conductive gel/sponge. This is a very simplified model, that over the years has been substituted by 3D homogeneous patches with uniform conductivities between 1 S/m and 2 S/m (Sadleir et al., 2010; Neuling et al., 2012; Miranda et al., 2013) or as two layers of materials with different conductivities (metal on top of conductive gel) (Datta et al., 2009; Truong et al., 2013; Manoli et al., 2017; Foerster et al., 2018). In these studies, the surface of the electrodes

are modeled as well-conductive metal with a constant electric potential or a constant current density. Although, realistically, the pads are fed using small connectors. Thus, more recent works included the connectors in their modeling (Saturnino et al., 2015; Fiocchi et al., 2016; Manoli et al., 2017), this affects the electric field distribution that results in having higher intensities in the region below the connector. In this thesis, pad electrodes were considered and modeled as a metallic layer placed over a saline-soaked sponge, which is the part in contact with the model's skin. These electrodes were modeled using the CAD software 3dsMax, Autodesk Media and Entertainment. Feeding system consists in two cilindrical objects connecting each metallic layer to an iso-potential surface. In the example of Fig. 2.3, a bipolar configuration is considered. Figure 2.3 b shows computed E-field streamlines, confirming that field flows from anode (red pad) to cathode (black pad). Generated electric field distribution is shown in Fig. 2.3 c.

2.4 Modeling the human head

In the earlier 2000, most of the studies modeled NIBS applications in a rather simplistic way, that would consider the human head as a single-layer or a multi-layer sphere or poligonal shapes (Miranda et al., 2006; Wagner et al., 2007a; Im et al., 2008), losing the shape of the cortex and anatomical details, which have been demonstrated to strongly influence the distribution of the estimated E-field (Chen and Mogul, 2010; Opitz et al., 2011). Therefore, with the increase need of an accurate and precise modeling of NIBS application, the use of realistic and detailed anatomical head models became a more and more unavoidable requirement. Considering realistic head models allows to perform precise and systematic analyses of the variables affecting the EM exposure, such as the anatomical characteristic of a single subject or the position of the source (i.e. the stimulator) with respect to specific brain areas. Realistic human models, either head only or whole body, are usually obtained from medical images, such as MRI (i.e. magnetic resonance imaging) or CT (computed tomography) scans, and sometimes a combination of both. These two imaging techniques have the advantage of including volumetric information, therefore each body slice scanned is composed by voxels with dimensions that depends on the resolution of the image itself. The 3D human model can be reconstructed knowing the dimensions of the voxels and what tissue each voxel belongs to. This last information is acquired via the segmentation of the image, an

operation that consists in flagging with a specific color code all the voxels composing the same tissue. The contrast and resolution of the image influence the number of body structures that can be discerned, thus influencing the level of detail with which the model represents the human anatomy. Depending on the purpose of the study, patient-specific or generic head models can be considered.

Generic models The generic models are those obtained from MRI and/or CT scans of healthy volunteers that were recruited with the purpose of constructing the model per se (Gosselin et al., 2014; Iacono et al., 2015; Nagaoka et al., 2004; Makris et al., 2008), or from anatomical atlas (Laakso, 2018). Therefore, they are characterized by very high resolutions (0.5 mm - 1 mm) and by a very accurate and detailed representation of the human anatomy. An example is set by the models belonging to the Virtual Population (ViP. (Christ et al., 2010; Gosselin et al., 2014)), a set of license-based whole body models (downloadable from the IT'IS Foundation website) that include whole body male and female models going from the baby to the aged human, and count approximately 300 tissues, 40 of which are in the head. Models of only the head exist as well, such as the BOMA model (Makris et al., 2008), a downloadable (`https://phantoms.martinos.org`) freeware model which counts for 28 non-brain structures and 21-brain structures, or the MIDA model (Iacono et al., 2015). MIDA, acronym for Multimodal Imaging-Based Detailed Anatomical Model, is a novel and very detailed head model of an adult female, composed of 115 anatomical structures segmented from MRIs and CTs with a spatial resolution of 0.5 mm (Fig. 2.4). It is characterized by a very thorough representation of the different brain structures, cranial nerves and facial muscles. Additionally 19 brain nuclei were discerned after registration of the subject tomography with brain atlas. It was developed in collaboration between the US FDA, the Massachusetts General Hospital (MGH), the Swiss Federal Institute of Technology (ETH) and the IT'IS foundation. This model is distributed shareware and is downloadable from the IT'IS foundation website. Several literature studies conduct EM dosimetry on generic models, as they have the advantage of being highly detailed and allow to make considerations on the E-field induced in specific brain structures.

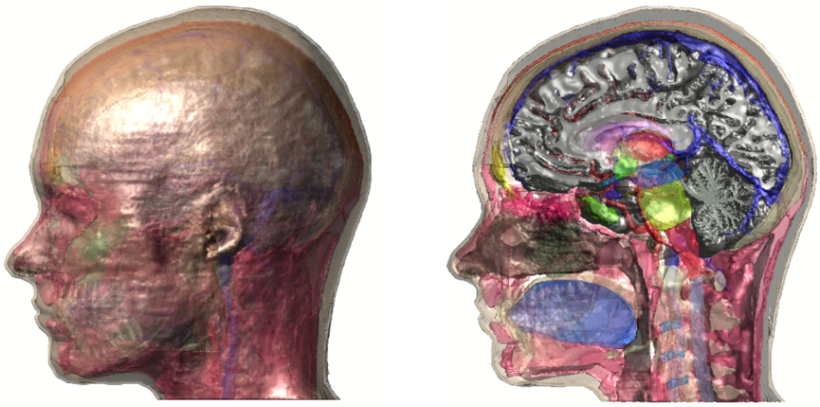

Figure 2.4: The MIDA model (Iacono et al., 2015). A sagittal cut shows the different head structured included.

For instance, in (Fiocchi et al., 2018a), the MIDA model was considered to investigate deep TMS. In fact, it is well known that dTMS target deep brain areas, such as hypothalamus, amygdala, hippocampus, and nucleus accumbens, hence the necessity of considering a model that separately accounts for these structures. Models from the ViP are often considered as well in those studies that aim at characterizing the electric field distribution generated by different type of coils or electrode in conditions that are not related to clinical outcomes (Parazzini et al., 2015; Fiocchi et al., 2018a; Manoli et al., 2017).

Patient-specific models

Conversely, whenever the dosimetric analysis is applied to clinical studies and linked to physiological outcomes, the use of anatomical models that represent the anatomy of the subject under investigation is suggested (Laakso et al., 2018b; Mikkonen et al., 2018; Gomez et al., 2020). The patient-specific models are obtained from custom made pipelines that acquire the scans of the patient under treatment, segment them and build the 3D model. As this operation has to be fast, these models are usually head-only and count the main tissues solely, such as the scalp (an average model of skin, subcutaneous fat and muscles), skull, cerebrospinal fluid (CSF), grey matter (GM) and white matter (WM) (Petrov et al., 2017; Weise et al., 2020). The advantage of considering patient-specific models is that they precisely take into account individual anatomical details, and investigate how it effects the E-field distribution, although they lack in precision within the single model and this could lead to inaccuracy in the results. Particularly

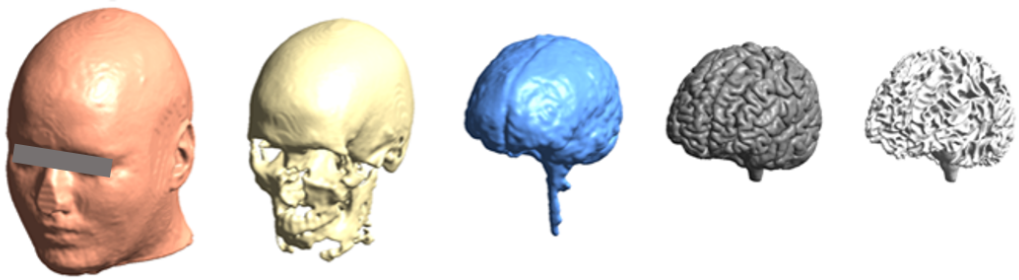

Figure 2.5: An example of patient specific model, generated from the dataset available from `https://simnibs.github.io/simnibs/build/html/dataset.html`.

critical is the fact that no skin layer is considered, although this is an important detail to take into account, specially in tDCS applications where it has been demonstrated that current concentrates near hair follicles or sweat glands (Khadka and Bikson, 2020).

2.4.1 Assigning the dielectric properties

Once the model is created, the electric conductivities must be assigned to each tissue. Comprehensive databases are available to furnish a reference value for the permittivity and conductivity of different human tissues(Gabriel et al., 1996; Hasgall et al., 2018). Although,at lower frequencies (< 1 MHz), where the literature values are scarce and there is still a high variability (Gabriel et al., 2009), these databases furnish more of a "best estimate" of the property value, which can be extracted by literature studies (Hasgall et al., 2018) or extrapolated from measurements at higher frequencies (Gabriel et al., 2009). For this reason there is no consensus in the values assigned across different studies. For instance, LF IT'IS database suggest to assign 0.236 S/m (Hasgall et al., 2018) to the grey matter, which differs from 0.106 S/m reported in (Gabriel et al., 1996). Nontheless, many studies assign 0.276 S/m, among which are (Opitz et al., 2014; Janssen et al., 2015; Huang et al., 2017; Manoli et al., 2017; Gomez et al., 2018), which is taken from (Geddes and Baker, 1967). Furthermore, using a four Cole-Cole parametric model, a conductivity of 0.215 S/m was found in (Laakso and Hirata, 2013), and used in other studies (Laakso et al., 2018b; Mikkonen et al., 2018). Similarly, a value of 0.265 S/m is assigned to the white matter in the LF IT'IS data base, while in (Gabriel et al., 1996) and in (Geddes and Baker, 1967) different values are proposed, i.e. 0.0276 S/m and 0.276 S/m, respectively. Albeit differences in the conductivity

values can be found in any tissue, the most critical one to be characterized is the skin, since its conductivity is highly sensitive to external factors such as hydration level, corneum layer thickness or body part considered for the measurements (Tarao et al., 2012; De Santis and Chen, 2014; De Santis et al., 2016). Among the different studies the values assigned spans across three order of magnitude form 10^{-4} (Gabriel et al., 1996) to 10^{-1}. The issue about assigning proper skin conductivity values has been studied in this thesis and will be discussed in the next chapter. A recent study by Huang and co-workers numerically found conductivity values for the main head tissues, among which were scalp, CSF, GM, and WM, in tDCS applications, by minimizing the error between the simulations and intracranial measurements. The values found in this work are linked to the head model constructed and cannot be extended to other head models (Huang et al., 2017). Another debated issue when it comes to assigning the dielectric properties to single tissues is whether or not anisotropy of white matter (WM) and grey matter (GM) should be considered. In fact most of the studies so far have assigned isotropic conductivity to WM and GM, although it is known that WM is mainly composed of axons that are organized in fascicles oriented in specific directions, thus determining an anisotropic behaviour. Conversely, in the grey matter the measured apparent diffusivity of water molecule is largely independent of the orientation of the tissue, nonetheless the degree of anisotropy is not negligible, albeit much less than in the white matter (Pierpaoli and Basser, 1996; Shimony et al., 1999; De Lucia et al., 2007; McNab et al., 2013; Kroenke, 2018) .It has been shown that taking into account the anisotropic properties of the brain alters the distribution of the electric field, with differences up to 25 % from isotropic modeling , all located in the white matter (De Lucia et al., 2007; Opitz et al., 2011). Different methods are used in literature to derive the conductivity tensor needed to model the anisotropy, from the diffusion tensor, which is obtained by MRI diffusion tensor imaging (DTI). In (De Lucia et al., 2007), the conductivity tensor was calculated for each voxel as a quantity proportional to the diffusion tensor, as theorized in (Tuch et al., 2001). Similar approach was considered in (Opitz et al., 2011) and (Windhoff et al., 2013), although the scaling factor was computed from the isotropic conductivity of white matter and grey matter, weighted for eigenvalues of the diffusion tensor. This method is known as the direct mapping approach (Opitz et al., 2011; Windhoff et al., 2013). In the recent study by Weise and co-workers, the conductivity tensor was calculated considering the volume normalize approach (Güllmar et al., 2010), that consists in multiplying the

isotropic conductivity for the geometric mean of the tensor eigenvalues. In this thesis, an alternative method to derive the conductivity tensor from DTI information was developed and will be described in Chapter 4.

Chapter 3

Effect of Skin Conductivity on the Electric Field Induced by Transcranial Stimulation Techniques in Different Head Model

3.1 Abstract

This study aims at quantifying the effect that using different skin conductivity values has on the estimation of the electric (E)-field distribution induced by Transcranial Magnetic Stimulation (TMS) and Transcranial Direct Current Stimulation (tDCS) in the brain of two anatomical models. The induced E-field was calculated with numerical simulations inside MIDA and Duke models, assigning to the skin a conductivity value estimated from a multi layered skin model and three values taken from literature. The effect of skin conductivity variations on the local E-field induced by tDCS in the brain was up to 70%. In TMS, minor local differences, in the order of 20%, were obtained in regions of interest for the onset of possible side effects. Results suggested that an accurate model of the skin is necessary in all numerical studies that aim at precisely estimating the E-field induced during TMS and tDCS applications. This also highlights the importance of further experimental studies on human skin characterization,

especially at low frequencies[1].

3.2 Introduction

Transcranial magnetic and electric stimulations are techniques that use electric or magnetic fields for the treatment of several neuronal and psychiatric disorders (Ilmoniemi et al., 1999; Nitsche et al., 2008). Differently from other clinical applications, such as Deep Brain Stimulation (DBS) (Paffi et al., 2015a) transcranial stimulation techniques have the great advantage of being non-invasive treatments. Among them, the most widespread ones are Transcranial Magnetic Stimulation (TMS) and Transcranial Direct Current Stimulation (tDCS). In TMS applications, an intense sinusoid like pulsed current, varying in time at a rate of a few kHz, flows through a coil placed on the scalp. Time-varying current generates a time-varying magnetic field that, in turns, induces an electric (E)-field inside the brain. If the E-field induced in specific cortical regions overcomes a threshold level, it is thought to directly activate neuronal axons (Kammer et al., 2011), even though other interaction mechanisms are not excluded (Bungert et al., 2017). TMS is generally used for the treatment of schizophrenia (Bais et al., 2017; Ray et al., 2015; Rotenberg et al., 2014), epilepsy (Rotenberg, 2010; Vanhaerents et al., 2020), Parkinson's disease (Chen and Chen, 2019; Nardone et al., 2020), tinnitus (Schoisswohl et al., 2019) and depression (Kumar et al., 2018; Valero-Cabré et al., 2011; Habib et al., 2018). Other interesting possible applications are currently under investigation, including obsessive compulsive disorder (Carmi et al., 2018; Zhou et al., 2017), post-stroke rehabilitation (Fisicaro et al., 2019; He et al., 2019; Watanabe et al., 2018; Zhao et al., 2018), chronic pain (Yang and Chang, 2020), dependencies, addiction and dementia (Horvath et al., 2014; Lefaucheur et al., 2014; Najib et al., 2011). Conversely, tDCS makes use of a low-intensity (260 μA – 2 mA) direct or alternating current flowing between two metallic electrodes placed on the scalp (Nitsche et al., 2008; Nitsche and Paulus, 2001; Priori et al., 1998). The induced E-field penetrates deep inside the brain but its strength is several orders of magnitude lower than in TMS so that it modulates the spontaneous neuronal activity (Knotkova et al., 2019; Nitsche and Paulus, 2001) by means of mechanisms allowing neuronal detection of weak signals (Gammaitoni et al., 1998; Paffi et al., 2013). Possible clinical applications for tDCS are

[1]This chapter is published as an article in Physics in Medicine and Biology (Micol Colella et al 2021 *Phys. Med. Biol.* **66** 035010, doi: `https://doi.org/10.1088/1361-6560/abcde7`)

the treatment of psychiatric disorders, such as depression (Brunoni and Palm, 2019; Kekic et al., 2016) and, depending on the electrodes position on the scalp and polarity of stimulation, beneficial effects have been found when applying tDCS to patients affected by schizophrenia (Fröhlich et al., 2016; Mondino et al., 2015), neuropathic pain (David et al., 2018), stroke rehabilitation (Fleming et al., 2018; Elsner et al., 2018) and Parkinson's disease (Fregni et al., 2006c; Lattari et al., 2017; Nitsche et al., 2008; Dobbs et al., 2018). For both techniques, the accurate placement of the coil or the electrodes in correspondence of the target brain region can be supported by the use of neuro-navigation systems, which grant to visualize a 3D model of the subject's brain and track the position of the coil/electrodes with respect to it (Comeau, 2014; De Witte et al., 2018; Krieg et al., 2017). Further optimization of a TMS or a tDCS treatment derives from an accurate knowledge of the E field distribution inside the brain. This allows to predict the stimulated brain areas, as well as to optimize both stimulation techniques during the treatment. In fact, especially in TMS applications, the most advanced neuro-navigation systems include real-time E field calculation while placing the coil over the scalp, in order to simultaneously facilitate the best coil position and the best stimulation parameters (Comeau, 2014; Hannula et al., 2005; Nummenmaa et al., 2013; Paffi et al., 2015b; Ruohonen and Karhu, 2010). Both real-time and offline dosimetric calculations have always played a key role to optimize TMS and tDCS applications and to understand their interaction with the neuronal tissue. Many papers were published in the last years aiming at numerically evaluating the E-field distribution induced by TMS (Bungert et al., 2017; Deng et al., 2013; Gomez et al., 2020; Laakso et al., 2018b; Opitz et al., 2014, 2016; Paffi et al., 2015b; Weise et al., 2020) and tDCS (Datta et al., 2009, 2010, 2011; Fiocchi et al., 2018c; Laakso et al., 2018a, 2015; Manoli et al., 2017; Parazzini et al., 2015, 2011; Truong et al., 2013; Opitz et al., 2018; Puonti et al., 2019) inside the brain. These papers used different calculation methods and human head models, that spanned from simple homogeneous or multilayered spheres (Deng et al., 2013; Miranda et al., 2003, 2006) up to realistic patient-specific or standard anatomical models obtained from Magnetic Resonance Images (MRIs) (Chen and Mogul, 2010; Datta et al., 2009, 2010, 2011; Fiocchi et al., 2018c; Gomez et al., 2020; Laakso et al., 2015, 2018a,b; Paffi et al., 2015b; Parazzini et al., 2011, 2015; Salinas et al., 2009; Starzynski et al., 2002; Truong et al., 2013). Neuro navigation systems usually consider spherical geometries or anatomical head models that count for few tissues, given the need of a real-time E-field computation (Krieg et al., 2017;

Paffi et al., 2015b). The offline dosimetric studies, like those used for the treatment planning, may consider patient-specific and semi-specific models (Colella et al., 2020) as well as standard detailed anatomical head models. These models include a fine and detailed representation of different tissues and brain structures and are obtained from high-resolution MRIs scans (1 mm or less), such as those from the Virtual Population (Gosselin et al., 2014), the Japanese models (Nagaoka et al., 2004), MIDA (Iacono et al., 2015), and others (Makris et al., 2008), or are based on freely available online anatomy atlas (Laakso, 2018). Although the available anatomical models are getting increasingly accurate and realistic, the assignment of dielectric properties to different tissues remains an important question. Comprehensive databases are available to furnish a reference value for permittivity and conductivity of different human tissues (Gabriel et al., 2009, 1996; Hasgall et al., 2015), nevertheless, there is no agreement on the value used by the different dosimetric studies currently published, especially regarding the conductivity of the skin. This wide range of values used for skin conductivity is partially due to the lack of an accurate knowledge of skin dielectric properties, especially at DC or in the low frequency (LF) range, up to 10 kHz (De Santis et al., 2016) (De Santis et al., 2015). Furhtermore, skin properties strongly depend on internal, physiologic or pathologic conditions, and on external, environmental or experimental factors (Tarao et al., 2012). In fact, skin conductivity is highly variable with hydration level, corneum layer thickness, healthy or ill status, subject age, gender and the body part considered. Moreover, factors external to the body, such as environmental temperature and humidity or the presence of sponges and electrodes, can considerably modify skin conductivity (Tarao et al., 2012). The impact of skin conductivity on the estimated induced E field was studied for safety assessment purposes under a uniform B-field corresponding to the the reference level for the general public (ICNIRP, 2010) at frequencies up to 1 MHz (Schmid et al., 2013) and it was found to be less than 15% at the level of the Central Nervous System (CNS); however, differences up to a factor of 100 were found in specific regions of the skin where pain receptors are located (Schmid et al., 2013). When simulating TMS applications, authors may not consider an accurate skin model and include the head's outer tissues (skin, fat, muscle) in a single layer of scalp (Datta et al., 2013; De Lucia et al., 2007; Gomez et al., 2020; Opitz et al., 2014; Thielscher et al., 2011; Weise et al., 2020). This choice is acceptable when assuming that the induced primary E-field, which is proportional to the time derivative of the induced magnetic B-field, predominates over the secondary E field, related to the

charge accumulation at the interface between two tissues. Nonetheless, variability in skin thickness was shown to affect the induced electric field in the brain with changes below 5%, and up to 11% locally in the skin (Rashed et al., 2019). A recent study on a simple multilayered sphere revealed that a 15% change in the skin conductivity, caused a variation of about 1% on the induced E field in the brain, however much less than those induced by other sources of variability, such as the uncertainty in coil positioning (Gomez et al., 2018). In a preliminary study (Colella et al., 2019) with the TMS coil placed at the top of the head of two anatomical models, it was found that skin conductivity affected the maximum and the average E-field in the brain in a negligible way with respect to the anatomical differences. Despite the low percentage variations found in previous studies, further investigation of local differences is needed, specially where pain receptors are located, as this would be the site of possible side effects onset. However, variability over the skin conductivity in realistic anatomical models deserves to be further investigated in different anatomical regions for an accurate estimation of the induced E-field, not only to assess TMS efficacy but also to control possible side effects, particularly on the local pain receptors on the skin (Rossini et al., 2015). Beside the global statistical values on the E-field in single tissues, sensitive observables comparing local E field distributions should be considered as well (Armstrong, 1978). For what concerns tDCS, the effect of outer tissue layers on the E-field induced in the brain is instead supposed to be much higher than in TMS, due to the capacitive coupling. This was also confirmed by a recent sensitivity study on a simplified anatomical model that included five different tissues (Saturnino et al., 2019a). Moreover, since the clinical response to tDCS varies from patient to patient, due to inter-individual differences in the E field generated inside the brain (Laakso et al., 2015; Mikkonen et al., 2018), it is of paramount importance to quantify how much the E-field would be affected by different skin properties. In a recent work (Huang et al., 2017), in vivo intracranial recordings in epilpsy patients were used, for the first time, to validate computational head models. Validation was carried out in patient-specific models, including five different tissues, by assigning them the conductivity values that minimized the error between measurements and simulations, thus proposing a range of skin conductivity values supported indirectly by experiments. Herein an alternative approach to estimate the skin conductivity in detailed generic anatomic head models is proposed, for which experimental validation is not feasible. It is based on numerical simulations on a multilayered skin model (De Santis et al., 2015) and was used to

estimate an average skin conductivity value suitable for the two realistic and accurate anatomical models: MIDA (Iacono et al., 2015) and Duke (Christ et al., 2010). Beside this value, after an extensive literature review, three other skin conductivities values are herein considered, which represented the whole range of values assigned in the literature. By means of computational simulations the influence of skin conductivity on the E-field distribution induced inside MIDA and Duke, by TMS and tDCS applicators placed on the motor cortex was rigorously quantified, with global and local sensitive observables. The final aim of the present work is to demonstrate the importance of an accurate skin model for a precise estimation of the simulated E-field. Moreover, reliable indications are provided on which conductivity value should be used, once the level of detail considered when modeling the skin is known. This would be a solid support to all the numerical studies that want to correlate the induced E-field to the therapeutic response and/or to possible side effects.

3.3 Models and methods

3.3.1 Brief review of skin conductivity values used in literature

As reported in (De Santis et al., 2015), skin consists of several layers (stratum corneum, cellular epidermis and dermis) with different thicknesses and conductivities, thus an homogenization procedure is often considered (De Santis et al., 2016). In the literature dealing with LF dosimetry (from DC to 10 kHz), skin conductivity, σ_s, assumes several values (from 0.0002 S/m up to 0.465 S/m) spanning more than three orders of magnitude, as summarized in Table 3.1. The lowest value of σ_s found in literature is 0.0002 S/m, it is reported in the generic IT'IS database (Hasgall et al., 2018) and refers to the dry skin as predicted by the dispersive model of (Gabriel et al., 1996) from 10 Hz to 10 kHz. The highest σ_s is 0.465 S/m. It was derived in (Wagner et al., 2004) and typically refers to the scalp, a thick homogeneous tissue that incorporates the skin and the subcutaneous adipose tissue, as well as the fat and the muscle. Two noteworthy intermediate values for σ_s are 0.08 S/m and 0.17 S/m. The latter is reported in the low-frequency IT'IS database (Hasgall et al., 2018) and was obtained by extrapolating experimental values in accordance with the dispersion characteristics of biological tissues (Yamamoto and Yamamoto, 1976). The value 0.08 S m-1 is used in two models in which skin and fat are considered as a unique tissue (Laakso et al., 2018a, 2015), and

correspond to the conductivity of the fat as reported in (Gabriel et al., 2009).

Table 3.1: Values of skin conductivity (σ_s) (1st column) and related reference (2nd column) used in numerical studies (3rd column) dealing with different kinds of exposure (4th column) and frequencies (5th column).

σ_s **(S/m)**	**Reference for σ_s**	**Papers**	**Type of exposure**	**Frequency (Hz)**
0.0002	IT'IS database (Hasgall et al., 2018; Gabriel et al., 1996) (dry skin)	(Fiocchi et al., 2018c; Lu and Ueno, 2017; Tarao et al., 2012)	Contact currents; short magnetic dipole; tDCS; TMS	10^6
0.00045	(Gabriel et al., 1996) (wet skin)	(Aonuma et al., 2018)	TMS	10^4
0.012	(Parazzini et al., 2011)	(Paffi et al., 2015b; Parazzini et al., 2015, 2014, 2012)	tDCS	0
0.08	(Gabriel et al., 2009)(Same as fat)	(Laakso et al., 2018a, 2015)	tDCS	0

Continue on next page

Table 3.1 – continued from previous page

σ_s **(S/m)**	**Reference for σ_s**	**Papers**	**Type of exposure**	**Frequency (Hz)**
0.1	(Dimbylow, 1998)	(Dimbylow, 2005, 1998); (Hirata et al., 2011; Laakso et al., 2014; Laakso and Hirata, 2012; Tarao et al., 2012)	Uniform B; contact currents; tACS; TMS	30-10^6
0.17	IT'IS database, low freq (Hasgall et al., 2018); (Yamamoto and Yamamoto, 1976)	-	-	1-10^6
0.2	(Dawson et al., 1998; Gabriel et al., 2009)	(Dawson et al., 1998; De Santis et al., 2015))	Uniform B	1-10^4
0.22	(Haueisen et al., 1997)	(Im et al., 2008)	tDCS	< 2
0.25	(Truong et al., 2013)	(Bungert et al., 2017)	TMS	$\leqslant 10^4$

Continue on next page

Table 3.1 – continued from previous page

σ_s **(S/m)**	**Reference for σ_s**	**Papers**	**Type of exposure**	**Frequency (Hz)**
0.33	(Salinas et al., 2009)	(Salinas et al., 2009)	TMS	$< 10^4$
0.43	(Haueisen et al., 1997)	(Holdefer et al., 2006; Im et al., 2012; Neuling et al., 2012; Sadleir et al., 2012, 2010; Wagner et al., 2014)	tDCS, tACS	0; 10

Continue on next page

Table 3.1 – continued from previous page

σ_s **(S/m)**	**Reference for** σ_s	**Papers**	**Type of exposure**	**Frequency (Hz)**
0.465	(Wagner et al., 2004)	(Chen and Mogul, 2010; Datta et al., 2013; De Lucia et al., 2007; Gomez et al., 2020; Janssen et al., 2015, 2013; Opitz et al., 2014, 2011; Thielscher et al., 2011; Windhoff et al., 2013)	TMS, tDCS	10^4

3.3.2 A multi-layered model for skin conductivity estimation

To restrict the range of possible σ_s to be used in numerical simulations, the level of detail chosen to model the skin should be considered. As an example, both Duke and MIDA models have an average skin thickness of 1.5 mm (see Fig.3.5) at the level of the head. Thus, the lowest σ_s in Table I (0.0002 S/m), that well describes the stratum corneum (Birgersson et al., 2013; Gabriel, 1997), which is approximately 14 μm thick, should not be extended to the whole 1.5 mm thick skin. On the other hand, the highest σ_s in Table 3.1 (0.465 S/m) is appropriate only in simplified models, where a single thick compartment (scalp) including skin, subcutaneous adipose tissue (SAT), fat, and muscles is considered. Therefore, to estimate what skin conductivity value should be assigned to Duke-like or MIDA-like models, a 1.5 mm thick multi layered skin model was placed inside two metallic parallel plates (see Fig.3.7) and simulated

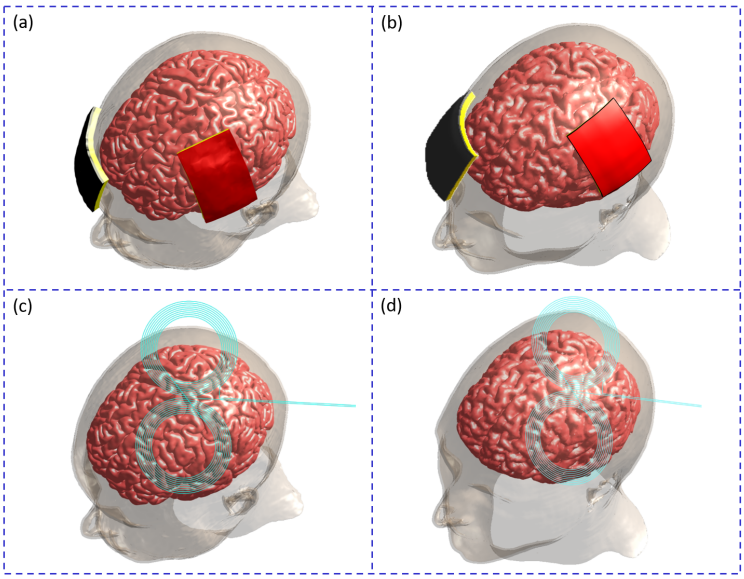

Figure 3.1: Positioning of the tDCS electrodes (panels a and b) and the TMS coil (panels c and d) in correspondence of the primary motor area (M1) of MIDA (panels a and c) and Duke (panels b and d).

with Sim4Life (Sim4Life-v4.4. SIMulation 4 LIFE Science Platform). The following layers were considered: stratum corneum (14 μm; σ=0.0002 S/m), cellular epidermis (61 μm; σ=0.009 S/m), dermis (1 mm; σ=0.526 S/m), and SAT (remaining thickness; σ=0.0417 S/m). Thicknesses and conductivities at 1 kHz for each layer were taken from the experimental data of (Tsai et al., 2019) and (Xu and Mandal, 2015). Further details are given in Appendix 3.8. The calculated equivalent σ_s resulted equal to 0.08 S/m. Taking into account the variations associated to each layer, as those reported in (Tsai et al., 2019), the estimated σ_s ranged from 0.07 to 0.1 S/m. Therefore, a first set of numerical simulations was performed assigning to the skin 0.08 S/m. To account for the wide range of values reported in literature three more σ_s values were considered: 0.0002 S/m, 0.17 S/m and 0.465 S/m. The same values were used for both stimulation techniques, as σ_s increases by less than 2% from 10 Hz to 10 kHz (Gabriel et al., 1996).

3.3.3 Head Models

The anatomical models used in this work are Duke, a 34 year-old male model of the whole human body, belonging to the Virtual Population (Christ et al., 2010; Gosselin et al., 2014), and MIDA, a 29-year-old female model of the head (Iacono et al., 2015).

From the whole Duke model, only the head and the neck were extracted, down to the carotid sinus, thus counting 38 different tissues, including all the basic head structures, such as the cerebrospinal fluid (CSF), grey matter (GM) and white matter (WM). The MIDA model includes 115 separate structures, with a detailed representation of nerves and vessels. However, to compare results obtained with the two models, the same level of anatomical detail for MIDA and Duke was considered by reducing the MIDA model to 38 different anatomical structures. This was done by merging together all tissues characterized by the same dielectric properties (see Appendix 3.7). By doing so, the dielectric discontinuities of the model are not altered. Both surface-based head models were imported in the commercial software Sim4Life (Sim4Life-v4.4. SIMulation 4 LIFE Science Platform) and discretized with a maximum spatial step of 1 mm in the three orthogonal directions. Dielectric properties of all the tissues (except the skin) were taken from the IT'IS database (Gabriel et al., 1996; Hasgall et al., 2018) at 3 kHz for TMS and 10 Hz for tDCS. The latter is the lowest frequency at which measurements have been conducted (Gabriel et al., 1996).

3.3.4 tDCS Electrodes model

tDCS electrodes were modeled as two rectangular pads of 5 cm x 7 cm that consisted of a metallic contact, modeled as Perfect Electric Conductor (PEC), and a saline soaked sponge ($\sigma = 1.4$ S/m) between the electrode and the scalp (see Fig. 3.1 a and b). The cathode, colored in black in Fig. 3.1 a, was placed over the contralateral supraorbital region, while the anode, colored in red, was placed over the primary motor cortex (M1) (Nitsche et al., 2008). M1 is anterior to the central sulcus and is one the most targeted areas in both tDCS and TMS (Laakso et al., 2014; Opitz et al., 2011; Thielscher et al., 2011).The different positioning of the anode between MIDA and Duke, evident from Figs. 3.1 a and b, is due to the anatomical differences in the cortical circumvolutions, specifically in the central sulcus. The electromagnetic (EM) problem was solved with the EM simulation software Sim4Life using the Electro Ohmic Quasi-Static (EQS) solver. Simulations were performed in static condition and with an injected current into the head equal to 1 mA.

3.3.5 TMS Coil model

The two head models were exposed to a commercial figure-8 coil (PN9925-00, MagStim Eden Prairie, MN), modeled as a current pathway made of two coplanar windings, 9 turns each, with the internal diameter of 6 cm and the external diameter of 8.6 cm, as described in (Paffi et al., 2015b) (Figs. 3.1 c and d). The coil was placed at a distance of 5 mm from the scalp in correspondence of M1 (Janssen et al., 2015). According to the specifications of the neurostimulator, the frequency was set to 3 kHz and the current amplitude was such to obtain a B-field of 1.2 T on the scalp surface just below the coil. The problem was solved using the Magneto Quasi-Static (MQS) module included in the LF solver of the EM simulation software Sim4Life.

3.3.6 Observables

For each different tissue, the E-field distribution was considered. Starting from that, the mean value, the maximum value and the percentiles were extracted to compare results obtained with different head models and σ_s. To avoid numerical artifacts, the 99th percentile was used as an estimation of the maximum value of the E-field (E_{max}), as suggested by the ICNIRP guidelines of 2010. To estimate E_{max}, other papers proposed either to use a dynamic approach (De Santis and Chen, 2014) or to use the 99.9^{th} and even the 99.99^{th} percentile (Soldati and Laakso, 2020). However, here the ICNIRP guidelines were followed and the 99th percentile was considered. Beside this global evaluation, to compare voxel-by-voxel the E-field distribution obtained with different σ_s, even in regions distant from the stimulation focus, the Symmetric Mean Absolute Percentage Error (SMAPE) (Armstrong, 1978), defined as in Eq. 3.1, was calculated.

$$SMAPE(i,j,k) = \frac{|E_\sigma(i,j,k) - E_{\sigma,ref}(i,j,k)|}{\frac{E_\sigma(i,j,k)+E_{\sigma,ref}(i,j,k)}{2}} \times 100 \tag{3.1}$$

where i, j and k are the indexes of the single voxel, while E_σ (i,j,k) and $E_{\sigma ref}$ (i,j,k) are the intensity of the E-field for the evaluated conductivity (E_σ) and the reference conductivity ($E_{\sigma ref}$) computed in the voxel (i,j,k). For the sake of convenience, the reference skin conductivity was chosen as the lowest one: 0.0002 S/m.

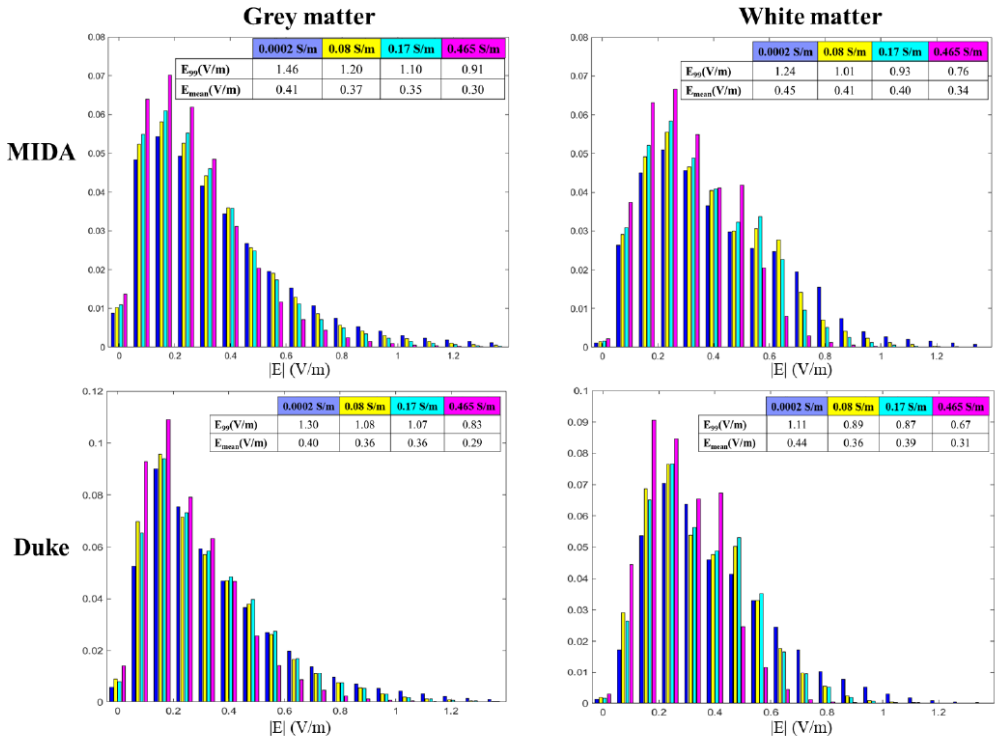

Figure 3.2: Normalized probability distribution of E-field intensity ($|E|$) induced by tDCS inside the grey matter (left) and the withe matter (right) for the two models: MIDA (upper row) and Duke (bottom row) and for different skin conductivities (σ): 0.0002 S/m (blue), 0.08 S/m (yellow), 0.17 S/m (cyan), and 0.465 S/m (magenta). In each panel the inset reports the 99_{th} percentile (E_{99}), considered as an accurate estimate of the maximum value, and the mean value (E_{mean}).

3.4 Results

3.4.1 tDCS

Probability distributions of the calculated E-field intensity inside the tissues involved in the stimulation, i.e., GM and WM, for MIDA and Duke are shown in Fig. 3.2, together with the average value (E_{mean}) and the 99_{th} percentile (E_{99}), reported in the inset of each panel. Comparing the different anatomical models, for both tissues, one can see that the distributions are very similar, with a maximum value around 1 V/m for almost all the investigated conductivities, as expected from literature (Parazzini et al., 2011; Truong et al., 2013). Higher values are induced in MIDA probably due

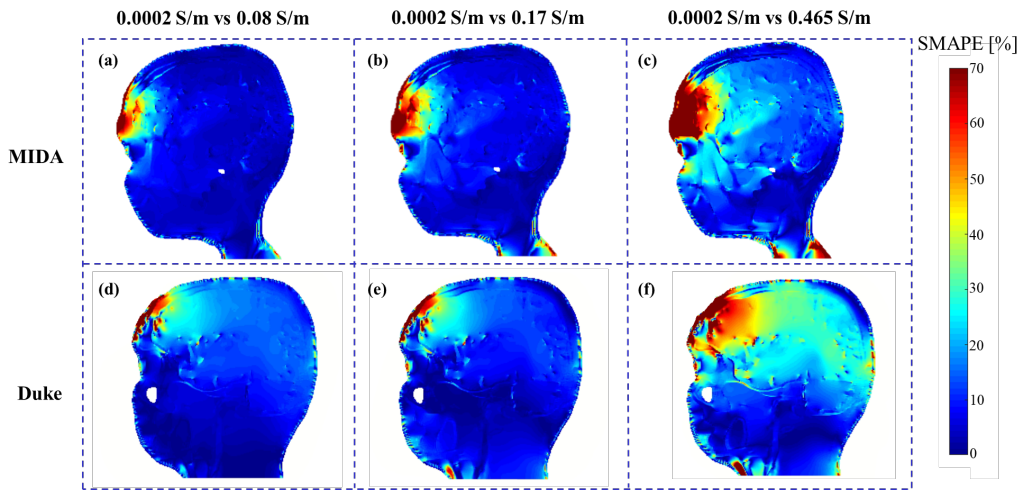

Figure 3.3: SMAPE distribution on the sagittal plane passing through the center of the cathode, calculated in tDCS stimulation, for the two models: MIDA (upper row) and Duke (bottom row), comparing σ=0.08 S/m with σ=0.0002 S/m (first column), σ=0.17 S/m with σ=0.0002 S/m (second column), and σ=0.465 S/m with σ=0.0002 S/m (third column).

to the smaller size of the head, with maximum differences between the models equal to about 12% for both E_{99} and E_{mean}. This result was in line with those obtained in (Parazzini et al., 2014), where both peak and median values of the E-field amplitude were higher in a child model than in adult ones. Both in Duke and MIDA, an increase of σ led to a reduction of the induced E-field in the inner structures due to a higher voltage drop across the skin layer. Maximum variations on E99 and Emean were, respectively, about 40% and 25% for MIDA model and 40% and 30% for Duke. This implied that the choice of skin conductivity might affect the predicted induced E field in the brain even more than the considered anatomical model. Moving to the local differences, Fig.3.3 shows the SMAPE on a sagittal plane passing through the center of the cathode for MIDA (upper row) and Duke (bottom row), calculated between each conductivity value and the "reference" value of 0.0002 S/m. Maximum differences were in the frontal region below the anode, and might reach values as high as 70% even inside the brain, revealing that prediction of stimulated areas strongly depends on the correct choice of skin conductivity.

3.4.2 TMS

The same analysis on statistical values conducted for TMS application revealed that the induced E-field in the brain (GM and WM) was much less sensitive to both the anatomical model and the skin conductivity than in tDCS. Variability between MIDA and Duke reached 1% for E_{99} and 1.5% for E_{mean} inside GM, whereas, for both models, the effect of skin conductivity on E_{99} and E_{mean} in the brain (GM and WM) was negligible, less than 1%. This was expected given that the induced E field follows closed streamlines, as the eddy currents. Therefore, just below the coil, it is almost tangential to the air-skin and skin-SAT boundaries and is only slightly affected by the conductivity contrast at the interfaces (Chen et al., 2013; De Santis et al., 2015, 2016). However, looking at the SMAPE on the sagittal plane of the left hemisphere at 1 mm from the center of the head, shown in Fig.3.4, it can be seen that there were some regions in both models where the SMAPE was quite large. Specifically, it was even higher than 10% in a region deep inside the brain, when comparing the two extreme values used for σ_s (see Figs.3.4c and f). Similar findings were obtained in (Colella et al., 2019) with the coil placed on the top of the head. Such SMAPE distributions could be explained by the fact the effect of skin conductivity variations is more relevant on the normal component of the E-field than it is on the tangential one, and in the deep brain regions the induced E-field is mainly oriented orthogonally to the interfaces between GW, WM and CSF. The region where the SMAPE resulted to be higher than 10% was calculated to be of about 26.1 cm^3 in the MIDA model and 8.5 cm^3 in the Duke model and included areas of the WM and GM, such as Caudate Nucleus, Accumbens Nucleus and Thalamus. Although these regions are not the preferred TMS targets, they are involved in cognitive and motor tasks and their malfunctioning is related to pathologies such as Parkinson's disease and Huntington's Corea (Weber and Eisen, 2002; Cincotta and Ziemann, 2008; Lefaucheur et al., 2014), attention deficit/hyperactivity disorder (ADHD) (Croarkin et al., 2011; Rotenberg et al., 2014) and Obsessive-compulsive disorder (OCD) (Carmi et al., 2019). Therefore, an accurate prediction of the E-field induced in these regions could be of importance for improving the efficacy of new TMS applications while reducing side effects. Significant SMAPE values, up to 20%, were also found in the skin and in correspondence of the carotid sinus in the neck (19.43% in the MIDA model).

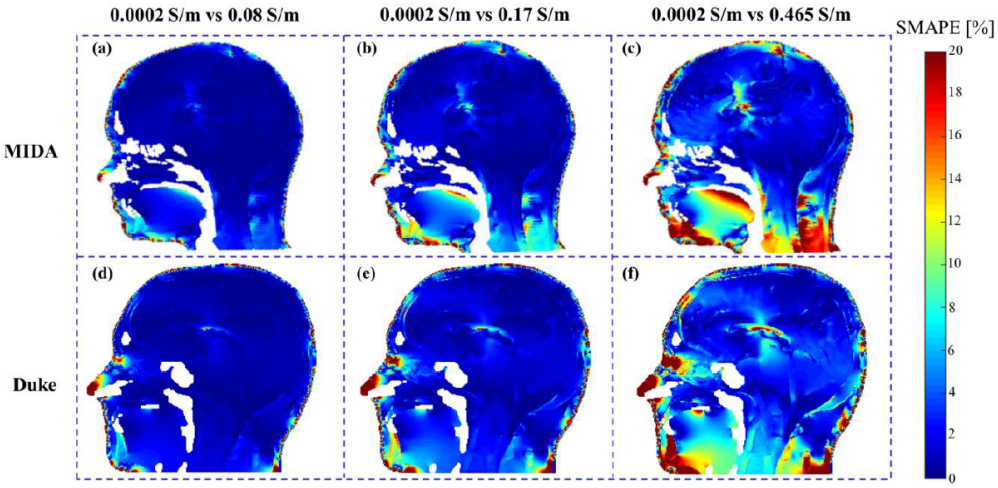

Figure 3.4: SMAPE distribution on the sagittal plane crossing the left hemisphere at 1 mm from the center of the head, calculated in TMS stimulation, for the two models: MIDA (upper row) and Duke (bottom row), comparing σ_s=0.08 S/m with σ_s=0.0002 S/m (first column), σ_s=0.17 S/m with σ_s=0.0002 S/m (second column), and σ_s=0.465 S/m with σ_s=0.0002 S/m (third column)).

3.5 Discussion

For both head models, changes of σ_s determined variations on E_{99} and E_{mean}, induced in the brain by tDCS, in the order of 40% and 30%, respectively. They were comparable to or even higher than those due to the use of different anatomical models (12%). Local percentage variations, quantified by the SMAPE, which is a sensitive local observable, reached 70% in the frontal region beneath the cathode, when comparing the highest and lowest values used for σ_s (0.0002 S/m and 0.465 S/m). Specifically, the induced E-field in the brain was overestimated for σ_s lower than the calculated equivalent σ_s and vice versa. These high differences were attributable to the capacitive coupling between the source (tDCS electrodes) and the tissues, so that an impedance variation of the outermost layer (skin) likely affected also the underlying layers (GM and WM). In fact, right below the electrodes, the E-field was almost orthogonal to the tissues interfaces and thus it was strongly sensitive to impedance discontinuity. Conversely, for TMS, the effect of skin conductivity on the induced E_{mean} and E_{99} in the brain was negligible. This is expected since the induced E-field is dominated by the time derivative

of B-field which is almost tangential to the interface between skin and subcutaneous tissue (Paffi et al., 2015b; Chen et al., 2013; De Santis et al., 2015). However, using the SMAPE, significant differences (higher than 10%) were found in deep regions of the brain belonging to the basal ganglia. Due to the importance of such regions in cognitive, motor and sensorial functions, an accurate evaluation of the induced E-field is desirable for assessment of TMS effects. Other regions where the SMAPE assumed high values (up to 20%) where the skin and blood vessels, in correspondence of the carotid sinus. Accounting for these differences may be relevant to control the onset of side effects, such as pain sensation due to stimulation of peripheral nerves in the epidermis. Such higher differences were related to the presence of the secondary E field, proportional to $-\nabla V$ (being V the electric scalar potential) generated by the charge accumulation at the tissue interfaces, which cannot be neglected. These different behaviors between TMS and tDCS were in line with results of (Saturnino et al., 2019b), where the skin, together with other sub-cutaneous tissues, was included in a single layer (scalp) whose conductivity assumed a beta distribution between 0.2 S/m and 0.5 S/m. Our results, compared to those reported in the literature, suggested that the choice of skin conductivity to be used in dosimetric studies is subject to the degree of anatomical accuracy used for the skin representation in each head model. Specifically, when considering models in which the skin is incorporated in a thick homogeneous scalp tissue, the average conductivity value to assign to said layer would take into account all cutaneous and extra-cutaneous tissues (e.g. dermis, SAT, muscle) included. For MIDA and Duke models a value of σ_s equal to 0.08 S/m. This value can be applied to all the models that represent the skin as a separate tissue about 1.5 mm thick. It is lower with respect to the one estimated in (Huang et al., 2017) by means of intracranial measurements (0.29 S/m). This discrepancy is attributable to the different thickness associated to the skin layer in the used models. In MIDA and Duke the skin was about 1.5 mm thick and included only a thin layer of SAT as sub-cutaneous tissue, whereas the patient-specific models used in (Huang et al., 2017) considered the skin as a thick layer of scalp, that included the muscle, which is characterized by a higher conductivity value.

3.6 Conclusions

The accurate estimation of the E-field induced in the brain by transcranial stimulation techniques has assumed increasing importance in the optimization of these clinical applications. Therefore, realistic dosimetric models are needed. An open question is the attribution of appropriate skin conductivity values, due to their variability with internal and external environmental factors and to the scarcity of experimental data, especially at DC. Results of this study on two different anatomical models, MIDA and Duke, showed that variability of skin conductivity in the range reported in the literature determined non negligible differences in the E-field induced in the brain by tDCS (globally up to 40% and locally up to 70%), much higher than those attributable to anatomical differences between the two models (12%). Conversely, the maximum and mean E-field induced inside the brain by TMS were sensitive to the anatomical differences between the two models (11%) and almost insensitive (¡ 1%) to changes in σ_s, as expected. Nevertheless, SMAPE values up to 20% were found on the skin, in deep brain areas and at the level of the peripheral nerves. In summary, the choice of a representative σ_s value is fundamental to accurately predict the induced E-field correlated to the effects of tDCS observed experimentally. Even in the TMS technique, a realistic skin model, separated from other extracutaneous tissues, should be considered to accurately simulate the induced E-field. In case it is not possible to obtain a realistic skin model, the error induced by the modeling approximation should be taken into account when estimating the E-field value induced to achieve the stimulation of target areas or that induced in non-target area. For both techniques, the most representative skin conductivity value should be evaluated in each head model, considering the geometric and dielectric properties of the different layers that compose the skin. Therefore, this equivalent value will depend on the level of detail with which the skin of the considered head model is segmented. For MIDA and Duke models, it was estimated to be 0.08 S/m, calculated on the basis of experimental data (Tsai et al., 2019) obtained from the forearm skin of healthy subjects at 1 kHz. Further experimental studies are advisable to measure thicknesses and conductivities of the layers composing the human skin in correspondence of the head, especially at frequencies below 1 kHz. This would give a more accurate value to the skin conductivity and to its variability to be used in dosimetric studies that assess transcranial stimulation techniques.

3.7 Appendix 1: Reducing the anatomical complexity of the MIDA model

Being a head only virtual human model, the main characteristic of MIDA is its high number of anatomical structures. This great level of detail particularly lays in the fact that it accounts separately for many substructures such as single facial muscles or cranial nerve, or small brain structures, as the putamen or the amygdala, that in other models are merged in a unique representation or not represented at all. With respect to MIDA, ViP Duke has a single muscle tissue, that runs over the entire body, representation of the cranial nerve is not as detailed and small brain structures are not considered. Nevertheless, despite the fact that in MIDA there are separate substructures, the tissues EM properties assigned are the same. Therefore, in a study in which accounting for single substructures is not necessary, as the one presented in this chapter, it is possible to merge tissues characterized by the same EM properties, thus decreasing the amount of geometrical discontinuities, without modifying the number of dielectric discontinuities. By doing so, the anatomical detail of the MIDA model was reduced to make it consistent when comparing it with Duke, as shown in Fig. 3.5

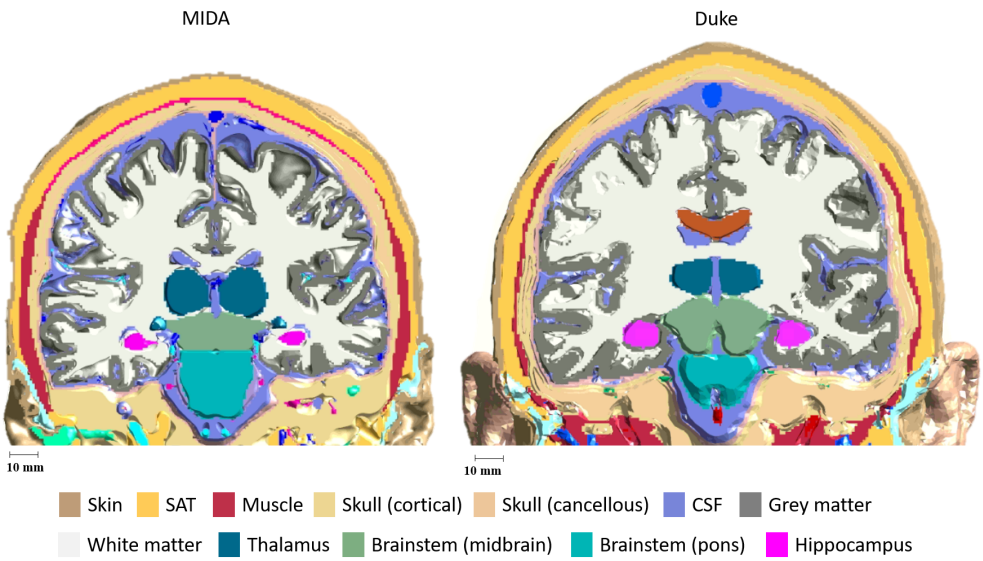

Figure 3.5: Coronal view of the two models MIDA and Duke taken at the center of the head. Nominal skin thickness is 1.5 mm for both models. All tissues common to both the models are listed in the legend.

Results obtained with the reduced version of the MIDA were compared with those obtained by simulating the full version, in order to confirm that such merging of tissues would not affect the distribution of the EM-quantities inside the brain. Figure 3.6 confirmed the hypothesis that the two models return the same results, thus allowing to use the reduced version to conduct the study presented in this chapter.

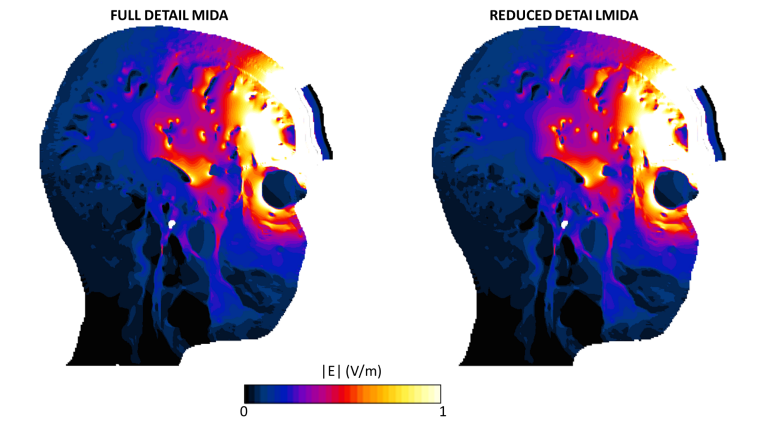

Figure 3.6: E-field intensity distribution over the sagittal plane crossing the cathode: comparison between full detail MIDA model and reduced MIDA model.

3.8 Appendix 2:A simplified multilayered model of the skin to estimate the average σ_s in Duke and MIDA

Figure 3.7 shows the multilayered model of the skin (1.5 mm thick) used to estimate the average σ_s in Duke and MIDA. Properties of the considered layers were taken from (Tsai et al., 2019): stratum corneum (14 ± 4 μm; σ=0.0002 S/m), cellular epidermis (61 ± 7 μm; σ=0.009 S/m), dermis ($1 \pm 0.2mm$; σ=0.526 S/m), and SAT (remaining thickness; σ=0.0417 S/m). It should be noted that the work by Tsai and co-workers considered the skin from the forearm of healthy subjects and not the head. Nevertheless, to the best of our knowledge, this was the study that included the most detailed information on human skin in terms of both conductivity and thickness of each layer. The multilayered skin-model was placed inside two metallic parallel plates and a voltage difference of 2 V was applied. Simulations were run using the Sim4Life Electro Quasi static solver at 1 kHz, as this was the frequency used in (Tsai et al., 2019). The overall conductivity

σ_s was estimated from the computed impedance Z using the formulation reported in (Wake et al., 2016):

$$\sigma_s = \frac{1}{R} \times \frac{d}{S} = \frac{cos(argZ)}{|Z|} \times \frac{d}{S} \tag{3.2}$$

where d and S are, respectively, the distance between the two electrodes and the surface of the electrodes (Fig. 3.7), while arg(Z) and $|Z|$ are the phase and amplitude of the impedance. Considering the aforementioned values of thicknesses and conduc-

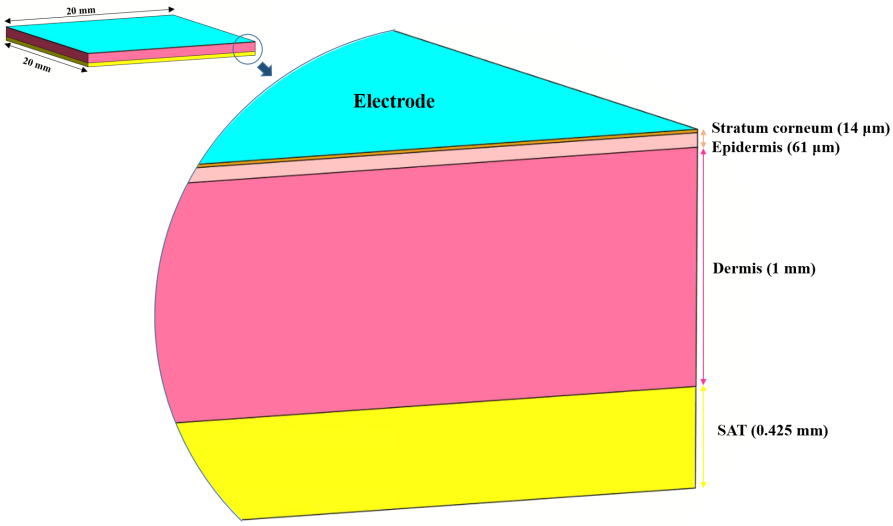

Figure 3.7: Multilayered skin model inside two metallic parallel plates ($20mm \times 20mm$). Overall thickness is 1.5 mm, individual thicknesses and electric conductivity for each layer are: stratum corneum - 14 μm; σ=0.0002 S/m, cellular epidermis - 61 μm; σ=0.009 S/m, dermis - 1 mm; σ=0.526 S/m, and SAT – 0.425; σ=0.0417 S/m.

tivities, σ_s was estimated equal to 0.08 S/m (3.2). In (Tsai et al., 2019), thicknesses of the stratum corneum, epidermis and dermis were reported to respectively have a variability of $\pm 4\mu m, \pm 7\mu m and \pm 0.2mm$, and conductivities of epidermis and dermis had a standard deviation of approximately 50% and 40%. Estimated σ_s varied from 0.067 S/m to 0.1 S/m (Tabs. 3.3-3.6), with a maximum variability of 25%. As stated in the discussion and conclusion of this chapter, herein is suggested a possible methodology that could be used to evaluate the most appropriate skin conductivity value, known the thickness of the skin and what layers and tissues it includes for a given model.

Table 3.2: Estimated overall σ_s considering the reference values of thickness and conductivity given in (Tsai et al., 2019) (SC = Stratum corneum).

Reference Values		
Tissue	σ (S/m)	Thickness (mm)
SC	0.0002	0.014
Epidermis	0.009	0.061
Dermis	0.53	1
SAT	0.042	0.425
Overall σ_s = 0.08 S/m		

Table 3.3: Estimated overall σ_s considering the lower extremity value of thickness for stratum corneum (SC), epidermis and dermis and reference values for conductivity, as given in (Tsai et al., 2019).

Minimum Thickness		
Tissue	σ (S/m)	Thickness (mm)
SC (-4 μm)	0.0002	0.01
Epidermis (-7 μm)	0.009	0.054
Dermis (-0.2 mm)	0.53	0.8
SAT	0.042	0.636
Overall σ_s = 0.067 S/m		

Table 3.4: Estimated overall σ_s considering the upper extremity value of thickness for stratum corneum (SC), epidermis and dermis and reference values for conductivity, as given in (Tsai et al., 2019).

Maximum Thickness		
Tissue	σ (S/m)	Thickness (mm)
SC (+4 μm)	0.0002	0.018
Epidermis (+7 μm)	0.009	0.068
Dermis (+0.2 mm)	0.53	1.2
SAT	0.042	0.214
Overall σ_s = 0.1 S/m		

Table 3.5: Estimated overall σ_s considering the reference value of thickness for stratum corneum (SC), epidermis and dermis and lower std deviation for conductivity of epidermis and dermis, as given in (Tsai et al., 2019).

Minimum Conductivity		
Tissue	σ (S/m)	Thickness (mm)
SC	0.0002	0.014
Epidermis (-40%)	0.006	0.061
Dermis (-50%)	0.35	1
SAT	0.042	0.425
Overall σ_s = 0.067 S/m		

Table 3.6: Estimated overall σ_s considering the reference value of thickness for stratum corneum (SC), epidermis and dermis and upper std deviation for conductivity of epidermis and dermis, as given in (Tsai et al., 2019).

Minimum Conductivity		
Tissue	σ (S/m)	Thickness (mm)
SC	0.0002	0.014
Epidermis (+40%)	0.015	0.061
Dermis (+50%)	1.053	1
SAT	0.042	0.425
Overall σ_s = 0.099 S/m		

Chapter 4

Combining TMS, MRI and computational dosimetry: The effective navigated (En-)TMS

4.1 The effective navigated (En-)TMS: A novel approach for EM-dosimetry

As pointed out in Section 1.3.2, TMS has been extensively used over the years, not only to treat many psychological diseases and neurological disorders, but also as a diagnostic and neuro-investigational tool, particularly suitable for cortical motor (Cavaleri et al., 2017; Gunduz et al., 2020) or language mapping (Rosler et al., 2014; Karhu et al., 2014; Sakreida et al., 2018). In fact, TMS can be used to study intracortical and cortico-cortical connectivity, which, in case of motor cortex stimulation, can be measured by electromyographical recordings of the motor action potentials (MEPs), which are stimulus-induced responses (Bashir et al., 2013). MEPs reflect the excitatory motor functions of the cortex and of the spinal cord and, therefore, are the main observable during cortical mapping that aims at diagnosing and following-up motor diseases (Pitkänen et al., 2018). TMS has also been used to study cortical control of language functions in healthy volunteers (Devlin and Watkins, 2007; Sakreida et al., 2018) or patients with tumors (Rosler et al., 2014; Picht, 2014; Motomura et al., 2020), in which case a precise mapping is of paramount importance in association with neurosurgery when operating tumors in the vicinity of the presumed language eloquent areas,

to reduce the risk of post-operative deficits (Mäkelä and Laakso, 2017; Motomura et al., 2020). To this regard, a crucial issue is the correct position of the TMS coil over the target brain area. Still nowadays, positioning of the coil is sometimes performed based on standard external landmarks on the head, therefore causing an inaccurate knowledge of the anatomical target in the cortex (Hannula and Ilmoniemi, 2017). In fact, the size of the head and the anatomical shape of the brain, which vary from patient to patient, influence the position of the coil and its distance from the cortex. Placement and orientation of the coil should be defined individually for each subject rather than following the standardized placements over fixed generic points. In order to achieve an accurate coil placement, a new technique, known as navigated (n-)TMS, was developed and allows to use individual MRI (Ruohonen and Karhu, 2010; Hannula and Ilmoniemi, 2017), rather than fixed landmarks. The n-TMS system requires both information about the physical parameters of the coil (location, orientation, tilt, size, and shape), and of the subject's head and brain (Hannula and Ilmoniemi, 2017). Such structural information can be obtained from tomographical images of the head, particularly MRIs, that are read by the software to create a 3D model of the brain and skin. Therefore, the scans need to include the whole head so that the nose, ears, and head surface are all visible and accessible as landmarks that will be used to register the subject's head to the space of the acquired images (Comeau, 2014). Such registration is usually performed considering the homologous points method, that tracks unambiguous landmarks on the subject's head, using an optic pen, whose position is recorded by a position sensor, that transfer the spatial information to the navigation software. Usually these landmarks are the nasion, the tip of the nose and the super-tragal notch on the ear (Comeau, 2014). The accurate placement of the coil over the target cortex area is ensured by placing an optical tracker on the coil it self. The relative position between the tracker and the coil is used to calibrate the position sensor, so that when it detects the tracker's position, an offset is applied and information on the coil's center location is transferred to the navigation software. Currently, two strategies can be followed to localize the stimulation spot on the subject's head, one is the line navigated TMS (Ln-TMS) and the other one is the electric field, or effective, navigated TMS (En-TMS) (Hannula and Ilmoniemi, 2017; Sollmann et al., 2016). In Ln-TMS the stimulation spot is assumed to be on the line that passes through the geometric center of the coil and is perpendicular to the coil surface, whereas in En-TMS it is represented via the stimulating electric field that is calculated and visualized on the surface of the

cortex. Therefore, En-TMS and Ln-TMS may indicate the stimulation spot in different gyri depending on local head curvature and coil tilting (Sollmann et al., 2016; Hannula and Ilmoniemi, 2017; Fang et al., 2019). Moreover, Ln-TMS requires the coil to be held continuously tangentially to the scalp, or the stimulation spot would be imprecise (Sollmann et al., 2016; Hannula and Ilmoniemi, 2017; Fang et al., 2019). Between the two, En-TMS is considered to be more accurate and many data are available in clinical practice, which allowed for it to be FDA-approved for tumor-patient diagnostic. With the increasing clinical relevance that En-TMS has gained over the years, the necessity of a fast, and yet exact, knowledge of the induced E-field for accurate targeting and dosimetry is enhanced. A first step implemented in the En-TMS systems to speed-up E-field calculation is to use pre-computed or pre-measured B-field maps generated by the stimulating coil. Such information can be determined experimentally by means of a magnetometer that maps the space around the coil, or computed numerically if the geometry of the coil is known (Paffi et al., 2015b). Once the magnetic field distribution is determined, it must be registered to coil's position in order to accurately map it in the images space. The magnetic field generated by the coil is then used as the input for the electric field calculation (Comeau, 2014). Finally, to fulfill the real-time requirement, most of the existing En-TMS systems estimate the induced E field using spherical conductor models (Hannula et al., 2005; Ruohonen and Karhu, 2010). In order to consider a realistic model of the head, it is necessary to develop numerical methods that have a low computational time, as was proposed in (Nummenmaa et al., 2013) and in (Paffi et al., 2015b). Nevertheless, in (Nummenmaa et al., 2013) a 1-layer BEM was implemented, therefore computing the E field only on the brain surface, thus neglecting its penetration in deeper regions, whereas in (Paffi et al., 2015b), the E-field is computed using the admittance method in the entire head volume. Nonetheless, the head model is characterized by a coarse spatial resolution of 3 x 3 x 3 mm^3, diminishing the accuracy of the E-field calculation. To improve such accuracy, a realistic model, with a high spatial resolution is desirable. Moreover, it has been shown how solution of computed E-field is strongly influenced by the tissues dielectric properties (Saturnino et al., 2019a). Furthermore, a precise brain modeling would require to consider both GM and WM as anisotropic tissues. Notwithstanding, no existing En-TMS has ever included such information in the modeling. Increasing the resolution and assigning anisotropic properties to the brain would certainly increase the accuracy of the solution, that would be translated in guiding more precisely the stimulation towards

optimal placement and intensity. Nonetheless, an increase of the computational time would be unavoidable.

4.1.1 The En-TMS project

Given the current lack of neuronavigation systems that are able to provide an accurate EM solution to guide TMS applications, a dedicated project (the Effective Navigate (En-)TMS project, POR FESR LAZIO 2014 – 2020) is currently ongoing in collaboration with Sentech S.r.l., InfoSolution S.p.a., and the department of Physiology and Farmacology "Vittorio Erspamer", at University of Rome "La Sapienza", with the aim to develop a novel software for nTMS application that combines EMG recording and E-field calculation to provide a precise positioning of the TMS coil. This is guaranteed by the use of a high-resolution anisotropic patient specific head model obtained from MRI and DTI data. The EM-dosimetry code to be integrated in such software is an upgraded version of the custom code developed and validated in (Paffi et al., 2015b), that has been modified in order to manage mutli-compartments, anisotropic head models at a resolution of $1 \times 1 \times 1$ mm^3. The solution approach and the methodology used to obtain the anisotropic brain are reported as follows, together with initial results.

4.2 Custom EM-code: Solution approach

The overall simulation strategy applied in this work is reported in the flowchart in Fig.4.1 and follows the same used in (Paffi et al., 2015b). With respect to EM-dosimetry code developed in this previous work, an upgraded version is herein presented which is able to manage a 1 mm-resolution inhomogeneous head model, with anisotropic brain properties. The procedure and methodology considered is reported as follows and was fully implemented in the C++ environment. The anisotropic head model considered to test the method was provided by SenTech S.r.l.

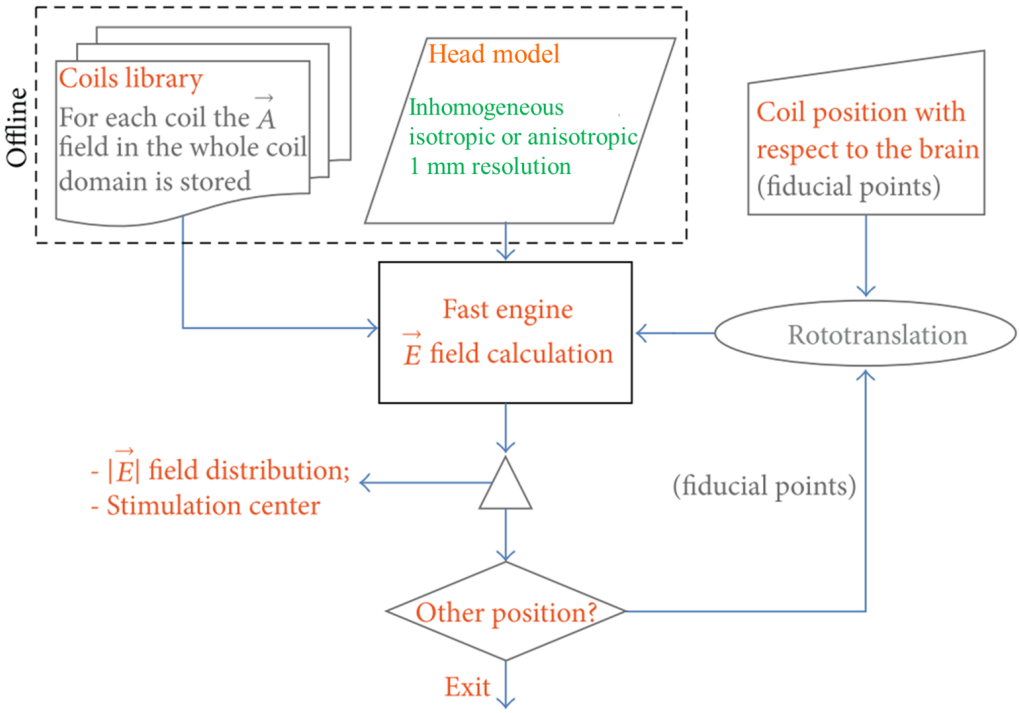

Figure 4.1: Flowchart summarizing the overall strategy adopted to perform E-field calculation (Scheme adapted from (Paffi et al., 2015b))

The first input in the calculation code is the distribution of the magnetic vector potential **A** generated by the coil considered during the simulation. Such file is stored inside a special library created off-line prior to any application, and that collects the **A** field distribution for different TMS coils. The **A** distribution is computed inside a domain that surrounds the coil model (i.e. the coil domain), which is discretized in a Cartesian cubic grid with a 1 mm resolution, and considering a current of 1 A flowing inside the coil. Thus, the **A** file recalled from the library works as the source of the stimulation, after being properly scaled by a factor equal to the chosen current intensity, given the linear relationship between I and **A**. The head model is the second input needed to compute the induced E-field. It must be a voxel based model described by a text file containing geometrical and anatomical information, such as the position of each voxel and its corresponding tissue, marked as a label, in a segmentation-like manner. Such information is processed by the code in order to reconstruct the three-dimensional model (i.e. the *head domain*) and correctly assign the dielectric properties

to the tissues. Additionally, the head model file contains information about brain anisotropy that is used to reconstruct the anisotropic conductivity tensor, as will be described in detail in section 4.2.1. The resolution of the head model must be equal to the resolution of the coil domain. Once that the **A** distribution is retrieved and the head model is reconstructed, the coil must be properly placed over the head, in order to target the desired cortical spot. This is achieved by dynamically roto-translating the head domain with respect to the coil domain, using information about three fiduciary points of the coil that represent its position over the head (Fig. 4.2), according to the following transformation (Paffi et al., 2015b):

$$\begin{bmatrix} x_1 \\ y_1 \\ z_1 \end{bmatrix} = \begin{bmatrix} C_x \\ C_y \\ C_z \end{bmatrix} + \begin{bmatrix} u_{1x} & u_{2x} & u_{3x} \\ u_{1y} & u_{2y} & u_{3y} \\ u_{1z} & u_{2z} & u_{3z} \end{bmatrix} \begin{bmatrix} x \\ y \\ z \end{bmatrix} \tag{4.1}$$

Where (C_x, C_y, C_z) are the coordinates of the center of the coil in the head domain, and (u_{1x}, u_{1y}, u_{1z}), (u_{2x}, u_{2y}, u_{2z}), $(u_{3x}, u_{3y}, u_{y3z})$ are the coordinates of the unitary vectors u_1, u_2 and u_3 that identify the coil domain with respect to head domain. Such transformation maps each point (x, y, z) of the head domain in a point (x_1, y_1, z_1) of the coil domain, as shown in Fig.4.2. Therefore, dimensions of the coil domain have to ensure that the brain area is always contained in it. It should be noted that, in the two discretized domains, the correspondence between cells is not necessarily a one-to-one, since the roto-translation operation is not conformal (Paffi et al., 2015b). Nevertheless, the maximum error committed by implementing this operation is equal to a cell size (1 mm), thus, it is inside the accepted tolerance. A list of different fiducial points can be given as input, as shown in Fig.4.1. Once that the desired relative position between head domain and coil domain is achieved, the **E** field is calculated using the Admittance method, following the formulation described in Section 2.2.2. In this work, the tolerance level e, computed as in eq. 2.11, is set to 1×10^{-5}.

4.2.1 Reconstruction of the anisotropic conductivity tensor

The code developed in this work is able to consider the grey (GM) and the white matter (WM) as inhomogeneous anisotropic tissues, therefore each GM or WM voxel is described by its own conductivity tensor, rather than by a unique scalar value representing the overall electric conductivity σ_{GM} or σ_{WM}. It is known that the electric

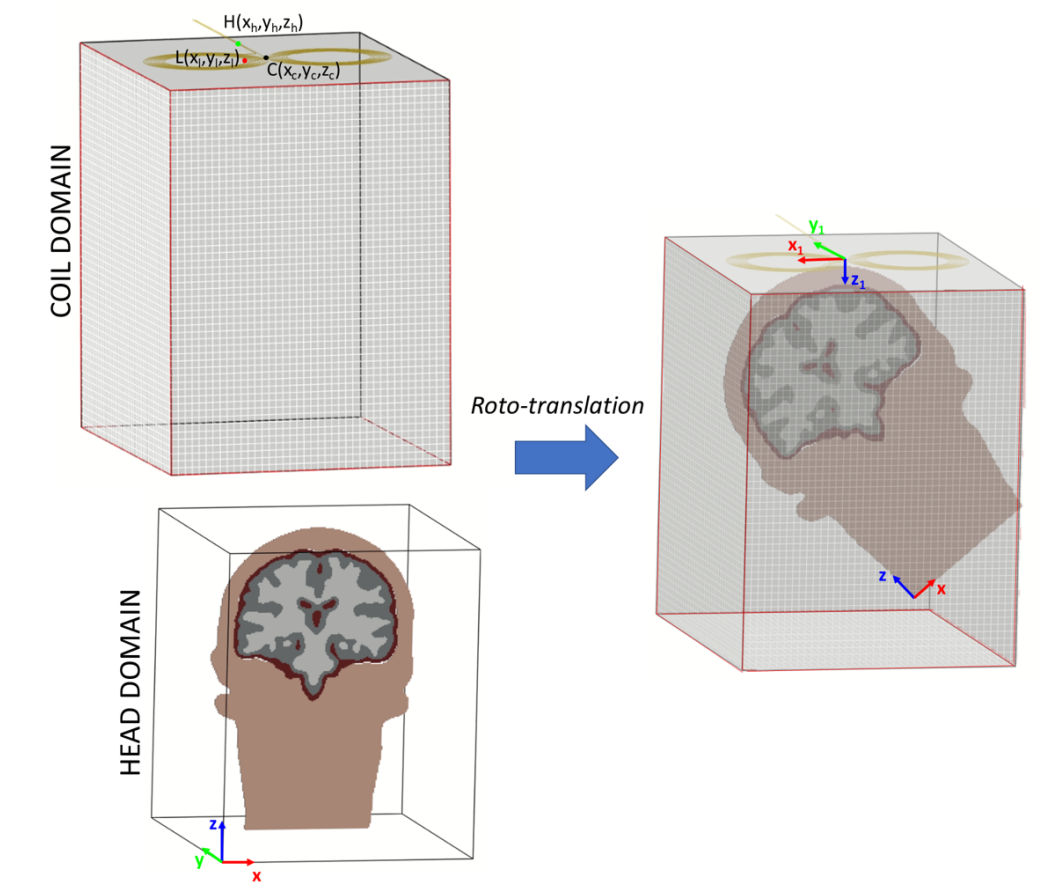

Figure 4.2: Sketch showing the rototranslation operation of coil and brain domains.

conductivity tensor $[\sigma]$ of a given tissue can be computed knowing the corresponding diffusion tensor [D], which can be obtained through diffusion tensor imaging (DTI), an MR based imaging technique used to trace the connectivity of neural pathways in the nervous systems (Lee et al., 2018). The diffusion tensor is a 3×3 symmetric, positive-definite matrix, that can be described by three orthogonal eigenvectors $(\epsilon_1, \epsilon_2, \epsilon_3)$ and three positive eigenvalues $(\lambda_1, \lambda_2, \lambda_3)$ (Wu et al., 2018), that together describe the diffusion properties of a tissue. In fact, the eigenvectors describe the direction of diffusivity, while the eigenvalues, that correspond to the length of each eigenvector, are used to define the amount of diffusion asymmetry within an image voxel, i.e. Fractional Anisotropy (FA), according to the following Eq. 4.2 (Minati and Weglarz, 2007):

$$FA = \sqrt{\frac{3}{2}}\sqrt{\frac{(\lambda_1 - \langle\lambda\rangle)^2 + (\lambda_2 - \langle\lambda\rangle)^2 + (\lambda_3 - \langle\lambda\rangle)^2}{\lambda_1 + \lambda_2 + \lambda_3}} \tag{4.2}$$

Where $\langle\lambda\rangle$ is the average of the eigenvalues. According to Eq. 4.2, $0 <= FA <= 1$.

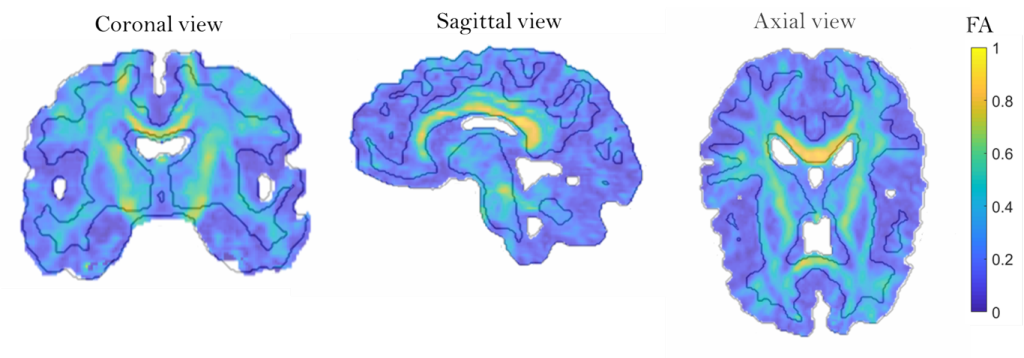

Figure 4.3: Fractional anisotropy map over the three coordinate planes: Coronal and sagittal planes crossing the center of the head, and axial plane crossing the center of the forehead. The solid lines mark the contour of the grey and the white matter

Therefore, if $\lambda_1 = \lambda_2 = \lambda_3$, FA is equal to 0 and the voxel is isotropic, while maximum level of anisotropy is represented by FA=1. For the tissues that composes the model considered in this work, FA of each voxel is given. The scalp and the CSF are considered isotropic with a FA=0, whereas voxels in the grey and in the white matter have FA values that can be greater than 0.2 (Fig.4.3), value considered consistent with a zero anisotropy (Shimony et al., 1999). It has been demonstrated that the electrical conductivity tensor of an anisotropic tissue can be determined from DTI data (Tuch et al., 2001; Rullmann et al., 2009; Güllmar et al., 2010), by establishing a relation between the corresponding eigenvalues. The eigenvalues of the conductivity tensor correspond to σ_{long} and σ_{trans}, that are parallel and perpedicular to the fiber direction respectively (Wolters et al., 2006).

In this work, the transversal conductivity σ_{trans} of both GM and WM was defined as equal to the correspondent isotropic conductivity value, whereas σ_{long} was set proportional to σ_{trans} by a factor known as the conductivity ratio, which depends on the FA

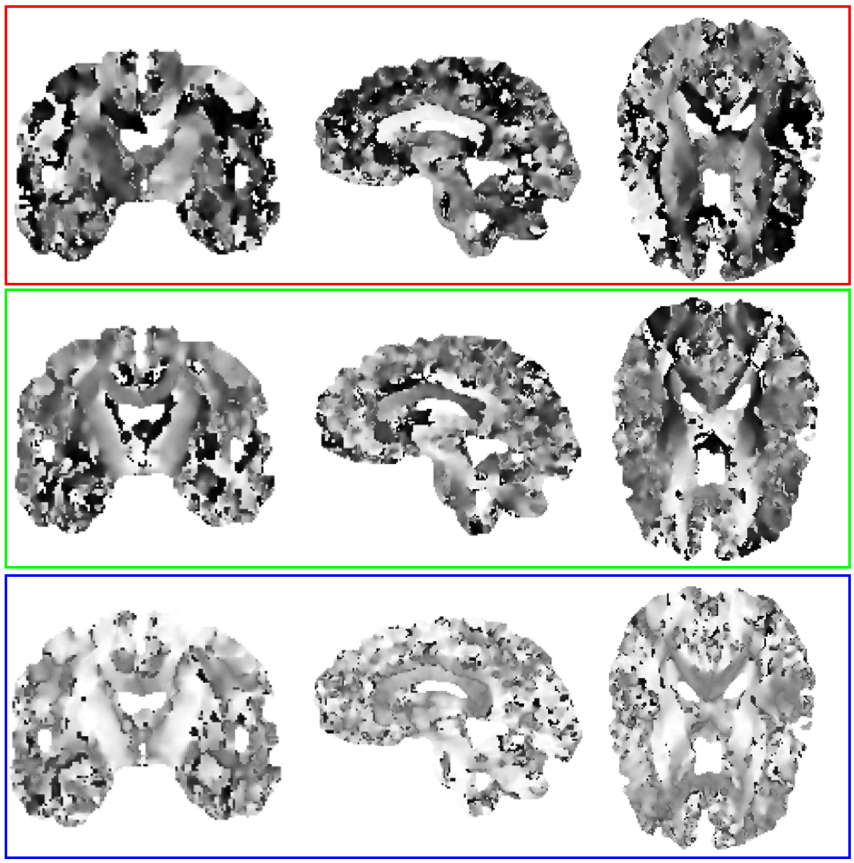

Figure 4.4: Direction cosines map along the three cartesian directions. Red panel: cos$x$ over the three coordinate planes (coronal, sagittal, axial). Green panel: cos$y$ over the three coordinate planes (coronal, sagittal, axial). Blue panel: cos$z$ over the three coordinate planes (coronal, sagittal, axial)

intensity, and was adapted from the values measured in (Bashar et al., 2008):

$$R_{lt} = \begin{cases} 10, & \text{FA} > 0.8 \\ 6, & \text{FA} > 0.7 \\ 4, & \text{FA} > 0.4 \\ 2, & \text{FA} > 0.2 \\ 1, & \textit{otherwise} \end{cases} \tag{4.3}$$

Additionally, information about the components of the main eigenvector ϵ_1 (i.e. the

three director cosines) are available, as well. In the anisotropic tissues, the main eigenvector is oriented along the diffusitivity direction. Particularly, in the white matter it is oriented along the nerve fiber, whereas ϵ_2 and ϵ_3 are oriented along the two orthogonal directions, thus defining a fiber reference system. Therefore, the director cosines represent the fiber orientation with respect to the head cartesian system x,y,z. This information can be used to transform the tensor from the local fiber coordinate system (i.e. $[\sigma_f]$) to the global cartesian coordinate system of the head, that is the same for all the volume elements (Hallez et al., 2005). The tensor $[\sigma_f]$ belonging to each voxel of the GM and WM can be written as in (Hallez et al., 2005):

$$[\sigma_{f,i}] = \begin{bmatrix} \sigma_{long} & 0 & 0 \\ 0 & \sigma_{trans} & 0 \\ 0 & 0 & \sigma_{trans} \end{bmatrix} \tag{4.4}$$

Where f indicates the fiber system and i is the index for the i-th voxel. In each voxel, the corresponding tensor is transformed in the head coordinate system:

$$[\sigma_i] = S_i^T [\sigma_{f,i}] S_i = \begin{bmatrix} \sigma_{xx} & \sigma_{xy} & \sigma_{xz} \\ \sigma_{yx} & \sigma_{yy} & \sigma_{yz} \\ \sigma_{zx} & \sigma_{zy} & \sigma_{zz} \end{bmatrix} \tag{4.5}$$

where S=$[\epsilon_1, \epsilon_2, \epsilon_3]$ is the rotation transform matrix from the fiber coordinate system to the head coordinate system. The two eigenvectors ϵ_2 and ϵ_3 were calculated from ϵ_1 to respect the condition of a cartesian coordinate system. As reported in Eq. 4.5, $[\sigma_i]$ is a positive symmetric matrix, of which off-diagonal elements are neglected. Therefore, the complex conductivity σ^* considered in Eq. 2.9 is different in each direction x,y or z, and can be written as:

$$\sigma * (f) = \sigma_{dd} + 2\pi f \epsilon_0 \epsilon^{''} + j 2\pi f \epsilon_0 \epsilon'(f) \tag{4.6}$$

Where dd can be xx, yy or zz and represents the direction of the conductivity, ϵ_0 is the free space permittivity, f the operating frequency, ϵ'(f) is the real part of the relative permittivity, and ϵ''(f) is the imaginary part, which represents the loss term associated to the displacement currents.

4.3 Custom EM-code: Simulation set-up

In order to perform the TMS simulation with the developed code, the magnetic vector potential **A** distribution computed for a commercial figure-8 coil (MAG-9925-00, Magstim, Fig. 2.2, panel a) was considered as the stimulation source. The distribution was independently computed by solving the discrete Poisson vector equation (See Eq. 2.4) over a coil model that consisted in a sequence of 2721 segments, with dimension *dl*, each identified by the coordinates of its midpoint in the coil reference system and carrying a sinusoidal current at the frequency that best approximate the TMS biphasic pulse (i.e. 3 kHz) (Paffi et al., 2018). Spatial resolution of coil and head domain was 1 mm. The stimulation intensity is a parameter that can be set during the simulation. Here an intensity of 2 kA was considered. To test the code, the coil was placed over the primary motor cortex, M1, as shown in Fig. 4.2, with the coil handle parallel to the interhemispheric fissure. The same set up was considered to conduct simulations on both the isotropic and anisotropic brain model. The human head model, provided by Sentech S.r.l, is a 4-compartments head and neck model, consisting in a thick layer of scalp, i.e. an homogeneous compartment including all extracerebral tissues (skin, fat, muscles, and the skull), a layer of cerebrospinal fluid (CSF), grey matter (GM) and white matter (WM). The isotropic electromagnetic properties of the tissues were taken from the IT'IS database at 3 kHz (Hasgall et al., 2018), with the exception of the scalp conductivity that was assigned as 0.465 S/m. The isotropic conductivity of GM and WM was used to compute the anisotropic conductivity tensor as described in Section 4.2.1. Fig. 4.5 shows the distribution map of σ_{xx}, σ_{yy} and σ_{zz} inside the grey and white matter, over the coronal plane through the center of the coil. As expected, few voxels of grey matter experience conductivity values greater than the $\sigma_{iso,GM}$ (0.106 S/m), reaching peaks of 0.4 S/m along the x direction and 0.24 S/m along the z direction. Along the y direction the highest values are below 0.2 S/m and can be found in farther areas from the surface of the cortex. For what concerns the white matter, as expected, the conductivity is mainly oriented along the x direction in the conjunction area between the two hemispheres, and along z at the interface with the GM, which is populated mostly by pyramidal neurons. In the following section, the dosimetric analysis conducted on both the isotropic and anisotropic brain model is presented.

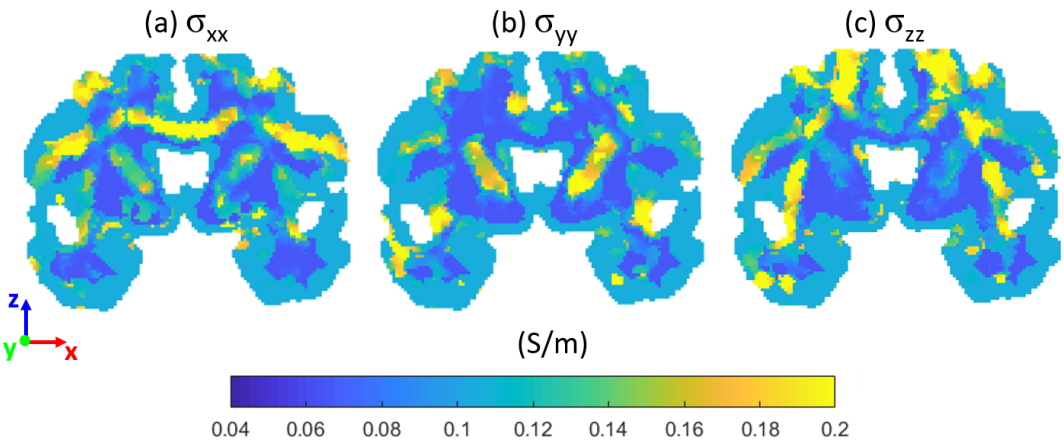

Figure 4.5: Conductivity tensor: distribution maps of σ_{xx}, σ_{yy} and σ_{zz} over the coronal plane that crosses the center of the head

4.4 Custom EM-code: Comparison between the isotropic and anisotropic brain model

As a first step, the impact of grey and white matter anisotropy on the estimation of the induced E-field was evaluated on the surface of the cortex, as shown in Fig. 4.6a-b. For both the anisotropic and isotropic model, the maximum E-field estimated as the 99.9^{th} percentile of the distribution is 75 V/m, thus the conductivity tensor did not seem to influence the E-field peak intensity on the surface of the grey matter. Furthermore, the Symmetric Mean Percentage Error (SMAPE, see Eq. 3.1) was calculated to quantify the differences in each point of the distribution (Fig. 4.6c) and it resulted to be lower than 10% under the coil. Position P of the peak slightly varied (∼1 mm): P_{iso}(130 mm, 127 mm, 210 mm) and P_{anis}(130 mm, 126 mm, 210 mm). Such low differences were expected since the fractional anisotropy does not exceed FA=0.5 on the cortex, with spots below the threshold value (FA=0.2). Consequently, in the anisotropic brain, the surface of the grey matter counts many voxels characterized by σ_{xx}=σ_{yy}=σ_{zz}=σ_{iso}. Nevertheless, Fig. 4.5 showed that some of the apical areas of the cortex have higher σ_{xx} and σ_{zz}.

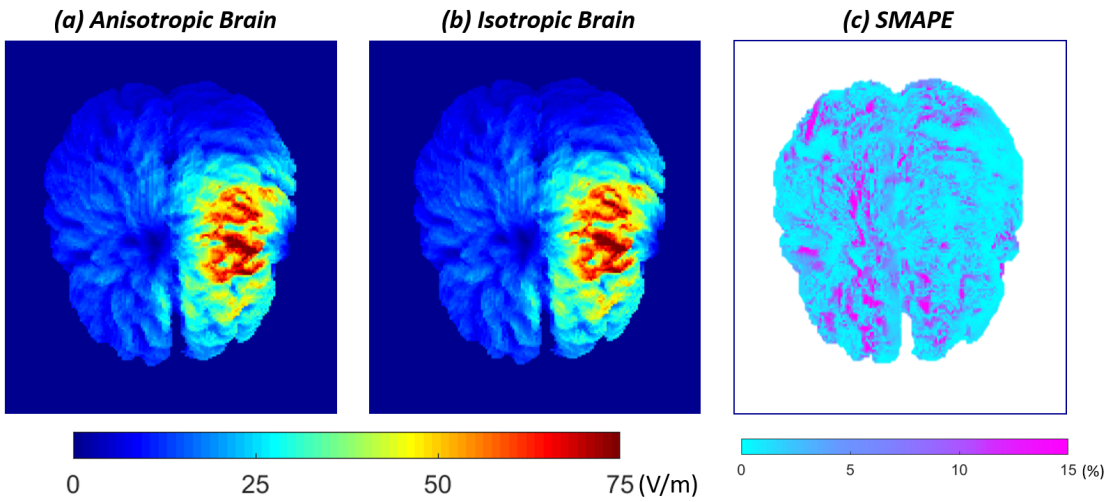

Figure 4.6: Comparison between the induced E-field computed on the anisotropic and isotropic brain. (a) $|E|$ distribution on the surface of the anisotropic brain cortex. (b) $|E|$ distribution on the surface of the isotropic brain cortex. (c) Distribution of the SMAPE between (a) and (b).

In order to assess the contribution from each conductivity direction, the E-field components $|E_x|$, $|E_y|$ and $|E_z|$ were observed, as reported in Fig. 4.7, together with the conductivity distribution along the corresponding direction. The maps show that σ_{xx} and σ_{zz} prevail over σ_{yy}, and assume values up to 0.4 S/m. Notwithstanding that the distributions of $|E_{d,anisotropic}|$ and $|E_{d,isotropic}|$, where d is the direction x or z, look very similar, differences can be noticed in the E-field components amplitude, with higher values that are induced in the isotropic brain, likely due to the lower value of the conductivity. The SMAPE between $|E_{x,isotropic}|$ and $|E_{x,anisotropic}|$ or between $|E_{z,isotropic}|$ and $|E_{z,anisotropic}$ can be as high as 30% under the coil and 40% in the opposite hemisphere. However, for both models, intensities of $|E_x|$ and $|E_z|$ are lower than $|E_y|$, with a peak of 20 V/m over 70 V/m (Fig. 4.7), suggesting that, for this coil position, $|E_y|$ is the main E-field component. Along the y direction, the conductivity σ_{yy} is equal to σ_{iso} in most of the brain surface and particularly below the coil (Fig.4.6 e). This justifies the SMAPE values below 5%, as reported in Fig. 4.6c. Higher differences than those reported on the surface of the cortex were found inside the brain, particularly at the interface between grey and white matter and in deeper regions, where the WM tissue predominates and it is highly anisotropic. Fig. 4.8 shows

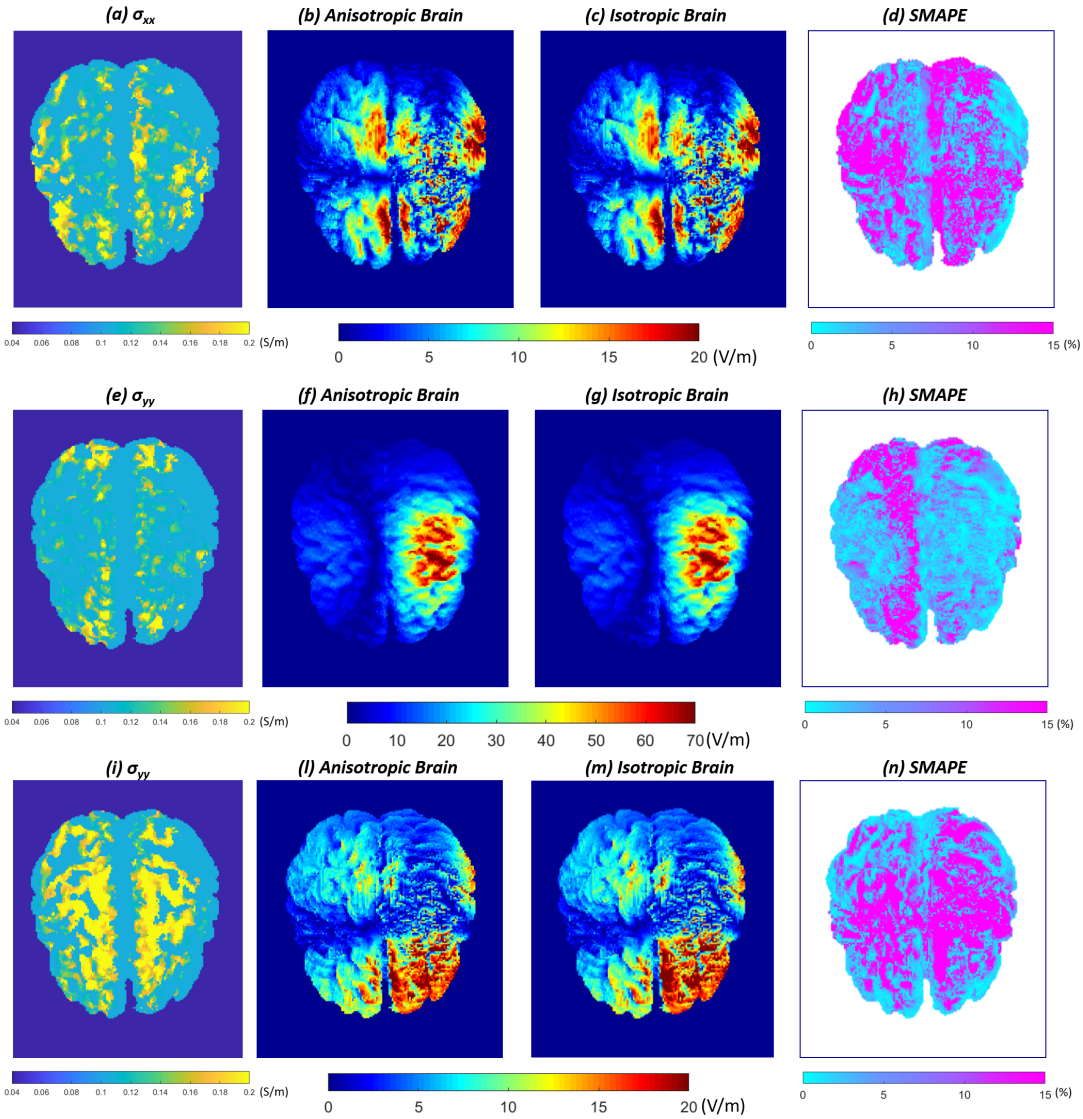

Figure 4.7: Analysis of the induced E-field components. (a) σ_{xx} values on the surface of the cortex. (b) $|E_x|$ distribution on the surface of the anisotropic brain cortex. (c) $|E_x|$ distribution on the surface of the isotropic brain cortex. (d) Distribution of the SMAPE between (b) and (c). (e) σ_{yy} values on the surface of the cortex. (f) $|E_y|$ distribution on the surface of the anisotropic brain cortex. (g) $|E_y|$ distribution on the surface of the isotropic brain cortex. (h) Distribution of the SMAPE between (f) and (g).(i) σ_{zz} values on the surface of the cortex. (l) $|E_z|$ distribution on the surface of the anisotropic brain cortex. (m) $|E_z|$ distribution on the surface of the isotropic brain cortex. (n) Distribution of the SMAPE between (l) and (m).

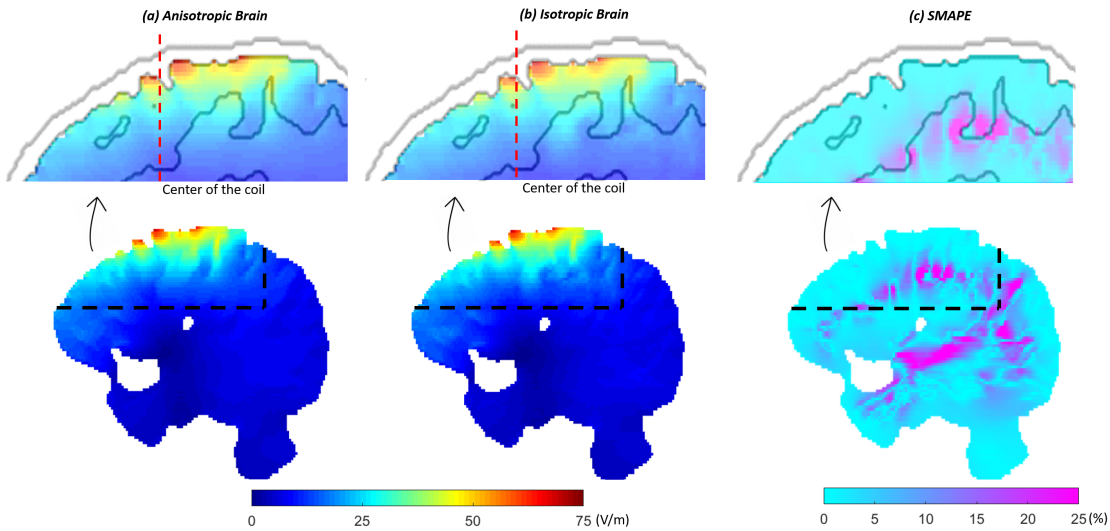

Figure 4.8: E-field and SMAPE distribution on the sagittal plane that crosses the coil center. (a)Results for the anisotropic brain. (b)Results for the isotropic brain. (c)SMAPE between (a) and (b). The area below the coil delimited by the dashed lines in expanded in the top row.

the distribution of the E-field along the sagittal plane that crosses the center of the coil. In panel (a) are the results from the anisotropic model, that can be compared with those from the isotropic one, panel (b). A peak intensity of 75 V/m, located in the area below the coil, is confirmed in both the E-field maps. For what concerns the deeper regions, the E-field distribution is affected by the local changes in the conductivity value as can be seen from the different patterns shown, such differences were quantified in each voxel by the SMAPE and can be up to 25%. By looking at the expansion in (Fig. 4.8), it can be seen that high differences can be found at the interface between the grey and the white matter, with a maximum value of 30%. Changes in the conductivity value shape the induce E-field differently, specially in the presence of a sulcus, where there is insertion of grey matter in the white.

4.5 A strategy for a real time solution

The final aim of the En-TMS project is to build a neuronavigation software able to show the stimulation site, and to correlate it with the recorded motor evoked potentials. The stimulation site is given by the maximum E-field induced on the cortex. The

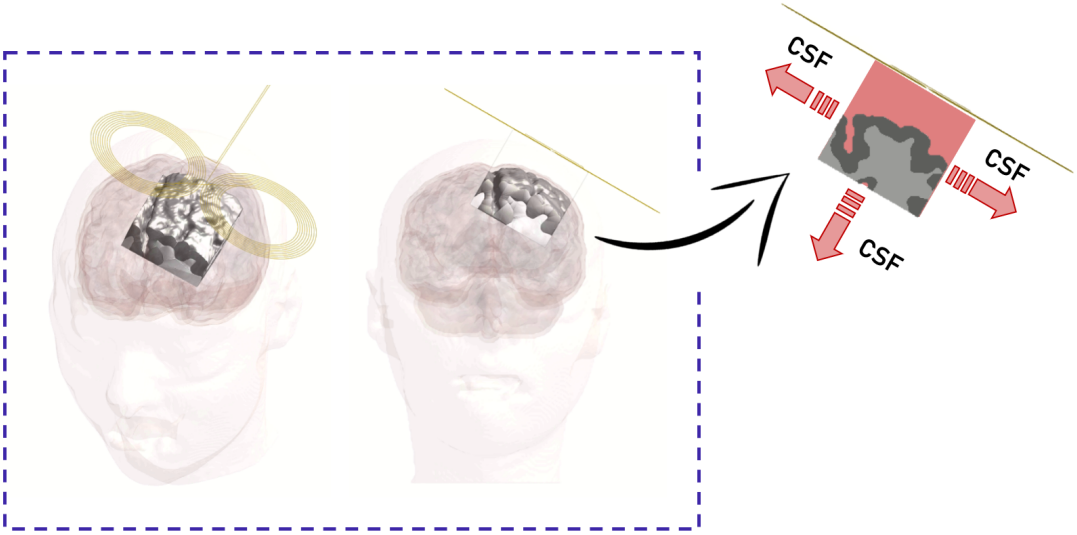

Figure 4.9: The methodology implemented for a real-time solution: the portion of brain below the center of the coil is selected and considered surrounded by a domain of CSF.

innovative aspect over currently available n-TMS software is that the induced E-field is calculated inside the patient's specific model, with a brain characterized by anisotropic properties, rather than a simplified multilayered sphere. In this regard, computing the EM-solution over the entire head requires timings that are not compatible with the real-time conditions imposed by the navigation. In this regard, a strategy to obtain dosimetric results in real time was implemented and is described as follows.

4.5.1 Methodology and results

In order to respect the real-time condition required by navigated systems, yet keeping a good degree of detail in the head model, the EM solution was computed inside a small portion of the brain (i.e. a box of 5 cm $\times$ 5 cm $\times$ 5 cm) below the area of the coil, rather than inside the entire head, as shown in Fig. 4.9. This extracted section of brain (i.e. brain box) is considered immersed in CSF, to properly close the domain, with twenty additional layers of CSF considered as an adapting condition. To test the method, simulations were performed considering the same parameters previously described. The figure-8 coil was placed over the hand area of M1 with the handle kept parallel to the interhemishpheric fissure and a 3 kHz sinusoidal current was considered

as input.

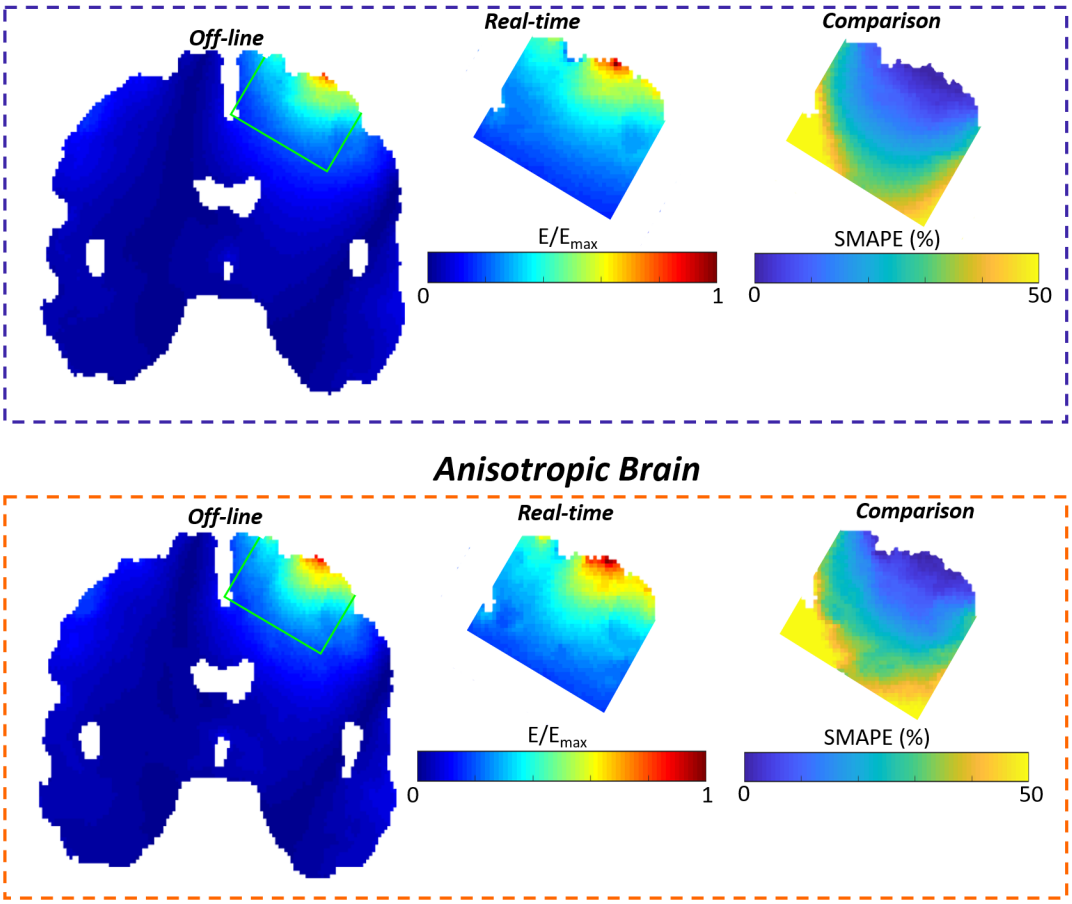

Figure 4.10: Comparison between the off-line and the real time solution: (Blue panel) Comparison on the coronal plane at y=127 mm for the isotropic brain. (Orange panel) Comparison on the coronal plane at y=126 mm for the anisotropic brain.

Coil and head domain discretization was kept to 1 mm in the three directions. The solution was computed on both the isotropic and anistropic brain and computation time was 60 s and 80 s respectively, over the 8 hours required to compute the solution inside the entire head. Goodness of the method was assessed by comparing normalized distribution of the E-field calculated over the entire head with that computed inside the brain box. Since the outcome of interest in navigated TMS applications is the position of the stimulation spot (i.e. the maximum E-field), P, rather than its intensity, it is necessary to guarantee that no shift occurred when reducing the domain dimensions. Results showed that in both the isotropic and anisotropic brain box, position of maximum E-field remained unchanged with respect to that obtained from the entire head, i.e. P_{iso}(130 mm, 127 mm, 210 mm) and P_{anis}(130 mm, 126 mm, 210 mm). Furthermore, the SMAPE (See Eq. 3.1 in Chapter 3 for definition) between the solution over the entire head and over the brain box was computed. Results of this comparison are reported for the two brain models in Fig. 4.10. Blue panel and orange panel show the normalized distributions for the isotropic and anisotropic brain respectively on the coronal plane that crosses the estimated stimulation point (i.e. y_{iso}=127 mm and y_{anis}=126 mm). The SMAPE values demonstrated that the differences between the solutions remained below the 10% in the area surrounding E_{max}.

4.6 Discussion and future work

In this chapter a novel code for EM-dosimetry is presented. By implementing the admittance method, such code is able to compute the E-field induced by TMS coils on anatomical, patient-specific head models with anisotropic brain. It was developed as part of the project "The Effective navigated TMS" (POR FESR LAZIO 2014 – 2020), in collaboration with Sentech S.r.l., InfoSolution S.p.a., and the department of Physiology and Farmacology "Vittorio Erspamer", at University of Rome "La Sapienza". The aim of the project is to build a neuronavigation software able to give information on the stimulation spot on the cortex, obtained by computing the induced E-field on a patient-specific, anisotropic head model.

Therefore, the methodology applied to achieve this goal was herein described, with particular attention to the method developed to obtain the conductivity tensor that is used to compute the induced E-field. Preliminary results were obtained in order to investigate the effect of considering the anisotropic properties of the brain. Thus, two

simulations were conducted with the same parameters (i.e. 3 kHz, 2 kA and coil tangent to M1, with handle parallel to the inter-hemipshere fissure) on both the head models, showing that, for such coil position, local changes in the conductivity derived from anisotropic properties slightly affect location of the maximum E-field on the surface of the cortex (1 mm), without changes in its intensity, confirming what found in other litterature works (De Lucia et al., 2007; Opitz et al., 2011). Such small differences can be justified by the fact that, over M1, σ_{yy} of the GM is equal to its isotropic conductivity, therefore the main E-field component, which is oriented along the y direction (i.e. nasion-inion), is only slighted affected ($< 5\%$) by changes in the conductivity value. In deeper regions and at the interface between GM and WM differences are higher (up to 30%) (Opitz et al., 2011). Nevertheless, this results also suggest that depending on the coil location and orientation, the brain anisotropy might have a greater impact on the E-field distribution, and possibly shift the hot-spot of the stimulation by few millimiteres. Further analysis will be conducted to investigate this aspect, as it would confirm the importance of considering a detailed head model in applications of En-TMS, that so far employ software packages that approximate the patient's head to a sphere (Comeau, 2014; Krieg et al., 2017). That being said, computing the E-field inside realistic models requires a calculation time that is not compatible with the real time constrain of En-TMS applications. A strategy to reduce the computation time was proposed and consisted in limiting the calculation in a volume of interest of few cm^3 (i.e. 5 cm $\times$ 5 cm $\times$ 5 cm), below the area of the coil. The solutions obtained from the full model and from the reduced domain were compared in both the isotropic and anisotrpic model, resulting in differences in the E-field distribution below 10% around the stimulation site, for which no shift occurred. Such low difference between the two solutions was considered accettable as it is below those caused by other numerical sources of errors such as the meshing or the conductivity values assigned to the tissues (Saturnino et al., 2019a) This methodology allowed for a conspicuous reduction in the simulation time ($\sim$1/480), while keeping a good level of detail and spatial resolution, therefore it is considered a valuable solution for a real-time dosimetry.

Part II

Computational dosimetry on innovative devices and applications: the effects of low intensity pulsed magnetic fields

Chapter 5

Exposure to low intensity, low frequency magnetic fields

5.1 Overview of the effects of ELF-MF exposure

A large number of studies has been conducted over the years to explore the effects of weak, extremely low-frequency (up to 300 Hz) magnetic fields (ELF-MFs) over the central nervous system, at cellular level and at system level on intact human brain. The interest on the interaction between ELF-MF and living organisms firstly arose in the field of protectionism to assess possible risks for the human health due to the so called electromagnetic environmental pollution and to investigate the effects of the exposure to external environmental MF sources, such as the electric power lines at 50 Hz (in Europe) or 60 Hz (in North America) (Graham et al., 1999; Cook et al., 2002). Contextually, different waverforms were investigated as well in a therapeutic oriented way (Grant et al., 1994; Shupak et al., 2004a). The amplitude of the magnetic fields reported in this section ranges from a few μTesla to a few Tesla and the frequency content spreads from a few Hz to few kHz. The waveforms used can be sinusoidal or pulsed. Continuous waves have been shown to influence changes at cellular level and to influence human brain activity, although pulsed electromagnetic fields (PEMFs) are considered to interact more efficiently with the biological system (Prato, 2015), due to the faster rate of change of the magnetic field (dB/dt), which is in the order of Teslas/seconds for peak values of the magnetic field in the range of μT and mT, and repetition frequency on the order of tens of the Hz (Di Lazzaro et al., 2013).

For both signal types, the interaction mechanisms of ELF-MF exposure acts on two different steps, the first is the interaction mechanism between the external MF and the biological system, and the second, is the cascade of biological events leading to the physiological and behavioral effect (Di Lazzaro et al., 2013). In fact, an external MF can either interact directly with endogenous magnets or magnetic field dependent chemical reactions, or indirectly, by inducing an electric field in the conductive tissues. The direct or indirect interaction with the MF involves a number of potential cellular targets that affects a variety of cells functions and tissue types.

5.1.1 In-vitro and in-vivo studies

Continuous waveforms

Several in-vitro and in-vivo studies studies showed that ELF-MFs could affect membrane functions by a local effect on ion fluxes or by altering the distribution and the functionality of membrane proteins which act as ion channels, enzymes, neurotransmitters and neurotransmitters receptors (Di Lazzaro et al., 2013). ELF-MF exposure has been shown to particularly affect serotonin, dopamine, nitric-oxyde and adenosine receptors. The serotonergic neurotransmission partecipates in the elaboration of an adapted response of the CNS to external or internal stimuli and therefore, it is involved in numerous physiological functions such as learning and memory, sleep, as well as in various pathological disorders, mood disorders, anxiety, stress, depression. Serotonergic functions are mediated by 5-HT receptors. Particularly 5-HT_{1B} receptor subtypes are located on serotonergic terminals and regulate the release of serotonin, thus playing an important role in the regulation of the serotonergic activity that modulates the functioning of the CNS (Massot et al., 2000). The effect of ELF-MFs on serotonin receptors was firstly investigated by Massot and colleagues in 2000. They found a decrease in the efficacy of 5-HT_{1B} receptor after exposure to a 50 Hz magnetic field with increasing intensities up to 2.5 mT. The MF enhanced serotonin uptake wich, in turn, increased synaptic serotonin content (Massot et al., 2000). In (Sieroń et al., 2004), a significant increase in the synthesis rate of serotonin was found in the frontal cortex of rats after exposure to ELF-MFs (10 Hz, 1.8–3.8 mT, 1 h daily) for 14 days. These results were confirmed in (Espinosa et al., 2006) where the authors reproduced the work by Massot and compared the effects of AC (50 and 400 Hz) and DC MFs on the binding properties of the G-protein coupled receptor (GPCR) of serotonin, 5-HT_{1B}. They found significant differences in the amplitude and nature of the effects observed

using AC and DC fields, adding an information about the importance of signal polarity. Other 5-HT receptors have been investigated as well, as in (Janać et al., 2009), where a decrease in the affinity of serotonin 5-HT_{2A} receptors and increase in their density was found in the prefrontal cortex, after exposing Wistar rats to a 50 Hz, 0.5 mT MF. More recently, male Sprague-Dawley rats were exposed to a 2 mT, 60 Hz magnetic field for 5 days, with a consequent significant increases in 5-HT receptors and 5-HIAA serotonin metabolite in the striatum, thalamus and hippocampus (Chung et al., 2015). These results were confirmed in (Shahbazi-Gahrouei et al., 2016) where a 15 days exposure of Wistar rats to a continuous semi sine wave magnetic field (10 Hz and 0.69 $\pm$ 0.01 mT RMS) caused a significant reduction of 5-HIAA concentration in the raphe nucleus. In the central nervous system, changes in serotonin levels are responsible for physiological functions and pathological disorders. Nonetheless, a modulation of serotonergic pathways is also able to help recovery of locomotor functions following spinal cord injury, as found in (Dey et al., 2017), where rats were exposed to a 17.96 μT, 50 Hz MF for for 8 weeks, 2 h a day. An improvement in the local concentration of 5-HT was reported in spinal cord sections from T5 to L5. It's been reported that ELF-MF also influences dopamine receptors as found for the first time in 2001 in (Sieroń et al., 2001). They showed that ELF-MF (10 Hz, 1.8–3.8 mT) exposure for 14 days (1 h daily) reduced reactivity of central dopamine D1 receptors in neonatal 6-hydroxydopamine-treated rats and increased the turnover of dopamine in frontal cortex of adult male Wistar rats. These findings were confirmed in other studies showing that exposure to 50 mT MFs during gestation increased dopamine levels in the rat striatum and exposure to 2.4 mT, (1 h/day, for one or seven days) (Lee et al., 2001; Shin et al., 2007). Stimulation of dopamine D1-like receptors by ELF-MF exposure is, at least in part, involved in the induced changes of locomotor activity found in ICR (Institute of Cancer Research) mice. Conversely, in 2009, Janac and co-workers found that ELF-MF (50 Hz, 0.5 mT for 1, 3, and 7 days) had no significant effect on the affinity and density of dopamine D1 and D2 receptors in the rat striatum (Janać et al., 2009). Nevertheless, the study described in (Chung et al., 2015), showed that a 5 days exposure of male Sprague-Dawley rats to a 2 mT, 60 Hz ELF-MF significantly increased concentration of dopamine in the thalamus. They hypothesized that this disagreement with previous results could arise from differences between animals used and experimental procedures. More recently, male BALB/c mice were exposed to a 50 Hz 1 mT MF continuously 3 hours/day for 30 days (Ebrahimi et al., 2019), showing a decrease in depression and increases in anxiety-

like behavior. Authors justified this result with previous literature findings on ELF-MF effects on neurotransmitters. Finally, effects on Nitric Oxyde (NO), a neurotransmitter involved in pain perception have also been investigated over the years. An effect was firstly found in 1998 on land snails (Kavaliers et al., 1998) and implicated in mice in 2006, when Jeong and colleagues attempted to identify a mechanism other than opioid system that could be involved in ELF MF-induced hyperalgesia (Jeong et al., 2006; Prato, 2015). In their hypothesis, a possible association between NO system and the hyperalgesic effects of the exposure of ELF-MF existed. This was demonstrated by exposing ICR mice to a 2 mT magnetic field at 60 Hz for 48 hours. Hyperalgesic effect resisted for 30 minutes and was attributed to the increase in NO concentration in the brain and spinal cord. Effects on nitric oxyde were found in follwing studies as well. In 2012, Cho and collegues exposed male Sprague-Dawley rats for 5 days to a 2 mT, 60 Hz magnetic field, showing an increase in the number of enzyme neuronal nNOS-IR (neural nitric oxyde synthase) cells in the cerebral cortex, striatum and hippocampus (Cho et al., 2012). The same exposure system was considered in (Chung et al., 2015), where MF exposure was exerted for 2 or 5 days. Their results showed that such exposure would produce a significant increase in the concentration of nitric oxyde (NO) in the striatum, for the 2 days exposure and in thalamus and hippocampus for the 5 days exposure. No changes in NO concentration were found in the cortex and cerebellum. Effects found on NO could justify the analgesic effect of ELF-MF in rats, as reported in several animal studies (Prato, 2015; Ozdemir et al., 2017, 2019; Demirkazik et al., 2019). NO is also involved in learning and memory, and in the development of anxiety and depression (Bagheri Hosseinabadi et al., 2019). In (Djordjevic et al., 2017) authors reported that short term exposure of Wistars albino rats to 50 Hz MF (10 mT) 24 h/day for 7 days induced anxiety-like behavior through oxidative stress and increasing NO concentration in the hypothalamus.

Pulsed waveforms

Under the hypothesis that pulsed MF would interact more efficiently with a biological system than a sinusoidal ELF-MF would, in 1997, Thomas and co-workers demonstrated that a pulsed field with frequency content below 500 Hz and an amplitude of 200 μT could induce analgesia in snails (Thomas et al., 1997; Prato, 2015). The same exposure signal, called the complex neuroelectromagnetic pulse (CNP, see Section 5.2 for details) was used to expose adult male Swiss CF-1 mice and produced effects similar to those produced following the administration of a moderate dose (5 mg/kg) of morphine (Shupak et al., 2004b). Pulsed electromagnetic fields can also modulate con-

centration of intracellular calcium, Ca^{2+}, regulating voltage-gated calcium channel, that, if inhibited, can reduce calcium influx, and upregulate the expression of proinflammatory genes inside ischemic tissues, inducing a protective effects against focal cerebral ischemia (Ross et al., 2019). This action was firstly discovered in 1994 in the study by Grant and co-workers, where the potential beneficial effect of a particular pulsed magnetic field (i.e. the I-ONE, see Section 5.2 for details) was evaluated on transient focal ischemia in rabbits (Grant et al., 1994). Similar results were found in (Pena-Philippides et al., 2014), where PEMFs exposure of a distal middle cerebral artery occlusion in mice, significantly influenced the expression profile of pro- and anti-inflammatory factors in the hemisphere ipsilateral to ischemic damage and mediated a significant reduction of infarct size. To better understand the mechanism of action behind anti-inflammatory effect of PEMFs exposure, many in vitro studies have been carried out (Varani et al., 2002, 2012; Vincenzi et al., 2017), some of which using the same stimulating signal applied in (Grant et al., 1994). Of particular interest is the interaction between PEMFs and the A1, A2A, A2B, and A3 adenosine receptors (ARs), and the metabolic pathways involved. Adenosine is an ubiquitous molecule involved in the functional regulation of many tissues and organs. Its effect is mediated through activation of a family of four G-protein-coupled adenosine receptors, namely, A1, A2A, A2B, and A3, and plays a significant role in the protection against cellular damage in regions with high metabolism and prevents the subsequent dysfunction of the affected organs (Di Lazzaro et al., 2013; Gessi et al., 2018). Adenosine levels rise following to increased metabolic demand and lack of oxygen, conditions that may occur in several pathological states, such as ischemic infarct (Gessi et al., 2018). It has been shown that PEMF exposure mediates a significant upregulation of A2A and A3ARs expressed in various cells and tissues in both the peripheral and central nervous system, that would primarily determine a significant reduction in some of the most relevant pro-inflammatory cytokines (Varani et al., 2017, 2018). Already in the early 2000s, Varani and colleagues demonstrated that A2A and A3 ARs' density in human neutrophilis is modified by PEMFs in function of the time and of the applied intensity with a significant increase in their number (Varani et al., 2002, 2003). A similar increase of A2A ARs by PEMFs was found in primary cultures of rat cortical neurons as well (Varani et al., 2012). Rat pheochromocytoma PC12 cells and human neuroblastoma cell line SH-SY5Y are often used to characterize molecular events responsible for PEMFs biological effects, as they are cell lines endowed with long term proliferative capacity

in-vitro and widely accepted as good neuron-like cell models. In Vincenzi et al., 2012, PEMF exposure of PC12 cells mediated a significant increase of A2A and A3 ARs' density without alterating the affinity values. This suggested that the receptor upregulation could involve modifications linked to the receptor recycling on the cell membrane associated with a regulatory effect at the transcriptional level (Vincenzi et al., 2012) . More recently, in PC12 cells and in SH-SY5Y cell line, Vincenzi and co-workers showed that PEMF treatment significantly decreased cell death and apoptosis provoked by hypoxia (Vincenzi et al., 2017). Their results suggested that defence mechanisms against reactive oxygen species (ROS), whose production is central in the progression of many inflammatory states, are activated by PEMFs and that this activation could counteract the hypoxic insult. Further investigation on PC12 cells exposure to PEMFs were conducted in (Gessi et al., 2019), where they characterized the protective pathways activated by PEMFs to relieve neuronal cell death. Specifically, P38 kinase cascade, which in turns enrolles heat-shock protein HSP70, a survival chaperone molecule, was activated by PEMFs. This caused a significant increase in CREB (cAMP response element-binding protein) phosphorylation within 24 hours from the exposure. After 48 hours, production of BDNF (brain-derived neurotrophic factor), important in the protective mechanisms operating after ischemic stroke was increased to enhance neuronal survival. Upregulation of BDNF expression mediated by PEMFs, following ischemic stroke in mice, was observed in (Urnukhsaikhan et al., 2017). In light of all the aforementioned possible effects on neuronal cells and networks, several studies have been conducted to assess how continuous and pulsed ELF-MF exposure could alter humans' physiological conditions and brain activity.

5.2 Studies on humans

Effects on ELF-MF exposure have been extensively investigated on humans under both a protectionist and a therapeutic point of view. In fact, the most diffused ELF-MF sources are the electric powerline that generate CW MF at 50 Hz in Europe (or 60 Hz in North America). Therefore, studies on humans have been conducted in order to determine MF intensity levels that would guarantee a safe exposure to both the general public and workers (Ziegelberger et al., 2020). Extensive reviews on the first studies conducted on ELF-MF exposure to assess effects on cognitive functions can be found in (Cook et al., 2002; Crasson, 2003; Cook et al., 2006), and more recently in

Protectionist studies

the review (Di Lazzaro et al., 2013). Already in the late 90s and early 2000, studies showed effects on human cognitive processes from 50 Hz or 60 Hz weak magnetic field exposure, albeit small. Some studies reported enhanced performances on the choice reaction time task, with exposed subjects committing fewer errors as compared with sham exposure (Cook et al., 2006; Di Lazzaro et al., 2013), while simple and choice reaction times, accuracy, time perception and figure perception were not affected by 55 min magnetic exposure, as reported in (Kurokawa et al., 2003). In a meta-analysis study conducted on 2010 by Barth and co-workers, they found little but significant changes in two cognitive dimensions: visual discrimination and flexibility (Barth et al., 2010). Conversely, population-based study on ELF-MF environmental exposure reported that it may increase the risk of severe cognitive dysfunction, assessed with mini-mental state examination (Davanipour et al., 2013). More recently, in (Legros et al., 2015), authors used fMRI to quantify brain functional activation during two different tasks (finger tapping and mental rotation) before and after exposure to a 60 Hz, 3 mT MF, showing significant differences in task-dependant brain areas without affecting speed or accuracy of the tasks, therefore without determining any physical behavioural impact. ELF-MF exposure has been demonstrated to affect motor control in terms of standing balance and tremor. Modulation of standing balance and postural control due to either pulsed MF exposure or 60 Hz MF exposure has been reported in several studies (Legros and Beuter, 2005; Legros et al., 2012; Van Nierop et al., 2015; Allen et al., 2016; Villard et al., 2019). In 2005, Legros and co-workers determined the effect of a 50 Hz, 1 mT MF centered at the level of the head on human index finger micro-displacements (Legros and Beuter, 2005). In (Legros et al., 2012), a 60 Hz and 18 mT magnetic field generated by two octagonal coils, parallel to one another, has been demonstrated able to reduce standing balance oscillations, that were slower and smaller in amplitude over the oscillations produced during the sham. Similar results were found in (Allen et al., 2016), after exposing subjects to a 100 mT and 120 Hz magnetic field generated by a headset exposure system placed behind the ears and targeting the vestibular system. As an opposite, in 2013 Van Nieport showed a detrimental effect of time varying magnetic field on postural body sway (Van Nierop et al., 2015), while no significant effects were reported in (Villard et al., 2019) after exposure to a 50 mT and 100 mT MF at 20 Hz, 60 Hz, 120 Hz and 160 Hz. However, authors justified this result also with the strong stabilizing effect of the mechanical characteristics of the MF exposure device itself, that would restrict the amplitude of the natural postural sway (Villard et al., 2019). Given

Therapeutic studies

the nociceptive and anti-inflammatory effects found in cell lines and animal models, ELF-MF, particularly in pulsed waveform, could represent a potentially useful non-invasive tool for the treatment of neuropathic and neuroinflammatory diseases. The first study on the effects of ELF-MFs on human pain perception dates back to the late 90's, when Papi and co-workers found an increase in sensitivity to electrically induced pain, after exposure to oscillating MFs (+70 to −20 μT) at 0.026, 0.043, 0.067 Hz (Papi et al., 1995). Similar results were obtained in (Ghione et al., 2004), where, after MF exposure at 37 Hz and 80 mT for 60 minutes, the nociceptive sensitivity to electrically induced pain was increased. More recently, studies focused on fibromyalgia treatment (Paolucci et al., 2016; Multanen et al., 2018) and muscoloskeletal pain (Hu et al., 2020), but still leading to unclear results.

The Complex Neuroelectromagnetic Pulse - CNP

A particular pulsed electromagnetic signal is the Complex Neuroelectromagnetic Pulse (CNP), briefely introduced in Section 5.1 and specifically designed to interact with the neurophysiology of biological systems (Thomas et al., 1997). Evolution in time of the CNP signal as taken from the patent (patent number: US6234953 B1 (Thomas et al., 2001b), Fig. 5.1), consists in a sequence of four bursts of varying refractory periods, meaning the time between one burst and another, of 110, 220, 330 ms followed by a longer fourth one of 1200 ms, total duration of a basic pattern is 5212 ms. Each burst contains 16 couples of biphasic waveform, similar to a neuron action potential, whose repetition frequency decreases in time. Additionally to being proven effective in modulating nociception in land snails (Thomas et al., 1997) and mice (Shupak et al., 2004a), the CNP signal has been investigated on humans as well, showing an increase in thermal pain sensitivity after uniform exposure delivered with Helmholtz coils (Shupak et al., 2004b). When delivered through a headset system, the CNP showed beneficial analgesic properties particularly in patients with rheumatoid arthritis, while mixed results were obtained on patients with fibromyalgia, where reduced scores in pain ratings were reported by the placebo group as well (Shupak et al., 2006). In 2010, Robertson and colleagues delivered the CNP through z-gradient coils and investigated how it influenced the processing of acute thermal pain in normal volunteers. Functional (f-)MRI inspection showed a decreased in the activation of the brain areas associated with the integration of the affective components of pain (Robertson et al., 2010b), i.e. the pain matrix. Significant correlations between the changes in neural activation and field strength were also found in (Robertson et al., 2010a). In other studies it has

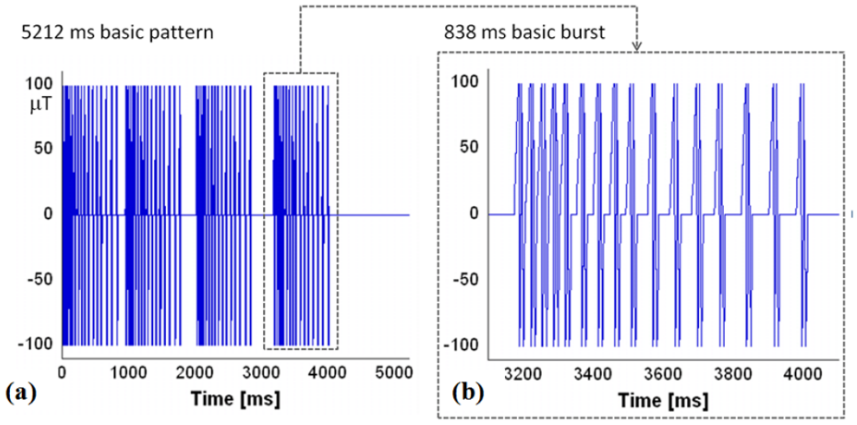

Figure 5.1: CNP signal pattern (Figure from (Camera et al., 2015))

been shown that exposure of volunteers to the CNP also improved their standing balance (Prato et al., 2001; Thomas et al., 2001a) and that it can modulate EEG activity (Cook et al., 2004, 2005, 2009). Some authors tried to deepen the understanding of the neuronal functioning under the stimulation of the CNP by means of neuronal models. In 2011, Stodilka and co-workers studied the effects of CNP on a cortical network model with 1000 neurons synaptically connected and highlighted an effect of synchronization of the network with signal levels higher than those used during human studies (Stodilka et al., 2011). A second neuronal modeling study was conducted in 2015 (Camera et al., 2015). This was a systematic analysis of the effects of the CNP signal on a neuronal network composed by 25 primary neurons linked to a coincident secondary neuron with AMPA (α-Amino-3-hydroxy-5-methyl-4-isoxazolepropionic acid) excitatory synapses (Paffi et al., 2013; Camera et al., 2015). Results revealed an overall inhibitory action on the neuronal model considered. Such response seemed congruent with experimental data on possible analgesic effects on humans and antinociception in snails and mice.

The I-ONE signal

The I-ONE pulsed electromagnetic field is a particular type of PEMF able to exert an anti-inflammatory and neuro-protective effect as it was demonstrated by in-vivo and in-vitro studies (see 5.1.1). It consists in a single pulse, 1.3 ms wide, delivered with a repetition frequency of 75 Hz. Thanks to its particular shape, with a rapid change

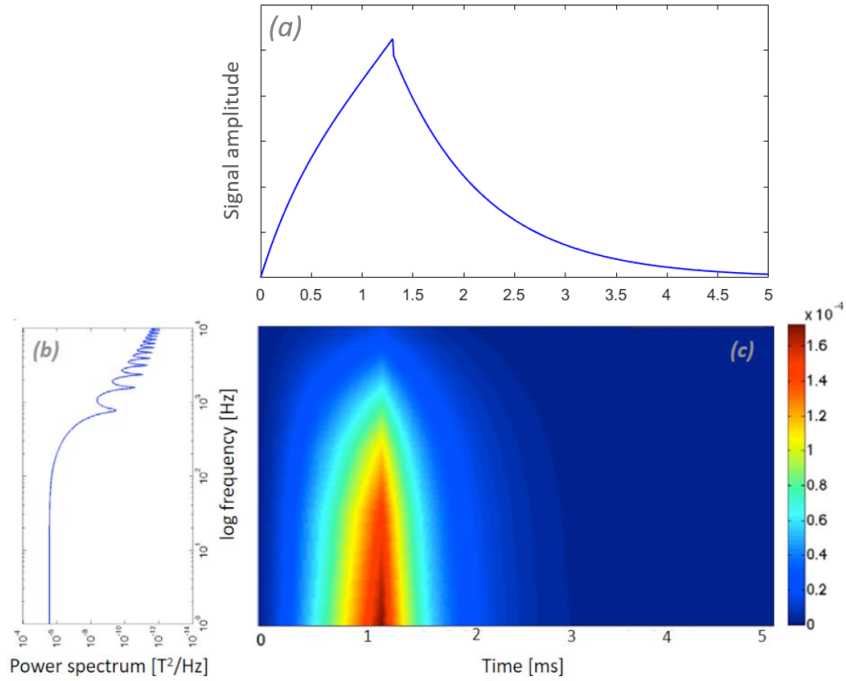

Figure 5.2: I-ONE signal in time, frequency, power spectrum, adapted from (Paffi et al., 2016).

in concavity between the rise and fall phase, it has a frequency content up to 10 kHz (Fig. 5.2). The I-ONE signal is currently FDA approved and CE certified for treatment of osteoarthritis lesion progression (Veronesi et al., 2014; Gobbi et al., 2014). Nonetheless, given its ability to interact with neuronal tissue, as demonstrated both in-vivo and in-vitro, its effect on human central nervous system has been investigated over the years. For the first time, in 2009, Capone and colleagues demonstrated that exposure to the I-ONE signal, with a 1.8 mT intensity, for 45 minutes would enhance cortical excitatory neurotransmission on healthy volunteers, without causing discomfort or pain (Capone et al., 2009). The exposure system used in this study consisted in a custom made coil by IGEA company (IGEA S.p.A., Carpi, Italy) with a shape adaptable to the head. The coil was placed tangentially to the inion and to a point 3 cm above the nasion and it was kept in place by a Velcro strap. More recently, the same exposure conditions were used to show that this type of signal doesn't affect LTP-like plasticity in human motor cortex (Capone et al., 2020). This is a relevant aspect since LTP is

considered one of the most important molecular mechanisms underlying learning and memory. In 2017, the I-ONE PEMF was tested in stroke patients for the first time, with the hypothesis that it could represent an innovative neuroprotective strategy for brain ischemia, based on a more physiologic modulation of adenosine receptors (Capone et al., 2017). The purpose of this exploratory study was to evaluate the safety and tolerability of ELF-MF in patients with acute ischemic stroke and to collect preliminary data about the interaction of such stimulus with human brain ischemic tissue. This study is the starting point for the work conducted during the thesis on the topic of the neuroprotective effect of PEMFs, as will be described in Chapters 6 and 7. In fact, not only computational dosimetry was conducted on three of the six patients enrolled in (Capone et al., 2017), in order to estimate the electromagnetic quantities induced inside the brain and inside the ischemic tissue, but a novel methodology to attain a dose-response curve for this potential type of treatment was assessed, as described in detail in Chapter 6. Furthermore, this methodology to attain a dose-response curve was applied to the ongoing multicentric, randomized, double blind, placebo controlled study (ClinicalTrials.gov, Identifier NCT02767778) that aims at validating PEMFs stimulation as a non-invasive, safe tool to promote recovery in acute ischemic stroke patients, as reported in Chapter 7 that is dedicated to describe the work conducted for the one-year interim analysis.

Chapter 6

Patient Semi-specific Computational Modeling Applied to Neuroprotective Treatments in Acute Ischemic Stroke

6.1 Abstract

Neuroprotective effects of pulsed electromagnetic fields (PEMFs) have been demonstrated both *in vivo* and *in vitro*. Moreover, preliminary clinical studies have been conducted and suggested PEMFs as a possible alternative therapy to treat acute ischemic stroke. In this work, it is shown that it's possible to build-up a patient semi-specific head model, where the 3D reconstruction of the ischemic lesion of the patient under treatment is inserted in the head of the human body model "Duke" (v.1.0, Zurich MedTech AG). The semi-specific model will be used in the randomized, placebo-controlled, double-blind study currently ongoing. Three patients were modelled and simulated, and results showed that each ischemic lesion experiences a magnetic flux density field comparable to the one for which biological effects have been attested. Such a kind of dosimetric analysis reveals a reliable tool to assess the correlation between levels of exposure and the beneficial effect. Thus, once the on-going double blind study is complete it will prove if PEMFs treatment triggers a clinical effect, and it will be then possible to characterize a dose-response curve with the methodology arranged

in this study[1].

6.2 Introduction

A cerebral stroke is a sudden insult that occurs after complete or partial blood flow interruption to the brain. Whether this lack of blood flow is due to a restriction or to a full occlusion of arterial vessels supplying the brain, the stroke is said to be ischemic. Ischemic stroke, which accounts for approximately 80% of all strokes, is the third cause of death worldwide and the main cause of chronic, severe adult disabilities(Moretti et al., 2015). The ischemic lesion consists of a central core, with severely compromise cerebral blood flow (CBF) which leads to immediate neuronal death. The core is surrounded by a rim of ischemic tissue characterized by impaired electrical activity but preserved cellular metabolism, known as the *penumbra*. As an opposite to the core, the penumbra is reversibly damaged. In this case, tissue salvage may be achieved when re-perfusion is established within a 6- to 8-hour period (Kauffman et al., 1998). Even though thrombolysis is nowadays the most wildly diffuse therapy to treat strokes, important advances made in the understanding of the pathophysiological mechanisms underlying the evolution of the ischemic penumbra have brought to light the alternative approach of neuroprotection. Neuroprotection aims to antagonize the harmful molecular and cellular events responsible for the ischemic damage, allowing brain cells to survive to the reduced CBF and to stabilize penumbra (Moretti et al., 2015). Because of this, several studies have suggested the hypothesis that electromagnetic fields exposure may be an interesting approach as a noninvasive treatment with a low impact on daily life (Varani et al., 2017). In the early 2000s, extremely low frequency magnetic fields have shown to enhance neurite outgrowth (McFarlane et al., 2000) and to save rat cerebellar granule neurons from apoptosis (Oda and Koike, 2004). More recently, Urnukhsaikhan et al. demonstrated a neuroprotective effect of low frequency-pulsed electromagnetic fields (LF-PEMF) in mice after ischemic stroke (Urnukhsaikhan et al., 2017). Specifically, the authors showed that LF-PEMF exposure increases resistance to apoptosis via activation of the TrkB/Akt/Bad pathway and the upregulation of brain-

[1]This chapter was published as an article in Scientific Report (Colella, M., Camera, F., Capone, F. et al. Patient Semi-specific Computational Modeling of Electromagnetic Stimulation Applied to Neuroprotective Treatments in Acute Ischemic Stroke. Sci Rep 10, 2945 (2020). https://doi.org/10.1038/s41598-020-59471-9

derived neurotrophic factor (BDNF) expression, while decreasing the level of inflammatory mediators, such as Interleukin 1 beta (IL-1β) and Matrix metalloproteinase-9 (MMP9). Moreover, LF-PEMF exposure was able to significantly improve mouse behavior during the recovery process. Pena-Philippides et al. studied the effects of PEMF exposure on infarct size and inflammation following distal middle cerebral artery occlusion (dMCAO) in mice (Pena-Philippides et al., 2014). This work demonstrated that PEMFs reduce the size of the ischemic lesion measured by MRI and modify the profile of pro-inflammatory cytokines causing an anti-inflammatory and anti-apoptotic effect. Segal Y et al. studied a very low intensity, low frequency, electromagnetic field treatment (VLIFE) on an in vivo stroke rat model (Segal et al., 2016). Brain MRI imaging showed a decrease in perilesional edema and lateral ventricle widening in the treated groups. Treated rats showed recovery of sensory-motor functional deficits, as demonstrated by Modified Neurological Severity Score and forelimb placement tests. The authors concluded that VLIFE stimulation promotes neuronal plasticity after stroke, thus improving clinical recovery. In 2002 Varani and co-workers (Varani et al., 2002) demonstrated that exposures to low frequency and low energy pulsed electromagnetic fields (PEMFs) induces the upregulation of A_{2A} adenosine receptors (ARs) in human neutrophils with a magnetic flux density in the range of $1 - 3.5$ mT. A subsequent study, conducted on rat cerebral cortex and cortical neurons, has also confirmed that the effect of PEMFs exposure is selective for A_{2A} and A_3 ARs (Varani et al., 2012). These are fundamental achievements, considering that A_{2A} and A_3 play a key role in protection against ischemic damage (Varani et al., 2012; Pedata et al., 2015). In order to better understand the effect of PEMFs in neuronal cells following hypoxia injury, Vincenzi and co-workers(Vincenzi et al., 2017) exposed human neuroblastoma cell line SH-SY5Y and rat pheochromocytoma PC12 cells, cell lines endowed with long term proliferative capacity in-vitro and widely accepted as good neuron-like cell models (Vekrellis et al., 2009; Vincenzi et al., 2012). Results showed that PEMFs stimulation significantly reduced hypoxia-induced cell death. The signal used for the in vitro experiments by the group of Varani (Varani et al., 2002, 2012; Vincenzi et al., 2017) is the same that has been used in the study conducted in Grant et al in 1994 (Grant et al., 1994), where they evaluated potential beneficial effect of PEMFs on rabbit cerebral damage. These results showed attenuated cortical edema, when considering magnetic resonance imaging (MRI), and in a reduced neuronal damage, assessed with histological examination. Besides, the aforementioned signal is also able to produce changes in the

excitability of the human cerebral cortex (Capone et al., 2009). Moving to human studies, an open-label, one-arm, dose-escalation, exploratory study (Capone et al., 2017) was carried out in order to evaluate the safety and tolerability of PEMFs in patients with acute ischemic stroke. The study consisted of a 5-day intervention phase and a 12-month follow-up phase. Within 48 hours from the stroke onset, the six enrolled patients underwent PEMFs treatment daily for 5 consecutive days. Clinical follow up lasted 12 months and brain MRI was performed before, and at the one month mark after the treatment. According to the protocol, the first group of three patients was stimulated for 45 min/day and the second group of three patients for 120 min/day. No adverse events occurred during the treatment and clinical conditions improved in all patients. In particular, lesion size was reduced in one of the patients stimulated for 45 minutes and in all of those stimulated for 120 minutes. This study opened the pathway to a new second research avenue: an on-going randomized, placebo-controlled, double-blind study (I-NIC, clinicaltrials.gov/NCT02767778). This clinical trial foresees approximately 124 patients, still in the recruiting phase, and will clarify whether PEMFs represent a novel approach to neuroprotection with the final aim to identify a dose-response curve. This is an essential pre-requistite to apply physical agents as PEMFs as a medical treatment in an *electroceuticals* perspective (Famm et al., 2013). The estimation of the electric and magnetic quantities inside the brain tissue that are able to elicit an effect is indeed an unavoidable step to an effective and reliable use of the electric or magnetic stimulation of the brain (Di Lazzaro et al., 2013); one of the most adopted approaches is the use of computational dosimetry (Apollonio et al., 2013; Paffi et al., 2016, 2015a,b; Nadeem et al., 2003; Salinas et al., 2009; Chen and Mogul, 2010; Starzynski et al., 2002; Miranda et al., 2003; Salinas et al., 2007; De Geeter et al., 2011; Howell and McIntyre, 2017; Salvador et al., 2011). The dosimetric computation can be performed by numerically solving the electromagnetic problem inside realistic brain models, stimulated by simplified or realistic sources models. The quantities calculated are the magnetic flux density field ($\mathbf{B}$), electric field ($\mathbf{E}$) and current density ($\mathbf{J}$) distributions induced in the brain. Indeed, knowledge of $\mathbf{B}$, $\mathbf{E}$, $\mathbf{J}$ field distribution is fundamental for evaluating position, level, and extent of the stimulation. Due to the generally high wavelength of the stimulating field with respect to the head size, most of these methods use quasi−static approximation to determine the distribution of the fields induced in the human brain (Nadeem et al., 2003; Salinas et al., 2009; Chen and Mogul, 2010; Starzynski et al., 2002; Miranda et al., 2003; Salinas et al., 2007;

De Geeter et al., 2011). The presented in this chapter aims to identify a methodology for a dose-response curve assessment, suitable to be applied in a large scale clinical study. In particular, it is preparatory for the computational dosimetry that will be carried out on the 124 patients recruited in the multicentric double blind I-NIC study. Therefore, a dosimetric study, based on a magneto-quasistatic solution at macroscopic level was performed, using a semi-specific head model of the patients. The novelty of semi-specific approach is to represent the ischemic volume of each patient inserted in the correct position inside a standard human head model. This leads to a faster and reliable procedure suitable for the analysis of a large sample of patients. Moreover, in order to assess a methodology able to identify a threshold and a dose-response curve, a post-treatment model of the ischemia was obtained for each patient, that was accurately placed in the semi-specific head model, to compare pre- and post-treatment ischemic volumes. Ratio of the volumes in the head space were correlated to the exposure intensity (**B**) field in order to quantify if, and where, a significant reduction could be observed. Similar calculations have been performed also for the **J** field. Such a methodology is applied here to the reduced sample of the three patients recruited in126(Capone et al., 2017) that underwent magnetic stimulation for 120 minutes (the same treatment duration as the one used in the I-NIC study. Such a pool of data seems to be consistent with the final aim since in both cases, the magnetic source is a single monolateral solenoid placed on the patient head, therefore the dosimetric methodology proposed here will be applicable for the I-NIC study. As shown in (Capone et al., 2017) this source application implied a gradient of **B** transverse to the head that decreases with the distance from the solenoid itself. From a dosimetric point of view, this opened the question on the exposure experimented by the different ischemic regions as a function of distance. This is a crucial point in order to be able to identify the minimal exposure threshold to attain the effect. This study lays the groundwork for a methodology, that once applied to the I-NIC patients, will be able to identify the stimulation threshold capable of triggering (if any) a neuroprotective effect.

6.3 Methods

The study complied with the Helsinki declaration and was approved by the local ethics committee (Università Campus Bio-Medico di Roma) and Italian Ministry of Health. Informed consent was obtained from all participants. The study was registered with

ClinicalTrials.gov, number NCT01941147 (September 9, 2013). The study protocol has been published (Capone et al., 2014). Numerical dosimetry was performed on the three subjects exposed for 120 minutes.

To perform the dosimetric analysis, the Magneto- Quasi Static module of the software Sim4Life v.3.4 (ZMT, Zurich MedTech AG) was applied. The model used to perform the EM simulations has been defined as semi-specific, this because the 3D model of the ischemic lesion of each patient that underwent the 120-minutes-treatment was entered in a standard human head model, obtained from the Virtual Population member Duke (v.1.0, Zurich MedTech AG (Christ et al., 2010)). This version of Duke is a 1 mm voxeled male model counting a total number of 77 different tissues, of which only the 40 structures of the head were selected. Electric properties of tissues are built-in in Sim4Life v.3.4 and they are based on IT'IS database (Hasgall et al., 2015). In order to perform the EM simulation, computational model of the stimulation device must be considered as well. The concept behind the semi-specific model and the final geometry are shown in Fig. 6.1. A detailed description is reported as follows.

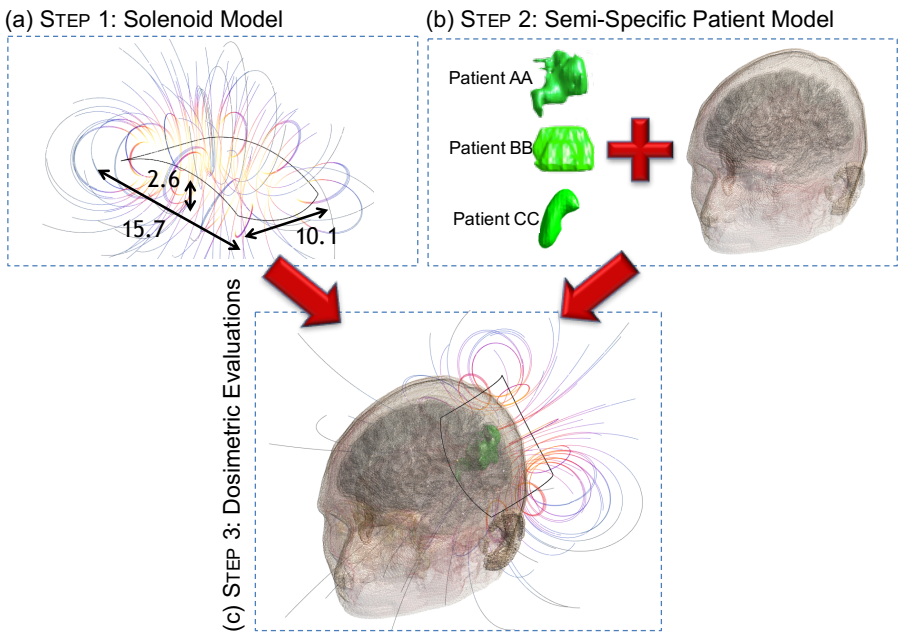

Figure 6.1: Sketch of workflow, (a)step 1: solenoid model (experimentally validated), (b) step 2: semi-specific model based on reconstructed ischemic volume for each patient, (c) step 3: dosimetric evaluations.

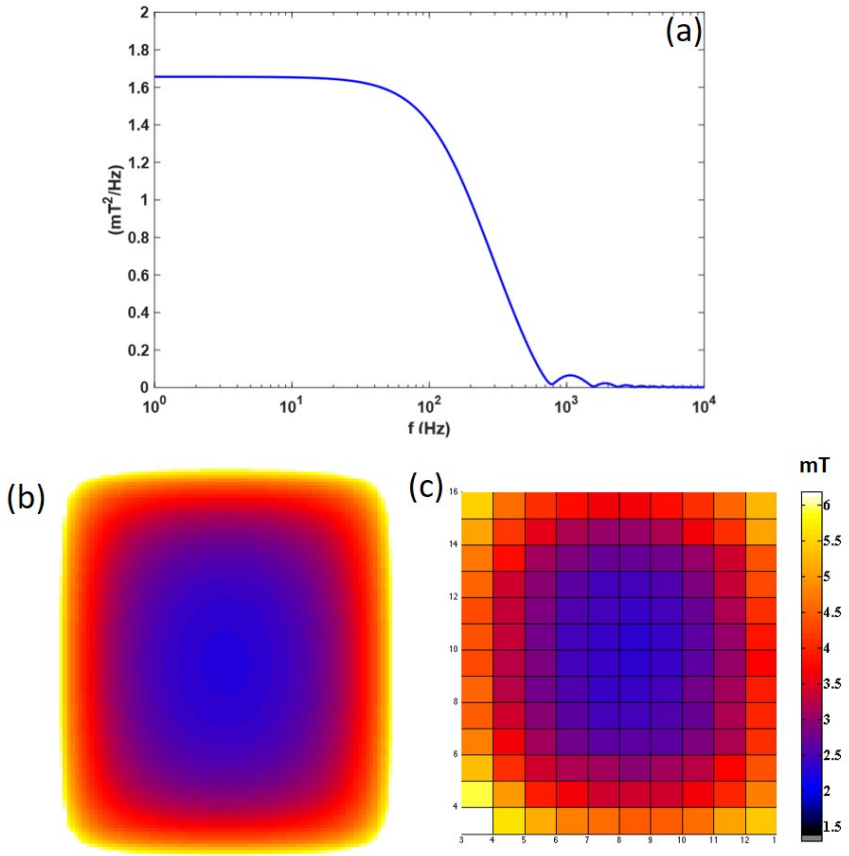

Figure 6.2: Stimulation model. (a) Pulsed signal in frequency domain; simulated $\|\mathbf{B}\|$ (c) and measured $\|\mathbf{B}\|$ (d) on the plane of the coil. Measurements are conducted with the Gaussmeter/Teslameter Model DG-50, from the company Laboratorio Elettrofisico.

6.3.1 Coil model and simulation parameters

The medical device used by IGEA company for both the study conducted in (Capone et al., 2017) and in the I-NIC clinical study to deliver PEMFs consists in a generator of a pulsed current signal that supplies an external coil (solenoid), that, in turn, generates a pulsed electromagnetic field, with a duration of the active phase of the signal equal to 1.3 ± 0.1 ms and a repetition frequency of 75 Hz (Capone et al., 2009). The coil is a 240-turned solenoid with a rectangular shape and is held in position upon the ischemic hemisphere with a helmet, placed on the head of the patient by means of a

Velcro strap (Capone et al., 2017). This geometry was reproduced in the simulation environment, where a single turn rectangular coil of 14 x 10.6 cm (mean length of the 240 turns of the solenoid), with no thickness, was designed. The peak value of the pulsed current signal that feeds the rectangular coil is 240 A. The solenoid model was validated after comparison between measured and simulated B field distribution over the coil plane at the time peak (Fig. 6.2 b-c). After validation, for the three different patient conditions, the coil, was properly warped in order to simulate the solenoid properties of being adaptable to the head shape (Fig. 6.1a). As it's not possible to work in time domain with the software Sim4Life, simulations were conducted at 250 Hz. This frequency was found to be the best to approximate the current density peak in each patient, as described in Appendix 6.6.

6.3.2 Ischemic volumes: from MR images to 3D model

The 3D model of the ischemic tissue was obtained by segmenting the MRI scans of each of the patient that underwent the treatment for 120 minutes. MRI data is shown in grey scale, giving the possibility to distinguish different tissues. Particularly, the ischemic lesion is clearly visible, among all the other brain structures, as it is strongly hyperintense. The procedure adopted to obtain the 3D model of the ischemia has been described in (Capone et al., 2017) and will be briefly summarized here:

1. Lesion area is segmented with a semi-automatic region growing segmentation tool, followed by a manual editing of the edges.

2. After the segmentation, the voxels belonging to the ischemic volume are marked with a unitary value, while all the others are considered equal to zero. In this way, a binary mask that contains only the geometry of the ischemia was obtained.

3. After conversion in a .raw file, each binary mask is imported in Sim4Life v.3.4 and processed in order to generate the surface of the ischemia. Since the resolution of these data, especially in the longitudinal axis, is lower than the one of the head model, a smoothing function with an iterative algorithm that adapts the two different discretizations have to be applied.

This procedure was implemented to obtain, for each patient, two different models of the ischemia: before and one month after the treatment. In Fig. 6.1b, the model of each

pre-treatment ischemia is reported in green. The model representing the pre-treatment volume was included in the dosimetric study, as it simulates the lesion treated with the PEMFs stimulation. Instead, post-treatment ischemia is considered only during post-processing to evaluate and quantify variations of the geometry, in terms of area and volume.

6.3.3 Assembling of the model and resolution of the dosimetric problem

Once both the coil and the ischemia models are created, they must be conveniently placed with respect to Duke's head, following the idea described in Fig. 6.1. First of all, it was necessary to put the ischemic volume inside the head model. A first placement was obtained by importing MRI slices of the whole head of each patient in Sim4life and adjusted to those of Duke, in order to find landmarks that helped for a first positioning of the ischemia. Final adjustment was obtained by visual inspection with physicians. After this, the coil was placed as close as possible to the head, with the ischemic volume centered along the coil axis. In this way, three different configurations corresponding to the three different patient conditions were obtained, as shown in Fig. 6.3. Additionally, to evaluate the effect of a possible misplacing of the stimulator during the treatment, the coil was shifted by ± 1 cm over the head along the longitudinal and transversal directions in patient AA. Results showed a 2% maximum variation for the peak of the histogram that shows frequency of occurrence of B field intensities inside the ischemic lesion (see 6.14), demonstrating robustness over changes in the position of the coil. As already discussed above, the electromagnetic problem was solved considering only the pre treatment ischemia, to which electric properties of the edema (Kent and Grill, 2014) were assigned, which means a conductivity σ equal to 1.7 S/m and the same relative permittivity ϵ_r as the grey matter. Head tissues were automatically assigned through IT'IS database. To perform the simulation, a 0.5 mm and a 1 mm isotropic resolution were imposed to the ischemia and to Duke's skin respectively, whereas Sim4Life default resolution of 0.625x0.625x0.625 mm was imposed to the remaining structures.

6.3.4 Comparison between pre-treatment and post-treatment volumes

Aiming to obtain a correlation between intensity of the electromagnetic quantities ($\mathbf{B}$ and $\mathbf{J}$) and changes in ischemic volume and geometry, a first surface-based analysis was

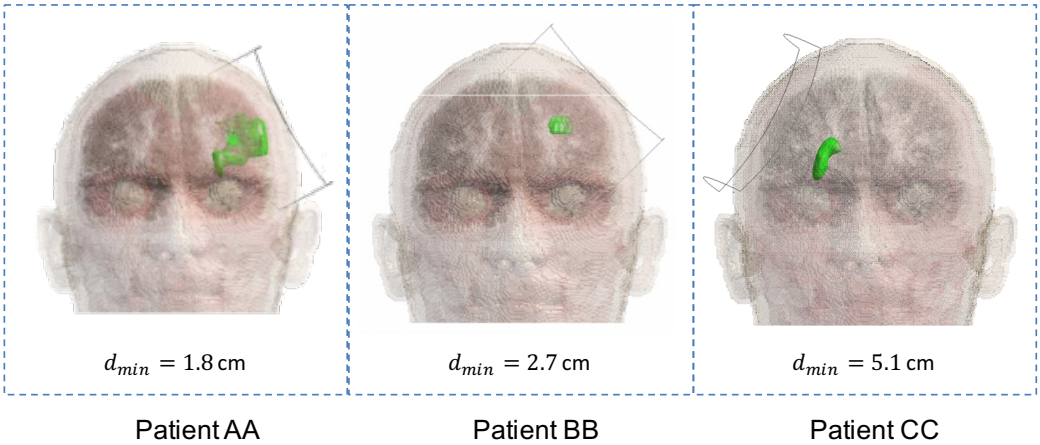

Figure 6.3: Final semi-specific patient models: all patients are shown on xz-plane. The shortest distance between the ischemia and the coil is defined as d_{min}.

conducted on single slices of the lesion. In this sense, the 3D models of pre-treatment and post-treatment ischemia were cut in slices along specific directions, with a relative distance between two consecutive slices equal to 5 mm. In order to conduct this study, it was decided to work with a coil-based frame of reference, instead of the default cartesian coordinate system X-Y-Z. The new system consists of three orthogonal axis, defined as d, f and t, where d is the normal to the *d-plane*, which is parallel to the coil, as it passes through its four vertices. While axes t and f are defined as the vectors normal to the *t-plane* and the *f-plane*, respectively. These two planes are orthogonal to the coil, because they pass through two of its four vertices, i.e. chosen as those belonging to the short or the long side of the coil, respectively. The three planes described above are shown in Fig. 6.4a, where it is also shown that each plane is shifted along its normal, in order to obtain the slicing of both pre-treatment (green) and post-treatment (cyan) lesion. With this procedure, a first evaluation of pre- and post-treatment regions was performed, as will be described in the results. However, this surface-based analysis is limited by the finite dimensions of the ischemia, which could cause a misreading of data for those slices bordering with the extremities of the object. For this reason, rather than performing a quantitative evaluation with this procedure, the focus was moved on volumetric considerations. The same concept was applied when considering both the magnetic flux density field, $\mathbf{B}$, and the induced current density, $\mathbf{J}$. Either way, specific intensities within the range of all the values experienced by the ischemic volume were

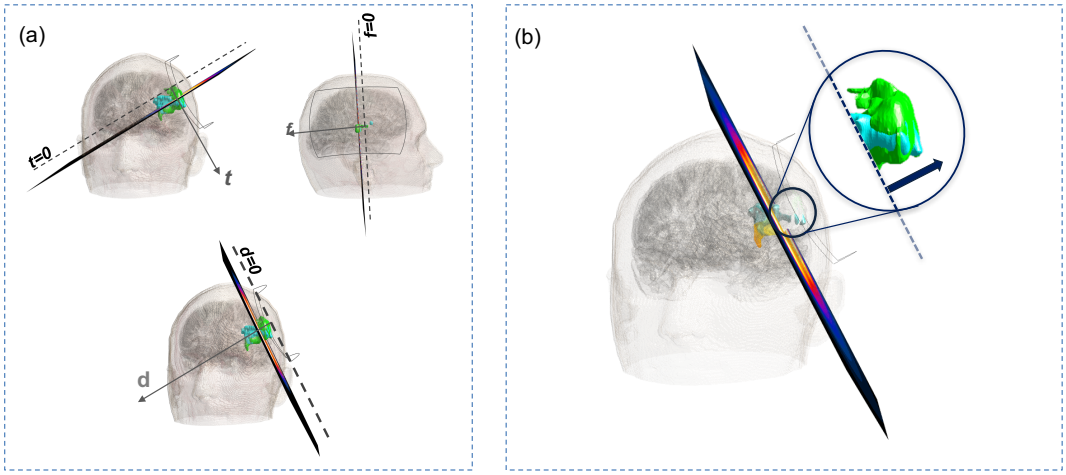

Figure 6.4: (a) Planes relative to the coil used to observe pre-treatment and post-treatment ischemic slices. (b) Example of volume selection: here the threshold is set for B to 1.7 mT. Inside the blue smaller circle: the volume of ischemia exposed to a B field equal or greater than 1.7 mT is represented in white; how that partial volume has changed after the treatment is shown in cyan.

selected as thresholds. The amount of pre-treatment volume exposed to a field equal or greater than the selected threshold was computed. In order to apply this evaluation to the post-treatment ischemia, exposure levels on brain regions where the ischemic volume is present one month after the treatment were identified. Thus, considering the same thresholds, it was possible to compute the amount of post-treatment ischemic volume that lies on regions previously exposed to the given field values. The purpose of this analysis was to assess how much post-treatment volume persisted in a region treated with intensities at least equal to the chosen threshold. In Fig. 6.4b a description of how this procedure works when considering the **B** field is reported: **B** is homogeneously distributed along the *d-plane* and its intensity depends only on the distance from the coil. For this reason, post- and pre-treatment ischemic volume exposed to a magnetic field equal or greater than the set threshold will be approximately all above the plane parallel to the coil, placed at a specific distance d from it. However, this simplified representation is only possible when considering the **B** field, while the distribution of **J** is strongly influenced by the encountered tissues.

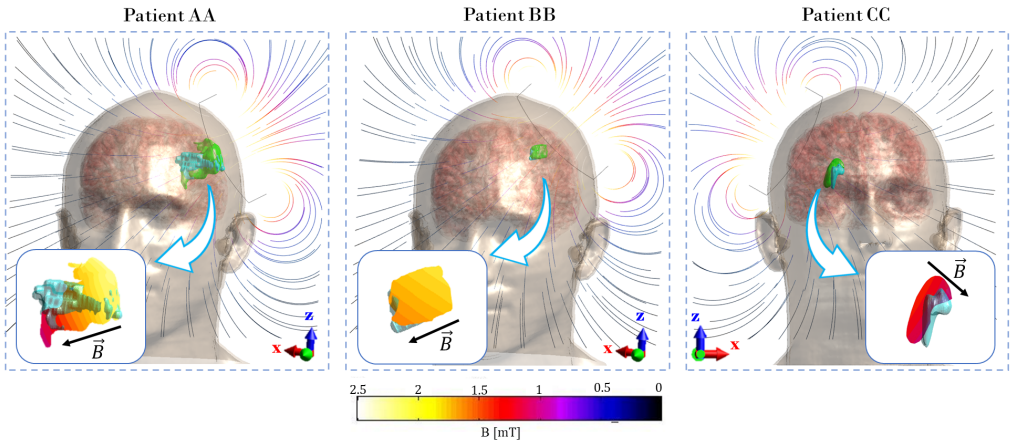

Figure 6.5: Streamline view of **B** field along the frontal plane (f-plane in the coil based coordinate) for the three patients shows direction of the B field inside the head. In green: pre-treatment ischemic volume; in cyan: post-treatment ischemic volume. Blue inset shows the spatial gradient of $\|\mathbf{B}\|$ which the ischemia is exposed to during the treatment.

6.4 Results

As expected, electromagnetic simulations show that the magnetic flux density field is not altered from the presence of the head, nor from each of its structures. In Fig. 6.5 streamline view of **B** field is shown together with the distribution of $\|\mathbf{B}\|$ over the surface of the ischemia (zoom in the inset) for each of the three patients. Data is shown through a color scale from black to white: intensities above 1 mT are represented as shading from red to white, while lower intensities ranges from purple to black. Here the gradient that the field experiences is clearly visible and its intensity is inversely proportional to the distance from the stimulating coil. *Patient AA* has the biggest lesion, which is exposed to a **B** field that varies from 1 mT to 2.2 mT, while those of *patient BB* and *patient CC* are smaller, so experiencing a more uniform **B** field. Between the two, being the ischemia of *patient BB* closer to the coil, it ensures an exposure to higher values (1.5 mT to 1.9 mT) with respect to that of *patient CC* (1 mT to 1.3 mT). Thus, the field that the lesion is exposed to depends on its dimension and position: the smaller the ischemia, the smaller the space variation of **B** values it experiences; the deeper, the lower is the intensity. In order to obtain the most reliable values of the **B** field and of the current density **J** induced in each voxel belonging to the ischemic volume the time course of the signal was reconstructed following the same

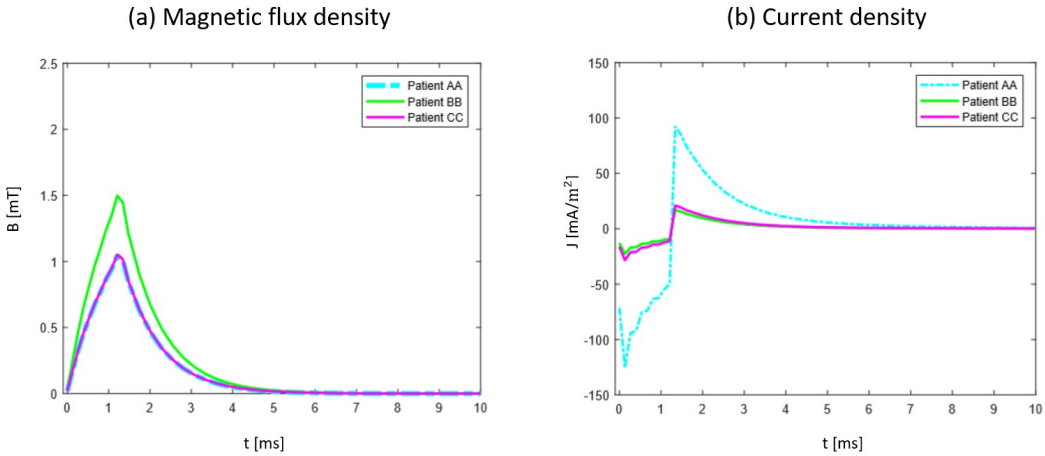

Figure 6.6: a) Time course of $\|\mathbf{B}\|$ field for all patients in the voxel of the pre-treatment ischemic volume that experiences the lowest B. All the three patients undergo to at least 1 mT; b) Time course of induced $\mathbf{J}$ for all patients in the voxel of the pre-treatment ischemic volume that experiences the highest value of $\mathbf{J}$.

approach to the electromagnetic solution as the one followed in (Paffi et al., 2016), where a total of 150 simulations were performed. Fig. 6.6 reports the time course of $\|\mathbf{B}\|$ in the voxel that experiences the lowest $\|\mathbf{B}\|$ (Fig. 6.6a), and the time course of $\mathbf{J}$ inside the voxel that experiences the highest $\mathbf{J}$ (Fig. 6.6b). The most important observation is that all the three lesions are exposed to a field greater than or equal to 1 mT, which is the threshold of attested biological effects (Vekrellis et al., 2009; Vincenzi et al., 2012). *Patient AA* and *patient CC* experience the same minimum value. This is because they both expand towards deeper regions of the brain. For the time course of $\mathbf{J}$ (Fig. 6.6b), *patient AA* is characterized by highest values due to the combined effect of the dimensions of the ischemia and the highest values of $\|\mathbf{B}\|$ (just above 2 mT). As a matter of fact, a greater induction in a wider surface is expected, according to Faraday's law. For *patient BB* and *patient CC*, the different cross-sections of the two lesions force the two current densities to have similar values, despite experiencing different $\mathbf{B}$ field intensities. The absolute value of the negative peak of $\mathbf{J}$ is above 100 mA/m^2 for *patient AA*, and above 20 mA/m^2 for *patient BB* and *CC*.

Robustness of the semi-specific model with respect to changes in the anatomy of the head have been proven by simulating the ischemic volume inside two other generic head models: the Glenn model (Christ et al., 2010; Gosselin et al., 2014) (ViP, cV3.1,

84-year-old man) and the MIDA model (Iacono et al., 2015) (28-year-old woman). For each model, the peak of the histogram that shows frequency of occurrence of B field intensities inside the ischemic volume was 2.01 mT and 1.95 mT, respectively, leading to a 5% maximum variation over the value computed with the Duke model (i.e. 2.05 mT), as shown in Fig.6.16, in Appendix 6.7. To better understand what the exposure level meant in terms of a possible reduction or containment of the growth of the ischemic volume, the 3D model of the one month post-treatment ischemia was superimposed to the pre-treatment one, as shown in Fig. 6.5 (cyan colored). Slices of the two volumes were compared in the coil-based coordinate system, as described in the previous section. As a representative example, results for *patient AA* are shown in Fig. 6.7 on planes parallel to the coil (*d-plane*). In this figure, the contours of pre- and post-treatment slices of ischemia are shown colored in light green and cyan respectively, at three different distances d from the coil. For each distance, left-side figures represent the slices inside the brain, for immediate inspection of the two contours. Distribution of $\|\mathbf{B}\|$ is shown in the right-side figures. From Fig. 6.7 one can observe higher post-treatment regions reductions with respect to pre-treatment ones with increasing intensity of $\mathbf{B}$ field.

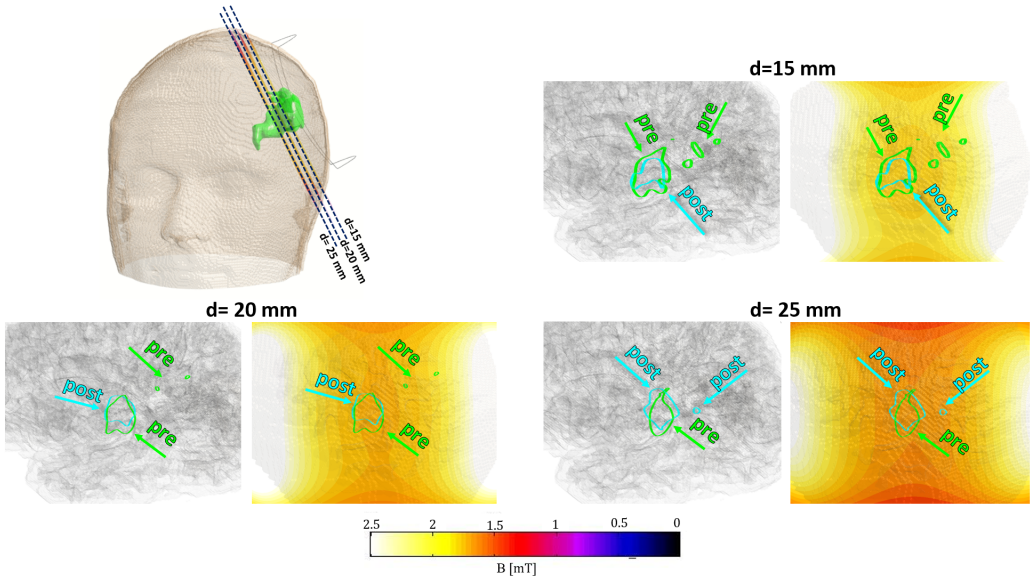

Figure 6.7: $\|\mathbf{B}\|$ field distribution of *patient AA* on the planes parallel to the coil. Analysis is carried out at different distances d from the coil. For each distance, the edges of the slice of ischemia before (pre, in light green) and after (post, in cyan) the treatment are given, in order to compare the dimensions.

Similar analysis was conducted considering the distribution of $\|\mathbf{J}\|$ intensities. Results for *patient AA* on *d-plane* and *f-plane* are shown in Fig. 6.8 and 6.9. The data represented in Fig. 6.7 allows us to hypothesize that the volume reduction is an increasing function of the intensity of the fields experienced within the ischemic volume. In principle, this will permit the identification of a dose-response curve under proper conditions. Therefore, the following analysis was conducted in order to assess the best approach to attain such a result. Since the lesions are exposed to intensities greater than 1 mT, this is taken as the minimum exposure value. At first four ranges were chosen for the **B** field and 5 for the **J** field and the partial volume of ischemia that is within each range was quantified, both for the pre-treatment ischemic lesion (V_{pre}) and for the post- one (V_{post}).

Table 6.1 reports, for each exposure range, the lesion variations quantified as the ratio between V_{post} and V_{pre}. Thus, a value above 1 indicates that the ischemic volume has enlarged, while a value below 1 shows that there's been a reduction of the volume. Looking at the **B** field for *patient AA* and *patient BB*, it can be noticed that there is a visible reduction of the ischemic lesion (over 50%) when the exposure level is greater than 1.7 mT. However, when it comes to the regions exposed to less than 1.7 mT, data for *patient AA* show a two fold increase of the volume after the treatment, a value that is closer to the volume increase typical of untreated lesions. The same cannot be said for *patient BB* or *CC*, for whom the respective volumes exposed to the range from 1.3 mT to 1.7 mT (upper limit excluded) or from 1 mT to 1.3 mT (upper limit excluded) have slightly reduced after the treatment (up tp 12%). When considering **J**, each ischemic volume exposed to intensities above 5 mA/m^2 has reduced for all the three patients (see Table 6.2).

Such data confirm that it is possible to assess a dose response behavior but, due to intrinsic biological and patient variability, all the data needs to be pooled together in order to attain statistical significance. To move forward in this direction, a similar analysis was conducted, although looking at volumes defined only by lower limit thresholds instead of exposure ranges, as was described in Section 6.3.4.

Fig. 6.10a shows the ratio between post-treatment and pre-treatment volumes as a function of $\|\mathbf{B}\|$ thresholds for all the three patients. The ratio is expressed as a percentage, so a value equal to 100% allows us to say that no reduction was obtained for that specific intensity. Since all the markers are below 100%, it is possible to state that this treatment led to an overall reduction of the ischemic volume in the three

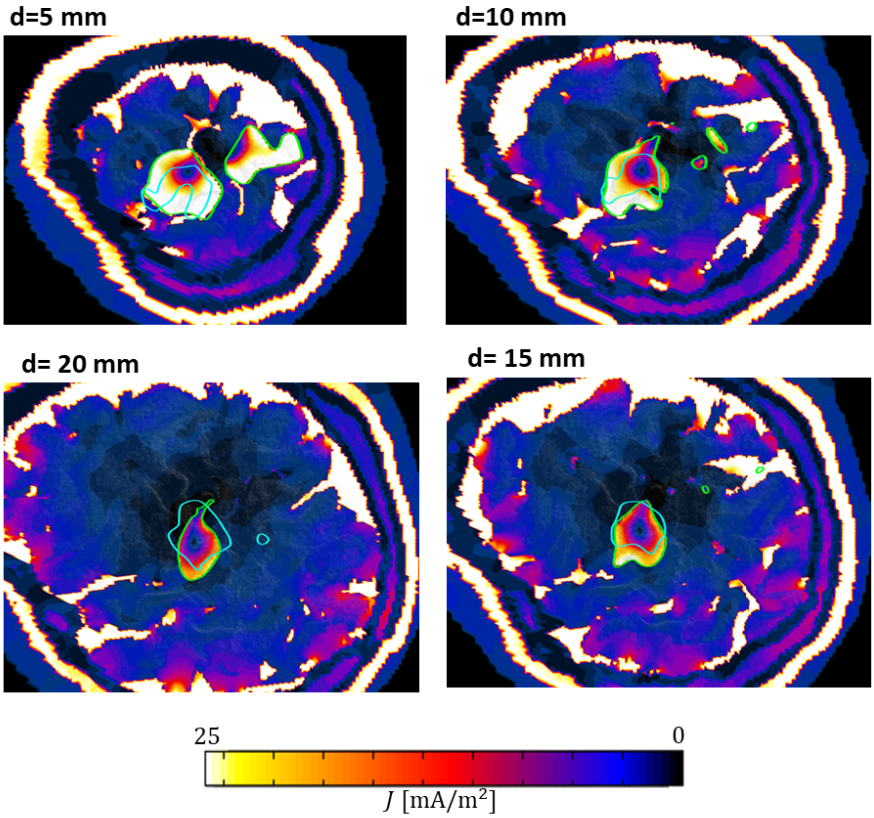

Figure 6.8: Distribution of $\|\mathbf{B}\|$ on the plane parallel to the coil, for patient AA. Analysis is carried out at different distances 'd' from the coil. For each distance, the edges of the slice of ischemia before (pre, in light green) and after (post, in cyan) the treatment are given, in order to compare the dimensions.

patients considered. This analysis quantitatively confirms what previously inferred; each patient is characterized by different ratios but, from an overall consideration, the higher is the intensity of exposure, the most effective is the treatment (i.e. the lower is the percentage of the post-treatment volume). Fig. 6.10a also shows an exponential fitting for data points of all patients pooled together; it is shown that a decaying exponential function well fits the values of this reduction. The function used for the fitting is defined as $f(x) = Me^{ax}$, with x = B and M and a respectively equal to 79.38 and -0.1. The same analysis was conducted over the current density $\mathbf{J}$, where a decaying exponential trend was found as well (Fig. 6.10b).

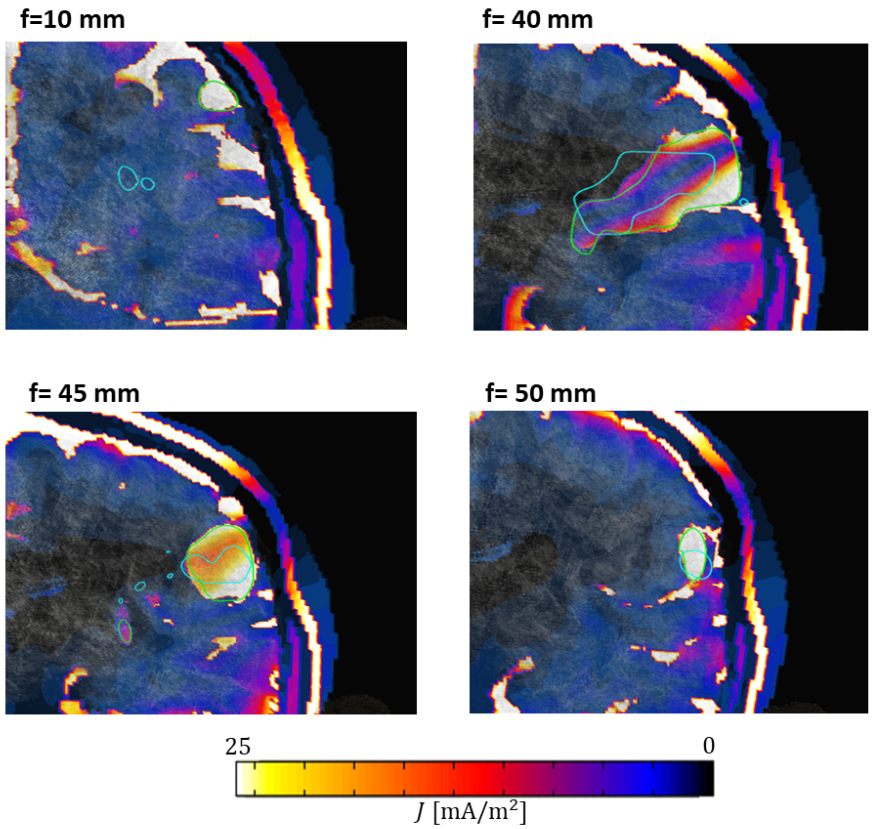

Figure 6.9: Distribution of $\|\mathbf{B}\|$ on the frontal plane orthogonal to the coil (f-plane), for patient AA. Analysis is carried out at different distances 'f' from the coil. For each distance, the edges of the slice of ischemia before (pre, in light green) and after (post, in cyan) the treatment are given, in order to compare the dimensions.

6.5 Discussion and conclusions

In the context of biomedical applications based on electromagnetic stimulation, computational dosimetry is a fundamental tool to quantify the induced electromagnetic quantities related to the dose necessary to exert the effect. This is extremely important for the optimization of the application and to deepen the underlying mechanisms. Particularly, in the framework of stroke studies, some papers investigated how the presence of a lesion can alter the distribution of induced electric field and current inside the brain. Wagner and co-workers (Wagner et al., 2006) followed a stroke in its chronic

	Ranges	**patient AA** V_{post}/V_{pre}	**patient BB** V_{post}/V_{pre}	**patient CC** V_{post}/V_{pre}
B (mT)	$1 \div 1.3$	2.33	/	0.93
	$1.3 \div 1.7$	2.41	0.88	0.00
	$1.7 \div 2$	0.47	0.33	/
	≥ 2	0.14	/	/

Table 6.1: Ratio between post-treatment and pre-treatment ischemic volume regions, selected based on the different ranges of exposure they experience. The slash symbol shows that neither pre-treatment nor post-treatment ischemia is present in that specific region.

	Ranges	**patient AA** V_{post}/V_{pre}	**patient BB** V_{post}/V_{pre}	**patient CC** V_{post}/V_{pre}
J (mA/m^2)	$1 \div 5$	5.77	0.76	2.34
	$5 \div 15$	0.64	0.42	0.51
	$15 \div 30$	0.30	0.06	0.17
	$30 \div 45$	0.16	/	0.00
	≥ 45	0.05	/	/

Table 6.2: Ratio between post treatment and pre treatment ischemic region of volumes, selected based on the different ranges of exposure they experience. The slash symbol shows that neither pre treatment nor post treatment ischemia is present in that specific region.

state to understand the effects that electrical and anatomical changes can have on the current induced in the brain after exposure to TMS. To do so, they considered a numerical human healthy head model and 11 stroke models of different sizes and geometries. The stroke models were implemented by altering the cortical geometry and properties of the healthy head model guided by brain MRIs of patients with cortical strokes. They demonstrated that a stroke can drastically affect TMS application, by altering the location of the maximum current density and modifying the focus of the stimulation. A similar approach was adopted to estimate the electric field distribution inside brain stroke patients receiving tDCS (transcranial direct current stimulation) (Manoli et al., 2017). Here a generic spherical volume was placed inside the head of the human body models Ella and Glenn (Virtual Population - ViP (Christ et al., 2010; Gosselin et al., 2014)), to simulate an ischemic lesion. Additionally, electromagnetic properties of the sphere were varied to take into account both acute and chronic phase of the stroke.

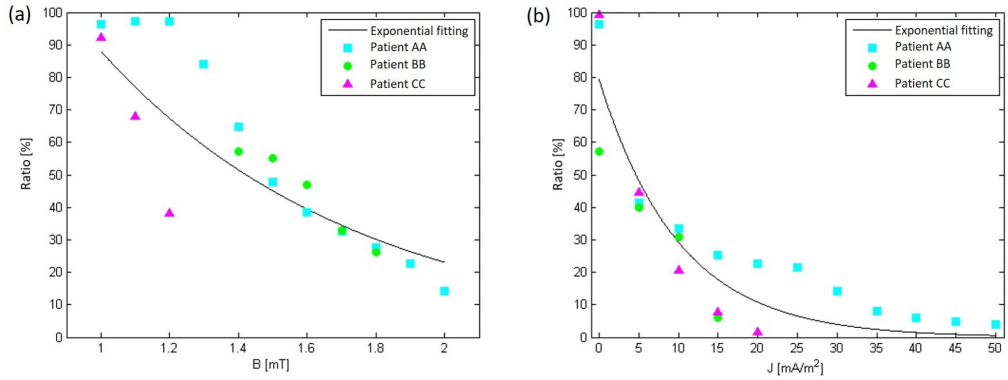

Figure 6.10: Scatter plot of the percentage quantity "ratio" with respect to increasing values of lower bound B field thresholds. Data for the three patients are pooled together, resulting in a decaying exponential function. Ratio is defined as the percentage of $\text{Volume}_{post}/\text{Volume}_{pre}$, where:
Volume_{pre}= Ischemic pre-treatment volume that was exposed to B intensity greater than or equal to a certain threshold during the treatment.
Volume_{post} = Ischemic post-treatment volume that is present in a region of the brain that was exposed to a B intensity greater than or equal to a certain threshold, during the treatment.

Similar to what was found for the TMS, results in (Manoli et al., 2017) showed that the presence and type of lesion affected the maximum value and the distribution of the field induced in the brain after exposure to tDCS. Moreover, Manoli and co-workers (Manoli et al., 2017) demonstrated that patients in chronic phase benefit more from tDCS than patients in acute phase, given the higher contrast in tissue conductivity. The limitation of both these studies is that they don't consider a realistic shape of the stroke, which becomes crucial when the dosimetric analysis is required to support a dose-response study on patient specific clinical treatment.

Specifically, in the context of ongoing studies intended to demonstrate whether PEMFs are able to elicit a neuroprotective effect on patients with ischemic stroke, the objective of the work inhere presented was to identify a methodology for a dose-response curve assessment suitable to be applied in a large scale clinical study. To this scope, the exposure undergone in the study (Capone et al., 2017) was analyzed in detail. In particular, the aim is to demonstrate that the type of exposure obtained with a single solenoid placed laterally to the head and co-centered with the ischemic lesion is able to induce a magnetic pulse with peak values above 1 mT under proper conditions. This intensity has been shown to exert effects on neuronal cells at the molecular level, increasing the density of adenosine receptors A_{2A} and A_{3A} on the cell

membrane (Varani et al., 2002, 2012). To verify the intensity of **B** field which each patient has been exposed to during the treatment, electromagnetic simulations were performed. Such model was realized using the geometric information of the ischemic area, obtained from the MRI data of the patient, that had been then placed inside a standard computational model. Results of the simulations showed that the ischemic volumes in the brain experienced a magnetic flux density field always above the desired 1 mT. Moreover, quantitative post-elaboration studies were performed on the ischemic lesion. Particularly, while the analysis of ischemic slices qualitatively suggested us a correlation between ischemic lesion reduction and **B** field values experienced, the volumetric analysis allowed us to assess the percentage of volume associated to specific thresholds. In this sense, the fitting curve of Fig. 6.10 takes into account post- and pre-treatment volumes ratio above a certain given lower field threshold, showing that increasing such a value (i.e. excluding volumes experiencing lower fields) decreases the ratio, ultimately indicating a better efficiency in eliciting the effect. As an example, by looking at Fig. 6.10 one could say that a 50% reduction of the volume was obtained by exposing to a **B** field of intensity around 1.4 mT, or, similarly, by inducing a current density of about 5 mA/m^2 (Fig. 6.6b. Fig. 6.10a can be considered the example on how to attain a dose response curve when a sample of volunteers large enough will be used. In conclusion, it is herein demonstrated that, by using electromagnetic simulations on virtual body models combined with patient specific lesions, it is possible to build a dose−response curve in an "*electroceutical*" perspective (Famm et al., 2013) when dealing with a large number of patients. This is necessary if one, aiming to introduce a new electromagnetic−based therapy, like the I-NIC, wants to follow an approach similar to the drugs clinical trials, as an example one can think to a typical *Phase*2 study (Friedman et al., 2015). *Limitations*: This methodology was conceived for the ongoing I-NIC study, but here it is applied to the reduced sample of the three patients recruited in (Capone et al., 2017) that underwent magnetic stimulation for 120 minutes (the same treatment duration as the one used in the I-NIC study). Thus, such an approach will be a powerful tool to a reliable assessment of a dose-response threshold of the treatment when a large number of patients will be evaluated.

6.6 Appendix 1: Analysis on the best approximating frequency

As described in detail in Section 6.3.1, the dosimetric analysis of I-NIC exposure was carried out in the frequency domain, as the software used to perform the simulations couldn't consider a time varying signal. Nevertheless, the I-NIC pulse, whose characteristics are identical to those of the I-ONE (see Fig. 6.2 and Fig 5.2 in Chapter 5), has a frequency content in the LF range, thus fulfilling the quasi-static (QS) conditions. Under QS approximation, exclusively the induced elecrtical quantities depend from the frequency, while the generated B field remains constant. Therefore, the strategy that was applied to numerically study the exposure to the I-NIC signal, was to carry out simulations at each frequency component and chose the one that best approximated the time solution. A total of 200 simulations were performed in the frequency range [50-10000] Hz, each 50 Hz, and they were used to reconstruct the time domain solution as described in (Paffi et al., 2016). Comparison between frequency and time domain was conducted by studying the current density induced inside the ischemic lesion (J_{isch}), as in the context of this application this is the electrical quantity of interest. The current density calculated at each spectral component, $J_{isch}(f_i)$ was compared with the one calculated at the negative time peak, J(t_{peak}) (highest intensity, Fig. 6.11), and the frequency that minimized the difference was chosen to carry out the entire dosimetrical analysis described in this chapter.
To quantify the differences, the average SMAPE (Eq. 6.1) between results in the frequency domain and in the time domain was calculated inside the ischemic lesion.

$$\overline{SMAPE} = \frac{1}{N}\sum_{k=1}^{N} \frac{J_{isch,k}(f) - J_{isch,k}(t_{peak})}{\frac{J_{isch,k}(f)+J_{isch,k}(t_{peak})}{2}} \times 100 \tag{6.1}$$

Where $J_{isch,k}$ is the current density induced inside the k-th voxel of the ischemic lesion and N is the total amount of voxels. Eq. 6.1 was calculated for each simulated frequency. Fig. 6.12 shows the results of this analysis for the three simulated patients, i.e. Patient AA, Patient BB and Patient CC. The $\overline{SMAPE}$ is plotted as a function of the frequency, to follow the trend. After 1 kHz differences above 100% were found, similarly at extremely low frequencies. The lowest percentage difference was found at 250 Hz, where $\overline{SMAPE}$ was as low as 2 %.

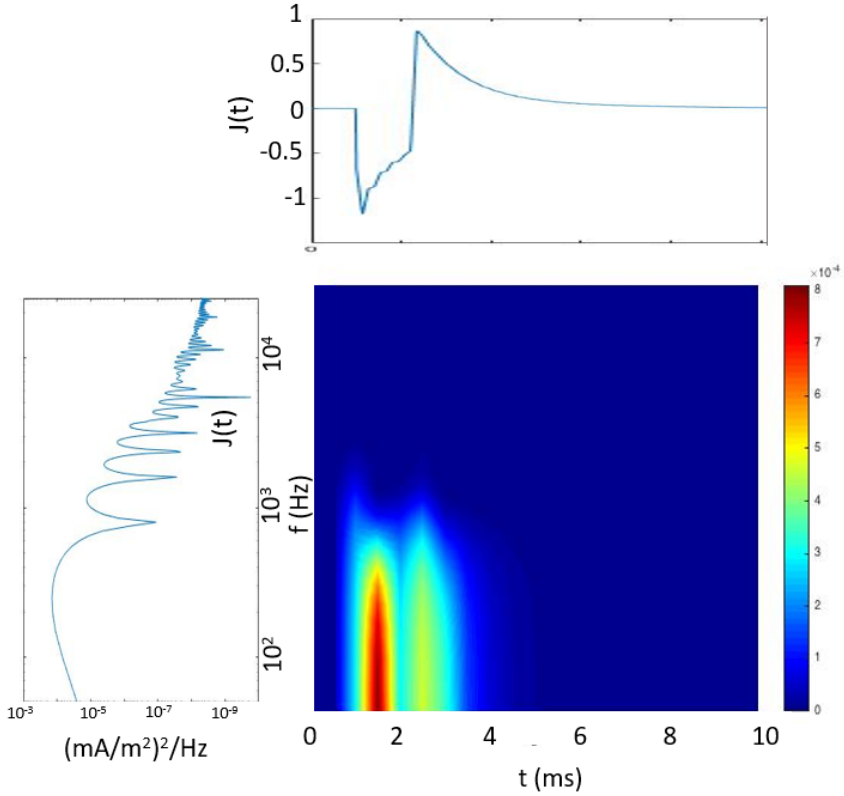

Figure 6.11: Spectrogram of the current density signal. On top the time course is reported. On the side the spectrum.

Such results remained consistent for all the three patients. Looking at Fig. 6.12, 250 Hz corresponded to the frequency that best approximated the maximum of the induced current density inside the ischemic lesion. Therefore, this was chosen as the frequency at which the dosimetrical analysis was conducted.

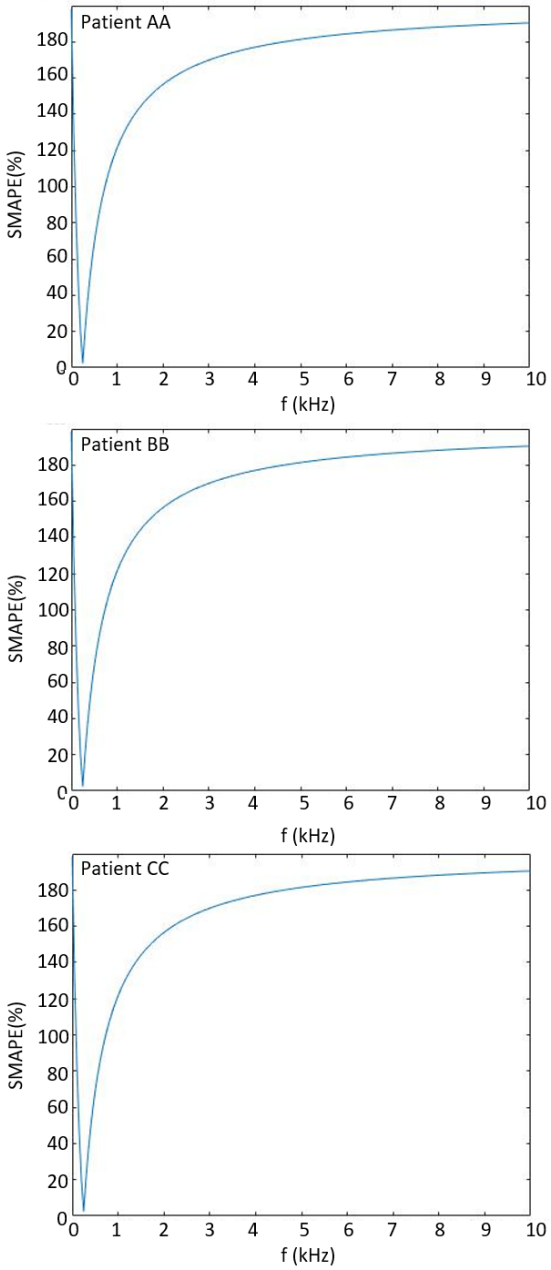

Figure 6.12: Plot of the mean SMAPE over the frequency.

6.7 Appendix 2: Variability assessment

6.7.1 Position of the coil

It should be considered that the precise position of the coil over the patient's head is not known. The optimal location should be with the lesion placed below the center of coil, nevertheless a possible misplacement of the coil during the treatment might have occurred. In order to investigate robustness of the dosimetrical analysis conducted in this chapter over possible relative shifts between the ischemia and the coil, additional simulations were performed on Patient AA model. The coil was moved by ± 1 cm along two directions, transversal (i.e., left/right) and longitudinal (i.e. up/down), as shown in Fig. 6.13.

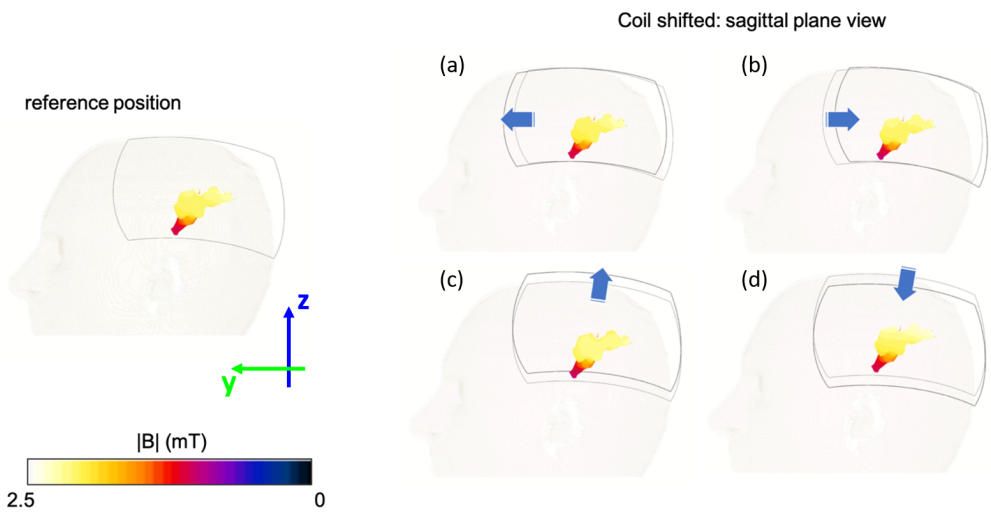

Figure 6.13: Coil misplacement. Left panel: reference position of the coil. Right panel: representation of the coil shifts by 1 cm along the transversal (top) and longitudinal (bottom) direction. $\|\mathbf{B}\|$ distribution on the surface of the coil is reported.

Fig. 6.13 shows that the $\|\mathbf{B}\|$ on the surface of the lesion is not affected by the coil shifts. Nevertheless, a quantitative analysis carried out over the entire ischemic volume showed variations in B_{max} and in the distribution across the voxels, as shown in Fig. 6.14. The coil shifted as in Fig. 6.13d determines a greater B_{max} over the other placements (2.35 mT over 2.2 mT), see histogram Long-1cm in Fig. 6.14). Nevertheless, the peak of the

histogram is the lowest (2.01 mT) with the smallest number of voxels involved, meaning that, overall, the ischemic lesion would be less exposed. The other misplacements do not affect the B_{max}, while variations of the histogram peak remain below 2 %. This results suggest a substantial robustness of the induced B field with respect to coil positioning.

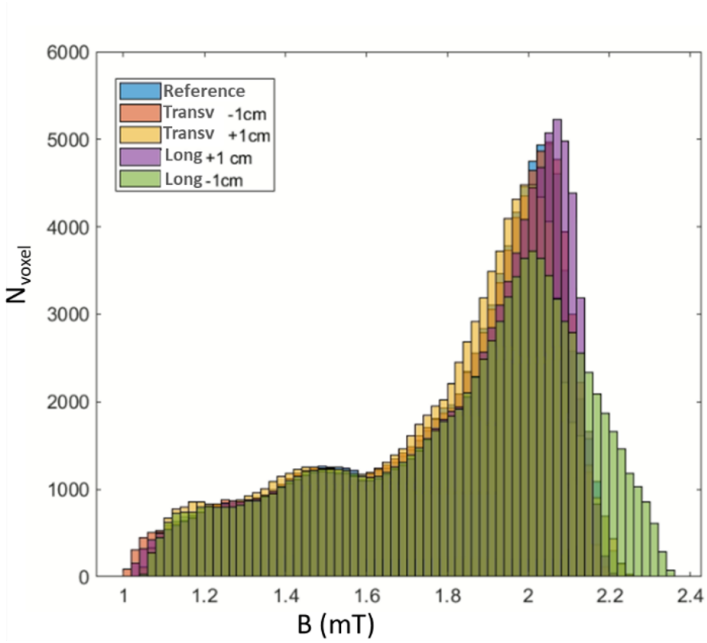

Figure 6.14: Histograms showing frequency of occurrence of $\|\mathbf{B}\|$ inside the ischemic volume when placing the coil in different positions over the head.

6.7.2 Generic head model

The methodology applied to conduct the dosimetrical analysis of the experiments reported in (Capone et al., 2017) consists in considering a head model taken from literature in place of the head model of the real patients. This was done with the aim to avoid the step related to the MRI segmentation and to guarantee a sufficient level of detail, which is fundamental for an accurate estimation of the induced electric quantities. Nevertheless, considering a different head anatomy has an influence in the relative position between the ischemic lesion and the coil, therefore it was fundamental to assess the robustness of the semi-specific modeling approach over the anatomy of the head. In order to do so, two additional simulations were conducted on Patient AA considering the Glenn model (84 year-old man, ViP v.3, (Gosselin et al., 2014)) and the MIDA model (29 year-old woman, (Iacono et al., 2015)) as the generic head. Results of the B field were compare with reference computed on the Duke model (Fig. 6.15).

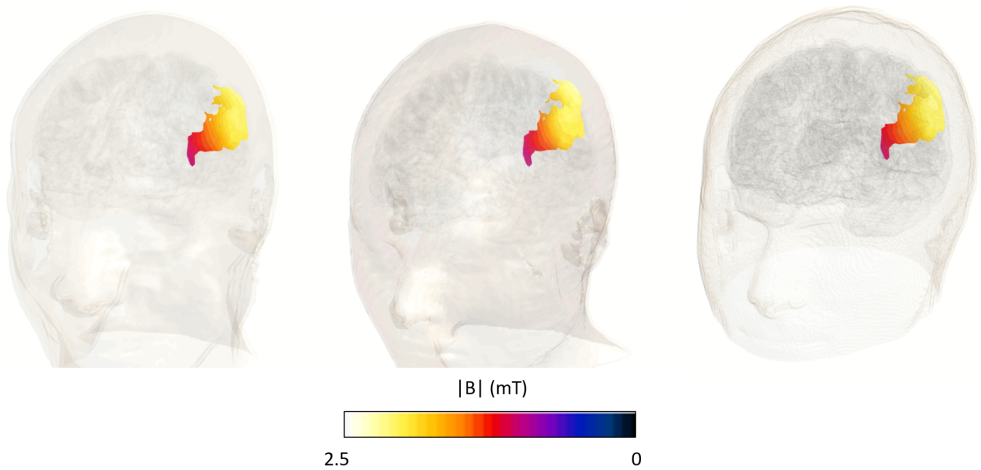

Figure 6.15: The semi-specific head model built-up with ViP Glenn (left panel), MIDA (central panel) and ViP Duke (right panel). $\|\mathbf{B}\|$ on the surface of the ischemic lesion is reported for all the three models.

The B field intensities experienced by the surface of the ischemia are similar in the three models. Therefore, to further investigate how the head anatomy may influence the dosimetric analysis, the distribution of $\|\mathbf{B}\|$ values over the entire ischemic volume were evaluated with histogram plots, as shown in Fig. 6.16. Inside the MIDA model, the ischemic lesion experiences slightly smaller B field intensities than those inside Glenn or Duke (1.8 %). This is probably to be attributed to the a thicker layer of cutaneous and subcutaneous tissues in the MIDA model, that increases the distance between the coil and the brain cortex. Overall, the three histograms show similar distributions with a maximum variation of 5 % calculated at the peak. Such results allowed to conclude that the semi-specific model is a robust methodology over possible anatomical differences between the generic head considered and the real patient.

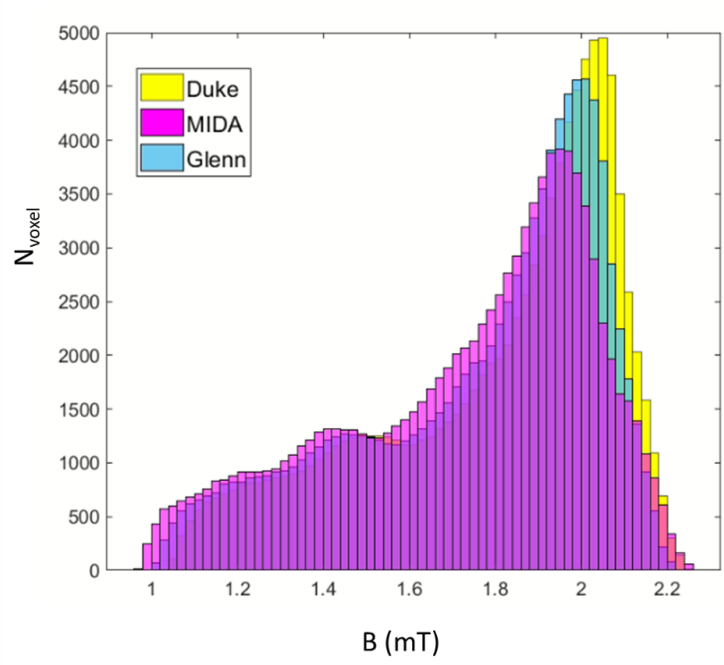

Figure 6.16: Histograms showing frequency of occurrence of $\|\mathbf{B}\|$ inside the ischemic volume when placed in three different human head models, i.e. Duke, Glenn and MIDA.

Chapter 7

The I-NIC project: A multicentric, randomized, double blind, placebo controlled study to assess LF PEMFs efficacy in ischemic patients

7.1 Introduction

As reported in detail in Section 5.1 and in Section 6.2, a great interest has been shown in literature on the effects exerted by low intensity, low frequency pulsed electromagnetic fields at cellular and human level. Particularly, in the neurological field, several in-vitro studies demonstrated how PEMFs can modulate the synaptic transmission by acting on membrane proteins and neurotransmitters, such as glutamate and adenosine A_{2A} (Varani et al., 2002), that play a key role during the neuroprotective action triggered by an ischemic damage. The neuroprotective effect of PEMFs was confirmed in-vivo as well, and the ability to reduce the dimensions of the ischemic lesion was shown (Pena-Philippides et al., 2014).
On the basis of these results, and after confirming safety and tolarability of PEMFs on healthy humans (Capone et al., 2009), the open label one-arm dose escalation study described in (Capone et al., 2017) was conducted to assess the exposure duration on

acute ischemic patients and to gather preliminary clinical information on a possible therapeutic effect. A dosimetric evaluation was conducted on these preliminary data, not only with the aim to quantify each patients' exposure conditions in terms of the experienced B field, but also, and mainly, to assess a methodology to obtain a dose response curve for this type of clinical application, as reported in detail in Chapter 6. The promising results from the preliminary open-label study opened the way to the currently on-going randomized, placebo-controlled, double-blind study (I-NIC, clinicaltrials.gov/NCT02767778), that is described in this chapter. This is a clinical trial that foresees approximately 124 patients, of which 23 have been recruited so far, and will clarify whether PEMFs represent a novel approach to neuroprotection with the final aim to identify a dose-response curve. The main purpose of this multicentric study is the validation of pulsed ELF-MF stimulation as a non-invasive and safe tool to promote recovery in acute ischemic stroke patients. In this chapter the one year interim analysis is reported, which was conducted only on the patients that completed the 45 days follow-up (i.e. 18 patients). Such analysis consisted in the neuroradiological evaluation of each patient's MRI scan in the acute phase (i.e. at base line T_0, within 48 hours from the ischemic insult) and in the chronic phase (i.e. at T_{45}, after 45 days from the treatment), carried out with the support of the expert neuroradiologists involved in the project. The aim was to quantify and compare the volume of the acute and the chronic lesion as well as to address the presence of a possible evolution of the ischemic pathological features. Afterwards, the semi-specific head model was build in order to conduct the electromagnetic dosimetry to address a correlation between the EM quantities and the volume variations. Differently from what previously done in Chapter 6, the 3D model of the ischemic lesion is inhere placed inside the brain of the 84-year-old Virtual Population model Glenn (ViP, v.3), to represent the population of patients enrolled. In the frame of this project, a two-weeks internship was completed at the Neuro-radiology research laboratory of San Raffaele Hospital in Milan, under the supervision of Prof. Nicoletta Anzalone. The aim was to address the best software and find the best procedure to be adopted for an accurate segmentation of the MRI sequences and extraction of the ischemic volume. The selected methodology is presented Section 7.3.

7.2 Study protocol

Within 48 hours from the onset of the stroke, the enrolled patients underwent clinical evaluation and brain MRI, which was repeated 7 days and 45 days after treatment. Each recruited patient was randomly assigned to real or sham group. Patients were stimulated with pulsed ELF-MF (75 Hz, 1.8 mT), for 120 min daily, for 5 consecutive days, starting within 48 hours from the onset of stroke (Fig. 7.1). Inclusion criteria required a mono-hemispheric ischemic stroke in the middle cerebral artery territory, onset of symptoms within 48 hours, National Institutes of Health Stroke Scale (NIHSS) score between 4 and 25, and a signed written informed consent. Whereas exclusion criteria was the presence of an acute intracranial hemorrhage, a previous ischemic or hemorrhagic stroke, a lacunar stroke, defined as not involving the cortex and a maximum diameter < 2.0 cm, measured on MRI diffusion-weighted images.

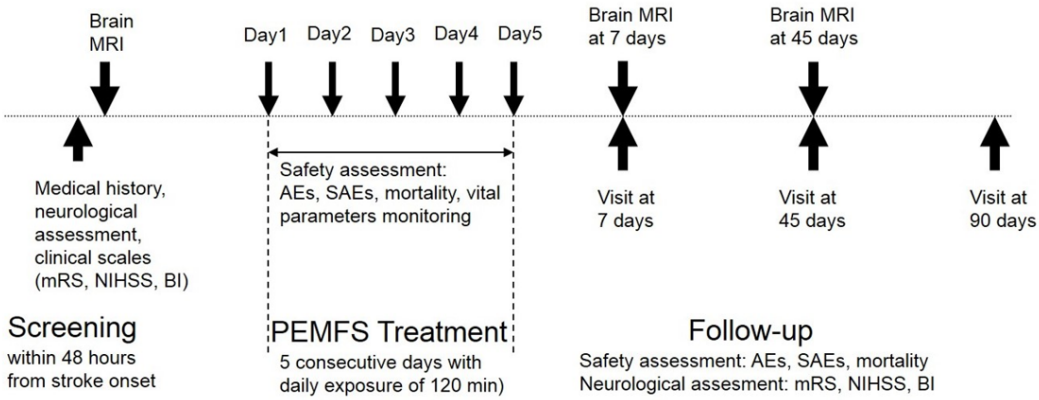

Figure 7.1: Flow-chart of the I-NIC study

So far, recruitment started in 5 different centers across Italy:

- Campus Bio-Medico University, Rome;
- Nuovo Ospedale Civile S.Agostino Estense, Modena;
- San Raffaele University Hospital, Milan;
- University Hospital of Ferrara, Ferrara;
- Torvergata University of Rome, Rome.

Pulsed ELF-MF stimulation was administrated by a rectangular, flexible coil, placed upon the ischemic hemisphere and connected to the pulse generator (B-01; IGEA, Carpi, Italy) producing a single-pulsed signal at 75±2 Hz, with a pulse duration of 1.3 ms and a peak intensity of the magnetic field of 1.8±0.2 mT. Whereas, sham pulsed ELF-MF stimulation was administrated by the same coil, over the ischemic hemisphere and connected to a device for sham stimulation which is identical to the one used during active stimulation, although without the stimulating effect on the brain.

7.3 Neuroradiological evaluation of the lesions and extraction of the 3D model

The primary outcome of this study is a possible reduction of the infarct growth, as measured from the MRI at the chronic phase and compared with that at the acute phase. Therefore, all the MRI scans were analyzed to identify such potential effect of PEMFs on the brain ischemic tissue. To do so, MRIs were segmented to quantify the volume of the ischemic lesion during the treatment and after 45 days. Acute lesions are segmented from DWI sequences, as they provide an estimation of the ischemic volume that might progress to a permanent demage (Wheeler et al., 2013), whereas chronic lesions are segmented from FLAIR sequences, typically used for follow-up evaluations (Subbanna et al., 2019). Segmentations were performed using the software 3D slicer (NA-MIC, Grant U54 EB005149). This was considered the most suitable to be used among other options such as ITK-Snap `www.itksnap.org` or Intellispace PACS, Philips S.p.A., since it allows to easily import and manipulate MRI DICOM files, and to extract a 3D model from the segmentation labeled maps. According to the procedure defined within the interniship at San Raffaele Hospital, the segmentation was carried out using the automatic tools of thresholding and level tracing, available in the software. From DWIs at baseline, the ischemia is characterized by an high signal level, and it appears hyperintense over the rest of the brain. Therefore, it can be segmented with the thresholding tool, by selecting the minimum and the maximum signal level of the ischemic voxels. The minimum level (Thr_{min}) must be carefully chosen since it affects the resulting ischemic volume. An example is shown in Fig. 7.2. In panel (A) a Thr_{min} =141.24 was chosen, in order to include less bright areas, whereas in panel (B), a higher Thr_{min} was used, that partially excluded them. Both segmentations can be

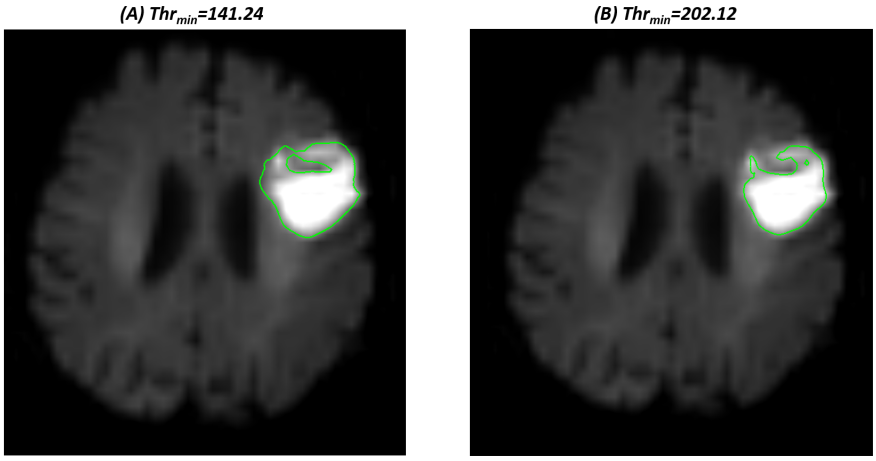

Figure 7.2: Results of segmentation using the thresholding method: comparison between two different values of Thr_{min}.

considered correct, nonetheless the estimated volumes were 28.84 cm^3 and 25.89 cm^3, respectively, meaning that the higher thershold determines an underestimation of the ischemic volume by the 2%. Therefore, in this study we decided to be more conservative by including less birght areas as well.

Differently from the acute lesion, the chronic lesion, as bright as it appears from the FLAIR sequence, is isointense with respect to other head structures, such as the skull, therefore the level tracing was considered a more suitable tool, as it allows to select contours of contiguous voxels characterized by the same signal intensity. All the automatic segmentations were manually refined and, finally, were reviewed by expert neuroradiologists. Since the DWI and the FLAIR sequences were obtained at different time points and with different tilt angle, a registration was necessary to guarantee the correct alignment between the two ischemic volumes. This operation doesn't influence the measure of the ischemic volume, but is crucial to guarantee an optimal relative placement between the pre-treatment (at baseline T_0) and the post-treatment ischemia (at T_{45}). Examples of segmentations from pre- and post-treatment lesions are reported in Fig. 7.3 for two patients, Modena 8 (top panel) and Modena 1 (bottom panel). To segment the acute lesions, threshold were respectively selected as (Thr_{min} =141.24, Thr_{max} =511) and (Thr_{min} =99, Thr_{max} =377.13).

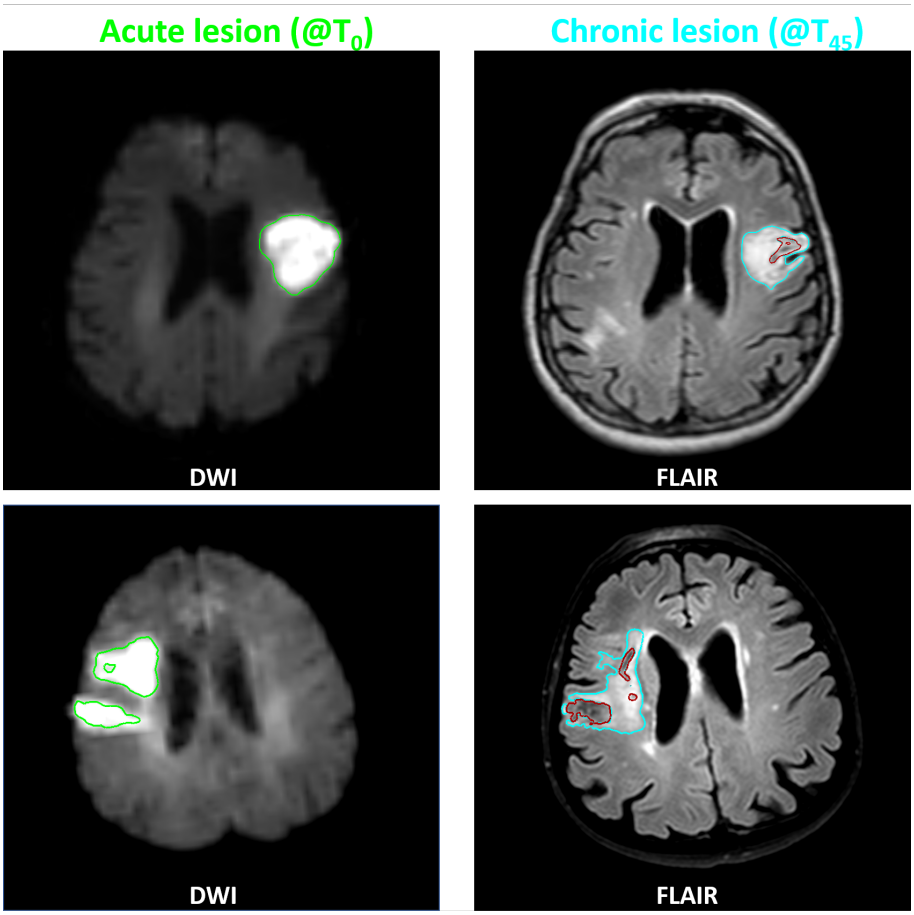

Figure 7.3: Examples of segmentation. Top: Segmentation from an active patient recruited at Nuovo Ospedale Civile S.Agostino Estense, Modena. In red is the segmentation of hypointense areas. Bottom: Segmentation from a placebo patient recruited at Nuovo Ospedale Civile S.Agostino Estense, Modena. In red is the segmentation of hypointense areas.

From the analysis of the FLAIR sequences at T_{45}, it was noted that chronic ischemic lesions could be composed of two separate areas characterized by different MRI signal levels: one area appeared hypointense with respect to the grey and white matter, and one appeared hyperintense. FLAIR hypointense areas can be caused by either an intracranial hemorrhage or by a colliquative necrosis. To have a differential diagnosis between these areas, T_2* sequences were analyzed, since intracranial hemorrhage is characterized by low T_2* levels, whereas colliquative necrosis by high T_2* levels. In those cases where the T_2* sequence was not available, sequence T_1 was considered as an

alternative, since in T_1 the colliquative necrosis appears with lower signal levels than the intracranial hemorrhage. To quantify the severity of the intracranial hemorrhage, a score was used, derived from SITS-MOST (Safe Implementation of Thrombolysis in Stroke-Monitoring Study) classification (see Fig. 7.4):

- 0: Absence of hemorrhage → only presence of hyperintense areas in T_2*;
- 1: Minimal hemorrhage → spots of hypointense areas in T_2*;
- 2: Large hemorrhage → large hypointense areas in T_2*;

Final results from the neuroradiological evaluation are reported in Table 7.1 for all the patients. For each patient that concluded the 45 days follow-up, volume at baseline T_0 and at T_{45} was obtained from the segmentations and the ratio between the two was calculated to quantify the lesion reduction. Volume at T_{45} is considered as the sum of the hyperintense and hypointense volumes, that were segmented separately. Additionally, the intracranial hemorrhage score is reported.
Once that this analysis was completed, the acute and chronic lesion models were obtained for each patient and were placed inside the ViP Glenn model (Gosselin et al., 2014) to perform the dosimetric study. In the following section, solution of the dosimetric problem is reported for two patients (one active, one placebo) that were comparable in terms of volume and cortical location.

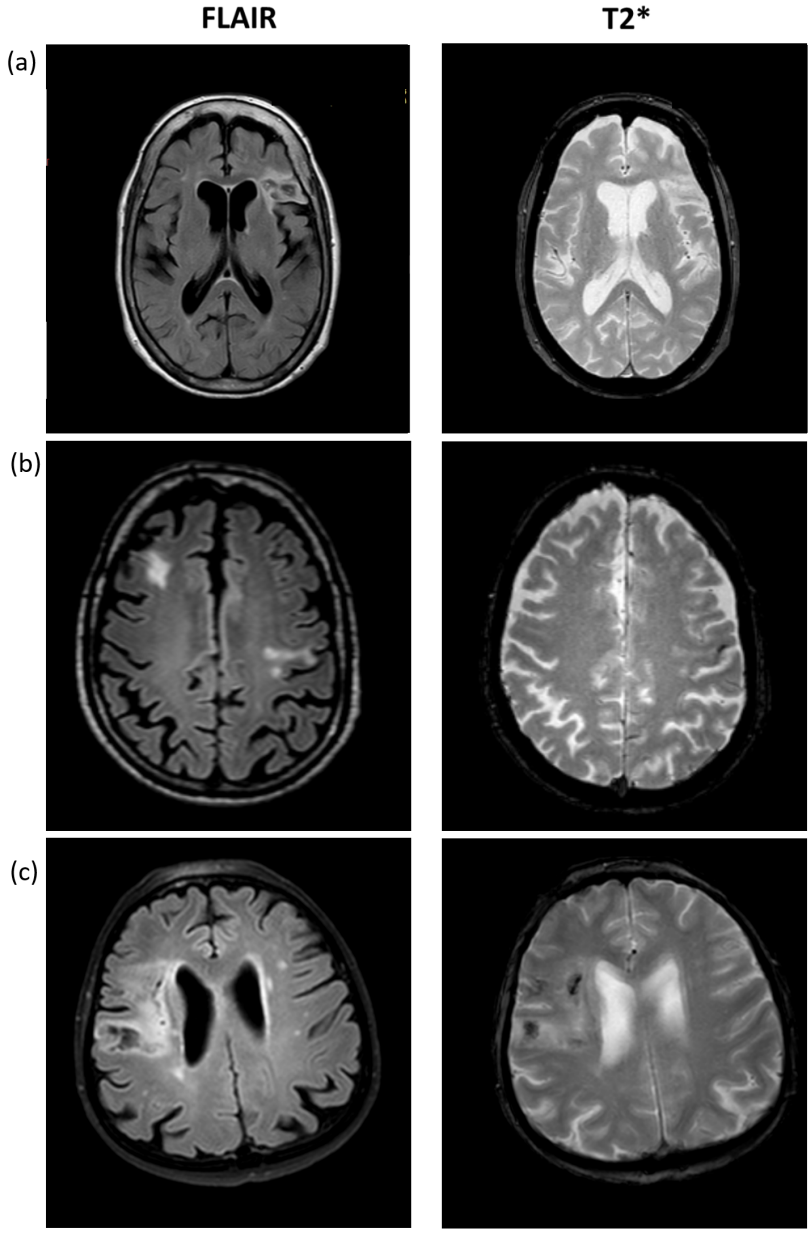

Figure 7.4: Example of intracranial hemorrhage score. (a) Patient with score 0.(b) Patient with score 1.(c) Patient with score 2.

CENTER	PT. CODE	T_0 (Vol. @T_0)	T_{45} (Vol. @ T_{45})	T_{45}/T_0 (%)	Intracranial hemorrhage score
		DWI/ cm^3	FLAIR/ cm^3	%	
MODENA	8	28.84	16.31	56.6	0
CAMPUS	4	23.86	12.88	53.98	*
TORVERGATA	3	23.78	10.86	45.67	No hypointense areas
MILANO	1	15.04	11.52	76.6	0
MILANO	2	13.85	6.77	48.8	2
MODENA	1	12.72	15.59	122.6	2
MODENA	2	11.35	8.05	70.9	1
FERRARA	1	5.23	5.04	96.4	0
CAMPUS	6	4.55	4.11	90.33	0
TORVERGATA	2	4.44	5.19	117	0
MODENA	7	4.11	2.68	65.2	No hypointense areas
MODENA	3	4.11	1.79	43.5	2
FERRARA	4	2.79	1.55	55.5	No hypointense areas
MODENA	4	2.41	2.75	114	1
MODENA	6	2.4	2.66	96.2	0
MODENA	5	1.22	1.19	97.5	0
CAMPUS	1	0.93	0.16	17	0
CAMPUS	2	0.74	0.71	96	0

Table 7.1: Results of the neuroradiological evaluation. (*) Indicates presence of hypointense areas of which it was not possible to determine the entity, due to the absence of T_2* and T_1 sequences.

7.4 Dosimetrical analysis

Dosimetrical analysis was performed using the Magneto-Quasi Static module of the simulation software Sim4Life v.5 (ZMT, Zurich MedTech AG), at 250 Hz (see Appendix 6.6. The model used to perform the EM simulations has been defined as semi-specific, since the 3D model of the ischemic lesion of the patient was placed inside a standard human head model, i.e. Glenn (v.3, ViP (Gosselin et al., 2014)). Glenn is a 84-year-old male whole-body model, and it was chosen as it properly represents the anatomical and morphological characteristics of the elder population. The stimulating coil was modelled as previously done in Chapter 6. Afterwards, it was properly bent in order to follow Glenn's head line and it was placed coaxially with respect to the lesion. Electric properties of the edema (σ = 1.7 S/m) (Kent and Grill, 2014) were assigned to the ischemic lesion while head tissues were automatically assigned through the LF IT'IS

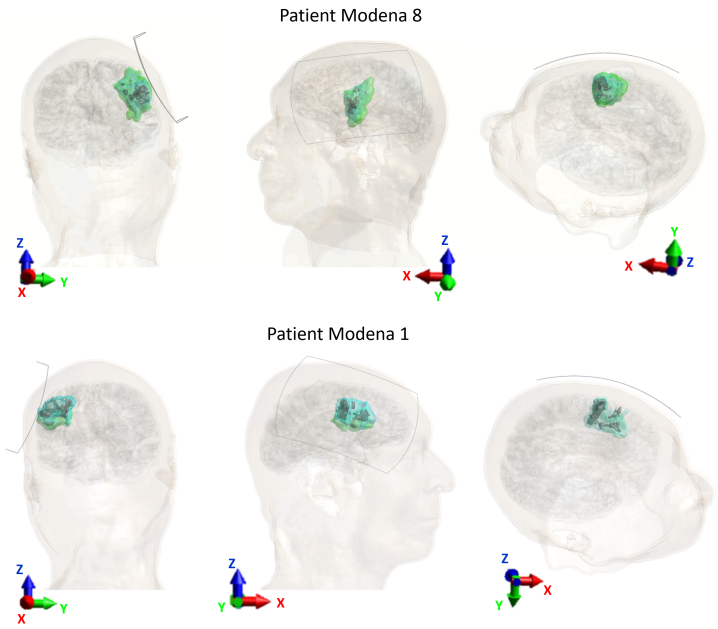

Figure 7.5: Semi-specific model for two recruited patients. Top panel: Active patient Modena 8. Bottom panel: Placebo patient Modena 1. In green and in cyan are the pre- and post-treatment lesions respectively. In grey the chronic ischemic volume affected by a hypointense signal level is reported. The stimulating coil is modeled as a current wire placed over the head.

database (Hasgall et al., 2018).

7.4.1 Assembling the semi-specific model

After registration of the MRI sequences and segmentation of the ischemic lesions, the 3D volumes were exported from 3DSlicer and imported in Sim4Life where they were placed inside Glenn's head. An optimal placement was achieved by reproducing in Glenn the same relative position between the pre-treatment lesion and patient's head landmarks, such as the CSF ventricles or other sulci, and measuring their distance. To finalize the placement, a slice by slice comparison between Glenn's and the patient's head was performed. The semi-specific head model was assembled for the two patients inhere studied and is reported in Fig. 7.5. Following the same color code used in Chapter 6, pre-treatment ischemia is represented in green, whereas post-treatment one is represented in cyan. Additionally, the hypointense areas are modeled separately and colored in grey.

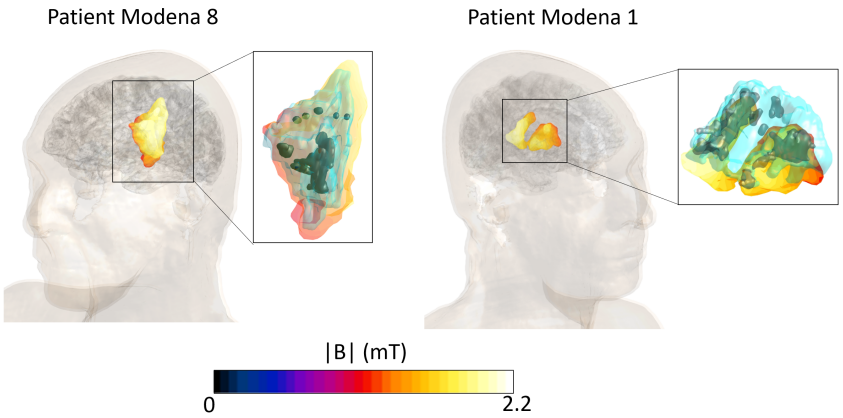

Figure 7.6: B field distribution on the surface of the ischemic lesions that are characterized by a volume above 10 cm^3

7.4.2 Results

Fig. 7.6 shows the B field distribution on the surface of the ischemic volume for the patient exposed to the real stimulation (Modena 8) and the one exposed to sham stimulation (Modena 1). Both patients had cortical lesions characterized by a volume greater than 10 cm^3, therefore, they were both estimated to experience a broad range of B field intensities that spanned from 1 mT to 2 mT. It should be noted that this analysis estimates the B field experienced during the treatment only by the active patient. While it shows the intensities that would have been experienced by the placebo patient in the case of a real exposure, thus comparing the different evolution processes for the two lesions. As expected, in the active patient Modena 8 there is a containment in the lesion growth and a re-absorption in correspondence of intensities above 1.8 mT. Conversely, in the placebo patient, there is no containment in the lesion growth, although hypothetically exposed to the same B field intensities. Moreover, patient Modena 1 is characterized by the presence of a greater hypointense volume for B field intensities over 1.8 mT. With the aim to compare the reduction and relate it to the B field strength, the B-field distributions over planes parallel to the coil was observed for each patient, at different distances, as reported in Fig. 7.7 (Modena 8) and Fig. 7.8 (Modena 1). Superimposed to the distribution are the contour of the pre- and post-treatment lesion, to compare the two sizes. A 0 mm distance corresponds to the closest distance from the coil, at which ischemic lesion is visible.

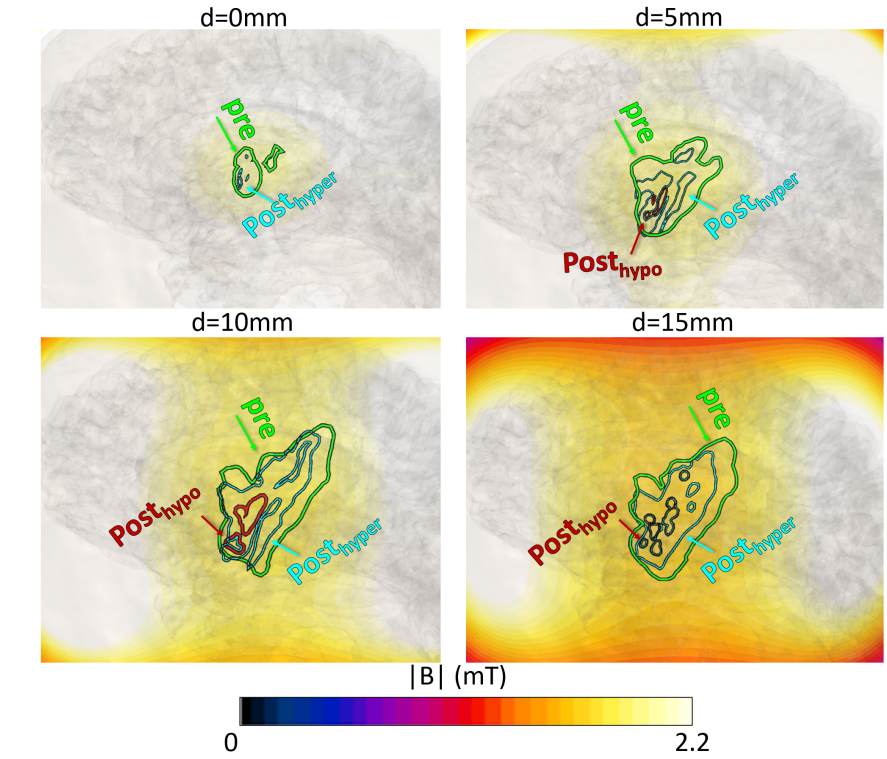

Figure 7.7: Patient Modena 8: B field distribution on planes parallel to the coil and at different distances d. For each distance, contours of slices of ischemia before (pre,in light green) and after (post hyperintense in cyan and post hypointense in red) the treatment are given, in order to compare the dimensions.

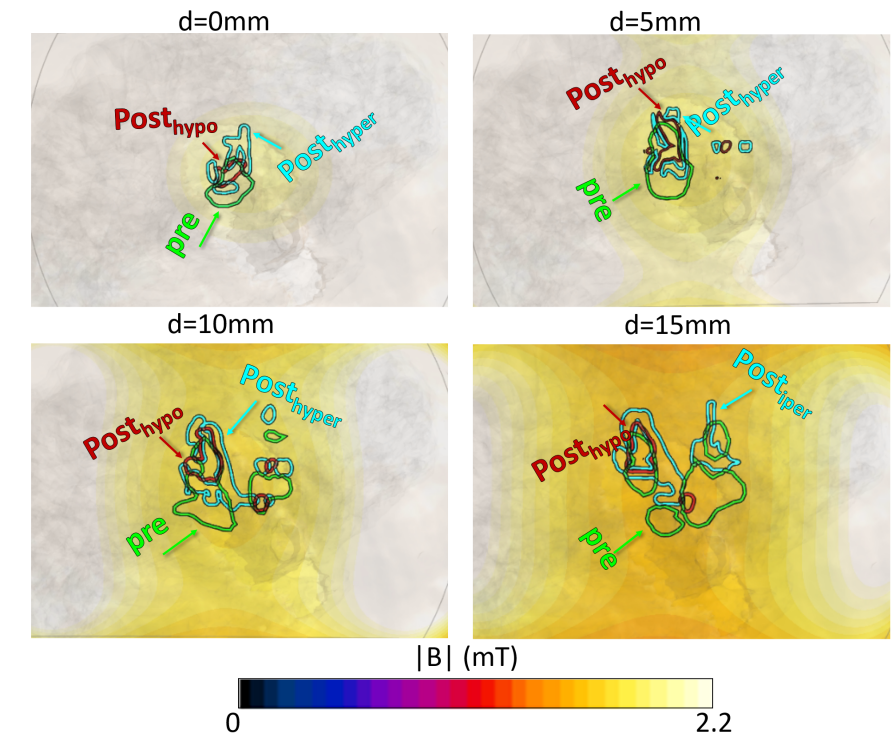

Figure 7.8: Patient Modena 1: B field distribution on planes parallel to the coil and at different distances d. For each distance, contours of slices of ischemia before (pre,in light green) and after (post hyperintense in cyan and post hypointense in red) the treatment are given, in order to compare the dimensions.

	Ranges	**Modena 1** V_{post}/V_{pre}	**Modena 8** V_{post}/V_{pre}
B (mT)	$1 \div 1.3$	1.14	0.48
	$1.3 \div 1.7$	1.07	0.65
	$1.7 \div 2$	1.50	0.46

Table 7.2: Ratio between post-treatment and pre-treatment ischemic volume regions, selected based on the different ranges of exposure they experience.

.

In patient Modena 8 there is a reduction of the ischemic area at all the four distances, where intensities are estimated to be above 1.6 mT. In patient Modena 1, the lesion is located so to be hypothetically exposed to the same field strength as in Modena 8 (see Fig. 7.8), nonetheless post-treatment lesion (considered as the total of hyperintense and hypotense volumes) outgrew the pre-treatment ischemia. Results in Fig. 7.7 and Fig. 7.8 suggest that a stronger reduction can be found in active patients over placebo, supporting the hypothesis of a possible neuroprotective effect of PEMFs. This was confirmed by analyzing the volume reduction per range of B-field exposure intensities (Table. 7.2). For ranges above 1 mT, the patient exposed to the placebo treatment (i.e. Modena 1) did not show any reduction for increasing ranges of exposure, conversely a correlation can be found in the patient that underwent active exposure (i.e. Modena 8), for which a reduction occurred in for all the considered intensities. Finally, all the recruited patients that concluded the study protocol. For each active and placebo patient the corresponding dose response values were extracted employing the methodology assessed in Chapter 6 and described in Section 6.3.4, so to quantify the correlation between the volume reduction and the B-field strength. The box plot representation was chosen to show the ratio between post-treatment and pre-treatment volumes as a function of B intensities for all the simulated patients, including both active (red set) and placebo (blue set) exposure (see Fig. 7.9). This way allowed to account for the variability given the higher number of patients with resepect to those analyzed in Chapter 6. The ratio is expressed as a percentage, so a ratio lower than 100% means that a reduction occurred for that specific intensity, whereas ratios above 100% mean an enlargement of post-treatment lesion. From the two sets

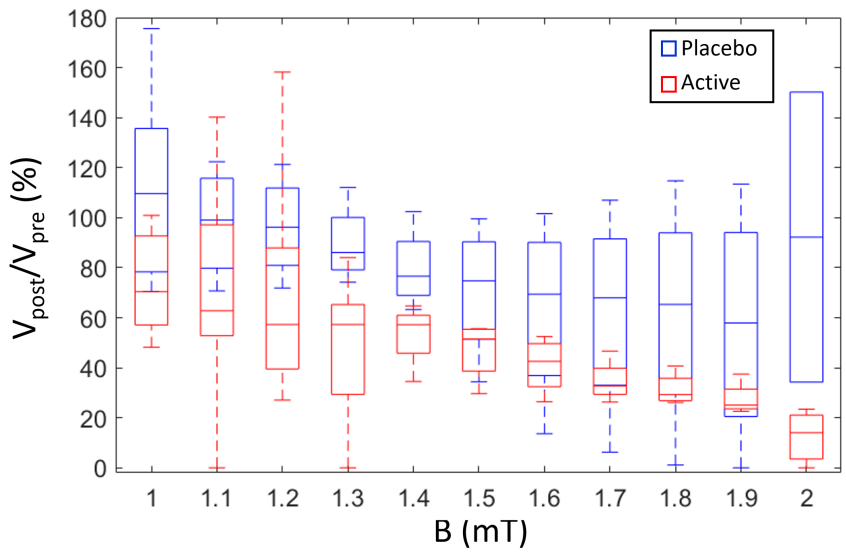

Figure 7.9: Boxplot of the ratio between post-treatment and pre-treatment volumes as a function of B-field intensities, for active (red) and placebo (blue) patients. In the boxplot, top and bottom line of the box are the 1st and 3rd quartile respectively, inside line is the mean value. The vertical lines (or whiskers) show maximum and minimum value of the distribution.

.

of boxplots it can be noticed that the mean reduction for the active patients can be as small as 20% ($V_{post}/V_{pre} = 80\%$) for an exposure to 1 mT and can be higher than 80% ($V_{post}/V_{pre} < 20\%$) for an exposure to 2 mT, and has a descending trend with increasing field strengths. Conversely, the mean reduction in placebo patients for each B-field threshold has always higher values and is above $V_{post}/V_{pre} = 60\%$, meaning it can be as low as 30%, and the descending trend is almost completely lost. Height of the boxplot, together with the extension of the whiskers, represents how data is distributed for each B intensity threshold. Furthermore, comparing active (red) and placebo (blue) patients, it is evident from Fig. 7.9 how, under PEMF exposure, a decrease in the spread occurs with increasing B-field values, as can be seen from 1.4 mT to 2 mT, where the inter-quartile range (IQR) is kept between 17 and 8, while it can be up to 42 for B<1.4 mT. In placebo patients IQR ranges between 115.9 and 21.5, and the maximum IQR is found at 2 mT.

7.5 Conclusions

The work conducted in this chapter was carried out in collaboration with IGEA Clinical Biophysics SpA, that developed the exposure system and patented the pulsed signal. The aim of this ongoing multicentric randomized double blind study is to clarify whether PEMFs are able to elicit a neuroprotective effect and whether they could represent an alternative approach to treat acute ischemic lesions. To pursue this objective, a methodology for a dose-response curve assessment was developed and presented in Chapter 6 and applied in this larger scale clinical study. Prior to the dosimetry, a neuroradiological evaluation was conducted for each recruited patient. FLAIR sequences of the chronic lesion (after 45 days from the treatment) revealed the presence of hypointense areas that were classified as colliquative necrosis or intracranial hemorrhage. Afterwards, the dosimetrical analysis was conducted on all the patients recruited at this stage, including both the real and the placebo exposure, so to investigate, albeit in a small sample of subjects, whether differences could be addressed in the evolution of treated and untreated ischemic lesions. Results showed that the patients that underwent the real PEMFs exposure reported a greater reduction over the sham. Comparison between the trend of the responses to real and sham exposure suggests that PEMFs may exert a neuroprotective effect, that strengthen the endogenous attempt of the injured brain to repair the structural and functional damage (Moretti et al., 2015).

Part III

Computational dosimetry on innovative devices and applications: noninvasive magnetic stimulation with miniaturized coils

Chapter 8

Electric field focality: a limitation in today's coils

8.1 Importance of a focal TMS

As extensively reviewed in Part I, and particularly in Chapters 1 and 4, TMS is used not only in clinics, for the treatment of different neurological disorders and psychological diseases, but also as a neuroinvastigative tool to understand the functional role of specific brain cortical areas, for research as well as for diagnostic purposes. An applied TMS pulse can transiently disrupt the function of the target cortical area by creating a temporary "virtual lesion". Consequently, if a cortical process is contributing to a specific behavior, TMS of the cortical areas involved in it will result in a deteriorated performance of that behavior (Weissman-Fogel and Granovsky, 2019), thus giving fundamental insights between brain areas and the associated task. The virtual lesion approach was firstly applied to the visual cortex, where a functional disruption of the occipital cortex blocked the detection of visual stimuli (Amassian et al., 1987), and nowadays has been generalized to other neurocognitive processes, such as speech and language representation (Krieg et al., 2017; Sakreida et al., 2018) or motor cortical mapping (Cavaleri et al., 2017; Gunduz et al., 2020). In clinical practice, such cortical mapping of language, as well as the systematic exploration of the motor cortical outputs, can be beneficial for the presurgical evaluation of patients in order to characterize eloquent cortex while reducing the need for intraoperative evaluation in patients with brain tumors or epilepsy (Tarapore et al., 2016; Chowdhury et al., 2020). In Chapter 4,

it was highlighted how a precise placement of the coil is extremely important for an accurate cortical mapping. Nonetheless, there is a second critical aspect for TMS employed in this type of application. Despite the great potential, a critical barrier is the limited spatial resolution, which is intrinsic in the technique as it strongly depends on the coil geometry, shape and position over the scalp (Wagner et al., 2009). The coils currently available and used in clinics, have dimensions up to 20 cm, comparable with the size of the human head. Therefore, despite being able to generate a maximum E-field that would be localized in the target spot, the induced field distribution is forced to spread in surrounding regions, that may hold inhibitory or facilitatory connections, thus generating competing nodal effects that may alter the expected stimulation outcome (Wagner et al., 2009).

Another application in which a high stimulation focality is desirable is in the field of animal experiments. Animal TMS models are particularly useful for studying the cellular and molecular effects related to the long-lasting effects determined by a prolonged rTMS stimulation (Funke, 2017) and to understand the molecular mechanisms that underlie the therapeutic effect exerted by TMS on psychological and neurological disorders. For instance, several studies showed that rTMS could be a potential treatment for Parkinson's disease (PD), although is still not possible to conclude its efficacy, due to the mixed results obtained so far (Lefaucheur et al., 2020). Nonetheless, it is well known that PD occurs as a result of degenerating cell death of dopaminergic neurons at the level of nigrostriatal terminals (Lee et al., 2013; Cacace et al., 2017) that causes impairment in the induction of DA-dependent corticostriatal plasticity, such as long-term potentiation or long-term depression (LTD) (Cacace et al., 2017), that are both phenomena on which TMS, exerted in the repetitive form or in theta-burst (TBS), can elicit an effect. Therefore, studies conducted on animal PD models can provide information on physiological adaptations that occur in the parkinsonian striatum following rTMS or TBS stimulation and may help to disclose the real potential of this technique in treating PD (Cacace et al., 2017; Ba et al., 2019). Similarly for rTMS applied on stroke patients, research groups are accumulating evidence of the potential of TMS as a therapeutic tool, due to the ability of modulating cortical excitability, but the precise therapeutic mechanism of action is still unidentified and there is no consensus over a standardized treatment protocol (Boonzaier et al., 2018). Assessment of the effects of TMS on endogenous recovery processes in animal stroke models offers an excellent opportunity for the exploration of neuroplastic and neuromodulatory mechanisms, which

could lead to the optimization of treatment protocols for clinical applications (Boonzaier et al., 2018). Despite the great potentials of animal models, realizing stimulation conditions resembling those supposed to occur in the human brain is not trivial, due to the very different ratio between size of the brain and size of the coil that results in a widespread stimulation of the entire rodent brain (Tang et al., 2017; Funke, 2017; Boonzaier et al., 2020). The use of large human coils in such small targets not only determines the loss of focality but also reduces the efficacy of the stimulation, due to the fact that a smaller head captures a proportionally smaller fraction of the total flux of the magnetic field, according to Faraday's law of induction (Salvador and Miranda, 2009; Tang et al., 2017).
In principle, smaller coils would be the most straightforward solution to increase spatial focality of TMS, however, their development has been limited by technological constraints of conventional coils which use few turns (<30) of wire winding inside an insulation housing. As the dimension of the coil shrinks (diameter <2 cm), larger electric currents are required to induce an effective stimulating field (Vahabzadeh-Hagh et al., 2012), that would produce excessive amount of heat and large magnetic forces that are not tolerated by conventional wires, hence the effort of many research groups to improve TMS focality by developing innovative coils with particular geometries and shielding materials (Kim et al., 2006; Lu et al., 2008; Gomez et al., 2013; Koponen et al., 2015; Tang et al., 2016; Gomez et al., 2018; Liu et al., 2020).

8.2 Solutions to augment TMS focality

To increase TMS focality has been a major goal for many researchers that aimed at improving such a promising non invasive brain stimulation technique. Already in the early 90s, the strong need of a localized stimulation arose, from the observation that single circular coils caused broad areas of the brain to be stimulated simultaneously (Ueno et al., 1988). To overcome this shortcoming, Ueno and co-workers proposed for the first time to employ what is now called the figure-8 coil, meaning a pair of oppositely connected coils, as a way to increase the induced electric field in the target area of the brain (Ueno et al., 1988). From that time on, the figure-8 has been the standard choice for focal TMS, nevertheless, there is a considerable number of studies that proposes new geometries and strategies to further increase TMS spatial focality (Deng et al., 2013). A thorough modeling study was conducted in 2013 by Deng and co-worker to

compare focality among 50 different coils, whether commercially available or proposed in research (Deng et al., 2013). Among the commercial coil, the smallest coil is the Magstim 25mm figure-8 (P/N 1165) (Hovey and Jalinous, 2006), which was developed specifically for animal applications and therefore is not suitable for a more focal stimulation of the human brain. As a matter of fact, an optimal coil design for human applications should take into account not only the focality, but the penetration depth as well, which is unavoidably affected by the reduction in the coil size, as shown in Fig. 8.1 (Deng et al., 2013; Gomez et al., 2018). Conventional figure-8 coils appear

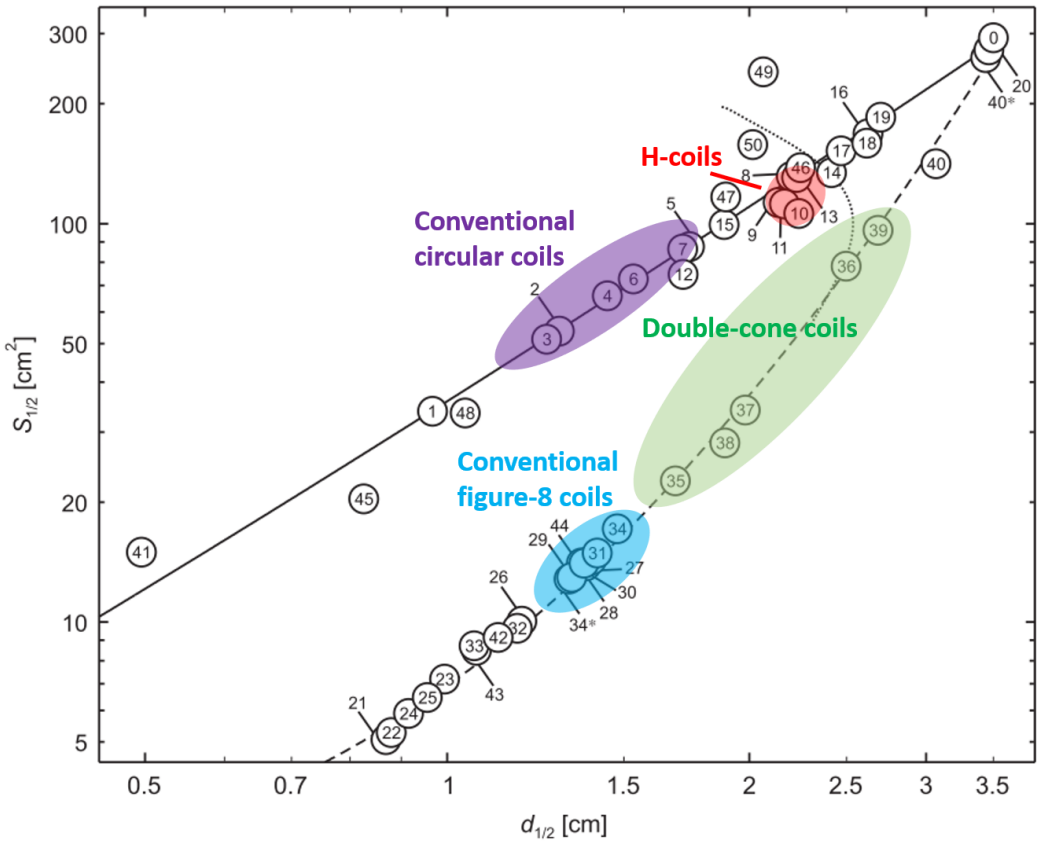

Figure 8.1: Figure taken and adapted from (Deng et al., 2013; Gomez et al., 2018): Optimal trade-off between focality $S_{1/2}$, and depth, $d_{1/2}$ for the 50 coil studied in (Deng et al., 2013), see the reference for identification of the specific coils corresponding to the numbers.

.

to have the best trade-off between penetration depth and focality, which hasn't been overcome yet (Gomez et al., 2018; Koponen and Peterchev, 2020). In Fig 8.1, all the

miniaturized figure-8 coils proposed in literature for human applications are numbered from #21 to #25. Coil #21 is a 3-layer miniaturized ($\approx$ 3 cm) double coil, made up of braided Litz wire, wound in 13 turns (Talebinejad and Musallam, 2010). The multilayer solution allows for an increase in magnetic field intensity while keeping the coil area constant. Other attempts to increase TMS focality were proposed in the late 90s with the slinky coil (Zimmermann and Simpson, 1996; Lin et al., 2000). The slinky coil consisted in a 3D coil composed of 7 butterfly coils each characterized by a different bending angle. The shape of the butterfly coils could be either circular (#23) or rectangular (#24) and maximum dimension was below 8 cm. In 2010, Ai and Li proposed the double-butterfly coil (#22), which consisted in a 8-shaped like planar coil with one external winding of 7 cm and one internal winding of 3.5 cm (Ai et al., 2010). The limitation in such smaller coils is that they require higher feeding currents with consequent larger power losses and overheating with respect to larger coils (Koponen and Peterchev, 2020). Consequently, all the aformentioned coils have been studied numerically but they have never been successfully used for stimulation on humans. An optimization technique was proposed in (Gomez et al., 2018) to computationally design TMS coils that achieve optimal trade-off between E-field focality, depth, and energy (fdTMS coils). Nevertheless, the dimensions of such designed coils can be up to 32×32 cm^2, which are still incompatible with mapping applications. In order to achieve an augmented focality by scaling the coil dimensions, alternative techniques to standard TMS design and manufacturing must be employed. In this sense, novel miniaturized coils are presented in the following chapters, that were manufactured following microtechnology guided approaches. This innovation allows for a significantly smaller coil size with consequent improved spatial resolutions. Furthermore, the smaller size should allow for potential arrays of coils to stimulate concurrently different brain areas, as done during standard invasive electrical brain mapping. The proposed approach moved its basis from the study on implantable sub-millimeter sized coils (μMS) conducted by Bonmassar and co-workers (Bonmassar et al., 2012; Park et al., 2013). These coils consisted in microscopic multilayer inductors that have been tested in vitro, where activation of retinal ganglion cells occurred (Bonmassar et al., 2012), and in vivo, where they showed that (μMS) is able of activating neurons of the inferior colliculus in rodents. Following this results, flex circuit technology was adapted to develop circular miniaturized multilayer coils that can be wrapped around an air or ferromagnetic core in a high number of turns (100 or greater). Such circular coils can

be assembled together in order to form different geometries, as the classic figure-8 coil, and their feeding system is not bond to the standard TMS feeding system, that would require an excessive amount of power. In the following chapters the first generation of miniaturized coils is reported as it was tested on healthy volunteers to demonstrate its ability to elicit peripheral action potentials (Chapter 9). Furthermore a numerical comparison between different geometries was conducted (Chapter 10). This work was conducted in the frame of the NIH Research Project *Micro-TMS technology for ultra-focal brain stimulation*, conducted in collaboration with the Athinoula A. Martinos Center for Biomedical Imaging, Massachussets General Hospital, Boston and the Beth Israel Deaconness Medical Center, Boston.

Chapter 9

A novel micro-technology device for focal noninvasive neural tissue stimulation

9.1 Abstract

Transcranial Magnetic Stimulation (TMS) has been rapidly expanding in both brain research and clinical applications. However, as currently administered, TMS has significant limitations in the focality of the affected cortical target. To overcome this limitation, a novel system for focal noninvasive magnetic stimulation (f-NIMS) was developed, employing miniaturized coils (m-Coils) with hundreds of turns in a 30 mm diameter, and class-D amplifiers. In this chapter is demonstrate for the first time the capacity of this highly focal m-Coil system to activate neural tissue and elicit sensory nerve action potentials (SNAPs) from the radial nerve of healthy volunteers. Numerical simulations extend the experimental findings and reveal a focality of 2.2 cm^2 on the cortex, nearly four times more focal than conventional TMS stimulators. This increased spatial resolution makes f-NIMS with m-Coils suitable for peripheral nervous system applications and will enable much greater precision and accuracy than conventional TMS for transcranial cortical stimulation[1].

[1]Major content of this chapter was used in a manuscript ready for submission to Nature Communications (Colella M., Laher R.M., Press D.Z., McIlduff C.E., Rutkove S.B., Cassarà A.M., Apollonio F., Liberti M., Pascual-Leone A., Bonmassar G., *A novel micro-technology device for focal noninvasive neural tissue stimulation*).

9.2 Introduction

Transcranial magnetic stimulation (TMS) allows for the human cortex's noninvasive stimulation, enabling breakthroughs in both clinical applications (Stultz et al., 2019; Sonmez et al., 2019; Stubbeman et al., 2018; Williams et al., 2018; Moisello et al., 2015; Carmi et al., 2018) and basic neuroscience research (Fox et al., 2014; Baumer et al., 2020; Bestmann et al., 2008). Clinically, several TMS devices have been FDA-cleared for the treatment of medically refractory depression, certain migraine headaches, and obsessive-compulsive disorder, and over 2 million of these treatments have been performed in 10's of thousands patients (Perera et al., 2016). Most insurance companies have established medical coverage policies for TMS therapy, including government-funded agencies such as the VA, Medicare, and Medicaid (in some states) (Reti, 2013). Furthermore, as mentioned in previous chapters, a TMS device has been cleared for noninvasive cortical mapping of motor and language functions, which can guide the planning, improve outcomes, and substantially shorten the duration of neurosurgical procedures (Najib et al., 2011). In the research realm, hundreds of labs around the world have published over 1400 articles per year (Lawson McLean, 2019) over the past decade using this technique applied to the cerebral cortex to cause a brief and controllable disruption of cortical activity in a specific brain region to explore brain-behavior relations and gain fundamental insights into the causal chronometry of a given brain area for a given cognitive or behavioral ability (Cincotta et al., 2006; Cincotta and Ziemann, 2008; Civardi et al., 2009; Martinez et al., 2009; Karl et al., 2001; Wassermann et al., 1999). TMS can be used to study the dynamic interaction and effective connectivity across the hemispheres (Sack et al., 2005) or between cortical brain regions (Koponen et al., 2018; Kujirai et al., 1993; Arai et al., 2011). Such applications have appealing translational relevance as TMS can be applied in animal models, humans across the age-span, and patients with different conditions. Additionally to the applications previously discussed in this thesis, TMS can also be delivered to the peripheral nervous system, where it can be used to stimulate at both the spinal root level and at the peripheral nerve level and may offer diagnostic and therapeutic potential for neuropathic pain (Lefaucheur et al., 2012, 2006; Schwenkreis et al., 2010; Krause et al., 2006), and musculoskeletal impairments (Zschorlich et al., 2019; Beaulieu and Schneider, 2015; Flamand and Schneider, 2014). However, there are critical barriers to further advancement of TMS applications due to the size and limited focality of existing stimulation

coils (Deng et al., 2013; Thielscher and Kammer, 2004). Therefore, it is challenging to know if stimulation of a given cortical region does not also "bleed" into neighboring areas or define the virtual site's specific location of maximal depolarization in central or peripheral applications. These limitations are dramatically increased when attempting TMS studies in non-human primates and rodents, where enhanced focality is critical. Several attempts have been made to increase TMS's spatial resolution by reducing the dimension of the stimulating coil (Salinas et al., 2009; Talebinejad and Musallam, 2010; Tischler et al., 2011). However, attempts were mostly limited by the use of a few turns of conventional wires. Using novel miniaturization techniques (Bonmassar et al., 2012; Park et al., 2013), it was possible to overcome such constraints and to develop a miniaturized multi-layered coil (m-Coil), designed to stimulate with greater focality. A novel system that includes class-D amplifiers was built to feed the m-Coil properly. Modeled after the development of TMS in the mid-1980s (Barker, 1991), the present study aimed to demonstrate the feasibility of stimulating neural tissue noninvasively with the m-Coil and demonstrate the excellent focality even when penetrating a given distance through the skin and other tissues. We stimulated the superficial radial nerve of healthy subjects. We recorded sensory nerve action potentials (SNAPs), comparing the efficacy and focality of standard, peripheral nerve electric stimulation with the m-Coil. The hypothesis is that the new m-Coil system would have similar efficacy as conventional electrical stimulation but without the discomfort associated with it and could induce an electric E-field capable of stimulating the peripheral nerves with greater precision and focality than conventional TMS.

9.3 The m-Coil and the f-NIMS system

Rather than conventional copper wire, a four-layered miniaturized coil (m-Coil) was built adopting adhesive-free copper-clad (26.1 μm) coated polymide film (25.4 μm) technology. We achieved 123 turns in a diameter of 15 mm and 8 mm of height (purple inset of Fig. 9.1). A figure-8 coil geometry, which enables more focal stimulation, was obtained by pairing two single m-Coils side-by-side with the current flowing in the reverse direction of each other, thus obtaining a structure with a maximum dimension of 30 mm, up to 5 times smaller than standard TMS coils, as shown in Fig. 9.1. The current in standard TMS systems is generated by a pulse generator, which is composed of a power source that charges a capacitor connected to a high-power switch that

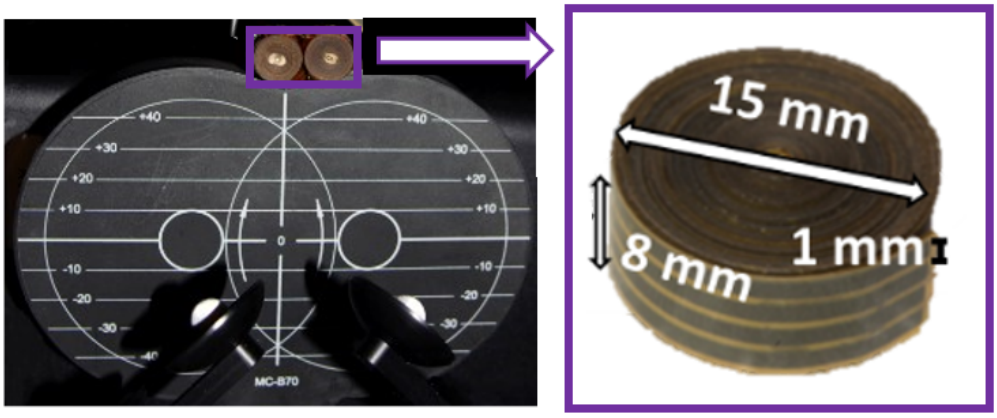

Figure 9.1: Comparison between the m-Coil and a commercial figure-8 coil. Purple inset shows the dimensions of a single m-Coil.

distributes the current to the TMS coil when turned on by a controller.
Such a circuit works well with the currently available commercial coils with inductances that do not exceed 35 μH (Peterchev et al., 2008). However, the m-Coil was designed with each layer having a higher inductance to compensate for the smaller size of the coils (see Section 9.3.1), thus requiring Class-D amplifiers as the feeding source. The architecture of the f-NIMS system is shown in Fig.9.2. The system is composed of a controller (i.e., Microsoft PC running Windows 10), a scope (Tektronix MDO3014) with high voltage active probes (Tektronix THDP0200) and a generator (Tektronix AFG1062), audio amplifiers (Behringer iNUKE 12000), and two digital thermometers (TC01, National Instrument). The system utilizes four high-powered 12kW class-D amplifiers. Each amplifier input is connected to the pulse generator. The outputs are connected to feed the figure-8 m-Coil and to the scope for monitoring purposes. The set of two USB digital thermometers monitored the temperature on the surface of each m-Coil that composes the figure-8, as it is adjacent to the participant's skin during the experiments. Finally, an AIO (all in one) computer running a custom programmed LabView interface (v. 2018, National Instrument Inc.) monitors the amplitude of the voltage feeding the coils and shuts down the power supply to the amplifiers in case of instabilities, for safety purposes.

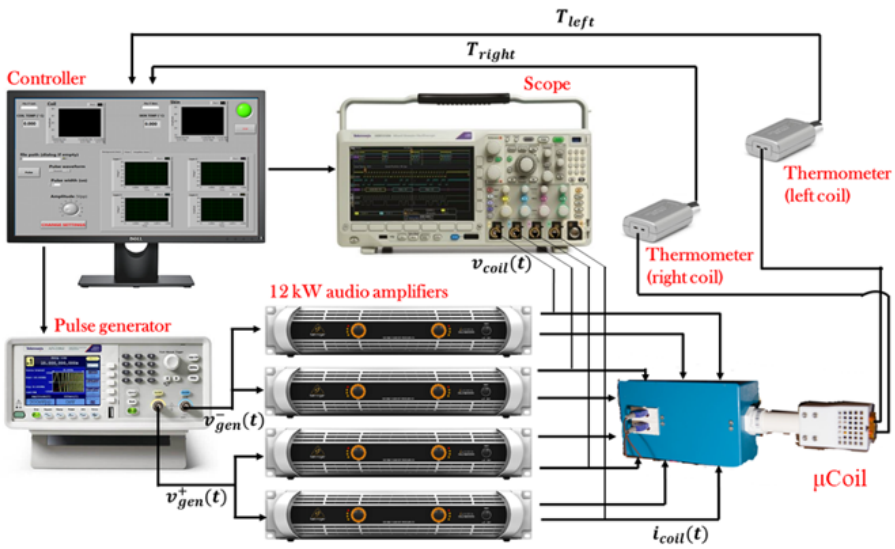

Figure 9.2: Block diagram of the f-NIMS system

Moreover, the Labview interface allows the user to set the amplitude, width, and shape of the voltage pulse from the waveform generator (i.e., from 1 Vpp to 5 Vpp; 200 μs, 400 μs or 600 μs; square or sinusoidal pulse). As previously explained, the manufactured m-Coil has an overall diamater of 30 mm as compared to the 140 mm of a standard figure-8 TMS coil. Such difference required this new approach to feed the coil in order to provide the amount of power necessary to maintain the pulse formation and give flexibility to the system in terms of pulse shape, width, and amplitude. A summary of the differences between the f-NIMS system and the standard TMS system is reported in Table 9.1. All the equipment, including the amplifiers, the pulse generator, the computer-controller, and the routing wire, met the CE standard.

	f-NIMS system	Standard TMS system
Figure-of-8 coil maximum dimension	30 mm	140 mm
Coil circuitry	Flex circuit	Copper wire
Peak of dB/dt at PNS stimulation threshold on the surface of the coil	3.5 kT/s	3.2 kT/s
Temperature limit on the surface at maximum output	50 °C	40 °C
Sound Pressure Level	60dB (peak)	100dB (peak)

Table 9.1: Comparison between the f-NIMS system and a Standard TMS system.

Similar to TMS, one of the issues of concern is the risk of induction of skin burns due to the heating of the coil generated by the Joule effect. The resistance of the m-Coil was designed to be almost 2 Ω to be compatible with the class-D amplifier, which caused the m-Coil to warm up. However, we embedded temperature sensors into the surface of the m-Coil and in contact with the participant's skin during the stimulation session in order to be able to monitor temperature continuously throughout the experiments. As an added safety feature, computer-controlled feedback would switch-off the system whenever the temperature reached the selected safety threshold ($\sim$ 50°C). A second possible concern, again like conventional TMS, is the sound pressure level (Tringali et al., 2012). The interaction of currents passing through the four layers of the m-Coil and their resultant high magnetic fields generate radially inward and outward Lorentz forces, which generate a clicking sound, as the compressional waves in all radial directions along the cylindrical cross-section reach the surrounding air (Rossi and Besnerais, 2015). We have measured the noise from the m-Coil and found that the intensity was no louder than a verbal conversation (around 60 dB). Such a low sound pressure level (SPL) intensity of the m-Coil poses less than minimal risk to participants for either tinnitus or hearing loss. By comparison, standard TMS coils can cause pulses at a high SPL intensity (up to 110 dB), and participants have to wear earplugs to protect their hearing46. Even when wearing earplugs, a few cases of

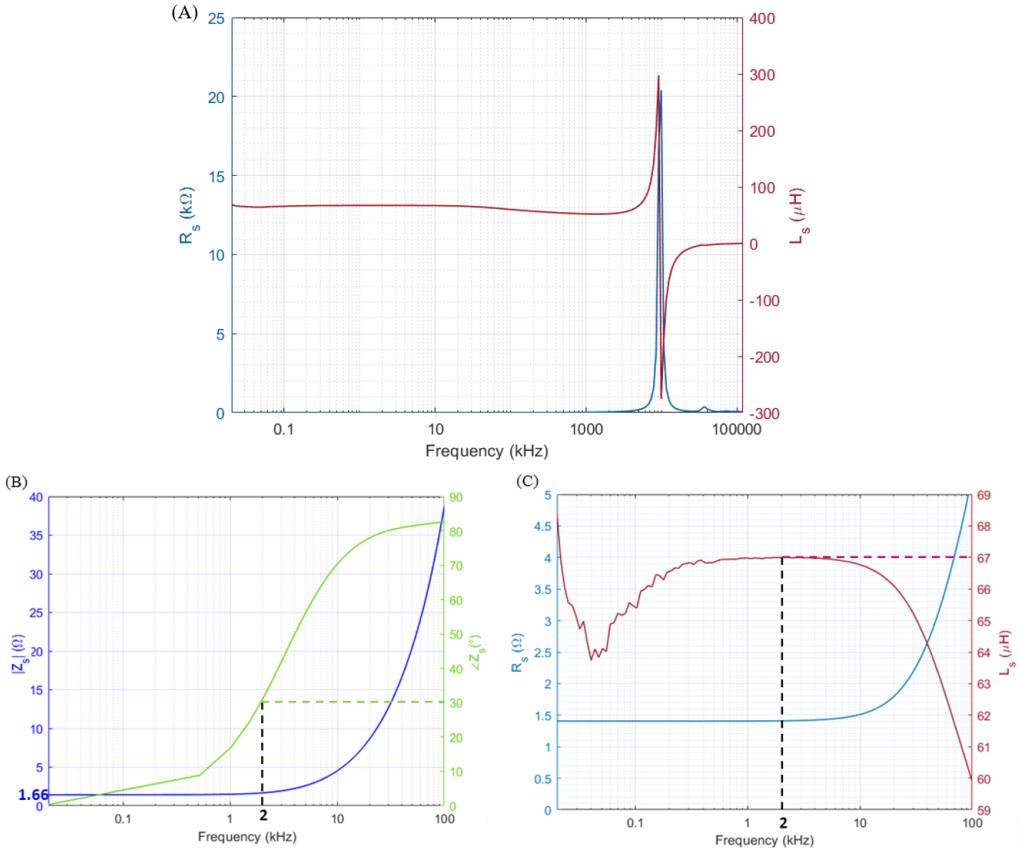

Figure 9.3: Electrical characterization. (A) Frequency response of the m-Coil on the range from 20 Hz to 120 MHz. (B) Magnitude and phase of the impedance Zs and (C) Series resistance Rs and inductance Ls in the frequency range 20 Hz – 100 kHz.

hearing alterations have been reported after audiometric studies following exposure to TMS noise (Tringali et al., 2012).

9.3.1 Electrical characterization of the m-Coil

The resistance (R) and inductance (L) measurements of the m-Coil were performed with the Keysight Impedance Analyzer E4990A. Characterization was obtained in the frequency range 20 Hz – 120 MHz showing resonance at 9 MHz, as reported in Fig. 9.3 A. Fig. 9.3 B shows m-Coil impedance Z in the frequency range of 20 Hz – 100 kHz. Module ($\|Z\|$) and phase ($\phi(Z)$) match those of a nonideal inductor, characterized by an RL series circuit. In the frequency range in which m-Coil was tested for application (2

kHz), the series resistance (R_s) is 1.4 Ω and inductance is 67 μH (Fig. 9.3 C).

9.3.2 Set-up of the m-Coil maximum output parameters

To set the proper amplitude and duration of the voltage pulse for the experiments, the activating electric field, dB/dt (T/s), generated by the m-Coil was calibrated to match the one generated by the MagStim figure-8 coil, powered by the MagStim Super Rapid2 at the PNS motor threshold, that was measured equal to 3.2 kT/s. By feeding the m-Coil at the maximum power available from the f-NIMS system, it was possible to obtain a dB/dt peak value of 3.5 kT/s. All dB/dt measurements were conducted using the BNC-type MagProbe from Magventure Inc. Voltage and current pulse sent to the m-Coil during the experiments are shown in Fig. 9.4 A and B. The voltage pulse was measured using the TDHP0200 differential high voltage probe from Tektronix, Inc. and reached a peak of 150 V, while the current had a value of 70 A. The current pulse was measured using the Allegro Microsystems Hall-effect current sensor (ACS772 200B series, Allegro Microsystems, Inc.).

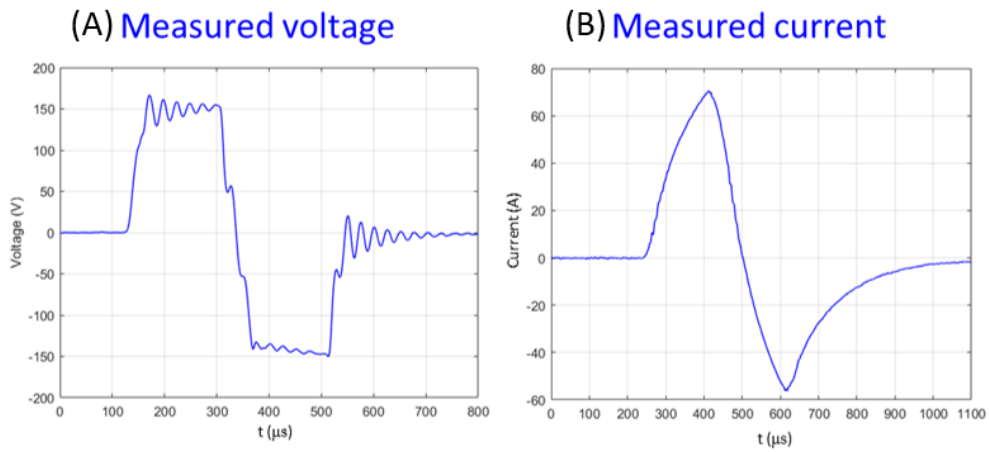

Figure 9.4: Output of the f-NIMS system measured from the positive channel (v+) at experimental conditions: (A)Voltage pulse, (B)Current pulse.

9.4 Stimulation experiments with the f-NIMS system

Experiments were conducted at the Berenson Allen Center of Beth Israel Deaconess Medical Center in Boston. Eleven subjects were recruited to assess the safety and efficacy of the m-Coil. All recruited subjects were healthy volunteers of age between 18 and 50 years old. The experimental sessions consisted of an initial nerve conduction velocity (NCV) test, with electrical stimulation comparable to clinical electromyography (EMG) studies, to assess nerve function and identify the location of the radial nerve (Fig. 9.5 A). Two surface recording electrodes were placed over the snuffbox and the thumb, and a surface reference electrode was placed on the distal thumb. SNAPs were obtained using standard technique and supramaximal stimulation intensity. A note was also made of the "threshold" stimulation intensity at which the SNAP first became apparent. Following the electrical stimulation, the m-Coil stimulation was then applied to the same site (Fig. 9.5 B and C).

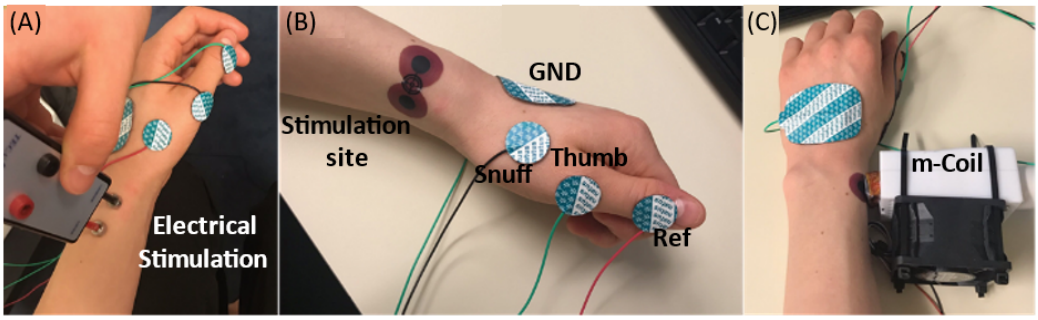

Figure 9.5: Recorded sensory nerve action potentials (SNAPs): (A) Position of stimulating electrodes to detect the radial nerve. (B-C) Position of the m-Coil and recording electrodes during the stimulation

SNAPs were recorded using EMG surface electrodes placed at 5.5 cm (snuffbox area) and 7.5 cm (thumb) from the stimulation location (Fig. 9.5 B). This allowed for characterizing and comparing the evoked responses and the conduction velocities between the two techniques. Fig. 9.6 A and B shows the recorded responses after electric and m-Coil stimulation in the two stimulation positions, snuff box and thumb. Latencies were computed as differential measurements between the snuff box and thumb as the exact location of depolarization was unknown. Nevertheless, with both techniques, Δ_t was approximately 0.35 ms, and Δ_s was 2 cm (Kon et al., 2017), giving approximately equal conduction velocities of 57 m/s. Furthermore, the responses to

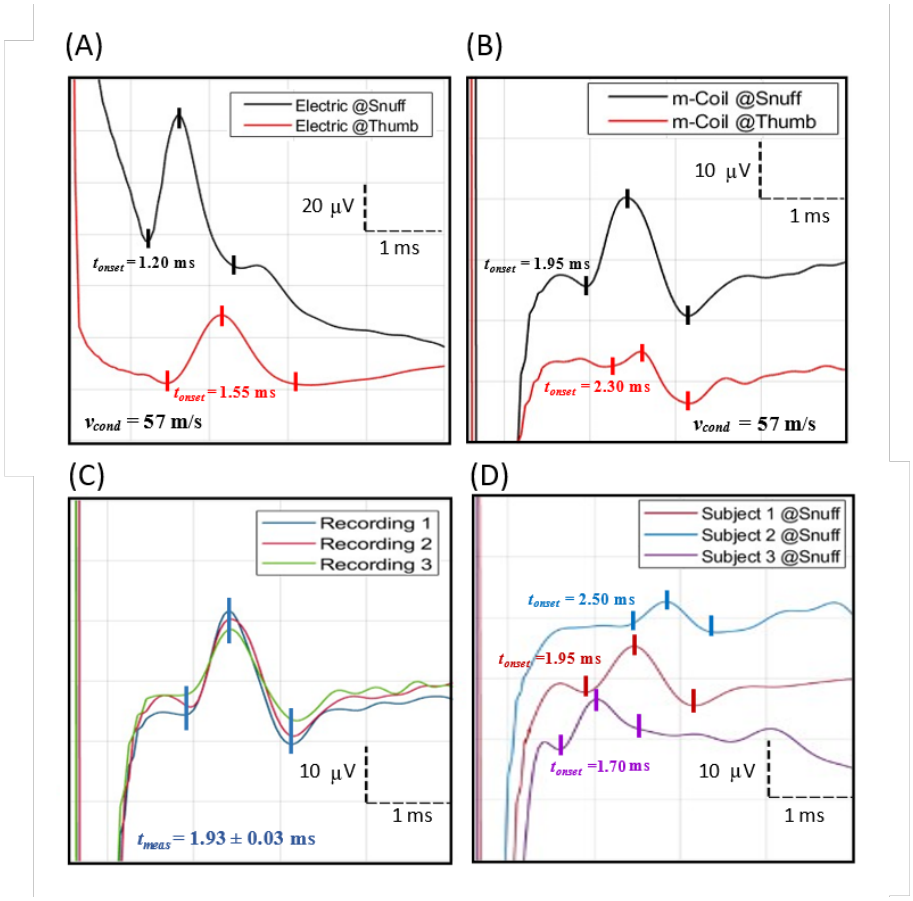

Figure 9.6: Recorded sensory nerve action potentials (SNAPs): (A)-(B) Electric stimulation and m-Coil stimulation on the same subject: recording from snuff (black trace) and from the thumb (red trace). (C) m-Coil stimulation: different recordings from the snuff of the same subject. (D) m-Coil stimulation: recording from the Snuff of different subjects.

different pulses delivered at the same location to a given subject were stable in terms of amplitude and onset time, as shown in Fig. 9.6 C, while variability was seen among subjects (Fig. 9.6 D). All the SNAPs were recorded using the Synergy software and were processed using a custom code written in MATLAB (MathWorks, Inc.) that implemented a low pass IIR filter with order 12 and 3dB at a frequency of 30 kHz. All participants tolerated the f-NIMS sessions without any adverse effects. Specifically, no subjects reported any skin redness, discomfort, hearing changes, or perceived tinnitus after inquiry.

9.5 Electromagnetic modeling of the m-Coil and neuronal dynamics simulations

Each of the four copper traces that compose the m-Coil was modeled inside the EM simulation software Sim4Life v5.0 (ZMT Zurich Medtech AG, Zurich, Switzerland) as a planar loop coil of 123 turns, with an inner radius of 0.35 mm, corresponding to the radius of the copper pin, and an outer radius of 7.5 mm. Each loop was placed in the middle of the corresponding trace, and the space between two consecutive loops was designated to be 1.5 mm. The overall height of the m-Coil model was 4.5 mm. The geometry modeled very closely the figure-8 m-Coil that was built and tested. EM simulations were computed using the Low Frequency (LF) Magneto-Quasi static solver in Sim4Life. This solver implemented the quasi-static approximation, i.e., $\omega^2 \mu \epsilon d^2 \ll 1$, where d is the maximum dimension of the object, ω is the maximum angular frequency, and μ and ϵ are, respectively, the magnetic permeability and electric permittivity of each object in the simulation domain. The description of the theory behind the solver and the equation solved can be found in Section 2.2, Chapter 2 (Eqq. 2.4,2.5, 2.6).

9.5.1 EM Exposure Comparison with a standard TMS coil

The FEM simulations were performed on the figure-8 m-Coil model described above and on the validated model of the commercial figure-8 coil (MAG-9925, PN9925-00, Magstim Inc., Prairie, MN), which will be herein called the TMS coil, for simplicity. This model has been used in this thesis to perform the studies reported in Chapters 3 and 4. At first, each coil was simulated on top of a rectangular slab of dielectric material (i.e., muscle), and over the anatomical head model MIDA (Iacono et al., 2015), in correspondence to the hand area of the motor cortex. EM properties assigned to each tissue were taken from the LF IT'IS database embedded in Sim4Life (Hasgall et al., 2018). In both cases, the two coils' geometrical centers coincided, thus ensuring exposure of the same area. A 1.9 kHz sinusoidal excitation was chosen as a good approximation of the biphasic pulse sent by the novel system (Fig. 9.4 C). The m-Coil and the TMS coil were fed with an amplitude of 70 A and 660 A, respectively, corresponding to the maximum output of the novel feeding system (Fig. 9.4 C), and the output of the TMS system at the median nerve motor threshold (i.e., 15% of maximum output). In both the coil models, the direction of the current flow was chosen to ensure

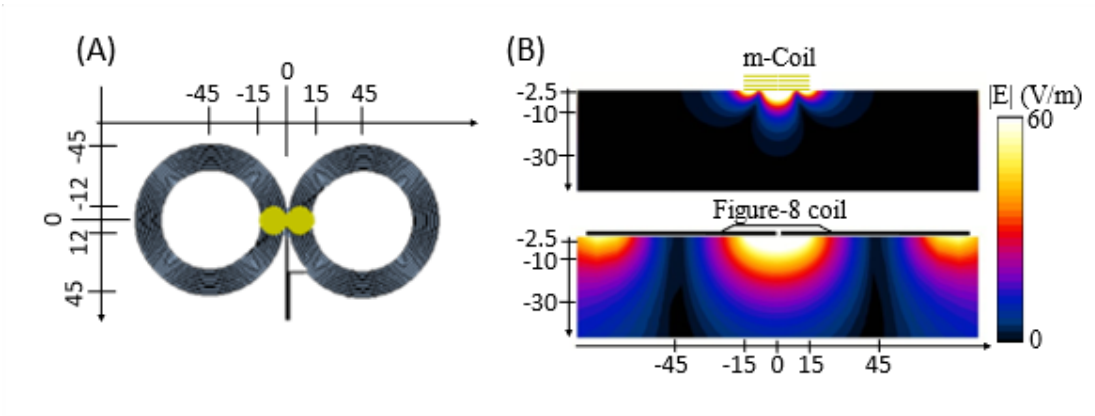

Figure 9.7: Numerical comparison between the m-Coil and the standard Figure-8 TMS coil. (A).The m-coil model and MagStim figure-8 (PN9925-00) model. (B) Electric field intensity distribution generated by the m-Coil at 1.9 kHz (top) and by the figure-8 coil at 3 kHz (bottom) on a slab of dielectric material (σ=0.3 S/m).

that the currents flowing in the two lobes of the figure-8 coil would sum up at the center. Fig. 9.7 B shows a comparison between the E-field intensity distributions induced by the m-Coil and the TMS coil on a rectangular slab of dielectric material ($\sigma = 0.3$ S/m), while comparison on the cortex of the anatomical human head model MIDA (Iacono et al., 2015) is reported in Fig. 9.8. The E-field distribution induced by both type of coils presented a "Mexican hat" shape with one global maximum in the center and two local maxima corresponding to the two outer rims of the coil (Fig. 9.7 B). Nevertheless, the distance between the two local maxima is approximately 3 cm for the m-Coil, and 18 cm for the MagStim TMS coil. This different aspect ratio suggested a different focality between the two coils. Thus, focality evaluation was conducted when modeling exposure of the cortex and found to be 4-times smaller in the m-Coil.

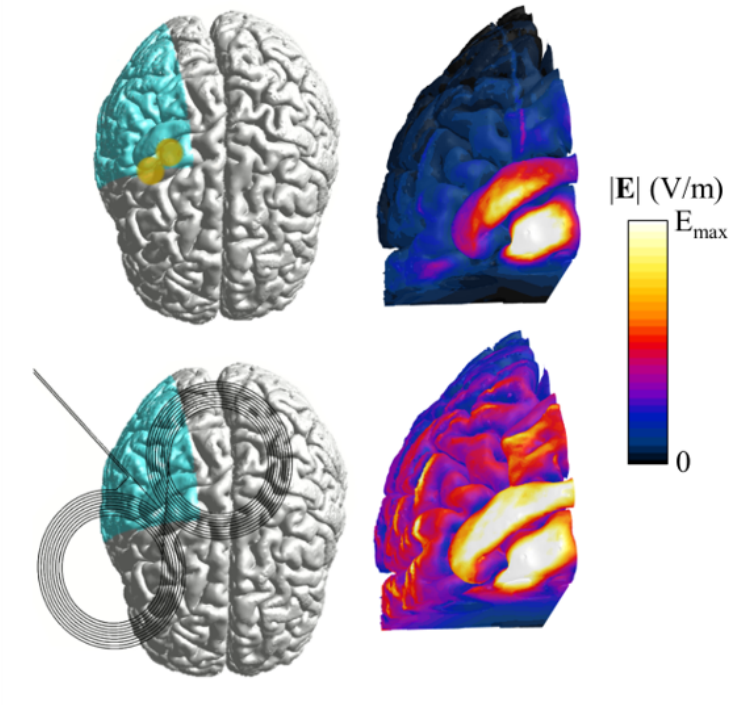

Figure 9.8: Electric field intensity distribution generated by the m-Coil (top) and by the figure-8 coil (bottom) in the section of cortex highlighted in cyan.

The focality was defined as the half spread value, as in (Deng et al., 2013) $S_{1/2} = V_{1/2}/d_{1/2}$, where $V_{1/2}$ is the half value volume, meaning the volume exposed to an electric field equal to or greater than $E_{max}/2$, and $d_{1/2}$ is the half-value depth, meaning the distance from the surface to the deepest point where the electric field strength is half of E_{max}. According to (Deng et al., 2013), the MagStim coil has a focality, computed on a sphere of approximately 15 cm^2 and a half value depth of approximately 1.5 cm. The TMS coil model herein used, applied to a realistic model of the human cortex, matches such results well with a $d_{1/2}$ = 1.74 mm, while $S_{1/2}$ was equal to 8.5 cm^2. Results on the cortex were normalized with respect to the maximum E-field induced by each coil. With this level of focality, the m-Coil would allow exposure of defined, single cortical areas, as shown in Fig. 9.8, once fed with power high enough to induce an E-field intensity above the stimulation threshold of the cortex (i.e., 70 V/m – 100 V/m).

9.5.2 Numerical modeling of peripheral nerves stimulation experiments: Methods

To numerically reproduce experiments conducted on healthy subjects, the m-Coil model was placed over the wrist of the anatomical, neurofunctionalized body model Yoon-Sun (Gosselin et al., 2014) in correspondence of the superficial branch of the radial nerve, as it was performed during experiments (Fig. 9.9). As the magneto-quasi-static simulations are executed in the frequency domain, to reproduce the experimental stimulation sessions, the numerical m-Coil was fed with a 70 A sinusoidal current at 1.9 kHz, corresponding to the measured amplitude and frequency of the real short current pulse delivered to the m-Coil during the experiments (Fig. 9.4).
In a multiphysics approach, the predicted E-field distributions were fed into the NEURON solver version embedded in Sim4Life (Carnevale and Hines, 2006), as the source of the electric stimulation to study the neuroelectric response of the nerves to the applied stimulation. The Yoon-Sun anatomical model includes nerve trajectories that were used in this work to model electrophysiological axon fibers and to create a homogeneous nerve tissue around the trajectory. The fibers' excitable behavior was simulated using a neuronal model based on the McIntyre-Richardson-Grill (MRG) model (McIntyre et al., 2002; McIntyre and Grill, 2002) with parameters that characterized the sensory fibers (Gaines et al., 2018).

Figure 9.9: Modeling the experiments: position of the m-Coil over the wrist of one subject (left). Position of the m-Coil model over the wrist of the neurofunctionalized model Yoon-Sun, position of the stimulation area and recording site are shown as well.

This model represents the axon as a double cable. Such representation allowed separating electrical representations for the myelin and underlying internodal axolemma. Sim4life also allows the execution of a titration analysis, which permits the quantification of the nerve stimulation threshold by stimulating the fibers with increasing and decreasing current intensities in the coil following a bisection search scheme. A threshold is identified as the minimal current intensity that initiates an action potential (AP) in the fiber with 1% error. As well, an AP is identified as a variation in transmembrane potential of 80 mV with respect to the fiber resting potential. Neuronal simulations were conducted using sinusoids at two different frequencies, corresponding to the two pulse widths investigated during the experimental sessions, i.e., 400 μs and 600 μs.

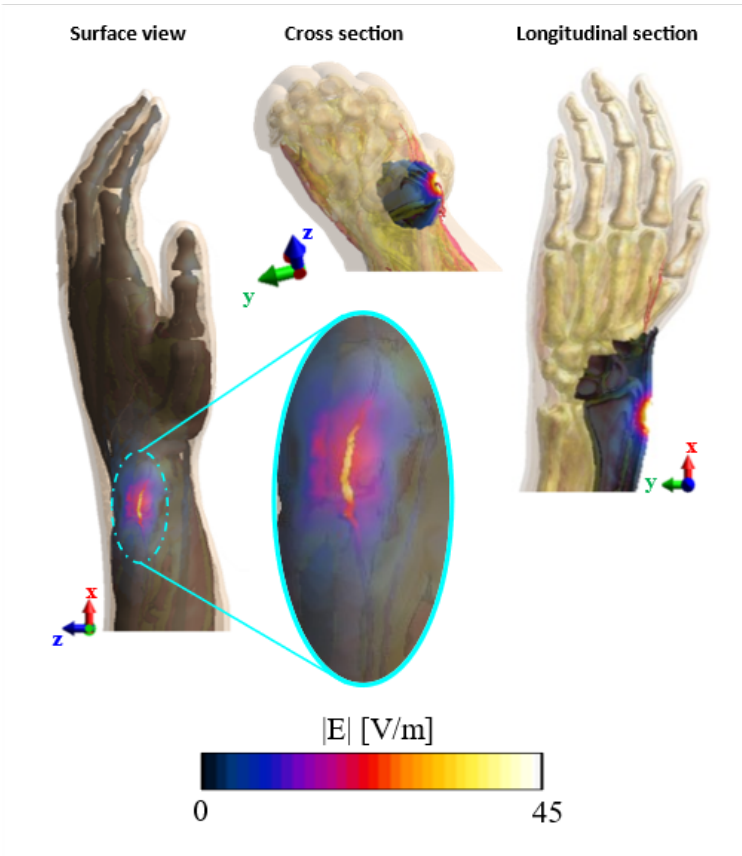

Figure 9.10: Distribution of $|E|$. Left: $|E|$ on the surface of nerve and muscles (cyan inset shows detail below the coil). Center and Right: $|E|$ on two cross-sectional planes of the arm - sagittal (Right) and transversal (Center) - that pass through the center of the m-Coil.

9.5.3 Numerical modeling of peripheral nerves stimulation experiments: Results

The resulting E-field distribution induced by the m-Coil remained confined in a small area and reached a maximum intensity of 39 V/m in the nerve (Fig. 9.10 and Fig. 9.11, blue panel, top). The longitudinal and transversal distributions along the whole arm are shown in Fig. 9.10. By coupling the EM results obtained on the human arm model with the neuronal dynamic analysis, we were able to elicit action potentials numerically, therefore confirming the microscopic electrophysiologic and anatomical origin of the measured SNAPs. The fibers' excitable behavior was simulated using a modified version of the McIntyre-Richardson-Grill model (McIntyre et al., 2002; McIntyre and Grill, 2002) developed for sensory nerve fibers (Gaines et al., 2018). The fibers were modelled as immersed in a homogeneous nerve model, with conductivity 0.030 S/m ensuring a surrounding homogeneous electrical environment.

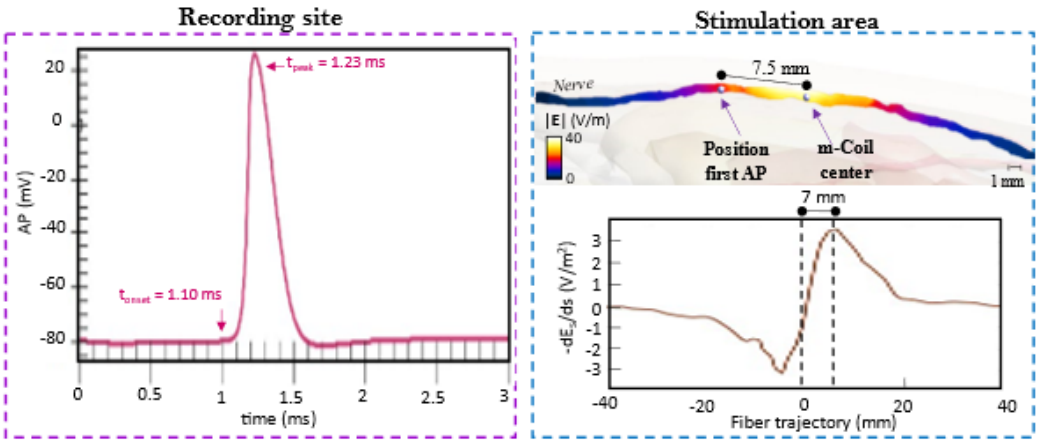

Figure 9.11: Lilac sub panel shows the action potential computed for the suprathreshold stimulation at the recording site. Blue sub-panel panel shows (Top) distribution of $\mid E \mid$ on the surface of the nerve. Two spheres represent the center of the coil and the position of the first action potential (AP), as computed from neuron. Distance between the two is 7.5 mm. (Bottom) Activating function (AF) along the nerve fiber. Distance between center of the coil and position of first AP, as estimated by the activating function is 7 mm.

A titration analysis was conducted to estimate the minimum current required to elicit the stimulation. Results estimated that, for shorter pulses (i.e. 400 μs), by applying a current of 70 A we were working at threshold level, whereas a suprathreshold stimulation was estimated for longer pulses (i.e. 600 μs). Hence, the simulations revealed that the E-field induced by the m-Coil driven at 70 A can elicit fibers' action potentials (Fig. 9.11, lilac panel), therefore confirming the ability to generate SNAPs at the level of the snuff box, as experimentally shown (Fig. 9.6).

9.6 Discussions and conclusions

Despite the growing adoption and great potential of TMS, a significant limitation of commercially available coils is their size and lack of focality. Several studies of coil designs have attempted to improve focality, most of which make use of optimization algorithms to guarantee a compromise between focality and energy efficiency without reducing the coil size (Gomez et al., 2018; Ren et al., 1995; Hsu and Durand, 2001; Kim et al., 2006). The present study shows how changing the coil manufacturing approach can reduce coil size and enhance focality while achieving noninvasive neural tissue stimulation. This is the first time that such a result has been obtained with a miniaturized coil applied to humans to the best of our knowledge. To demonstrate the efficacy of the f-NIMS system, we focused on the stimulation of peripheral nerves, adopting the same approach as employed in the original development of TMS with conventional, larger coils. The mechanisms of action for the noninvasive magnetic stimulation of peripheral nerves are similar to those of transcutaneous electrical nerve stimulation. Both are based on the nonlinear Hodgkin-Huxley response to the induced E-field (Roth and Basser, 1990), described by the nerve fiber cable model. Our stimulation experiments reveal very similar SNAPs shapes (Olney et al., 1990; Bischoff et al., 1995) and amplitudes changes in the electric and magnetic stimulation conditions. However, f-NIMS amplitudes were up to 10 times smaller, indicating that fewer fibers were excited at the maximum of the induced electric field derivative with the m-Coil (Ravnborg et al., 1990). Reassuringly, the relative latencies recorded at two different locations (snuffbox and thumb) yielded similar velocities. Focality has always been the most significant challenge and hope for magnetic neurostimulation(Gomez et al., 2018). However, efforts have been limited by conventional technology constraints, and nearly all the coils with diameters of less than 20 mm were designed for either invasive (Tischler et al., 2011)

or small animal applications (Salinas et al., 2009). Moving from the (μMS) experience in (Bonmassar et al., 2012; Park et al., 2013), a miniaturized coil (m-Coil) was developed with an intrinsic high focality, capable of eliciting a response from neural tissue as shown in human neurophysiologic experiments and characterized by careful simulations. The new f-NIMS system will allow for many experimental designs currently not possible with standard TMS, including safe and more precise brain cortical mapping and detailed characterization of cortico-cortical interactions and effective connectivity.

9.7 Appendix

9.7.1 Experimental validation

In order to verify that the developed m-Coil model was a good representation of the real device, an initial validation with experimental measurements was conducted. The integrated AAK001-14E monoaxial B-field analog sensor from NVE Corporation was used to measure one single component of the B-field. Such sensor is mounted on a printed board and is characterized by dimensions of 1.1 mm $\times$ 1.1 mm. Furthermore, it is able to precisely sense fields up to 400 mT with a highly linear behavior up to 250 mT. In order to stay in the linear range of the sensor, measurements were conducted at 20 A, which corresponds to the 30% of the f-NIMS maximum output. For this purpose, B_z component, which is orthogonal to the coil plane, was chosen for comparison, as it is the main component below the coil surface, as can be seen from Fig. 10.2 c, Chapter 10.

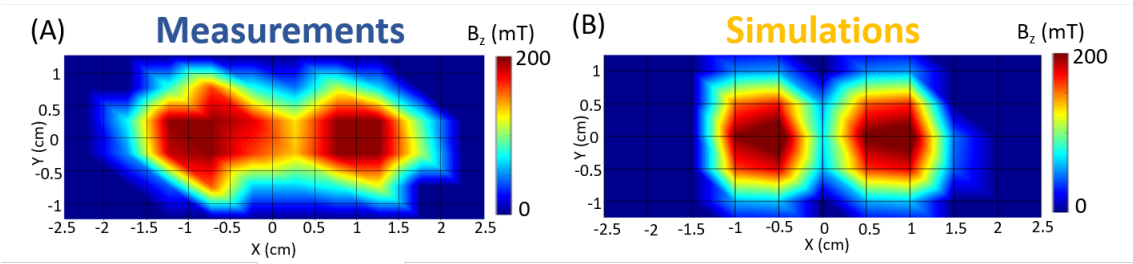

Figure 9.12: (A) Z-component of the B field (B_z) generated by the physical m-Coil when fed at 20 A (left) and position of the m-Coil during the experiments. (B) Simulated Z-component of the B-field (B_z) generated by the m-Coil model fed at 20 A (right).

The sensor was placed on a rigid support that was shifted transversally along the X and the Y directions by a 5 mm spatial step, and scanned an area of 5 cm × 2.5 cm. In order to compare the model and the measurements, simulations results were computed at 20 A and were downsampled to the same 5 mm spatial step considered during the measurements. Both the numerical and the experimental data were post-processed in MATLAB (MathWorks, Inc.). Results of this initial validation are reported in Fig. 9.12. Measurements and simulations showed a good agreement in terms of both distribution and intensity, with a differences of 0.5% below the center of the coil. The measured distribution appeared to enlarge at the left extremity of the domain, while the simulated distribution is confined inside 1.5 cm. This is likely due to signs of wear caused by the montage or the heating.

9.7.2 Numerical variability study

Given the high experimental outcome variations from subject to subject, a variability study on the numerical model was conducted to determine how the stimulation threshold was influenced by the relative position between coil and nerve and by the arm model's anatomy. The coil was moved by ± 5 mm along the longitudinal direction and ± 5 mm along the transversal direction. Additionally, the coil was moved 2.5 mm away from the arm, as well as tilted by 5° around the wrist (Fig. 9.13, left panel). To evaluate the effect of the coil misplacement, for each fiber simulated in the neurofunctionalized model, the maximum variation Δ_{max} between Δ_- and Δ_+ was evaluated. $\Delta_\pm$ was computed as in Eq. 9.1:

$$\Delta_\pm = \frac{Th_{ref} - Th_{var\pm}}{Th_{ref}} \times 100 \tag{9.1}$$

where Th_{ref} represents the reference stimulation threshold value, and $Th_{var\pm}$ represents the threshold computed after positive or negative variation from the reference position. Results of this analysis are reported as box plots in Fig. 9.13, right panel, to account for a statistics over all the fibers included in the model. A longitudinal shift along the nerve direction or a lift from the surface of the wrist would cause variations below 30%, similar to tilting the coil. Conversely, a transversal shifting would cause an increase in stimulation threshold by 160 %. This is expected since such shifting would cause the nerve fibers to exit the coil focus. Thus, the modeling confirmed the experience with the participants that adjustment of the coil position even by few mil-

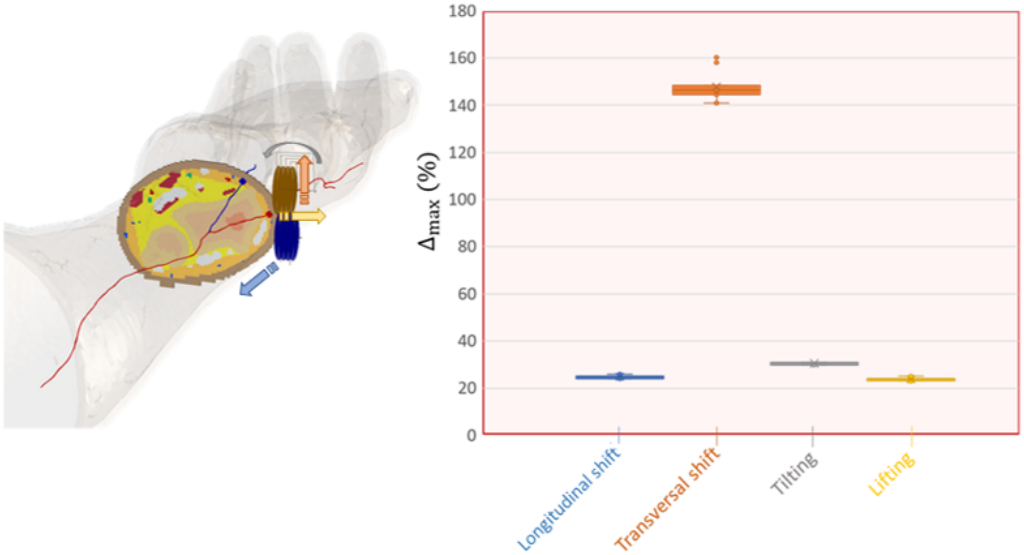

Figure 9.13: Box plot representation of the distribution of Δ_{max} (maximum variation with respect to the m-Coil position) computed over the 20 superficial fibers available in the model(red splines). Top and bottom line of the box are the 1st and 3rd quartile respectively, the x represents the mean value. The vertical lines (or whiskers) show maximum and minimum value. Inner points and outliers are also reported.Arrows show direction of longitudinal shifting (Blue), transversal shifting (orange), tilting (grey) and lifting (yellow).

limeters would lead to consistent presence or absence of significant SNAPs, supporting the notion of focality. An intersubject variability study was conducted, as well, to estimate effect of different anatomies. In fact, different participants have variability in the circumference of the arm, and thus position of the nerve, that might affect the outcome of the stimulation. Therefore, an additional set of simulations was performed with a male neurofunctionalized model, i.e. Jeduk (ViP v.4 (Gosselin et al., 2014)). The Jeduk model is characterized by a larger wrist with respect to that of the Yoon-Sun model (i.e., 6 cm vs. 5 cm) and a deeper radial nerve (i.e., 8 mm vs. 3 mm), as shown in Fig. 9.14. A variation in the stimulation threshold of 27% was calculated when considering a wrist model with a different relative position between the coil and the fibers, comparable to that obtained with a longitudinal misplacement or a coil lift from the surface of the skin.

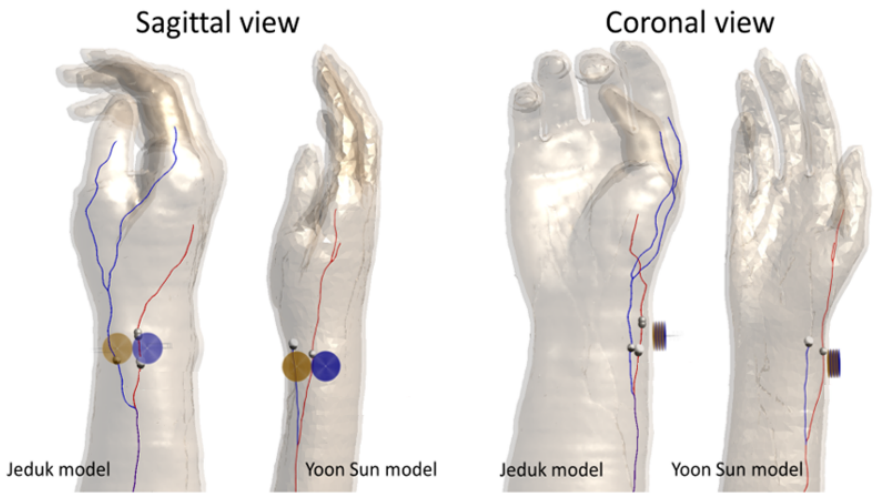

Figure 9.14: Sagittal and coronal view of the two anatomical models Jeduk and Yoon-Sun. Blue splines represent the deep branch of the radial nerve. Red splines represent the superficial branch of the radial nerve. Grey spheres show location of numerically estimated stimulation site.

Finally, in order to further assess the estimated stimulation threshold, the effects of changes in the electrical conductivities of tissues proximal to the fibers were evaluated. In fact, as demonstrated in Chapter 3, even in magnetic stimulation techniques the induced E-field can be affected up to a 20% by changes in the tissues' EM properties, and so would be the stimulation threshold. Thus, additional simulations where conducted in which the assigned EM properties of skin, fat, muscle, and nerve tissues were increased or decreased by 50%, one at a time, according to Table 9.2.

Table 9.2: Electric conductivity of the simulated tissues: values considered in the variability study.

Tissue	σ_{ref} **(S/m)**	σ_{ref}**+50%**	σ_{ref}**-50%**
Skin	0.17	0.25	0.085
Fat	0.04	0.06	0.02
Muscle	0.33	0.49	0.16
Nerve	0.03	0.04	0.01

As for the variability over the m-Coil position, Δ_{max} was evaluated to assess the effect of tissue conductivity on the stimulation threshold (see Eq. 9.1). Results of this analysis are reported in the boxplot of Fig. 9.15. Confirming what previously found in Chapter 3, the effect of changes in skin conductivity can't be neglected when modeling magnetic stimulation techniques. In the context of the m-Coil model, skin and fat are the tissues that affect stimulation threshold the most (up to 7%), while changes in the nerve or muscle conductivity would affect it by less than 1%.
In conclusion, for this dosimetrical study, changes in the parameters that depend on the simulation set-up, such as the tissues conductivity, determine changes in the estimated stimulation threshold that are below those caused by the experimental sources of uncertainty.

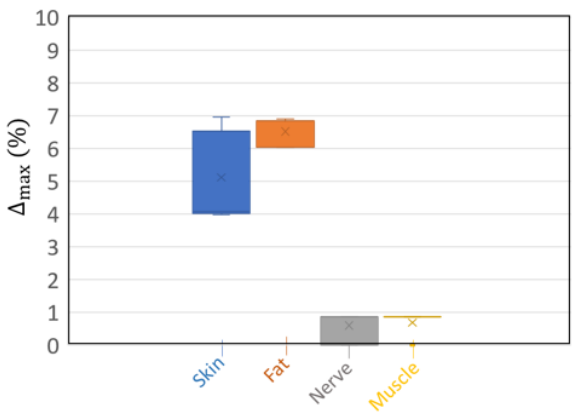

Figure 9.15: Variability study over changes in the conductivity. The box plot represents the distribution of Δ_{max} (maximum variation) computed over the 20 superficial fibers available in the model. Top and bottom line of the box are the 1st and 3rd quartile respectively, the x represents the mean value. The vertical lines (or whiskers) show maximum and minimum value.

Chapter 10

Numerical investigation of different miniaturized coil designs

10.1 Abstract

Transcranial magnetic stimulation (TMS) is a non-invasive brain stimulation technique used in the clinic to treat several neurological disorders and psychiatric diseases. One of TMS's significant limitations is its low spatial resolution, which often results in a mismatch between the target area in the brain and the stimulation site on the scalp. To enhance its spatial resolution, we designed and built a complete stimulation system complete with a millimetric-diameter coil and microscopic traces (m-Coil). The first tests conducted on healthy volunteers, and described in Chapter 9, showed that the m-Coil stimulation of the radial nerve in the wrist could indeed evoke sensory nerve action potentials (SNAPs). In this chapter, this nerve stimulation system is studied with electromagnetic and Neuron simulators on a neurofunctionalized model from the Virtual Population (ViP v.4) and different m-Coil geometries. In particular, it is investigated how changes in the m-Coil geometry, such as the number of layers, shape, and presence of an iron or air core, may help to promote the generation of sensory nerve action potentials.[1].

[1]This chapter was published in the book Brain and Human Body Modeling 2020, by Makarov S., Noetscher G., Nummenmaa A. (Colella M., Liberti M., Apollonio F., Bonmassar G. (2021) A Miniaturized Ultra-Focal Magnetic Stimulator and Its Preliminary Application to the Peripheral Nervous System. In: Makarov S.N., Noetscher G.M., Nummenmaa A. (eds) Brain and Human Body Modeling 2020. Springer, Cham. https://doi.org/10.1007/978-3-030-45623-8_9

10.2 Introduction

Transcranial magnetic stimulation (TMS) is a non-invasive brain stimulation technique that employs a high intensity pulsed magnetic field sent through the scalp by a stimulating coil. According to Faraday's law, a time-varying magnetic field induces inside the brain tissue an electric field, which may elicit a neuronal response. Due to the lack of physical contact, TMS results in almost a painless stimulation compared to electric non-invasive techniques, and for this reason, it has been deeply investigated over the past decades. Many studies have demonstrated the effectiveness of TMS as a therapeutic solution for the treatment of different neuropsychiatric conditions, among which is major depression (Pascual-Leone et al., 2000), chronic pain (Kobayashi and Pascual-Leone, 2003; Fitzgerald et al., 2006; Najib et al., 2011; Valero-Cabré et al., 2011), epilepsy (Rotenberg, 2010) and obsessive-compulsive disorder (OCD) (Carmi et al., 2018). Furthermore, TMS is extensively adopted in neuroscience research to investigate intracortical, cortico-cortical, and cortico-subcortical interactions (Rotenberg, 2010; Horvath et al., 2011; Rotenberg et al., 2014) and to assess causal relations between brain activity and behavior, as during speech (Jennum et al., 1994; Wassermann et al., 1999; Epstein et al., 1999) and motor mapping (Wassermann et al., 1992; Brasil-Neto et al., 1992; Cincotta et al., 2006; Cincotta and Ziemann, 2008; Civardi et al., 2009; Martinez et al., 2009; Karl et al., 2001). Despite the success, there are critical barriers to employing TMS in neuroscience research. One major restriction of TMS in its present form is its limited spatial resolution, which makes the task of focusing the stimulation exclusively to the targeted cortical region very challenging. The spatial resolution of TMS depends on the stimulating coil's geometry and dimensions. A deep investigation of the focality of the electric field induced by 50 TMS coils has been conducted by (Deng et al., 2013). In this work, the authors showed that figure-8 coils are more focal than circular coils. For example, the Magstim 70 mm figure-8 coil (P/N 9925, 3190) has a 15 cm^2 focality (Deng et al., 2013; Hovey and Jalinous, 2006), while the Magstim 90mm circular coil (P/N 3192) has a 70 cm^2 focality (Deng et al., 2013; Hovey and Jalinous, 2006). Also, smaller coils are, in general, more focal than larger coils, with focality that can be as small as 5 cm^2 (Deng et al., 2013). For this reason, several attempts have been made to increase the spatial resolution of TMS by reducing the dimension of the stimulating coil (Salinas et al., 2009; Talebinejad and Musallam, 2010; Tischler et al., 2011). To date, however, all the coils with reduced dimensions

were designed for either invasive (Tischler et al., 2011) or non-invasive animal applications (Talebinejad and Musallam, 2010). In fact, as the dimension of the coil shrinks (diameter less than 2 cm), larger electric currents (few hundreds of kiloamperes) are required to produce enough induced electric field in the human cortex (60-100 V/m). Given the conventional engineering approach which uses a few turns (<30) of wire winding inside an insulation housing, passing such large currents would produce excessive amounts of heat and large magnetic forces that may raise safety concerns or exceed specifications of conventional wires. To overcome such technological barriers, we have introduced flex circuit technology to design a new generation of miniaturized coils, which allows for a high number of turns (100 or greater) in a multi-layer structure characterized by a reduced diameter (15 – 20 mm). Such an approach has been at first used to develop microscopic coils for invasive magnetic stimulation (μMS) capable of activating neuronal circuitry both in-vitro (Bonmassar et al., 2012), and in vivo (Park et al., 2013). Based on these results, a flex circuit technology was adapted to develop the first generation of miniaturized coils for noninvasive magnetic stimulation (m-Coil). The concept behind the structure of the m-Coil consists of a certain number of parallel copper traces, named layers, deposited on a long flexible substrate wound in N turns around a core. The prototype of m-Coil was built using a four traces Kapton sheet, wound in 123 turns around a copper pin with a 1 mm diameter. Since each layer was 1 mm high, with a distance of 0.5 mm between two adjacent layers, we fabricated a single 8 mm-tall circular solenoid (m-Coil), with an outer diameter of 15 mm. A figure-8 stimulator was obtained by pairing two single m-Coils, thus obtaining a structure with a maximum dimension of 30 mm. To date, these coils are the only figure-8 coils capable of performing stimulation of the peripheral nervous system on healthy volunteers. In this chapter the behavior of six different m-Coils geometries is studied numerically to show how each coil geometry affects the peripheral nerve stimulation threshold.

10.3 Models and Methods

10.3.1 m-Coils modeling

The Electromagnetic simulation software Sim4Life (v.5, Zurich MedTech, Zurich) was adopted in all of the simulations. A planar loop coil geometry represented the actual copper traces configuration. The space between two consecutive loops of 1.5 mm was

selected to model the trace thickness and spacing. Six different geometries were considered, as shown in Fig. 10.1. The first geometry studied was a two-layered single circular coil, with each layer wound in 123 turns around a 1 mm air core. Second, two other layers, with the same characteristics as above, were added on top to make a four-layered single circular coil. The third geometry herein studied was the figure-8 configuration, which consisted of two four-layered single circular coils paired together and with currents circulating in the opposite phase. Three additional figure-8 coil models were built to study how the presence and length of an ideal iron core (i.e., linearity assumption: B= μ_rH with $\mu_r = 60$) would modify the magnetic and electric field generated by the m-Coil. Each solenoid was wound in 100 turns and had an inner and outer diameter of 10 mm and 21 mm, respectively. Three lengths of the iron core were considered: 9 mm, 23 mm and 41 mm. Of all the geometries, the circular four-layered m-Coil and the figure-8 m-Coil were manufactured and tested. The iron-core m-Coils were studied to enhance the magnetic field strength of the m-Coil for future cortical applications. The Electromagnetic simulations were conducted using the Magneto Quasi-static solver of the software Sim4life (v.5.9, Zurich MedTech, Zurich). This solver implements the quasi-static approximation that allowed decoupling the electric field from the magnetic field. Considering the source current density J, magnetic vector potential A was calculated from Ampere's law and used to compute the B and E field. EM simulations were performed by feeding a sinusoidal current with a 1.9 kHz frequency in each m-Coil and a phase of 0° in the first m-Coil and of 180° in the second m-Coil when considering the figure-8 coil. The two coils were placed in a figure-8 coil over the arm of the anatomical, neurofunctionalized body model Yoon-Sun (ViP., v4 (Gosselin et al., 2014)), in correspondence of the superficial branch of the radial nerve, as shown in Fig. 10.1. The Yoon-Sun model is characterized by a detailed representation of the peripheral nervous system and the various nerve fibers. The m-Coil driving sinusoidal currents were normalized to 1 A for comparison among different configurations.

10.3.2 Modeling Peripheral Nerve Stimulation: Titration analysis

To study the interaction between the induced electric field and the peripheral nervous system, the results of the EM simulations were fed into the dynamic Neuron solver version (v. 5.9) embedded in Sim4Life in a Multiphysics approach. The excitable behavior of the fibers was simulated using the McIntyre-Richardson-Grill model, which

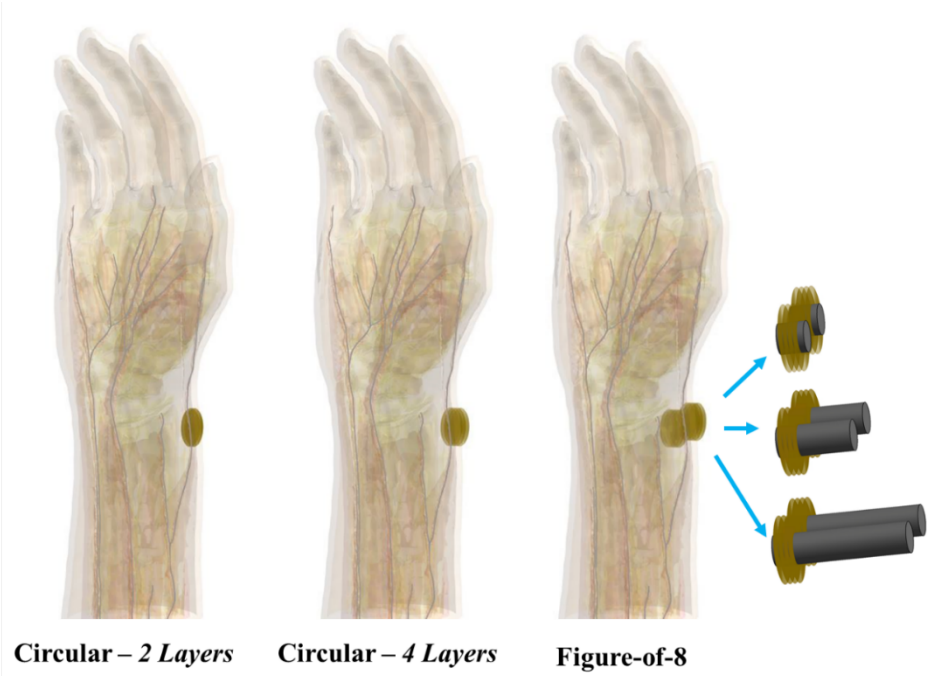

Figure 10.1: Four figure-8 m-Coils models: m-Coil models and placement over the right arm of the neurofunctionalized model Yoon-Sun, and the point where the two figure-8 m-Coils touch was precisely above the nerve trajectory in the wrist area.

is based on a double cable representation of the axon that allows separating electrical representations for the myelin and underlying internodal axolemma (McIntyre et al., 2002; McIntyre and Grill, 2002). In this work, a titration analysis was conducted for all the simulated m-Coil geometries. Titration is the iterative process that allows determining the stimulation threshold of a nerve by stimulating it with pulses of increasing intensity.

10.4 Results

10.4.1 Magnetic field generated by the m-Coils

Figure 10.2 shows the vector view of the B field generated by each m-Coil on the central cross-sectional plane. Inside the coil, the presence of more layers directs the B field along the axis of the coil. The magnetic field lines of forces diverge outside the coil and form closed loops. Doubling the number of layers increased the maximum intensity of

B induced on the skin from 30 mT to 40 mT, thus by a factor of 33% without changing its direction. When forming the 8-shaped coil by pairing two circular m-Coils fed in counter phase, the B field lines formed a third loop at the center of the figure-8 coil, due to the coupling between the two coils. The use of the iron core modified the direction of the B field that was along the coil axis for the whole length of the core and parallel to the surface of the coil in the space between the two cores. At the interface between iron and air, vector B was deviated to respect the continuity of the normal component to the surface. Moreover, at the level of the nerve (i.e., 2.5 mm from the surface of the skin) B field intensity for the coil with the 41 mm, long core is higher than that generated with the 23 mm long core and with the 9 mm long core, by 15% and 50% respectively.

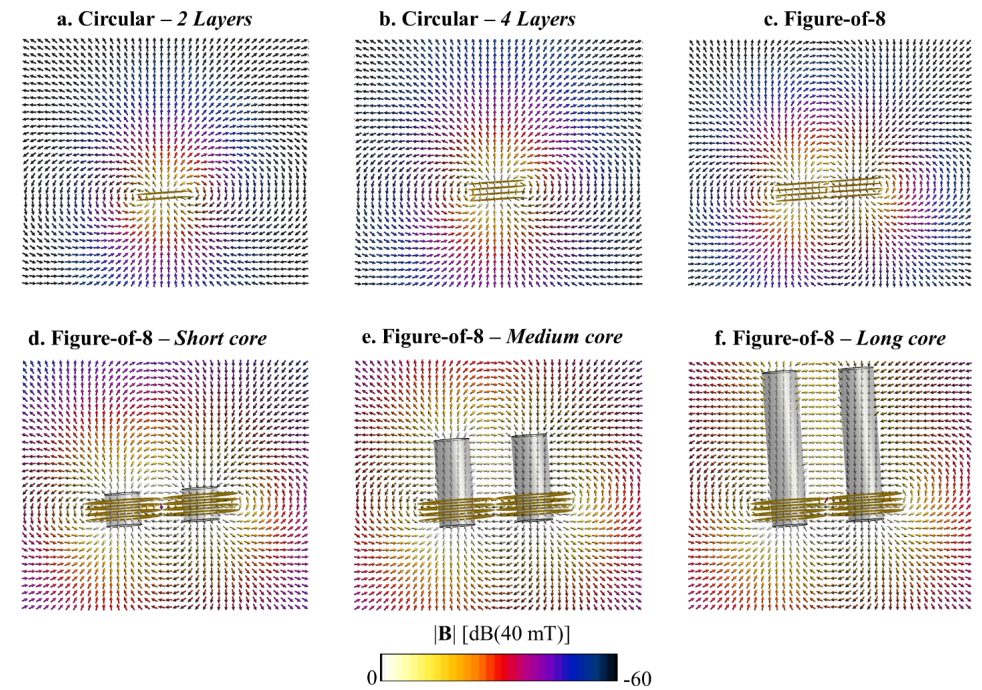

Figure 10.2: Vector view of the **B** field generated by each m-Coil model. Arrows show direction, orientation and intensity of **B**. Intensities of **B** are represented by a color bar in a logarithmic scale with 0 dB referenced to 40 mT, which is the maximum | **B** | induced on the surface of the skin by the air core figure-of-eight m-Coil (Panel c) when fed with 1 A.

10.4.2 Electric field induced by the m-Coils

The single circular coil that was composed of 4 layers induced inside the tissues an electric field stronger than the field induced by the two-layered coil: the maximum E field induced at the level of the nerve with 1 A was 0.27 V/m for the 2-layered circular coil and 0.40 V/m for the 4-layered one (see Fig 10.3, Panel a and b). The figure-8 coil configuration increased the intensity of the induced electric field on the nerve up to 0.6 V/m (Fig. 10.3, panel C). Moreover, the direction of the B field (Fig. 10.2) induced an E field-oriented mostly along the longitudinal axis of the arm and (therefore) along the radial nerve. The presence of an iron core further oriented E along the nerve, as shown by the vector arrows in Fig. 10.3 d and f. Moreover, the longer the core, the higher was the maximum intensity of the induced E: 2.5 V/m for 41 mm, 2.3 V/m for 23 mm, and 1.6 V/m for 9 mm. Figure 10.4 shows electric field components tangential (E_{tan}) and normal (E_{norm}) to the nerve fibers, for the two circular m-Coil and the air core figure-8 m-Coil. The figure-8 m-Coil induced a tangential component that was 5 and 7 times higher than that induced by a four-layered and a two-layered single circular m-Coil, respectively, and a normal component that was two times lower.

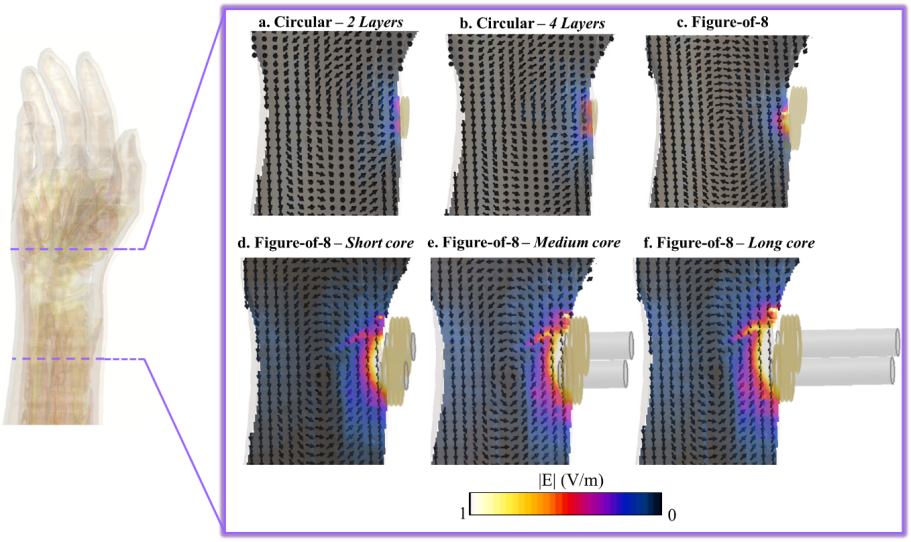

Figure 10.3: Direction, orientation, and intensity of the E field induced in the arm of the Yoon-Sun model on the longitudinal plane of the arm that crosses the center of the stimulating coil. A vector view of the E field is superimposed on the intensities distribution map.

10.4.3 Variation of the peripheral nerve stimulation threshold

When simulating exposure of the arm to the 2-layered single circular coil, the computed stimulation threshold for the radial nerve fibers varied between 259 A and 269 A. Nerve action potentials were generated near the extremities of the coil. Increasing the number of layers from 2 to 4, reduced the coil current threshold in each layer/coil to values between 177.56 A and 184.39 A, while the activation site of the neuronal response was not affected. The stimulation threshold was further reduced when simulating with a figure-8 coil: the five times higher induced tangential electric field of the figure-8 coil reduced the threshold to values between 58 A and 58.5 A, such a small range of variability may be due to the augmented focality. For all fibers, the activation site of the neuronal response was at the center of the figure-8 coil. On-set timing was not affected by the number of layers or by the change of coil shape and remained around an average time of 0.8 ms. A reduction of the on-set timing from 0.8 to 0.5 ms, meaning an earlier spike, was obtained when changing from air to iron core. The presence of the core also reduced the stimulation threshold from 58 A to 14 A, 10.1 A, and 9.4 A for the short, medium and long core respectively and further oriented E field along the direction of the nerve.

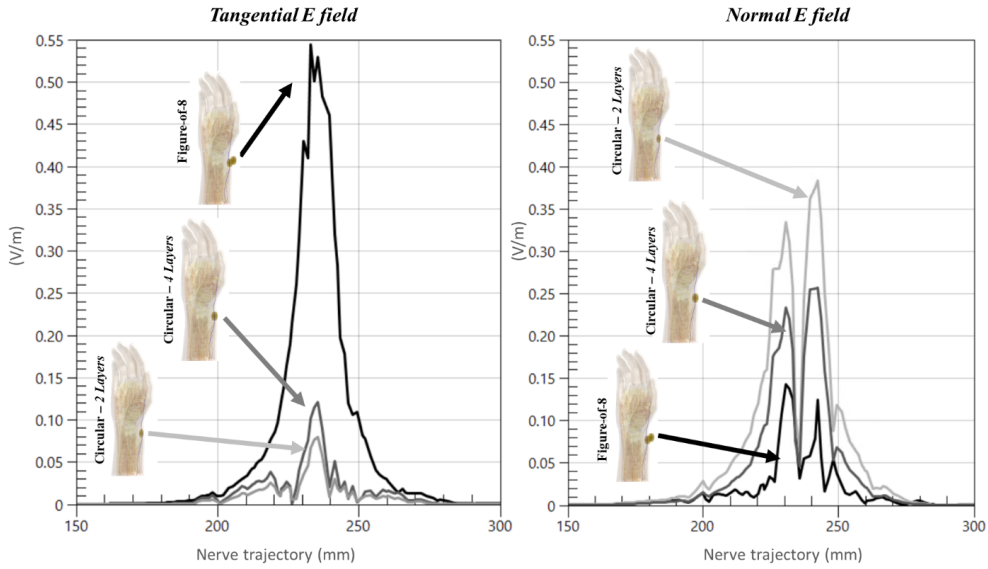

Figure 10.4: The tangential (left) and normal (right) components of the E field-induced along the nerve by the 2-layered circular m-Coil, the 4-layered circular m-Coil, and figure-8 m-Coil.

10.5 Discussion and conclusions

The lack of focality of TMS stimulators is a significant barrier for the future deployment of this type of non-invasive neurostimulator in the clinics or neuroscience research. Several solutions have been proposed during the past years to overcome this limitation. For example, in 2010, Talebinejal and Musallam conducted a numerical study on a multilayer miniaturized coil made up of braided Litz wire (Talebinejad and Musallam, 2010) and demonstrated the feasibility of realizing a TMS coil reduced in size. Moreover, they showed that adding more layers increased magnetic field intensity while keeping the coil area constant. Following a similar geometry, in (Tischler et al., 2011), a mini coil with an outer diameter of 26.5 mm was developed. It is crucial to notice that all the attempts made to reduce dimensions of the TMS coils were conceived for either invasive (Tischler et al., 2011) or noninvasive (Talebinejad and Musallam, 2010) animal models. To our knowledge, the newly developed figure-8 m-Coil, based on flex circuit technology, is the first prototype of miniaturized coil manufactured for on-human applications. Experiments conducted on the peripheral nervous system of healthy volunteers showed that the m-Coil could elicit sensory nerve action potentials (SNAPs) when the coil is placed over the superficial branch of the radial nerve. In this chapter, a numerical study was conducted with the aim to show how different possible m-Coil geometries can affect the radial nerve stimulation threshold. Six different typologies of m-Coils where modeled, based on the three different m-Coils actually manufactured: the single circular 4-layered and the figure-8 coils were originally designed to be tested on the PNS and the iron core figure-8 coil developed to target the cerebral cortex. Each coil was placed over the radial nerve superficial branch of the neurofunctionalized model Yoon-Sun (Gosselin et al., 2014). A multiphysics approach was herein considered and electromagnetic simulations were coupled with the dynamic neuronal solution. To study the effect of adding more layers, it was at first considered a 2-layered single circular m-Coil that was compared with the four-layered one. The results showed that increasing the number of layers from 2 to 4 increased the intensity of the B field by 50%, thus inducing a stronger E field. As a consequence, the stimulation threshold was lower for the 4-layered coil. A figure-8 coil was obtained by pairing together two 4-layered circular coils. Such m-Coil was able to generate a stronger magnetic field, thus inducing a stronger electric field on the nerve. Moreover, the figure-8 coil oriented the E field along the trajectory of the nerve fibers, leading to a better coupling between

the coil and the nerve and a lower stimulation threshold. This coupling is further enhanced by addition of an iron core. Additionally, the results showed that the presence of the core not only increased intensity of the induced electric field, as expected, but it also reduced the on-set timing of the first spike. Nevertheless, it should be noted that saturation of the iron core was not considered in this study. Thus, computed stimulation threshold was underestimated, due to the overestimation of both B and E field intensities. However, future work will account for the non-linearities of a real core. In this chapter is confirmed that the figure-8 coil was more efficient than the circular coil as it enhanced the focality and the coupling between nerve fibers and E-field. Moreover, the results showed that the presence of an iron core further reduced stimulation threshold while increasing depth, making this geometry suitable for investigating the m-Coil stimulation of the brain cortex.

Conclusions

The studies presented in this thesis evaluated computationally the use of electromagnetic fields in medicine for therapeutic applications based on noninvasive electric, and particularly magnetic, stimulation of the brain, commonly known as NIBS (noninvasive brain stimulation) techniques. NIBS therapy consists in modifying the brain activity by stimulating and/or neuromodulating target areas of the brain, through an EM field delivered from the stimulator through the scalp, and is part of the family of "Electroceuticals", which identify the branch of medicine that apply EM quantities as an alternative to systemic drug therapy, to treat a variety of disorders that are directly, or even indirectly, correlated to the nervous system. Despite the continuous growth of such techniques in the medical field, there are still open questions that move from the need to further investigate existing and well established methodologies, in order to improve their beneficial effects, to the need of assessing novel therapies to enlarge the spectrum of electroceutical applications. To satisfy these two aspects, computational dosimetry becomes a fundamental tool, as it helps to determine intensity and distribution of the EM quantities related to the dose necessary to exert an effect, and to investigate the parameters that may influence the experimental outcome. Having such information would open the way to precise treatment plannings that would guide the treatment session in a way for it to be effective, reproducible and robust. In this regard, the dosimetric model considered, that accounts for the patient's head and for the stimulator, should be an accurate representation of the real treatment. A wide literature production can be found on this topic and many research group are proposing numerical methodologies and modeling approaches to respond to the need of an accurate dosimetry applied to EM therapies. Moving from the current state of research,

the work carried out in this thesis focused on proposing methodologies to investigate and assess standard, as well as novel stimulation techniques. Each dosimetrical analysis was conducted ensuring resolution of the same equations governing the simulated problem, to maintain consistency among different applications. Particularly, both the solvers employed to study magnetic stimulation, one commercial (Sim4Life v.5, Zurich MedTech, AG) and one custom made, modelled the induced E-field as a summation of the primary electric field, generated by induction, and the secondary electric field, generated by the accumulation of charge at the interface between different tissues, as it is a fundamental aspect for accurately modeling magnetic NIBS techniques. Moving from this pillar, the common thread of this work is to show how realistic anatomical human models can be manipulated in order to respond to specific needs dictated by the purposes of the conducted research. Here, the analysis started with the use of human models that have been developed in literature for computational modeling studies that require anatomical accuracy. The strength of such models, whether free of charge, as the MIDA model of head and neck (Iacono et al., 2015) or license-based, as those from the Virtual Population (Gosselin et al., 2014), is their high level of anatomical detail, that goes from the presence of different separated brain structures, to an accurate representation of cutaneous and extra-cutaneous layers of the body. Such models are particularly suitable to investigate all the parameters that may affect the EM solution, as they reduce as much as possible the source of error generated by approximations in their anatomy. Therefore, they were herein employed in the first place in order to investigate a modeling aspect much debated in the literature about LF NIBS applications, which is the importance of an accurate representation of the skin in terms of dielectric properties. It was demonstrated in Chapter 3 how this would affect the estimated electric field on the brain not only when modeling electrical techniques such as tDCS, where differences up to 70% were found, as would be expected, but in magnetic techniques as well, such as transcranial magnetic stimulation, TMS. Results of this work showed that changes in the skin conductivity in the range reported in the literature determined differences in the E-field induced in the brain by TMS up to 20% respectively. It should be noticed that here the dependency from tissue properties relies solely on the secondary electric field, which therefore should not be neglected. Furthermore, a solution on how to choose the more suitable skin conductivity value during EM simulations is proposed. Moving from general dosimetric evaluations, whose undisputed importance leads the way to an increasingly accurate dosimetry, when it comes to dosimetry for

clinical applications, a personalized approach is desirable. A custome-made code for personalized EM dosimetry was developed in this thesis, as an upgraded version of the one presented in (Paffi et al., 2015b), and is presented in Chapter 4. The aim is for it to used as a software for the navigated (n-)TMS developed in the context of the POR FESR LAZIO 2014 – 2020 project, Effective navigated Transcranial Magnetic Stimulation (E-nTMS), that aims at guiding TMS stimulation using a detailed 4-compartment, anatomical, anisotropic head model, rather than a simplified spherical head, as currently done by available n-TMS systems. Within this project it was shown that considering the anisotropic properties of the brain can affect the location of the stimulation spot. For the coil position and orientation chosen in Chapter 4, a shift of 1 mm was found, although longer shifts may occur when considering other coil placements. Such results suggest that a proper modeling of TMS should include the anisotropic conductivity of the brain, specially in the context of clinical applications. Additionally, the strategy developed to reduce the computational time by reducing the dimensions of the simulating domain didn't affect the location of the stimulation spot, allowing to achieve a real-time solution while keeping an acceptable anatomical detail in the model. If, on one side, applications such as that of the effective navigated (En-)TMS can take advantage of a fully detailed anisotropic brain, and less detailed extracerebral structures, as long as the location of the stimulation spot is not affected, other studies, such as those that aim to introduce new electromagnetic−based therapies for lesion treatments, need to be assessed by following an evaluation approach similar to a typical $Phase2$ clinical study (Friedman et al., 2015), and thus require a fast methodology that allows to keep an adequate degree of realistic anatomical representation, with a precise representation of the patient's lesion. A solution for such applications was proposed in Chapter 6 and consisted in manipulating the highly detailed generic models to host the patient's lesion. This approach was first tested on three subjects, enrolled in the open labeled study conducted to assess safety and tolerability of PEMFs on ischemic patients (Capone et al., 2017). Following, this methodology for dose-response curve assessment was applied to the ongoing multicentric, randomized, double blind, placebo controlled study (ClinicalTrials.gov, Identifier NCT02767778) that aims to assess the efficacy of LF pulsed EMFs (LF-PEMFs) treatment on acute ischemic stroke, but it can be extended to tumors or other lesions located in several different part of the body. Finally, virtual body models can be integrated with a representation of their neurophysiological functions, by coupling them with proper neuronal models. This representation allows

to use a multiphysics solution to link the EM quantity to the elicited physiological outcomes of the stimulation. In the frame of this thesis, a dosimetrical analysis on the neurofunctionalized version of a human body model taken from the Virtual Population (i.e. Yoon-Sun, v.4 (Gosselin et al., 2014)) was conducted to support design and testing of a novel miniaturized coil (m-Coil) for noninvasive magnetic stimulation of neural tissues, that aims at overcoming one of the major limitations of transcranial magnetic stimulation (TMS), i.e. its reduced focality, that prevent from applying this techniques at its full potential. The m-Coil was developed in collaboration with the Athinoula A. Martinos Center for Biomedical Imaging of Boston and its numerical model was coupled with the Yoon-Sun model (Gosselin et al., 2014) to assess the experimental set up to be used to demonstrate it's ability to elicit neurostimulation on peripheral nerves (PN) of healthy humans. Considering the neurofunctionalized model allowed to obtain information about the PN stimulation threshold, that could be translated into output of the machine or position and orientation of the m-Coil at which stimulation was achievable. From this study it was found that the system at its maximum machine output (i.e. 70 A) was working at the threshold level and that a misplacement of the coil, even by few millimeters, could lead to absence of action potentials. Additionally, the modeling helped to characterize the m-Coil exposure and to compare its focality over a standard TMS figure-8 coil, that resulted to be four times less focal. Furthermore other possible geometries were investigated numerically with the aim to find a solution to increase the coil penetration depth and make this novel focal system suitable for stimulation of the brain cortex.

Curriculum Vitae

Micol Colella

Personal contacts:
Phone: +39 339 2723549
Personal e-mail: micol.colella@gmail.com
Work e-mail: micol.colella@uniroma1.it

PERSONAL RECORDS

Date of birth: September 16, 1993
Place of birth: Rome, ITALY
Citizenship: ITALIAN
Address: Via Giuseppe Troiani, 13, 00149, Rome (RM)

EDUCATIONAL BACKGROUND

2017 - 2020 PhD Course, University of Rome "La Sapienza", Department of Information Engineering, Electronics and Telecommunications (DIET), Division of Electronic Engineer, Rome, Italy.

2015 - 2017 **M.Sc.** in Biomedical Engineering, University of Rome "La Sapienza", master thesis at Department of Information Engineering, Electronics and Telecommunications (DIET), Rome, Italy
Thesis: "Variability factors in a computational model of a 1.5 T RF birdcage coil"
Grade 110 out of 110, cum laude

2012 - 2015 **B.S.** in Clinical Engineering, University of Rome "La Sapienza", bachelor thesis at Department of Information Engineering, Electronics and Telecommunications (DIET), Rome, Italy
Thesis: "Thin film photosensors for Lab-on-Chip systems"
Grade 109 out of 110

2007 - 2012 **High school** for humanities "Eugenio Montale", Rome, Italy**,** Subjects including Math's, Science, English
Grade 98 out of 100

RESEARCH EXPERIENCES

Period	2017-2020 (Three years)
Institute	Department of Information Engineering, Electronics and Telecommunications (DIET), University of Rome "La Sapienza".
Position	PhD student under supervision of Prof. Micaela Liberti (University of Rome "La Sapienza").
Research activities	**Numerical modeling of noninvasive magnetic and electric brain stimulation techniques to investigate their physiological effects on human brain.**

Period	2019-2020 (Six months)
Institute	Athinoula A. Martinos Center for Biomedical Imaging (Boston, MA, USA).
Position	Graduate Research Assistant under supervision of Prof. Giorgio Bonmassar (Harvard Medical School).
Research activities	**Development of the second generation of miniaturized coil for ultra-focal transcranial magnetic stimulation**.

Period	2019 (Two weeks)
Institute	IT'IS Foundation, Zurich, Switzerland
Position	Visiting PhD student**,** under supervision of Dr. Antonino Cassarà (IT'IS Foundation).
Research activities	**Assessment of new neuronal models to study noninvasive stimulation techniques of the peripheral nervous system.**

Period	2018 (Six months)
Institute	Athinoula A. Martinos Center for Biomedical Imaging (Boston, MA, USA).
Position	Graduate Research Assistant under supervision of Prof. Giorgio Bonmassar (Harvard Medical School).
Research activities	**Development of an ultra-focal TMS system for peripheral nerve stimulation**.

Period	2017 (Two weeks)
Institute	Neuro-radiology research laboratory, Ospedale San Raffaele, Milano, Italy.
Position	Visiting PhD student under supervision of Prof. Nicoletta Anzalone (Università Vita-Salute, Scientific Institute San Raffaele).
Research activities	**Segmentation of ischemic lesions from MR images of patients recruited in the I-NIC project - *A double-blind, randomized, placebo-controlled, multicentric study to evaluate the efficacy of low-frequency pulsed electromagnetic field (ELF-MF) in patients suffering from acute ischemic stroke.***

RESEARCH PROJECTS

From - To	
2018 - 2020	**Development and modeling of an ultra-focal TMS system for cortical and peripheral nerve stimulation**, *in collaboration with Athinoula A. Martinos Center for Biomedical Imaging (Boston, MA, USA)***.**
2017 - 2020	**Investigation the neuroprotective effect of low frequency (LF) and low intensity (LI) pulsed magnetic fields (PMFs) on ischemic lesions of real patients, by means of a computational semi-specific head model**, *I-NIC project, in collaboration with IGEA Medical, SPA and Università Campus Biomedico*.
2017 - 2020	**Study of MRI compatibility with partially implanted electrodes**, *in collaboration with the U.S. Food and Drug Administration (Silver Spring, MD, USA).*

TECHNICAL SKILLS AND COMPETENCES

-3D modeling, data postprocessing, electric measurements-

- **Programming**: Matlab for data postprocessing, LabView for computer/instrument interface; C++ and Python.
- **Electromagnetic and electronic simulation softwares**: Sim4Life, Comsol Multiphysics, Ansys Maxwell, LT Spice.
- **Software platform for medical image processing and 3D modeling**: ITK-Snap, 3DSlicer, Seg3D, Autodesk 3ds Max.
- **Devices for electrical measurements**: Oscilloscope, digital multimeter, RLC meter, Network analyzer.

AWARDS AND TRAVEL SUPPORTS

Year	Conference
2019	BioEM2019 Annual Joint Meeting, Montpellier, France: 1st place Platform Presentation Award and winner of Joseph James Morrissey Award.
2019	BioEM2019 Annual Joint Meeting, Montpellier, France: Student Travel Award.
2019	BMES/FDA Frontiers Conference, Washington DC, USA: Student Travel Award.
2019	41st EMB Conference2019, Berlin, Germany: Open finalist (Entitled to receive student support).

PARTECIPATION AT NATIONAL AND INTERNATIONAL CONFERENCES

Date	November 14th, 2020
Conference	7th International Conference on Non-Invasive Brain Stimulation, On-line Congress.
Presentation	Poster
Title	Ultra-focal magnetic stimulation: A numerical comparison between two different miniaturized coil.

Date	June 1st, 2020
Conference	6th Annual BRAIN Initiative Investigators Meeting, Virtual Meeting.
Presentation	Poster
Title	Computational analysis of the new ultra-focal miniaturized coil for noninvasive transcranial magnetic stimulation.

Date	July 26th, 2019
Conference	EMBC, 41st Annual International Conference of IEEE-EMBS, Berlin, Germany.
Session	Models of Organs and Medical Devices
Presentation	Oral platform
Title	Ultra-Focal Magnetic Stimulation Using a µTMS Coil: A Computational Study.

Date	July 26th, 2019
Conference	EMBC, 41st Annual International Conference of IEEE-EMBS, Berlin, Germany.
Session	Models of Organs and Medical Devices
Presentation	Oral platform
Title	Ultra-Focal Magnetic Stimulation Using a µTMS Coil: A Computational Study.

Date	July 25th, 2019
Conference	EMBC, 41st Annual International Conference of IEEE-EMBS, Berlin, Germany.
Session	Model Construction: Algorithms, Parameters and Sensitivity.
Presentation	Poster
Title	Influence of Anatomical Model and Skin Conductivity on the Electric Field Induced in the Head by Transcranial Magnetic Stimulation

Date	June 24th, 2019
Conference	BioEM2019 Annual Joint Meeting, Montpellier, France.
Session	Electric and magnetic stimulation of the nervous system.
Presentation	Oral platform
Title	A µTMS coil for ultra-focal noninvasive magnetic stimulation

Date	June 24th, 2019
Conference	BioEM2019 Annual Joint Meeting, Montpellier, France.
Presentation	Poster
Title	Numerical evaluation of the influence of RF-exposure conditions on heating induced by interventional catheters

Date	June 25th, 2019
Conference	BioEM2019 Annual Joint Meeting, Montpellier, France.
Presentation	Poster
Title	Influence of skin conductivity on the electric field induced in the head by noninvasive brain stimulation techniques.

Date	February 26th, 2019
Conference	3rd International Brain Stimulation Conference, Vancouver, Canada.
Presentation	Poster
Title	Numerical evaluation of the induced electric field in techniques of transcranial brain stimulation: influence of the anatomic model and skin conductivity.

Date	February 27th, 2019
Conference	3rd International Brain Stimulation Conference, Vancouver, Canada.
Presentation	Poster
Title	A microTMS System for Peripheral Nerve Stimulation.

Date	February 27th, 2019
Conference	3rd International Brain Stimulation Conference, Vancouver, Canada.
Presentation	Oral platform
Session	Innovative techniques for non-invasive, low-energy, brain stimulation: from models to potential clinical applications.
Title	Patient semi-specific computational modeling of electromagnetic stimulation.

Date	November 29th, 2018
Conference	5th ICEmB National Congress, Salerno, Italy.
Presentation	Oral platform
Session	Biomedical applications
Title	Patient semi-specific computational modeling of electromagnetic stimulation applied to regenerative treatments in acute ischemic stroke

SOCIETY MEMEBERSHIP

From	
February 2020	Student member of the European Bioelectromagnetics Association (EBEA)

ACADEMIC SERVICES

Date From April 2019 to September 2019

Institute DigiLab, Department of Informatics, "La Sapienza" University of Rome, Rome, Italy.

Activity Tutor (*i.e. Domain expert*) for the GamificationLab students during the development of a didactic game on non-invasive brain stimulation techniques, under the supervision of Prof. Francesco Lutrario and Prof. Micaela Liberti.

Date May 2020

Institute Department of Information Engineering, Electronics and Telecommunications, "La Sapienza" University of Rome, Rome, Italy.

Activity Lecturer on "The m-Coil: a miniaturized coil for noninvasive magnetic stimulation", for the class "Therapeutic applications of Low Frequency Electromagnetic fields", under supervision of Prof. Micaela Liberti and Prof. Francesca Apollonio.

Date May 2020

Institute Department of Information Engineering, Electronics and Telecommunications, "La Sapienza" University of Rome, Rome, Italy.

Activity Lecturer on "Numerical evaluation of the RF-induced heating when in presence of interventional catheter during MRI exams", for the course of Electromagnetic Compatibility under supervision of Dr. Alessandra Paffi

Date From January 2018 to present

Institute Department of Information Engineering, Electronics and Telecommunications, "La Sapienza" University of Rome, Rome, Italy.

Activity Trainer for nine bachelor students in Biomedical Engineering during their intern period, under the direction of Prof. Micaela Liberti and Dr. Alessandra Paffi. With thesis on:

- Numerical evaluation of the induced electric field in techniques of transcranical brain stimulation for human and animal applications;
- Development of the 3D model of the cortex pain matrix to conduct numerical dosimetric evaluation on the nociceptive effect of non-invasive brain stimulation techniques.
- Numerical evaluation of the RF-induced heating when in presence of interventional catheters.

Date From November 2017 to present

Institute Department of Information Engineering, Electronics and Telecommunications, "La Sapienza" University of Rome, Rome, Italy.

Activity Trainer for six bachelor students in Clinical Engineering during their intern period, under the direction of Prof. Micaela Liberti. With thesis on:

- Numerical evaluation of the exposure of ischemic tissue to LF-LI-PMF;
- Investigation on the role of tissue heterogeneity in the highly detailed, multimodal image-based anatomical model of a human head and neck, namely the MIDA model.
- Numerical evaluation of the induced electric field in techniques of transcranical brain stimulation.

•Tutor for the course of Electromagnetic Fields under the direction of Prof. Francesca Apollonio and

Prof. Micaela Liberti.

•Tutor for the course of Electromagnetic Fields and Nanosystems, under the direction of Prof. Micaela Liberti and Prof. Francesca Apollonio.
•Tutor for the course of Therapeutic applications of low frequency electromagnetic, fields under the direction of Prof. Micaela Liberti and Prof. Francesca Apollonio.

LANGUAGES

Mothertongue Italian

Other English: Fluent

PUBLICATIONS ON JOURNAL PAPERS AND BOOKS

Colella M., Camera, F., Capone, F. et al. "Patient Semi-specific Computational Modeling of Electromagnetic Stimulation Applied to Neuroprotective Treatments in Acute Ischemic Stroke." Sci Rep 10, 2945 (2020). https://doi.org/10.1038/s41598-020-59471-9

Colella M., Liberti M., Apollonio F., Bonmassar G., "A Miniaturized Ultra-Focal Magnetic Stimulator and Its Preliminary Application to the Peripheral Nervous System", In: Makarov S.N., Noetscher G.M., Nummenmaa A. (eds) Brain and Human Body Modeling 2020. Springer, Cham. https://doi.org/10.1007/978-3-030-45623-8_9

Colella M., Paffi A., De Santis V., Apollonio F., Liberti M., "Effect of Skin Conductivity on the Electric Field Induced by Transcranial Stimulation Techniques in Different Head Models.", *Phys. Med. Biol.* **66** 035010. https://doi.org/10.1088/1361-6560/abcde7

PUBLICATIONS ON INTERNATIONAL CONFERENCES

Colella M., Liberti M., Apollonio F., Bonmassar G., "Ultra-focal magnetic stimulation: A numerical comparison between two different miniaturized coils". In Abstract Collection, 7th International Conference on Non-Invasive Brain Stimulation, November 10-14, On-line Congress.

Colella M., Camera F., Capone F., Setti S., Cadossi R, di Lazzaro V., Apollonio F., Liberti M., "Numerical evaluation of electromagnetic stimulation applied to neuroprotective treatments in acute ischemic stroke using patient semi-specific modeling". In Abstract Collection, BioEM Conference, June 21-26, 2020, Oxford, UK.

Colella M., Paffi A., De Santis V., Apollonio F., Liberti M., "Influence of skin conductivity and anatomical head model: A numerical study on TMS and tDCS". In Abstract Collection, BioEM Conference, June 21-26, 2020, Oxford, UK.

Colella M., Liberti M., Press D.Z., Apollonio F., Bonmassar G., "A numerical comparison between two different ultra-focal miniaturized coils for noninvasive magnetic stimulation". In Abstract Collection, BioEM Conference, June 21-26, 2020, Oxford, UK.

Paffi A., Apollonio F., **Colella M.,** Carducci F., Pellegrini V., Bellizzi L., Pignani A., Liberti M., "Effect of the TMS coil orientation on the electric field induced along neuronal structures". In Abstract Collection, BioEM Conference, June 21-26, 2020, Oxford, UK.

Colella M., Liberti M., Apollonio F., Bonmassar G., "Computational analysis of the new ultra-focal miniaturized coil for noninvasive transcranial magnetic stimulation". In Abstract Collection, 6th Annual BRAIN Initiative Investigators Meeting, June 1st-3rd, Virtual Meeting.

Colella M., Laher R.M., Press D. Z., McIlduff C.E., Rutkove S.B., Pascual-Leone A., Apollonio, F., Liberti M., Bonmassar, "Ultra-Focal Magnetic Stimulation Using a µTMS Coil: A Computational Study", *2019 41st Annual International Conference of the IEEE Engineering in Medicine and Biology Society (EMBC)*, Berlin, Germany, 2019, pp. 3987-3990, doi: 10.1109/EMBC.2019.8857349.

Colella M., Paffi A., Fontana S., Rossano F., De Santis V., Apollonio F., Liberti M., "Influence of Anatomical Model and Skin Conductivity on the Electric Field Induced in the Head by Transcranial Magnetic Stimulation", *2019 41st Annual International Conference of the IEEE Engineering in Medicine and Biology Society (EMBC)*, Berlin, Germany, 2019, pp. 2917-2920, doi: 10.1109/EMBC.2019.8856354.

Colella M., Paffi A., Fontana S., Rossano F., De Santis V., Apollonio F., Liberti M., "Influence of skin conductivity on the electric field induced in the head by noninvasive brain stimulation techniques". In Abstract Collection, BioEM Conference, June 23-28, 2019, Montpellier, France.

Colella M., Lucano E., Apollonio F., Zeng Q., Liu J., Lloyd T., Wedan S., Chen J., Kainz W., Liberti W., Angelone L.M., "Numerical evaluation of the influence of RF-exposure conditions on heating induced by interventional catheters". In Abstract Collection, BioEM Conference, June 23-28, 2019, Montpellier, France.

Colella M., Laher R.M., Press D. Z., McIlduff C.E., Rutkove S.B., Pascual-Leone A., Apollonio, F., Liberti M., Bonmassar, "A µTMS coil for ultra-focal noninvasive magnetic stimulation". In Abstract Collection, BioEM Conference, June 23-28, 2019, Montpellier, France.

Galli, M., **Colella M.**, Paffi A., Thomas A., Apollonio F., Prato F. S., Liberti M., "Dosimetric analysis on the pain matrix exposed to low-intensity extremely low-frequency magnetic fields". In Abstract Collection, BioEM Conference, June 23-28, 2019, Montpellier, France.

Capone, F., **Colella M.**, Motolese F., Rossi M. G., Camera F., Apollonio F., Di Lazzaro V., Micaela Liberti, "Extremely low-frequency magnetic fields as neuroprotective treatment in acute ischemic stroke: models, mechanisms and clinical application". In Abstract Collection, BioEM Conference, June 23-28, 2019, Montpellier, France.

Colella M., Laher R.M., Press D. Z., McIlduff C.E., Rutkove S.B., Pascual-Leone A., Apollonio, F., Liberti M., Bonmassar, "Non-invasive Magnetic Stimulation with a microTMS System: A Computational Study", In Abstract Collection, Photonics & Electromagnetics Research Symposium - PIERS, June 17-21, 2019, Rome, Italy.

Colella M., Lucano E., Apollonio F., Zeng Q., Liu J., Lloyd T., Wedan S., Chen J., Kainz W., Liberti W., Angelone L.M, "RF-Exposure Conditions vs. Induced Heating with Interventional Catheters: A Computational Study", In Abstract Collection of BMES/FDA Frontiers in Medical Devices Conference, March 19-21, 2019, Washington DC, USA.

Colella M., Camera F., Capone F., Setti S., Fusco R., Cadossi R, Apollonio F., di Lazzaro V., Liberti M., "Patient semi-specific computational modeling of electromagnetic stimulation", Brain Stimulation: Basic, Translational, and Clinical Research in Neuromodulation , Volume 12 , Issue 2 , 455.

Colella M., Laher R.M., Press D. Z., McIlduff C.E., Rutkove S.B., Liberti M., Pascual-Leone A., Bonmassar, G. "A microTMS System for Peripheral Nerve Stimulation". Brain Stimulation: Basic, Translational, and Clinical Research in Neuromodulation, Volume 12, Issue 2, 521.

Paffi A., **Colella M.**, Mambrini M., Apollonio F., De Santis V., Liberti M., "Numerical evaluation of the induced electric field in techniques of transcranical brain stimulation: influence of the anatomic model and skin conductivity", Brain Stimulation: Basic, Translational, and Clinical Research in Neuromodulation , Volume 12 , Issue 2 , 493.

Colella M., Camera F., Capone F., Setti S., Fusco R., Cadossi R, Apollonio F., di Lazzaro V., Liberti M., "Patient semi-specific computational modeling of electromagnetic stimulation applied to regenerative treatments in acute ischemic stroke". In: Abstract collection ICEmB Congress, November 28-30 2018, Salerno, Italy.

Colella M., Lucano E., Apollonio F., Zeng Q., Liu J., Lloyd T., Wedan S., Chen J., Kainz W., Liberti W., Angelone L.M., "RF-field vs. Induced Heating with Interventional Catheters: a computational investigation". In Abstract Collection, 1st EMF-Med world Conference on Biomedical Applications of Electromagnetic Fields, September 10-13 2018, Split, Croazia

Colella M., Camera F., Capone F., Setti S., Fusco R., Cadossi R, Apollonio F., di Lazzaro V., Liberti M., "Patient semi-specific computational modeling of electromagnetic stimulation applied to regenerative treatments in acute ischemic stroke". In: Abstract collection of BioEM 2018 Conference, June 24-29 2018, Portoroz, Slovenia.

In compliance with the Italian legislative Decree no. 196 dated 30/06/2003, I hereby authorize you to use and process my personal details contained in this document.

Date
Rome, 3/01/2021

Signature

Bibliography

Aberra, A. S., Wang, B., Grill, W. M., and Peterchev, A. V. (2020). Simulation of transcranial magnetic stimulation in head model with morphologically-realistic cortical neurons. *Brain Stimulation*, 13(1):175–189. [Cited on page 44]

Ahn, H., Woods, A. J., Kunik, M. E., Bhattacharjee, A., Chen, Z., Choi, E., and Fillingim, R. B. (2017). Efficacy of transcranial direct current stimulation over primary motor cortex (anode) and contralateral supraorbital area (cathode) on clinical pain severity and mobility performance in persons with knee osteoarthritis: An experimenter- and participant-blinded, randomized, sham-controlled pilot clinical study. *Brain Stimulation*, 10(5):902–909. [Cited on page 25]

Ai, Q., Li, J., Li, M., Jiang, W., and Wang, B. (2010). A new transcranial magnetic stimulation coil design to improve the focality. In *2010 3rd International Conference on Biomedical Engineering and Informatics*, volume 4, pages 1391–1395. [Cited on page 169]

Alam, M., Truong, D. Q., Khadka, N., and Bikson, M. (2016). Spatial and polarity precision of concentric high-definition transcranial direct current stimulation (HD-tDCS). *Physics in Medicine and Biology*. [Cited on page 24]

Alia, C., Spalletti, C., Lai, S., Panarese, A., Lamola, G., Bertolucci, F., Vallone, F., Di Garbo, A., Chisari, C., Micera, S., and Caleo, M. (2017). Neuroplastic changes following brain ischemia and their contribution to stroke recovery: Novel approaches in neurorehabilitation. *Frontiers in Cellular Neuroscience*, 11(March):1–22. [Cited on page 39]

Allen, A., Villard, S., Corbacio, M., Goulet, D., Plante, M., Souques, M., Deschamps, F., Ostiguy, G., Lambrozo, J., Thomas, A. W., and Legros, A. (2016). Impact of electromagnetic fields on human vestibular system and standing balance: Pilot results and future developments. *IOP Conference Series: Materials Science and Engineering*, 120(1). [Cited on page 113]

Amassian, V. E., Stewart, M., Quirk, G. J., and Rosenthal, J. L. (1987). Physiological basis of motor effects of a transient stimulus to cerebral cortex. [Cited on page 165]

Andre-Obadia, N., Magnin, M., Simon, E., and Garcia-Larrea, L. (2018). Somatotopic effects of rTMS in neuropathic pain? A comparison between stimulation over hand and face motor areas. *European Journal of Pain (United Kingdom)*, 22(4):707–715. [Cited on page 37]

Andreuccetti, D. and Zoppetti, N. (2006). Quasi-static electromagnetic dosimetry: From basic principles to examples of applications. *International journal of occupational safety and ergonomics : JOSE*, 12:201–15. [Cited on page 48]

Antal, A. and Paulus, W. (2013). Transcranial alternating current stimulation (tacs). *Frontiers in Human Neuroscience*, 7:317. [Cited on page 17]

Aonuma, S., Gomez-Tames, J., Laakso, I., Hirata, A., Takakura, T., Tamura, M., and Muragaki, Y. (2018). A high-resolution computational localization method for transcranial magnetic stimulation mapping. *NeuroImage*, 172(May):85–93. [Cited on page 67]

Aparício, L. V., Guarienti, F., Razza, L. B., Carvalho, A. F., Fregni, F., and Brunoni, A. R. (2016). A Systematic Review on the Acceptability and Tolerability of Transcranial Direct Current Stimulation Treatment in Neuropsychiatry Trials. [Cited on page 21]

Apollonio, F., Liberti, M., Paffi, A., Merla, C., Marracino, P., Denzi, A., Marino, C., and d'Inzeo, G. (2013). Feasibility for microwaves energy to affect biological systems via non-thermal mechanisms: A systematic approach. *IEEE TRANSACTIONS ON MICROWAVE THEORY AND TECHNIQUES*, 61:2031–2045. [Cited on page 122]

Arai, N., Muller-Dahlhaus, F., Murakami, T., Bliem, B., Lu, M. K., Ugawa, Y., and Ziemann, U. (2011). State-dependent and timing-dependent bidirectional associative plasticity in the human sma-m1 network. *J Neurosci*, 31(43):15376–83. [Cited on page 172]

Armitage, D. W., LeVeen, H. H., and Pethig, R. (1983). Radiofrequency-induced hyperthermia: computer simulation of specific absorption rate distributions using realistic anatomical models. *Physics in Medicine and Biology*, 28(1):31–42. [Cited on page 51]

Armstrong, S. J. (1978). *J. Armstrong, Long-range Forecasting: From Crystal Ball to Computer*. Wiley Interscience, Canada, 2nd edition. [Cited on pages 65, 73]

Arumugham, S. S., Vs, S., Hn, M., B, V., Ravi, M., Sharma, E., Thirthalli, J., and Reddy, Y. J. (2018). Augmentation Effect of Low-Frequency Repetitive Transcranial Magnetic Stimulation over Presupplementary Motor Area in Obsessive-Compulsive Disorder: A Randomized Controlled Trial. *Journal of ECT*, 34(4):253–257. [Cited on page 40]

Ashkan, K., Rogers, P., Bergman, H., and Ughratdar, I. (2017). Insights into the mechanisms of deep brain stimulation. *Nature Reviews Neurology*, 13(9):548–554. [Cited on page 15]

Ashrafi, A., Mohseni-Bandpei, M. A., and Seydi, M. (2020). The effect of tDCS on the fatigue in patients with multiple sclerosis: A systematic review of randomized controlled clinical trials. *Journal of Clinical Neuroscience*, 78:277–283. [Cited on pages 28, 29]

Attal, N., Ayache, S. S., Ciampi De Andrade, D., Mhalla, A., Baudic, S., Jazat, F., Ahdab, R., Neves, D. O., Sorel, M., Lefaucheur, J. P., and Bouhassira, D. (2016). Repetitive transcranial

magnetic stimulation and transcranial direct-current stimulation in neuropathic pain due to radiculopathy: A randomized sham-controlled comparative study. *Pain*. [Cited on pages 26, 37]

Ba, F., Zhou, Y., Zhou, J., and Chen, X. (2019). Repetitive transcranial magnetic stimulation protects mice against 6-OHDA-induced Parkinson's disease symptoms by regulating brain amyloid β1–42 level. *Molecular and Cellular Biochemistry*, 458(1-2):71–78. [Cited on page 166]

Bagheri Hosseinabadi, M., Khanjani, N., Ebrahimi, M. H., Haji, B., and Abdolahfard, M. (2019). The effect of chronic exposure to extremely low-frequency electromagnetic fields on sleep quality, stress, depression and anxiety. *Electromagnetic Biology and Medicine*, 38(1):96–101. [Cited on page 110]

Bais, L., Liemburg, E., Vercammen, A., Bruggeman, R., Knegtering, H., and Aleman, A. (2017). Effects of low frequency rTMS treatment on brain networks for inner speech in patients with schizophrenia and auditory verbal hallucinations. *Progress in Neuro-Psychopharmacology and Biological Psychiatry*, 78(February):105–113. [Cited on page 62]

Banerjee, P. K. and Butterfield, R. (1981). *Boundary element methods in engineering science*. McGraw-Hill, London. [Cited on page 51]

Barker, A. T. (1991). An introduction to the basic principles of magnetic nerve stimulation. *J Clin Neurophysiol*, 8(1):26–37. [Cited on page 173]

Barker, A. T., Brown, B. H., and Freeston, I. L. (1979). Determination of the distribution of conduction velocities in human nerve trunks. *IEEE Transactions on Biomedical Engineering*, BME-26(2):76–81. [Cited on page 12]

Barker, A. T., Jalinous, R., and Freeston, I. L. (1985). Non-invasive magnetic stimulation of human motor cortex. *Lancet*, 1(8437):1106–7. [Cited on page 13]

Barth, A., Ponocny, I., Ponocny-Seliger, E., Vana, N., and Winker, R. (2010). Effects of extremely low-frequency magnetic field exposure on cognitive functions: Results of a meta-analysis. *Bioelectromagnetics*, 31(3):173–179. [Cited on page 113]

Bashar, R., Li, Y., and Wen, P. (2008). Influence of white matter inhomogeneous anisotropy on EEG forward computing. *Australasian Physical and Engineering Sciences in Medicine*, 31(2):122–130. [Cited on page 93]

Bashir, S., Perez, J. M., Horvath, J. C., and Pascual-Leone, A. (2013). Differentiation of motor cortical representation of hand muscles by navigated mapping of optimal tms current directions in healthy subjects. *J Clin Neurophysiol*, 30(4):390–5. [Cited on page 85]

Bastani, A. and Jaberzadeh, S. (2013). a-tdcs differential modulation of corticospinal excitability: the effects of electrode size. *Brain Stimul*, 6(6):932–7. [Cited on page 23]

Baumer, F. M., Pfeifer, K., Fogarty, A., Pena-Solorzano, D., Rolle, C. E., Wallace, J. L., Rotenberg, A., and Fisher, R. S. (2020). Cortical excitability, synaptic plasticity, and cognition in benign epilepsy with centrotemporal spikes: A pilot tms-emg-eeg study. *J Clin Neurophysiol*, 37(2):170–180. [Cited on page 172]

Beaulieu, L. D. and Schneider, C. (2015). Repetitive peripheral magnetic stimulation to reduce pain or improve sensorimotor impairments: A literature review on parameters of application and afferents recruitment. *Neurophysiologie Clinique*, 45(3):223–237. [Cited on page 172]

Bennabi, D. and Haffen, E. (2018). Transcranial direct current stimulation (tDCS): A promising treatment for major depressive disorder? *Brain Sciences*, 8(5):1–10. [Cited on page 27]

Bestmann, S., Ruff, C. C., Blankenburg, F., Weiskopf, N., Driver, J., and Rothwell, J. C. (2008). Mapping causal interregional influences with concurrent tms-fmri. *Exp Brain Res*, 191(4):383–402. [Cited on page 172]

Bhattacharjee, S., Kashyap, R., Rapp, B., Oishi, K., Desmond, J. E., and Chen, S. H. (2019). Simulation Analyses of tDCS Montages for the Investigation of Dorsal and Ventral Pathways. *Scientific Reports*, 9(1):1–17. [Cited on page 22]

Bikson, M., Grossman, P., Thomas, C., Zannou, A. L., Jiang, J., Adnan, T., Mourdoukoutas, A. P., Kronberg, G., Truong, D., Boggio, P., Brunoni, A. R., Charvet, L., Fregni, F., Fritsch, B., Gillick, B., Hamilton, R. H., Hampstead, B. M., Jankord, R., Kirton, A., Knotkova, H., Liebetanz, D., Liu, A., Loo, C., Nitsche, M. A., Reis, J., Richardson, J. D., Rotenberg, A., Turkeltaub, P. E., and Woods, A. J. (2016). Safety of Transcranial Direct Current Stimulation: Evidence Based Update 2016. [Cited on page 21]

Bikson, M., Inoue, M., Akiyama, H., Deans, J. K., Fox, J. E., Miyakawa, H., and Jefferys, J. G. (2004). Effect of uniform extracellular DC electric fields on excitability in rat hippocampal slices in vitro. *Journal of Physiology*, 557(1):175–190. [Cited on page 19]

Bikson, M., Paulus, W., Esmaeilpour, Z., Kronberg, G., and Nitsche, M. A. (2019). *Mechanisms of Acute and After Effects of Transcranial Direct Current Stimulation*, pages 81–113. Springer International Publishing, Cham. [Cited on page 19]

Bindman, L. J., Lippold, O. C., and Redfearn, J. W. (1964). The action of brief polarizing currents on the cerebral cortex of the rat (1) during current flow and (2) in the production of long-lasting after-effects. *The Journal of Physiology*. [Cited on page 20]

Biou, E., Cassoudesalle, H., Cogne, M., Sibon, I., De Gabory, I., Dehail, P., Aupy, J., and Glize, B. (2019). Transcranial direct current stimulation in post-stroke aphasia rehabilitation: A systematic review. *Ann Phys Rehabil Med*, 62(2):104–121. [Cited on pages 16, 28]

Birgersson, U., Birgersson, E., Nicander, I., and Ollmar, S. (2013). A methodology for extracting the electrical properties of human skin. *Physiological Measurement*, 34(6):723–736. [Cited on page 70]

Bischoff, C., Riescher, H., Machetanz, J., Meyer, B. U., and Conrad, B. (1995). Comparison of various coils used for magnetic stimulation of peripheral motor nerves: physiological considerations and consequences for diagnostic use. *Electroencephalography and Clinical Neurophysiology/ Electromyography*, 97(6):332–340. [Cited on page 187]

Blumberger, D. M., Maller, J. J., Thomson, L., Mulsant, B. H., Rajji, T. K., Maher, M., Brown, P. E., Downar, J., Vila-Rodriguez, F., Fitzgerald, P. B., and Daskalakis, Z. J. (2016). Unilateral and bilateral MRI-targeted repetitive transcranial magnetic stimulation for treatmentresistant depression: A randomized controlled study. *Journal of Psychiatry and Neuroscience*, 41(4):E58–E66. [Cited on page 36]

Boggio, P. S., Bermpohl, F., Vergara, A. O., Muniz, A. L., Nahas, F. H., Leme, P. B., Rigonatti, S. P., and Fregni, F. (2007). Go-no-go task performance improvement after anodal transcranial DC stimulation of the left dorsolateral prefrontal cortex in major depression. *Journal of Affective Disorders*, 101(1-3):91–98. [Cited on page 27]

Boggio, P. S., Rigonatti, S. P., Ribeiro, R. B., Myczkowski, M. L., Nitsche, M. A., Pascual-Leone, A., and Fregni, F. (2008). A randomized, double-blind clinical trial on the efficacy of cortical direct current stimulation for the treatment of major depression. *International Journal of Neuropsychopharmacology*, 11(2):249–254. [Cited on page 27]

Bonmassar, G., Lee, S. W., Freeman, D. K., Polasek, M., Fried, S. I., and Gale, J. T. (2012). Microscopic magnetic stimulation of neural tissue. *Nature Communications*, 3(March):910–921. [Cited on pages 169, 173, 188, 195]

Boonzaier, J., Petrov, P. I., Otte, W. M., Smirnov, N., Neggers, S. F., and Dijkhuizen, R. M. (2020). Design and Evaluation of a Rodent-Specific Transcranial Magnetic Stimulation Coil: An In Silico and In Vivo Validation Study. *Neuromodulation*, 23(3):324–334. [Cited on page 167]

Boonzaier, J., van Tilborg, G. A., Neggers, S. F., and Dijkhuizen, R. M. (2018). Noninvasive Brain Stimulation to Enhance Functional Recovery After Stroke: Studies in Animal Models. *Neurorehabilitation and Neural Repair*, 32(11):927–940. [Cited on pages 166, 167]

Borckardt, J. J., Reeves, S. T., Milliken, C., Carter, B., Epperson, T. I., Gunselman, R. J., Madan, A., Del Schutte, H., Demos, H. A., and George, M. S. (2017). Prefrontal versus motor cortex transcranial direct current stimulation (tDCS) effects on post-surgical opioid use. *Brain Stimulation*, 10(6):1096–1101. [Cited on page 25]

Borges, H., Dufau, A., Paneri, B., Woods, A. J., Knotkova, H., and Bikson, M. (2019). Updated technique for reliable, easy, and tolerated transcranial electrical stimulation including transcranial direct current stimulation. *Journal of Visualized Experiments*, 2020(155). [Cited on pages v, 22]

Boutros, N. N., Mucci, A., Diwadkar, V., and Tandon, R. (2014). Negative symptoms in schizophrenia: A comprehensive review of electrophysiological investigations. 8(1). [Cited on page 41]

Brasil-Neto, J. P., Cohen, L. G., Panizza, M., Nilsson, J., Roth, B. J., and Hallett, M. (1992). Optimal focal transcranial magnetic activation of the human motor cortex: Effects of coil orientation, shape of the induced current pulse, and stimulus intensity. *Journal of Clinical Neurophysiology*, 9(1):132–136. [Cited on page 194]

Brighina, F., Curatolo, M., Cosentino, G., De Tommaso, M., Battaglia, G., Sarzi-Puttini, P. C., Guggino, G., and Fierro, B. (2019). Brain modulation by electric currents in fibromyalgia: A structured review on non-invasive approach with transcranial electrical stimulation. *Frontiers in Human Neuroscience*, 13:40. [Cited on page 26]

Brunoni, A. R., Chaimani, A., Moffa, A. H., Razza, L. B., Gattaz, W. F., Daskalakis, Z. J., and Carvalho, A. F. (2017). Repetitive transcranial magnetic stimulation for the acute treatment of major depressive episodes a systematic review with network meta-analysis. *JAMA Psychiatry*, 74(2):143–152. [Cited on pages 35, 36]

Brunoni, A. R., Ferrucci, R., Fregni, F., Boggio, P. S., and Priori, A. (2012). Transcranial direct current stimulation for the treatment of major depressive disorder: A summary of preclinical, clinical and translational findings. 39(1):9–16. [Cited on page 27]

Brunoni, A. R. and Palm, U. (2019). *Transcranial Direct Current Stimulation in Psychiatry: Mood Disorders, Schizophrenia and Other Psychiatric Diseases*, pages 431–471. Springer International Publishing, Cham. [Cited on pages 43, 63]

Bungert, A., Antunes, A., Espenhahn, S., and Thielscher, A. (2017). Where does TMS Stimulate the Motor Cortex? Combining Electrophysiological Measurements and Realistic Field Estimates to Reveal the Affected Cortex Position. *Cerebral Cortex*, 27(11):5083–5094. [Cited on pages 44, 48, 62, 63, 68]

Cacace, F., Mineo, D., Viscomi, M. T., Latagliata, E. C., Mancini, M., Sasso, V., Vannelli, A., Pascucci, T., Pendolino, V., Marcello, E., Pelucchi, S., Puglisi-Allegra, S., Molinari, M., Picconi, B., Calabresi, P., and Ghiglieri, V. (2017). Intermittent theta-burst stimulation rescues dopamine-dependent corticostriatal synaptic plasticity and motor behavior in experimental parkinsonism: Possible role of glial activity. *Movement Disorders*, 32(7):1035–1046. [Cited on page 166]

Cambiaghi, M. and Parent, A. (2018). From Aldini's galvanization of human bodies to the Modern Prometheus. *Medicina Historica*, 2(1):27–37. [Cited on pages 9, 10, 11]

Camera, F., Paffi, A., Thomas, A. W., Apollonio, F., D'Inzeo, G., Prato, F. S., and Liberti, M. (2015). The CNP signal is able to silence a supra threshold neuronal model. *Frontiers in Computational Neuroscience*, 9(April):1–11. [Cited on pages viii, 115]

Çan, M. K., Laakso, I., Nieminen, J. O., Murakami, T., and Ugawa, Y. (2019). Coil model comparison for cerebellar transcranial magnetic stimulation. *Biomedical Physics and Engineering Express*, 5(1). [Cited on page 52]

Cantone, M., Lanza, G., Vinciguerra, L., Puglisi, V., Ricceri, R., Fisicaro, F., Vagli, C., Bella, R., Ferri, R., Pennisi, G., Di Lazzaro, V., and Pennisi, M. (2019). Age, height, and sex on motor evoked potentials: Translational data from a large italian cohort in a clinical environment. *Frontiers in Human Neuroscience*, 13(June):1–20. [Cited on page 33]

Cao, X., Deng, C., Su, X., and Guo, Y. (2018). Response and remission rates following high-frequency vs. Low-frequency repetitive transcranial magnetic stimulation (rTMS) over right DLPFC for treating major depressive disorder (MDD): A meta-analysis of randomized, double-blind trials. *Frontiers in Psychiatry*, 9(SEP):1–7. [Cited on page 36]

Capone, F., Corbetto, M., Barbato, C., Pellegrino, G., Di Pino, G., Assenza, G., Setti, S., Cadossi, R., and Di Lazzaro, V. (2014). An open label, one arm, dose escalation study to evaluate the safety of extremely low frequency magnetic fields in acute ischemic stroke. *Austin Journal of Cerebrovascular Disease & Stroke*, 1:01–04. [Cited on page 124]

Capone, F., Dileone, M., Profice, P., Pilato, F., Musumeci, G., Minicuci, G., Ranieri, F., Cadossi, R., Setti, S., Tonali, P. A., and Di Lazzaro, V. (2009). Does exposure to extremely low frequency magnetic fields produce functional changes in human brain? *Journal of Neural Transmission*, 116(3):257–265. [Cited on pages 116, 122, 125, 147]

Capone, F., Liberti, M., Apollonio, A., Camera, F., Setti, S., Cadossi, R., Quattrocchi, C. C., and Di Lazzaro, V. (2017). An open-label, one-arm, dose escalation study to evaluate safety and tolerability of extremely low frequency magnetic fields in acute ischemic stroke. *Scientific Reports*, 7:1245. [Cited on pages 117, 122, 123, 125, 126, 137, 138, 144, 147, 206]

Capone, F., Pellegrino, G., Motolese, F., Rossi, M., Musumeci, G., and Di Lazzaro, V. (2020). Extremely Low Frequency Magnetic Fields Do Not Affect LTP-Like Plasticity in Healthy Humans. *Frontiers in Human Neuroscience*, 14(February):1–6. [Cited on page 116]

Carmi, L., Alyagon, U., Barnea-Ygael, N., Zohar, J., Dar, R., and Zangen, A. (2018). Clinical and electrophysiological outcomes of deep TMS over the medial prefrontal and anterior cingulate cortices in OCD patients. *Brain Stimulation*. [Cited on pages 40, 41, 62, 172, 194]

Carmi, L., Tendler, A., Bystritsky, A., Hollander, E., Blumberger, D. M., Daskalakis, J., Ward, H., Lapidus, K., Goodman, W., Casuto, L., Feifel, D., Barnea-Ygael, N., Roth, Y., Zangen, A., and Zohar, J. (2019). Efficacy and safety of deep transcranial magnetic stimulation for obsessive-compulsive disorder: A prospective multicenter randomized double-blind placebo-controlled trial. *American Journal of Psychiatry*, 176(11):931–938. [Cited on pages 40, 41, 76]

Carnevale, N. T. and Hines, M. L. (2006). *The NEURON book*. Cambridge University Press, Cambridge, UK. [Cited on page 184]

Cash, R. F., Isayama, R., Gunraj, C. A., Ni, Z., and Chen, R. (2015). The influence of sensory afferent input on local motor cortical excitatory circuitry in humans. *Journal of Physiology*, 593(7):1667–1684. [Cited on page 31]

Cash, R. F., Noda, Y., Zomorrodi, R., Radhu, N., Farzan, F., Rajji, T. K., Fitzgerald, P. B., Chen, R., Daskalakis, Z. J., and Blumberger, D. M. (2017). Characterization of Glutamatergic and GABA A-Mediated Neurotransmission in Motor and Dorsolateral Prefrontal Cortex Using Paired-Pulse TMS-EEG. *Neuropsychopharmacology*, 42(2):502–511. [Cited on page 31]

Castillo-Saavedra, L., Gebodh, N., Bikson, M., Diaz-Cruz, C., Brandao, R., Coutinho, L., Truong, D., Datta, A., Shani-Hershkovich, R., Weiss, M., Laufer, I., Reches, A., Peremen, Z., Geva, A., Parra, L. C., and Fregni, F. (2016). Clinically Effective Treatment of Fibromyalgia Pain with High-Definition Transcranial Direct Current Stimulation: Phase II Open-Label Dose Optimization. *Journal of Pain*, 17(1):14–26. [Cited on page 26]

Castillo Saavedra, L., Mendonca, M., and Fregni, F. (2014). Role of the primary motor cortex in the maintenance and treatment of pain in fibromyalgia. *Medical Hypotheses*, 83(3):332–336. [Cited on pages 25, 26]

Caulfield, K. A., Badran, B. W., DeVries, W. H., Summers, P. M., Kofmehl, E., Li, X., Borckardt, J. J., Bikson, M., and George, M. S. (2020). Transcranial electrical stimulation motor threshold can estimate individualized tDCS dosage from reverse-calculation electric-field modeling. *Brain Stimulation*, 13(4):961–969. [Cited on page 44]

Cavaleri, R., Schabrun, S. M., and Chipchase, L. S. (2017). The number of stimuli required to reliably assess corticomotor excitability and primary motor cortical representations using transcranial magnetic stimulation (TMS): A systematic review and meta-analysis. *Systematic Reviews*, 6(1):1–11. [Cited on pages 85, 165]

Chang, W. H., Kim, M. S., Cho, J. W., Youn, J., Kim, Y. K., Kim, S. W., Lee, A., and Kim, Y. H. (2016). Effect of cumulative repetitive transcranial magnetic stimulation on freezing of gait in patients with atypical parkinsonism: A pilot study. *Journal of Rehabilitation Medicine*, 48(9):824–828. [Cited on page 41]

Chase, H. W., Boudewyn, M. A., Carter, C. S., and Phillips, M. L. (2020). Transcranial direct current stimulation: a roadmap for research, from mechanism of action to clinical implementation. *Molecular Psychiatry*, 25(2):397–407. [Cited on page 20]

Chen and Mogul, D. J. (2010). Using increased structural detail of the cortex to improve the accuracy of modeling the effects of transcranial magnetic stimulation on neocortical activation. *IEEE Transactions on Biomedical Engineering*, 57 (5):1216–1226. [Cited on pages 55, 63, 70, 122]

Chen, K. H. S. and Chen, R. (2019). Invasive and Noninvasive Brain Stimulation in Parkinson's Disease: Clinical Effects and Future Perspectives. *Clinical Pharmacology and Therapeutics*, 106(4):763–775. [Cited on page 62]

Chen, X. L., Benkler, S., Chavannes, N., De Santis, V., Bakker, J., van Rhoon, G., Mosig, J., and Kuster, N. (2013). Analysis of human brain exposure to low-frequency magnetic fields: A numerical assessment of spatially averaged electric fields and exposure limits. *Bioelectromagnetics*, 34(5):375–384. [Cited on pages 76, 78]

Chervyakov, A. V., Chernyavsky, A. Y., Sinitsyn, D. O., and Piradov, M. A. (2015). Possible Mechanisms Underlying the Therapeutic Effects of Transcranial Magnetic Stimulation. *Frontiers in Human Neuroscience*, 9(June):1–14. [Cited on pages 32, 43]

Chistyakov, A. V., Kreinin, B., Marmor, S., Kaplan, B., Khatib, A., Darawsheh, N., Koren, D., Zaaroor, M., and Klein, E. (2015). Preliminary assessment of the therapeutic efficacy of continuous theta-burst magnetic stimulation (cTBS) in major depression: A double-blind sham-controlled study. *Journal of Affective Disorders*, 170:225–229. [Cited on page 36]

Chistyakov, A. V., Rubicsek, O., Kaplan, B., Zaaroor, M., and Klein, E. (2010). Safety, tolerability and preliminary evidence for antidepressant efficacy of theta-burst transcranial magnetic stimulation in patients with major depression. *International Journal of Neuropsychopharmacology*, 13(3):387–393. [Cited on page 36]

Cho, S. I., Nam, Y. S., Chu, L. Y., Lee, J. H., Bang, J. S., Kim, H. R., Kim, H. C., Lee, Y. J., Kim, H. D., Sul, J. D., Kim, D., Chung, Y. H., and Jeong, J. H. (2012). Extremely low-frequency magnetic fields modulate nitric oxide signaling in rat brain. *Bioelectromagnetics*, 33(7):568–574. [Cited on page 110]

Chou, Y. H., Hickey, P. T., Sundman, M., Song, A. W., and Chen, N. K. (2015). Effects of repetitive transcranial magnetic stimulation on motor symptoms in parkinson disease: A systematic review and meta-analysis. *JAMA Neurology*, 72(4):432–440. [Cited on page 41]

Chowdhury, F. A., Caciagli, L., Whatley, B. P., McLaughlin, C., Sanders, B., Wehner, T., and Diehl, B. (2020). Preoperative language mapping using navigated TMS compared with extra-operative direct cortical stimulation using intracranial electrodes: A case report. *Seizure*, 76:96–99. [Cited on page 165]

Christ, A., Kainz, W., Eckhart, G. H., Honneger, K., Zeffer, M., Neufeld, E., Rascher, W., Rolf, J., Bautz, W., Chen, J., Kiefer, B., Schmitt, P., Hollenbach, H. P., Shen, J., Oberle, M., Szczerba, D., Kam, A., Guag, J. W., and Kuster, N. (2010). The virtual family: development of surface-based anatomical models of two adults and two children for dosimetric simulations. *Physics in Medicine and Biology*, 55 (2):N23–N38. [Cited on pages 56, 66, 71, 124, 131, 136]

Chung, Y. H., Lee, Y. J., Lee, H. S., Chung, S. J., Lim, C. H., Oh, K. W., Sohn, U. D., Park, E. S., and Jeong, J. H. (2015). Extremely low frequency magnetic field modulates the level of neurotransmitters. *Korean Journal of Physiology and Pharmacology*, 19(1):15–20. [Cited on pages 109, 110]

Cincotta, M., Borgheresi, A., Balestrieri, F., Giovannelli, F., Ragazzoni, A., Vanni, P., Benvenuti, F., Zaccara, G., and Ziemann, U. (2006). Mechanisms underlying mirror movements in Parkinson's disease: A transcranial magnetic stimulation study. *Movement Disorders*, 21(7):1019–1025. [Cited on pages 172, 194]

Cincotta, M. and Ziemann, U. (2008). Neurophysiology of unimanual motor control and mirror movements. [Cited on pages 76, 172, 194]

Cirillo, G., Di Pino, G., Capone, F., Ranieri, F., Florio, L., Todisco, V., Tedeschi, G., Funke, K., and Di Lazzaro, V. (2017). Neurobiological after-effects of non-invasive brain stimulation. 10(1):1–18. [Cited on page 27]

Civardi, C., Vicentini, R., Collini, A., Boccagni, C., Cantello, R., and Monaco, F. (2009). Motor cortical organization in an adult with hemimegalencephaly and late onset epilepsy. *Neuroscience Letters*. [Cited on pages 172, 194]

Cobos Sánchez, C., Garcia-Pacheco, F. J., Rodriguez, J. M. G., and Hill, J. R. (2018). An inverse boundary element method computational framework for designing optimal TMS coils. *Engineering Analysis with Boundary Elements*, 88(April 2017):156–169. [Cited on page 51]

Colella, M., Camera, F., Capone, F., Setti, S., Cadossi, R., Di Lazzaro, V., Apollonio, F., and Liberti, M. (2020). Patient Semi-specific Computational Modeling of Electromagnetic Stimulation Applied to Neuroprotective Treatments in Acute Ischemic Stroke. *Scientific Reports*, 10(1):1–12. [Cited on page 64]

Colella, M., Paffi, A., Fontana, S., Rossano, F., De Santis, V., Apollonio, F., and Liberti, M. (2019). Influence of Anatomical Model and Skin Conductivity on the Electric Field Induced in the Head by Transcranial Magnetic Stimulation. *Proceedings of the Annual International Conference of the IEEE Engineering in Medicine and Biology Society, EMBS*, pages 2917–2920. [Cited on pages 65, 76]

Comeau, R. (2014). Neuronavigation for transcranial magnetic stimulation. In *Transcranial Magnetic Stimulation*, chapter 3, pages 31–56. Springer, New York. [Cited on pages 63, 86, 87, 103]

Cook, C. M., Saucier, D. M., Thomas, A. W., and Prato, F. S. (2006). Exposure to ELF magnetic and ELF-modulated radiofrequency fields: The time course of physiological and cognitive effects observed in recent studies (2001-2005). *Bioelectromagnetics*, 27(8):613–627. [Cited on pages 112, 113]

Cook, C. M., Saucier, D. M., Thomas, A. W., and Prato, F. S. (2009). Changes in human EEG alpha activity following exposure to two different pulsed magnetic field sequences. *Bioelectromagnetics*, 30(1):9–20. [Cited on page 115]

Cook, C. M., Thomas, A. W., Keenliside, L., and Prato, F. S. (2005). Resting EEG effects during exposure to a pulsed ELF magnetic field. *Bioelectromagnetics*, 26(5):367–376. [Cited on page 115]

Cook, C. M., Thomas, A. W., and Prato, F. S. (2002). Human Electrophysiological and Cognitive Effects of Exposure to ELF Magnetic and ELF Modulated RF and Microwave Fields: A Review of Recent Studies. *Bioelectromagnetics*, 23(2):144–157. [Cited on pages 107, 112]

Cook, C. M., Thomas, A. W., and Prato, F. S. (2004). Resting EEG Is Affected by Exposure to a Pulsed ELF Magnetic Field. *Bioelectromagnetics*, 25(3):196–203. [Cited on page 115]

Crasson, M. (2003). 50-60 Hz electric and magnetic field effects on cognitive function in humans: A review. *Radiation Protection Dosimetry*, 106(4):333–340. [Cited on page 112]

Croarkin, P. E., Wall, C. A., and Lee, J. (2011). Applications of transcranial magnetic stimulation (TMS) in child and adolescent psychiatry. *International Review of Psychiatry*, 23(5):445–453. [Cited on page 76]

Crosson, B., McGregor, K., Gopinath, K. S., Conway, T. W., Benjamin, M., Chang, Y. L., Moore, A. B., Raymer, A. M., Briggs, R. W., Sherod, M. G., Wierenga, C. E., and White, K. D. (2007). Functional MRI of language in aphasia: A review of the literature and the methodological challenges. [Cited on page 40]

Csifcsák, G., Boayue, N. M., Puonti, O., Thielscher, A., and Mittner, M. (2018). Effects of transcranial direct current stimulation for treating depression: A modeling study. *Journal of Affective Disorders*, 234:164–173. [Cited on pages 27, 48]

Cury, R. G., Fraix, V., Castrioto, A., Pérez Fernández, M. A., Krack, P., Chabardes, S., Seigneuret, E., Alho, E. J. L., Benabid, A.-L., and Moro, E. (2017). Thalamic deep brain

stimulation for tremor in parkinson disease, essential tremor, and dystonia. *Neurology*, 89(13):1416–1423. [Cited on page 15]

Da Silva, A. F., Volz, M. S., Bikson, M., and Fregni, F. (2011). Electrode positioning and montage in transcranial direct current stimulation. *Journal of visualized experiments : JoVE*, (51). [Cited on page 19]

Da Silva, R. d. M. F., Batistuzzo, M. C., Shavitt, R. G., Miguel, E. C., Stern, E., Mezger, E., Padberg, F., D'Urso, G., and Brunoni, A. R. (2019). Transcranial direct current stimulation in obsessive-compulsive disorder: an update in electric field modeling and investigations for optimal electrode montage. *Expert Review of Neurotherapeutics*, 19(10):1025–1035. [Cited on page 22]

D'Agata, F., Cicerale, A., Mingolla, A., Caroppo, P., Orsi, L., Mortara, P., Troni, W., and Pinessi, L. (2015). Double-cone coil TMS stimulation of the medial cortex inhibits central pain habituation. *PLoS ONE*, 10(6). [Cited on page 38]

Daskalakis, Z. J., Dimitrova, J., McClintock, S. M., Sun, Y., Voineskos, D., Rajji, T. K., Goldbloom, D. S., Wong, A. H., Knyahnytska, Y., Mulsant, B. H., Downar, J., Fitzgerald, P. B., and Blumberger, D. M. (2020). Magnetic seizure therapy (MST) for major depressive disorder. *Neuropsychopharmacology*, 45(2):276–282. [Cited on page 18]

Datta, A., Baker, J. M., Bikson, M., and Fridriksson, J. (2011). Individualized model predicts brain current flow during transcranial direct-current stimulation treatment in responsive stroke patient. *Brain Stimulation*, 4(3):169–174. [Cited on pages 45, 63]

Datta, A., Bansal, V., Diaz, J., Patel, J., Reato, D., and Bikson, M. (2009). Gyri-precise head model of transcranial direct current stimulation: improved spatial focality using a ring electrode versus conventional rectangular pad. *Brain stimulation*, 2(4):201–7, 207.e1. [Cited on pages 23, 24, 54, 63]

Datta, A., Bikson, M., and Fregni, F. (2010). Transcranial direct current stimulation in patients with skull defects and skull plates: High-resolution computational FEM study of factors altering cortical current flow. *NeuroImage*, 52(4):1268–1278. [Cited on pages 45, 63]

Datta, A., Zhou, X., Su, Y., Parra, L. C., and Bikson, M. (2013). Validation of finite element model of transcranial electrical stimulation using scalp potentials: Implications for clinical dose. *Journal of Neural Engineering*, 10(3). [Cited on pages 64, 70]

Davanipour, Z., Tseng, C.-C., Lee, P.-J., Markides, K. S., and Sobel, E. (2013). Severe Cognitive Dysfunction and Occupational Extremely Low Frequency Magnetic Field Exposure among Elderly Mexican Americans. *British Journal of Medicine and Medical Research*, 4(8). [Cited on page 113]

David, M. C. M. M., de Moraes, A. A., da Costa, M. L., and Franco, C. I. F. (2018). Transcranial direct current stimulation in the modulation of neuropathic pain: a systematic review. *Neurological Research*, 40(7):557–565. [Cited on page 63]

Dawson, T. W., Caputa, K., and Stuchly, M. A. (1998). High-resolution organ dosimetry for human exposure to low-frequency electric fields. *IEEE Transactions on Power Delivery*, 13(2):366–373. [Cited on page 68]

De Geeter, N., Crevecoeur, G., and Dupre, L. (2011). An efficient 3-d eddy-current solver using an independent impedance method for transcranial magnetic stimulation. *IEEE Transactions onBiomedical Engineering*, 58 (2):310–320. [Cited on pages 122, 123]

De Lucia, M., Parker, G. J., Embleton, K., Newton, J. M., and Walsh, V. (2007). Diffusion tensor MRI-based estimation of the influence of brain tissue anisotropy on the effects of transcranial magnetic stimulation. *NeuroImage*, 36(4):1159–1170. [Cited on pages 52, 59, 64, 70, 103]

De Paz, R. H., Serrano-Muñoz, D., Pérez-Nombela, S., Bravo-Esteban, E., Avendaño-Coy, J., and Gómez-Soriano, J. (2019). Combining transcranial direct-current stimulation with gait training in patients with neurological disorders: A systematic review. *Journal of NeuroEngineering and Rehabilitation*, 16(1):4–11. [Cited on page 28]

De Raedt, R., Vanderhasselt, M. A., and Baeken, C. (2015). Neurostimulation as an intervention for treatment resistant depression: From research on mechanisms towards targeted neurocognitive strategies. *Clinical Psychology Review*, 41:61–69. [Cited on page 35]

De Santis, V. and Chen, X. L. (2014). On the issues related to compliance assessment of ICNIRP 2010 basic restrictions. *Journal of Radiological Protection*, 34(2). [Cited on pages 59, 73]

De Santis, V., Chen, X. L., Cruciani, S., Campi, T., and Feliziani, M. (2016). A novel homogenization procedure to model the skin layers in LF numerical dosimetry. *Physics in Medicine and Biology*, 61:4402–4411. [Cited on pages 59, 64, 66, 76]

De Santis, V., Chen, X. L., Laakso, I., and Hirata, A. (2015). An equivalent skin conductivity model for low-frequency magnetic field dosimetry. *Biomedical Physics & Engineering Express*, 1(1):015201. [Cited on pages 65, 66, 68, 76, 78]

De Witte, S., Klooster, D., Dedoncker, J., Duprat, R., Remue, J., and Baeken, C. (2018). Left prefrontal neuronavigated electrode localization in tDCS: 10–20 EEG system versus MRI-guided neuronavigation. *Psychiatry Research - Neuroimaging*, 274(May 2017):1–6. [Cited on page 63]

Delvendahl, I., Lindemann, H., Jung, N. H., Pechmann, A., Siebner, H. R., and Mall, V. (2014). Influence of waveform and current direction on Short-interval intracortical facilitation: A Paired-pulse TMS study. *Brain Stimulation*, 7(1):49–58. [Cited on page 31]

Demirkazik, A., Ozdemir, E., Arslan, G., Taskiran, A. S., and Pelit, A. (2019). The effects of extremely low-frequency pulsed electromagnetic fields on analgesia in the nitric oxide pathway. *Nitric Oxide - Biology and Chemistry*, 92(January):49–54. [Cited on page 110]

Deng, Z. D., Lisanby, S. H., and Peterchev, A. V. (2013). Electric field depth-focality tradeoff in transcranial magnetic stimulation: Simulation comparison of 50 coil designs. *Brain Stimulation*, 6(1):1–13. [Cited on pages xii, 33, 63, 167, 168, 173, 183, 194]

Devlin, J. T. and Watkins, K. E. (2007). Stimulating language: Insights from TMS. *Brain*, 130(3):610–622. [Cited on page 85]

Dey, S., Bose, S., Kumar, S., Rathore, R., Mathur, R., and Jain, S. (2017). Extremely low frequency magnetic field protects injured spinal cord from the microglia- and iron-induced tissue damage. *Electromagnetic Biology and Medicine*, 36(4):330–340. [Cited on page 109]

Di Lazzaro, V., Capone, F., Apollonio, A., Borea, P. A., Cadossi, R., Fassina, L., Grassi, C., Liberti, M., Paffi, A., Parazzini, M., Varani, K., and Ravazzani, P. (2013). A consensus panel review of central nervous system effects of the exposure to low−intensity extremely low−frequency magnetic fields. *Brain Stimulation*, 6:469–476. [Cited on pages 18, 107, 108, 111, 113, 122]

Di Lazzaro, V., Oliviero, A., Pilato, F., Saturno, E., Dileone, M., Mazzone, P., Insola, A., Tonali, P. A., and Rothwell, J. C. (2004). The physiological basis of transcranial motor cortex stimulation in conscious humans. 115(2):255–266. [Cited on page 30]

Di Lazzaro, V., Pilato, F., Dileone, M., Ranieri, F., Ricci, V., Profice, P., Bria, P., Tonali, P. A., and Ziemann, U. (2006a). GABAA receptor subtype specific enhancement of inhibition in human motor cortex. *Journal of Physiology*, 575(3):721–726. [Cited on page 31]

Di Lazzaro, V., Pilato, F., Oliviero, A., Dileone, M., Saturno, E., Mazzone, P., Insola, A., Profice, P., Ranieri, F., Capone, F., Tonali, P. A., and Rothwell, J. C. (2006b). Origin of facilitation of motor-evoked potentials after paired magnetic stimulation: Direct recording of epidural activity in conscious humans. *Journal of Neurophysiology*, 96(4):1765–1771. [Cited on page 31]

Di Lazzaro, V., Restuccia, D., Oliviero, A., Profice, P., Ferrara, L., Insola, A., Mazzone, P., Tonali, P., and Rothwell, J. C. (1998). Magnetic transcranial stimulation at intensities below active motor threshold activates intracortical inhibitory circuits. *Experimental Brain Research*, 119(2):265–268. [Cited on page 30]

Di Lazzaro, V., Rothwell, J., and Capogna, M. (2018). Noninvasive Stimulation of the Human Brain: Activation of Multiple Cortical Circuits. *Neuroscientist*, 24(3):246–260. [Cited on pages 29, 30, 31, 35]

Dimbylow, P. (2005). Development of the female voxel phantom, NAOMI, and its application to calculations of induced current densities and electric fields from applied low frequency magnetic and electric fields. *Physics in Medicine and Biology*, 50(6):1047–1070. [Cited on page 68]

Dimbylow, P. J. (1998). Induced current densities from low-frequency magnetic fields in a 2 mm resolution, anatomically realistic model of the body. *Physics in Medicine and Biology*, 43(2):221–230. [Cited on page 68]

D'Inzeo, G., Esselle, K. P., Pisa, S., and Stuchly, M. A. (1995). Comparison of homogeneous and heterogeneous tissue models for coil optimization in neural stimulation. *Radio Science*, 30(1):245–253. [Cited on pages 49, 51]

Djordjevic, N. Z., Paunović, M. G., and Peulić, A. S. (2017). Anxiety-like behavioural effects of extremely low-frequency electromagnetic field in rats. *Environmental Science and Pollution Research*, 24(27):21693–21699. [Cited on page 110]

Dmochowski, J. P., Datta, A., Bikson, M., Su, Y., and Parra, L. C. (2011). Optimized multi-electrode stimulation increases focality and intensity at target. *Journal of Neural Engineering*, 8(4):046011. [Cited on page 24]

Dobbs, B., Pawlak, N., Biagioni, M., Agarwal, S., Shaw, M., Pilloni, G., Bikson, M., Datta, A., and Charvet, L. (2018). Generalizing remotely supervised transcranial direct current stimulation (tDCS): Feasibility and benefit in Parkinson's disease. *Journal of NeuroEngineering and Rehabilitation*, 15(1):1–8. [Cited on page 63]

Dodd, K. C., Nair, V. A., and Prabhakaran, V. (2017). Role of the contralesional vs. ipsilesional hemisphere in stroke recovery. *Frontiers in Human Neuroscience*, 11:469. [Cited on page 39]

Dones, I. and Levi, V. (2018). Spinal cord stimulation for neuropathic pain: Current trends and future applications. *Brain Sciences*, 8(8). [Cited on page 16]

Du, J., Tian, L., Liu, W., Hu, J., Xu, G., Ma, M., Fan, X., Ye, R., Jiang, Y., Yin, Q., Zhu, W., Xiong, Y., Yang, F., and Liu, X. (2016). Effects of repetitive transcranial magnetic stimulation on motor recovery and motor cortex excitability in patients with stroke: a randomized controlled trial. *European Journal of Neurology*, 23(11):1666–1672. [Cited on page 39]

Duprat, R., Desmyter, S., Rudi, D. R., Van Heeringen, K., Van Den Abbeele, D., Tandt, H., Bakic, J., Pourtois, G., Dedoncker, J., Vervaet, M., Van Autreve, S., Lemmens, G. M., and Baeken, C. (2016). Accelerated intermittent theta burst stimulation treatment in medication-resistant major depression: A fast road to remission? *Journal of Affective Disorders*, 200:6–14. [Cited on page 36]

Ebrahimi, M., Seraj, M., Ardebili, K. M., Khoshdel, A., and Barzoki, H. S. (2019). The effects of extremely low-frequency electromagnetic field on depression, anxiety, thyroid hormones, and gene expression in mice. *Activitas Nervosa Superior Rediviva*, 61(3-4):148–154. [Cited on page 109]

Elsner, B., Kugler, J., and Mehrholz, J. (2018). Transcranial direct current stimulation (tDCS) for upper limb rehabilitation after stroke: Future directions. 11 Medical and Health Sciences 1109 Neurosciences Alan Godfrey; Rodrigo Vitorio. *Journal of NeuroEngineering and Rehabilitation*, 15(1):10–13. [Cited on page 63]

Epstein, C. M., Meador, K. J., Loring, D. W., Wright, R. J., Weissman, J. D., Sheppard, S., Lah, J. J., Puhalovich, F., Gaitan, L., and Davey, K. R. (1999). Localization and characterization of speech arrest during transcranial magnetic stimulation. *Clinical Neurophysiology.* [Cited on page 194]

Espinosa, J. M., Liberti, M., Lagroye, I., and Veyret, B. (2006). Exposure to AC and DC magnetic fields induces changes in 5-HT1B receptor binding parameters in rat brain membranes. *Bioelectromagnetics*, 27(5):414–422. [Cited on page 108]

Fagerlund, A. J., Hansen, O. A., and Aslaksen, P. M. (2015). Transcranial direct current stimulation as a treatment for patients with fibromyalgia: A randomized controlled trial. *Pain*, 156(1):62–71. [Cited on page 26]

Famm, K., Litt, B., Tracey, K. J., Boyden, E. S., and Slaoui, M. (2013). Drug discovery: A jump-start for electroceuticals. *Nature*, 496(7444):159–161. [Cited on pages 3, 9, 13, 122, 138]

Fang, X., Liu, M., Lu, C., Zhao, Y., and Liu, X. (2019). Current status and potential application of navigated transcranial magnetic stimulation in neurosurgery: A literature review. *Chinese Neurosurgical Journal*, 5(1):1–7. [Cited on page 87]

Feng Liu, Huawei Zhao, and Crozier, S. (2003). On the induced electric field gradients in the human body for magnetic stimulation by gradient coils in mri. *IEEE Transactions on Biomedical Engineering*, 50(7):804–815. [Cited on page 51]

Fertonani, A., Ferrari, C., and Miniussi, C. (2015). What do you feel if I apply transcranial electric stimulation? Safety, sensations and secondary induced effects. *Clinical Neurophysiology*. [Cited on page 21]

Fiocchi, S., Chiaramello, E., Luzi, L., Ferrulli, A., Bonato, M., Roth, Y., Zangen, A., Ravazzani, P., and Parazzini, M. (2018a). Deep transcranial magnetic stimulation for the addiction treatment: Electric field distribution modeling. *IEEE Journal of Electromagnetics, RF and Microwaves in Medicine and Biology*, 2(4):242–248. [Cited on page 57]

Fiocchi, S., Chiaramello, E., Parazzini, M., and Ravazzani, P. (2018b). Influence of tissue conductivity on foetal exposure to extremely low frequency magnetic fields at 50 Hz using stochastic dosimetry. *PLoS ONE*, 13(2):1–17. [Cited on pages 45, 48]

Fiocchi, S., Chiaramello, E., Ravazzani, P., and Parazzini, M. (2018c). Modelling of the Current Density Distributions during Cortical Electric Stimulation for Neuropathic Pain Treatment. *Computational and Mathematical Methods in Medicine*, 2018:1–12. [Cited on pages 45, 48, 63, 67]

Fiocchi, S., Parazzini, M., Liorni, I., Roth, Y., Zangen, A., and Ravazzani, P. (2015). Deep transcranial magnetic stimulation for the treatment of neuropsychiatric disorders in elderly people: Electric field assessment. *Proceedings of the 2015 International Conference on Electromagnetics in Advanced Applications, ICEAA 2015*, pages 448–451. [Cited on pages 34, 45, 52]

Fiocchi, S., Ravazzani, P., Priori, A., and Parazzini, M. (2016). Cerebellar and Spinal Direct Current Stimulation in Children: Computational Modeling of the Induced Electric Field. *Frontiers in Human Neuroscience*, 10(October):1–13. [Cited on page 55]

Fisicaro, F., Lanza, G., Grasso, A. A., Pennisi, G., Bella, R., Paulus, W., and Pennisi, M. (2019). Repetitive transcranial magnetic stimulation in stroke rehabilitation: review of the current evidence and pitfalls. *Therapeutic Advances in Neurological Disorders*, 12. [Cited on pages 39, 62]

Fitzgerald, P. B., Fountain, S., and Daskalakis, Z. J. (2006). A comprehensive review of the effects of rTMS on motor cortical excitability and inhibition. [Cited on page 194]

Fitzgibbon, B. M., Hoy, K. E., Knox, L. A., Guymer, E. K., Littlejohn, G., Elliot, D., Wambeek, L. E., McQueen, S., Elford, K. A., Lee, S. J., Enticott, P. G., and Fitzgerald, P. B. (2018). Evidence for the improvement of fatigue in fibromyalgia: A 4-week left dorsolateral prefrontal cortex repetitive transcranial magnetic stimulation randomized-controlled trial. *European Journal of Pain (United Kingdom)*, 22(7):1255–1267. [Cited on page 38]

Flamand, V. H. and Schneider, C. (2014). Noninvasive and painless magnetic stimulation of nerves improved brain motor function and mobility in a cerebral palsy case. *Archives of Physical Medicine and Rehabilitation*. [Cited on page 172]

Fleming, M. K., Rothwell, J. C., Sztriha, L., Teo, J. T., and Newham, D. J. (2017). The effect of transcranial direct current stimulation on motor sequence learning and upper limb function after stroke. *Clinical Neurophysiology*, 128(7):1389–1398. [Cited on page 22]

Fleming, M. K., Theologis, T., Buckingham, R., and Johansen-Berg, H. (2018). Transcranial direct current stimulation for promoting motor function in cerebral palsy: A review. *Journal of NeuroEngineering and Rehabilitation*, 15(1):1–8. [Cited on page 63]

Foerster, Á. S., Rezaee, Z., Paulus, W., Nitsche, M. A., and Dutta, A. (2018). Effects of cathode location and the size of anode on anodal transcranial direct current stimulation over the leg motor area in healthy humans. *Frontiers in Neuroscience*, 12(JUL):1–12. [Cited on pages 22, 45, 54]

Fox, M. D., Buckner, R. L., Liu, H., Chakravarty, M. M., Lozano, A. M., and Pascual-Leone, A. (2014). Resting-state networks link invasive and noninvasive brain stimulation across diverse psychiatric and neurological diseases. *Proceedings of the National Academy of Sciences*, 111(41):E4367. [Cited on page 172]

Fregni, F., Boggio, P. S., Lima, M. C., Ferreira, M. J., Wagner, T., Rigonatti, S. P., Castro, A. W., Souza, D. R., Riberto, M., Freedman, S. D., Nitsche, M. A., and Pascual-Leone, A. (2006a). A sham-controlled, phase II trial of transcranial direct current stimulation for the treatment of central pain in traumatic spinal cord injury. *Pain*, 122(1-2):197–209. [Cited on page 26]

Fregni, F., Boggio, P. S., Nitsche, M. A., Rigonatti, S. P., and Pascual-Leone, A. (2006b). Cognitive effects of repeated sessions of transcranial direct current stimulation in patients with depression [1]. [Cited on page 27]

Fregni, F., Boggio, P. S., Santos, M. C., Lima, M., Vieira, A. L., Rigonatti, S. P., Silva, M. T. A., Barbosa, E. R., Nitsche, M. A., and Pascual-Leone, A. (2006c). Noninvasive cortical stimulation with transcranial direct current stimulation in Parkinson's disease. *Movement Disorders*, 21(10):1693–1702. [Cited on page 63]

Fregni, F., El-Hagrassy, M. M., Pacheco-Barrios, K., Carvalho, S., Leite, J., Simis, M., Brunelin, J., Nakamura-Palacios, E. M., Marangolo, P., Venkatasubramanian, G., San-Juan, D., Caumo, W., Bikson, M., and Brunoni, A. R. (2020). Evidence-based guidelines and

secondary meta-analysis for the use of transcranial direct current stimulation (tDCS) in neurological and psychiatric disorders. *International Journal of Neuropsychopharmacology.* [Cited on pages 19, 20, 21, 24, 25, 26, 27, 28]

Fregni, F., Priori, A., Celnik, P., Stagg, C., Nitsche, M., Antal, A., Wenderoth, N., Liebetanz, D., Reato, D., Paulus, W., Brunoni, A., Bikson, M., Cohen, L., Miniussi, C., Knotkova, H., Miranda, P., Woods, A., Boggio, P., Kappenman, E., and Herrmann, C. (2015). *A technical guide to tDCS, and related non-invasive brain stimulation tools*, volume 127. International Federation of Clinical Neurophysiology. [Cited on page 19]

Fried, P. J., Jannati, A., Davila-Pérez, P., and Pascual-Leone, A. (2017). Reproducibility of single-pulse, paired-pulse, and intermittent theta-burst TMS measures in healthy aging, Type-2 diabetes, and Alzheimer's disease. *Frontiers in Aging Neuroscience*, 9(AUG):1–13. [Cited on page 29]

Friedman, L. M., Furberg, C. D., DeMets, D., Reboussin, D. M., and Granger, C. B. (2015). *Fundamentals of Clinical Trials.* Springer International Publishing, 5 edition. [Cited on pages 138, 206]

Fröhlich, F., Burrello, T. N., Mellin, J. M., Cordle, A. L., Lustenberger, C. M., Gilmore, J. H., and Jarskog, L. F. (2016). Exploratory study of once-daily transcranial direct current stimulation (tDCS) as a treatment for auditory hallucinations in schizophrenia. *European Psychiatry.* [Cited on pages 28, 63]

Funke, K. (2017). T009 Animal models of brain stimulation – TMS. In *Clinical Neurophysiology*, volume 128, pages e3–e4. [Cited on pages 166, 167]

Gabriel, C. (1997). Comments on 'dielectric properties of the skin'. *Physics in medicine and biology*, 42(8):1671–3. [Cited on page 70]

Gabriel, C., Peyman, A., and Grant, E. H. (2009). Electrical conductivity of tissue at frequencies below 1 MHz. [Cited on pages 58, 64, 67, 68]

Gabriel, S., Lau, R. W., and Gabriel, C. (1996). The dielectric properties of biological tissues: II. Measurements in the frequency range 10 Hz to 20 GHz. *Physics in Medicine and Biology*, 41(11):2251–2269. [Cited on pages 58, 59, 64, 66, 67, 71, 72]

Gaines, J. L., Finn, K. E., Slopsema, J. P., Heyboer, L. A., and Polasek, K. H. (2018). A model of motor and sensory axon activation in the median nerve using surface electrical stimulation. *Journal of Computational Neuroscience*, 45(1):29–43. [Cited on pages 184, 186]

Galhardoni, R., Da Silva, V. A., García-Larrea, L., Dale, C., Baptista, A. F., Barbosa, L. M., Bahia Menezes, L. M., De Siqueira, S. R., Valério, F., Rosi, J., De Lima Rodrigues, A. L., Mendes Fernandes, D. T. R., Lorencini Selingardi, P. M., Marcolin, M. A., De Souza Duran, F. L., Ono, C. R., Lucato, L. T., Fernandes, A. M. B., Da Silva, F. E., Yeng, L. T., Brunoni, A. R., Buchpiguel, C. A., Teixeira, M. J., and De Andrade, D. C. (2019). Insular and anterior cingulate cortex deep stimulation for central neuropathic pain disassembling the percept of pain. *Neurology*, 92(18):E2165–E2175. [Cited on page 38]

Gammaitoni, L., Hanggi, P., Jung, P., and Marchesoni, F. (1998). Stochastic resonance. *Reviews of Modern Physics*, 70(1):223–287. [Cited on page 62]

Geddes, L. A. (1991). History of magnetic stimulation of the nervous system. *Journal of Clinical Neurophysiology*, 8(1):3–9. [Cited on page 12]

Geddes, L. A. and Baker, L. E. (1967). The specific resistance of biological material-A compendium of data for the biomedical engineer and physiologist. *Medical and biological engineering*, 5(3):271–293. [Cited on page 58]

Gessi, S., Merighi, S., Bencivenni, S., Battistello, E., Vincenzi, F., Setti, S., Cadossi, M., Borea, P. A., Cadossi, R., and Varani, K. (2019). Pulsed electromagnetic field and relief of hypoxia-induced neuronal cell death: The signaling pathway. *Journal of Cellular Physiology*, 234(9):15089–15097. [Cited on page 112]

Gessi, S., Merighi, S., and Varani, K. (2018). *Adenosine Receptors: The Status of the Art*, pages 1–11. Springer International Publishing, Cham. [Cited on page 111]

Ghione, S., Del Seppia, C., Mezzasalma, L., Emdin, M., and Luschi, P. (2004). Human Head Exposure to a 37 Hz Electromagnetic Field: Effects on Blood Pressure, Somatosensory Perception, and Related Parameters. *Bioelectromagnetics*, 25(3):167–175. [Cited on page 114]

Gobbi, A., Lad, D., Petrera, M., and Karnatzikos, G. (2014). Symptomatic Early Osteoarthritis of the Knee Treated With Pulsed Electromagnetic Fields: Two-Year Follow-up. *Cartilage*, 5(2):78–85. [Cited on page 116]

Gomez, L. J., Dannhauer, M., Koponen, L. M., and Peterchev, A. V. (2020). Conditions for numerically accurate TMS electric field simulation. *Brain Stimulation*, 13(1):157–166. [Cited on pages 44, 48, 51, 52, 53, 57, 63, 64, 70]

Gomez, L. J., Goetz, S. M., and Peterchev, A. V. (2018). Design of transcranial magnetic stimulation coils with optimal trade-off between depth, focality, and energy. *Journal of Neural Engineering*, 15(4):1–31. [Cited on pages xii, 58, 65, 167, 168, 169, 187]

Gomez, L. J., Hernandez-Garcia, L., Grbic, A., and Michielssen, E. (2013). Single-source multicoil transcranial magnetic stimulators for deep and focused stimulation of the human brain. In *2013 USNC-URSI Radio Science Meeting (Joint with AP-S Symposium)*, pages 8–8. [Cited on page 167]

Gomez Palacio Schjetnan, A., Faraji, J., Metz, G. A., Tatsuno, M., and Luczak, A. (2013). Transcranial direct current stimulation in stroke rehabilitation: a review of recent advancements. *Stroke Res Treat*, 2013:170256. [Cited on page 28]

Gomez-Tames, J., Hamasaka, A., Laakso, I., Hirata, A., and Ugawa, Y. (2018). Atlas of optimal coil orientation and position for TMS: A computational study. *Brain Stimulation*, 11(4):839–848. [Cited on page 45]

Gomez-Tames, J., Laakso, I., Murakami, T., Ugawa, Y., Ugawa, Y., and Hirata, A. (2020). TMS activation site estimation using multiscale realistic head models. *Journal of Neural Engineering*, 17(3). [Cited on page 44]

Gosselin, M., Neufeld, E., Blumenfeld-Katzir, T., Moser, H., Huber, E., Farcito, S., Gerber, L., Jedensjo, H., Hilber, I., Di Gennaro, F., and Lloyd, B. (2014). Development of a new generation of high-resolution anatomical models for medical device evaluation: the virtual population 3.0. *Physics in medicin and biology*, 59:5287. [Cited on pages 56, 64, 71, 131, 136, 144, 153, 155, 184, 190, 196, 201, 205, 207]

Graham, C., Cook, M. R., Cohen, H. D., Riffle, D. W., Hoffman, S., and Gerkovich, M. M. (1999). Human exposure to 60-Hz magnetic fields: Neurophysiological effects. *International Journal of Psychophysiology*, 33(2):169–175. [Cited on page 107]

Grant, G., Cadossi, R., and Steinberg, G. (1994). Protection against focal cerebral ischemia following exposure to a pulsed electromagnetic field. *Bioelectromagnetics*, 15:205–216. [Cited on pages 107, 111, 121]

Guan, Y. Z., Li, J., Zhang, X. W., Wu, S., Du, H., Cui, L. Y., and Zhang, W. H. (2017). Effectiveness of repetitive transcranial magnetic stimulation (rTMS) after acute stroke: A one-year longitudinal randomized trial. *CNS Neuroscience and Therapeutics*, 23(12):940–946. [Cited on page 40]

Guerra, A., Ranieri, F., Falato, E., Musumeci, G., Di Santo, A., Asci, F., Di Pino, G., Suppa, A., Berardelli, A., and Di Lazzaro, V. (2020). Detecting cortical circuits resonant to high-frequency oscillations in the human primary motor cortex: a TMS-tACS study. *Scientific Reports*, 10(1):1–11. [Cited on page 33]

Güllmar, D., Haueisen, J., and Reichenbach, J. R. (2010). Influence of anisotropic electrical conductivity in white matter tissue on the EEG/MEG forward and inverse solution. A high-resolution whole head simulation study. *NeuroImage*, 51(1):145–163. [Cited on pages 59, 92]

Gunduz, M. E., Pinto, C. B., Velez, F. G. S., Duarte, D., Pacheco-Barrios, K., Lopes, F., and Fregni, F. (2020). Motor cortex reorganization in limb amputation: A systematic review of TMS motor mapping studies. *Frontiers in Neuroscience*, 14(April). [Cited on pages 85, 165]

Habib, S., Hamid, U., Jamil, A., Zainab, A. Z., Yousuf, T., Habib, S., Tariq, S. M., and Ali, F. (2018). Transcranial Magnetic Stimulation as a Therapeutic Option for Neurologic and Psychiatric Illnesses. *Cureus*, 10(10):e3456–e3456. [Cited on page 62]

Hallez, H., Vanrumste, B., Van Hese, P., D'Asseler, Y., Lemahieu, I., and Van De Walle, R. (2005). A finite difference method with reciprocity used to incorporate anisotropy in electroencephalogram dipole source localization. *Physics in Medicine and Biology*, 50(16):3787–3806. [Cited on page 94]

Hand, B. J., Opie, G. M., Sidhu, S. K., and Semmler, J. G. (2020). TMS coil orientation and muscle activation influence lower limb intracortical excitability. *Brain Research*, 1746(March):147027. [Cited on page 30]

Hannula, H. and Ilmoniemi, R. J. (2017). *Basic Principles of Navigated TMS*, pages 3–29. Springer International Publishing, Cham. [Cited on pages 86, 87]

Hannula, H., Ylioja, S., Pertovaara, A., Korvenoja, A., Ruohonen, J., Ilmoniemi, R. J., and Carlson, S. (2005). Somatotopic blocking of sensation with navigated transcranial magnetic stimulation of the primary somatosensory cortex. *Human Brain Mapping*, 26(2):100–109. [Cited on pages 63, 87]

Hasgall, P., Di Gennaro, F., Baumgartner, C., Neufeld, E., Lloyd, B., Gosselin, M., Payne, D., Klingenböck, A., and Kuster, N. (2018). IT'IS Database for thermal and electromagnetic parameters of biological tissues, Version 4.0. [Cited on pages 58, 66, 67, 68, 72, 95, 156, 181]

Hasgall, P. A., Neufeld, E., Gosselin, M. C., Klingenbck, A., and Kuster, N. (September, 2015). Itis database for thermal and electromagnetic parameters of biological tissues, version 3.0. *www.itis.ethz.ch/database*. [Cited on pages 64, 124]

Haueisen, J., Ramon, C., Eiselt, M., Brauer, H., and Nowak, H. (1997). Influence of tissue resistivities on neuromagnetic fields and electric potentials studied with a finite element model of the head. *IEEE Transactions on Biomedical Engineering*, 44(8):727–735. [Cited on pages 68, 69]

He, H., Lu, J., Yang, L., Zheng, J., Gao, F., Zhai, Y., Feng, J., Fan, Y., and Ma, X. (2017). Repetitive transcranial magnetic stimulation for treating the symptoms of schizophrenia: A PRISMA compliant meta-analysis. *Clinical Neurophysiology*, 128(5):716–724. [Cited on page 41]

He, Q., Xiao, K., Peng, L., Lai, J., Li, H., Luo, D., and Wang, K. (2019). An Effective Meta-analysis of Magnetic Stimulation Therapy for Urinary Incontinence. *Scientific Reports*, 9(1):1–10. [Cited on page 62]

Herrmann, C., Rach, S., Neuling, T., and Strüber, D. (2013). Transcranial alternating current stimulation: a review of the underlying mechanisms and modulation of cognitive processes. *Frontiers in Human Neuroscience*, 7:279. [Cited on page 17]

Hill, A. T., Rogasch, N. C., Fitzgerald, P. B., and Hoy, K. E. (2017). Effects of prefrontal bipolar and high-definition transcranial direct current stimulation on cortical reactivity and working memory in healthy adults. *NeuroImage*. [Cited on page 24]

Hirata, A., Takano, Y., Fujiwara, O., Dovan, T., and Kavet, R. (2011). An electric field induced in the retina and brain at threshold magnetic flux density causing magnetophosphenes. *Physics in Medicine and Biology*, 56(13):4091–4101. [Cited on page 68]

Hirata, A., Yanase, K., Laakso, I., Chan, K., Fujiwara, O., Nagaoka, T., Watanabe, S., Conil, E., and Wiart, J. (2012). Estimation of the whole-body averaged sar of grounded human models for plane wave exposure at respective resonance frequencies. *Physics in medicine and biology*, 57:8427–8442. [Cited on page 51]

Hodaj, H., Alibeu, J. P., Payen, J. F., and Lefaucheur, J. P. (2015). Treatment of chronic facial pain including cluster headache by repetitive transcranial magnetic stimulation of the motor cortex with maintenance sessions: A naturalistic study. *Brain Stimulation*, 8(4):801–807. [Cited on page 37]

Holdefer, R. N., Sadleir, R., and Russell, M. J. (2006). Predicted current densities in the brain during transcranial electrical stimulation. *Clinical Neurophysiology*, 117(6):1388–1397. [Cited on page 69]

Holzer, M. and Padberg, F. (2010). Intermittent theta burst stimulation (iTBS) ameliorates therapy-resistant depression: A case series. *Brain Stimulation*, 3(3):181–183. [Cited on page 36]

Horn, C. C., Ardell, J. L., and Fisher, L. E. (2019). Electroceutical targeting of the autonomic nervous system. *Physiology*, 34(2):150–162. [Cited on pages 13, 15]

Horvath, J. C., Najib, U., and Press, D. Z. (2014). Transcranial Magnetic Stimulation (TMS) Clinical Applications: Therapeutics. In *Transcranial Magnetic Stimulation*, pages 235–257. Springer, New York. [Cited on page 62]

Horvath, J. C., Perez, J. M., Forrow, L., Fregni, F., and Pascual-Leone, A. (2011). Transcranial magnetic stimulation: A historical evaluation and future prognosis of therapeutically relevant ethical concerns. *Journal of Medical Ethics*, 37(3):137–143. [Cited on pages 13, 194]

Hovey, C. and Jalinous, R. (2006). The guide to magnetic stimulation. *Magstim*, 20(4):284–287. [Cited on pages 168, 194]

Howell, B. and McIntyre, C. (2017). Role of soft-tissue heterogeneity in computational models of deep brain stimulation. *BRAIN STIMULATION*, 10(1):46–50. [Cited on page 122]

Hoyer, E. H. and Celnik, P. A. (2011). Understanding and enhancing motor recovery after stroke using transcranial magnetic stimulation. *Restorative Neurology and Neuroscience*, 29(6):395–409. [Cited on page 39]

Hsu, K. H. and Durand, D. M. (2001). A 3-D differential coil design for localized magnetic stimulation. *IEEE Transactions on Biomedical Engineering*, 48(10):1162–1168. [Cited on page 187]

Htet, A. T., Saturnino, G. B., Burnham, E. H., Noetscher, G. M., Nummenmaa, A., and Makarov, S. N. (2019). Comparative performance of the finite element method and the boundary element fast multipole method for problems mimicking transcranial magnetic stimulation (TMS). *Journal of Neural Engineering*, 16(2). [Cited on pages 51, 52]

Hu, H., Yang, W., Zeng, Q., Chen, W., Zhu, Y. B., Liu, W., Wang, S., Wang, B., Shao, Z., and Zhang, Y. (2020). Promising application of Pulsed Electromagnetic Fields (PEMFs) in musculoskeletal disorders. *Biomedicine and Pharmacotherapy*, 131:110767. [Cited on page 114]

Hu, Y. X., Zhang, T., Rajah, G. B., Stone, C., xu Liu, L., jie He, J., Shan, L., yu Yang, L., Liu, P., Gao, F., qi Yang, Y., li Wu, X., qing Ye, C., and dong Chen, Y. (2018). Effects of different frequencies of repetitive transcranial magnetic stimulation in stroke patients with non-fluent aphasia: a randomized, sham-controlled study. *Neurological Research*, 40(6):459–465. [Cited on page 40]

Huang, Y., Liu, A. A., Lafon, B., Friedman, D., Dayan, M., Wang, X., Bikson, M., Doyle, W. K., Devinsky, O., and Parra, L. C. (2017). Measurements and models of electric fields in the in vivo human brain during transcranial electric stimulation. *eLife*, 6:1–26. [Cited on pages 44, 58, 59, 65, 78]

Hughes, S. W., Ward, G., and Strutton, P. H. (2020). Anodal transcranial direct current stimulation over the primary motor cortex attenuates capsaicin-induced dynamic mechanical allodynia and mechanical pain sensitivity in humans. *European Journal of Pain (United Kingdom)*, 24(6):1130–1137. [Cited on page 25]

Hummel, F., Celnik, P., Giraux, P., Floel, A., Wu, W. H., Gerloff, C., and Cohen, L. G. (2005). Effects of non-invasive cortical stimulation on skilled motor function in chronic stroke. *Brain*. [Cited on page 22]

Iacono, M., Neufeld, E., Akinnagbe, E., Bower, K., Wolf, J., Vogiatzis Oikonomidis, I., Sharma, D., Lloyd, B., Bertram, B., Wyss, M., Pruessmann, K., Jakab, A., Makris, N., Cohen, E., Kuster, N., Kainz, W., and Angelone, L. M. (2015). MIDA: A multimodal imaging-based detailed anatomical model of the human head and neck. *Plos One*, 10 (4):e0124126. [Cited on pages vi, 56, 57, 64, 66, 71, 132, 144, 181, 182, 205]

Iannetti, G. D. and Mouraux, A. (2010). From the neuromatrix to the pain matrix (and back). *Experimental Brain Research*, 205(1):1–12. [Cited on page 38]

ICNIRP (2010). Guidelines for limiting exposure to time-varying electric and magnetic fields (1 Hz TO 100 kHz). *Health Physics*, 99(6):818–836. [Cited on page 64]

Ilmoniemi, R., Ruohonen, J., and Karhu, J. (1999). Transcranial Magnetic Stimulation - A New Tool for Functional Imaging of the Brain. *Critical reviews in Biomedical Engeneering*, 27(3-5):241–284. [Cited on pages 33, 62]

Im, C. H., Jung, H. H., Choi, J. D., Lee, S. Y., and Jung, K. Y. (2008). Determination of optimal electrode positions for transcranial direct current stimulation (tDCS). *Physics in Medicine and Biology*, 53(11). [Cited on pages 55, 68]

Im, C. H., Park, J. H., Shim, M., Chang, W. H., and Kim, Y. H. (2012). Evaluation of local electric fields generated by transcranial direct current stimulation with an extracephalic reference electrode based on realistic 3D body modeling. *Physics in Medicine and Biology*, 57(8):2137–2150. [Cited on page 69]

Islam, N., Aftabuddin, M., Moriwaki, A., Hattori, Y., and Hori, Y. (1995a). Increase in the calcium level following anodal polarization in the rat brain. *Brain Research*. [Cited on page 20]

Islam, N., Moriwaki, A., Hattori, Y., Hayashi, Y., Lu, Y. F., and Hori, Y. (1995b). c-Fos expression mediated by N-methyl-D-aspartate receptors following anodal polarization in the rat brain. *Experimental Neurology*. [Cited on page 20]

Jaberzadeh, S., Bastani, A., and Zoghi, M. (2014). Anodal transcranial pulsed current stimulation: A novel technique to enhance corticospinal excitability. *Clinical Neurophysiology*, 125(2):344 – 351. [Cited on page 17]

Jahangard, L., Haghighi, M., Shyayganfard, M., Ahmadpanah, M., Sadeghi Bahmani, D., Bajoghli, H., Holsboer-Trachsler, E., and Brand, S. (2016). Repetitive Transcranial Magnetic Stimulation Improved Symptoms of Obsessive-Compulsive Disorder, but Also Cognitive Performance: Results from a Randomized Clinical Trial with a Cross-Over Design and Sham Condition. *Neuropsychobiology*, 73(4):224–232. [Cited on page 40]

Jales Junior, L. H., Costa, M. d. D. L., Jales Neto, L. H., Ribeiro, J. P. M., Freitas, W. J. S. d. N., and Teixeira, M. J. (2015). Transcranial direct current stimulation in fibromyalgia: effects on pain and quality of life evaluated clinically and by brain perfusion scintigraphy. *Revista Dor*, 16(1). [Cited on page 26]

Jamil, A. and Nitsche, M. A. (2017). What Effect Does tDCS Have on the Brain? Basic Physiology of tDCS. *Current Behavioral Neuroscience Reports*, 4(4):331–340. [Cited on pages 20, 21]

Janać, B., Tovilović, G., Tomić, M., Prolić, Z., and Radenović, L. (2009). Effect of continuous exposure to alternating magnetic field (50 Hz, 0.5 mT) on serotonin and dopamine receptors activity in rat brain. *General Physiology and Biophysics*, 28(SPECIAL ISSUES):33–40. [Cited on page 109]

Janssen, A. M., Oostendorp, T. F., and Stegeman, D. F. (2015). The coil orientation dependency of the electric field induced by TMS for M1 and other brain areas. *Journal of NeuroEngeneering and Rehabilitation*, 12(47):1–13. [Cited on pages 45, 58, 70, 73]

Janssen, A. M., Rampersad, S. M., Lucka, F., Lanfer, B., Lew, S., Aydin, Ü., Wolters, C. H., Stegeman, D. F., and Oostendorp, T. F. (2013). The influence of sulcus width on simulated electric fields induced by transcranial magnetic stimulation. *Physics in Medicine and Biology*, 58(14):4881–4896. [Cited on pages 45, 70]

Jardri, R., Pouchet, A., Pins, D., and Thomas, P. (2011). Cortical activations during auditory verbal hallucinations in schizophrenia: A coordinate-based meta-analysis. *American Journal of Psychiatry*, 168(1):73–81. [Cited on page 41]

Jennum, P., Friberg, L., Fuglsang-Frederiksen, A., and Dam, M. (1994). Speech localization using repetitive transcranial magnetic stimulation. *Neurology*, 44(2):269 LP – 269. [Cited on page 194]

Jeong, J. H., Kum, C., Choi, H. J., Park, E. S., and Sohn, U. D. (2006). Extremely low frequency magnetic field induces hyperalgesia in mice modulated by nitric oxide synthesis. *Life Sciences*, 78(13):1407–1412. [Cited on page 110]

Jin, J. (2014). *The Finite Element Method in Electromagnetics*. Wiley Interscience, Canada, 3rd edition. [Cited on page 49]

Johnson, R. L. and Wilson, C. G. (2018). A review of vagus nerve stimulation as a therapeutic intervention. *Journal of Inflammation Research*, 11:203–213. [Cited on page 15]

Kammer, T., Beck, S., Thielscher, A., Laubis-Herrmann, U., and Topka, H. (2011). Motor thresholds in humans: a transcranialmagnetic stimulation study comparing different pulse

waveforms, current directions and stimulator types. *Clinical Neurophysiology*, 112:250–258. [Cited on page 62]

Kang, J. I., Lee, H., Jhung, K., Kim, K. R., An, S. K., Yoon, K. J., Kim, S. I., Namkoong, K., and Lee, E. (2016). Frontostriatal connectivity changes in major depressive disorder after repetitive transcranial magnetic stimulation: A randomized Sham-Controlled study. *Journal of Clinical Psychiatry*, 77(9):e1137–e1143. [Cited on page 35]

Karhu, J., Hannula, H., Laine, J., and Ruohonen, J. (2014). *Navigated Transcranial Magnetic Stimulation: Principles and Protocol for Mapping the Motor Cortex*, pages 337–359. Springer New York, New York, NY. [Cited on page 85]

Karl, A., Birbaumer, N., Lutzenberger, W., Cohen, L. G., and Flor, H. (2001). Reorganization of motor and somatosensory cortex in upper extremity amputees with phantom limb pain. *Journal of Neuroscience*, 21(10):3609–3618. [Cited on pages 172, 194]

Kaster, T. S., Downar, J., Vila-Rodriguez, F., Thorpe, K. E., Feffer, K., Noda, Y., Giacobbe, P., Knyahnytska, Y., Kennedy, S. H., Lam, R. W., Daskalakis, Z. J., and Blumberger, D. M. (2019). Trajectories of response to dorsolateral prefrontal rTMS in major depression: A three-D study. *American Journal of Psychiatry*, 176(5):367–375. [Cited on page 36]

Kauffman, A. M., Firlik, A. D., Fukui, M. B.and Wechsler, L. R., Jungries, C. A., and Yonas, H. (1998). Ischemic core and penumbra in human stroke. *American Heart Association*, 30:93–99. [Cited on page 120]

Kavaliers, M., Choleris, E., Prato, F. S., and Ossenkopp, K. P. (1998). Evidence for the involvement of nitric oxide and nitric oxide synthase in the modulation of opioid-induced antinociception and the inhibitory effects of exposure to 60-Hz magnetic fields in the land snail. *Brain Research*, 809(1):50–57. [Cited on page 110]

Kayser, S., Bewernick, B. H., Matusch, A., Hurlemann, R., Soehle, M., and Schlaepfer, T. E. (2015). Magnetic seizure therapy in treatment-resistant depression: clinical, neuropsychological and metabolic effects. *Psychological Medicine*, 45(5):1073–1092. [Cited on page 18]

Kekic, M., Boysen, E., Campbell, I. C., and Schmidt, U. (2016). A systematic review of the clinical efficacy of transcranial direct current stimulation (tDCS) in psychiatric disorders. *Journal of Psychiatric Research*, 74:70–86. [Cited on pages 24, 63]

Kent, A. R. and Grill, W. M. (August, 2014). Analysis of deep brain stimulation electrode characteristics for neural recording. *Journal of Neural Engineering*, 11 (4):046010. [Cited on pages 127, 155]

Kessler, S. K., Turkeltaub, P. E., Benson, J. G., and Hamilton, R. H. (2012). Differences in the experience of active and sham transcranial direct current stimulation. *Brain Stimulation*. [Cited on page 22]

Khadka, N. and Bikson, M. (2020). Role of skin tissue layers and ultra-structure in transcutaneous electrical stimulation including tDCS. *Physics in Medicine and Biology*, 65(22). [Cited on page 58]

Khadka, N., Borges, H., Zannou, A. L., Jang, J., Kim, B., Lee, K., and Bikson, M. (2018). Dry tDCS: Tolerability of a novel multilayer hydrogel composite non-adhesive electrode for transcranial direct current stimulation. *Brain Stimulation*, 11(5):1044–1053. [Cited on page 23]

Khadka, N., Woods, A. J., and Bikson, M. (2019). *Transcranial Direct Current Stimulation Electrodes*, pages 263–291. Springer International Publishing, Cham. [Cited on pages 21, 23, 24]

Khedr, E. M., Gamal, N. F. E., El-Fetoh, N. A., Khalifa, H., Ahmed, E. M., Ali, A. M., Noaman, M., El-Baki, A. A., and Karim, A. A. (2014). A double-blind randomized clinical trial on the efficacy of cortical direct current stimulation for the treatment of alzheimer's disease. *Frontiers in Aging Neuroscience*, 6:275. [Cited on page 28]

Khedr, E. M., Kotb, H. I., Mostafa, M. G., Mohamad, M. F., Amr, S. A., Ahmed, M. A., Karim, A. A., and Kamal, S. M. (2015). Repetitive transcranial magnetic stimulation in neuropathic pain secondary to malignancy: A randomized clinical trial. *European Journal of Pain (United Kingdom)*, 19(4):519–527. [Cited on page 37]

Khedr, E. M., Omran, E. A., Ismail, N. M., El-Hammady, D. H., Goma, S. H., Kotb, H., Galal, H., Osman, A. M., Farghaly, H. S., Karim, A. A., and Ahmed, G. A. (2017). Effects of transcranial direct current stimulation on pain, mood and serum endorphin level in the treatment of fibromyalgia: A double blinded, randomized clinical trial. *Brain Stimulation*. [Cited on page 26]

Kim, D. H., Georghiou, G. E., and Won, C. (2006). Improved field localization in transcranial magnetic stimulation of the brain with the utilization of a conductive shield plate in the stimulator. *IEEE Transactions on Biomedical Engineering*, 53(4):720–725. [Cited on pages 167, 187]

Kim, M. S., Chang, W. H., Cho, J. W., Youn, J., Kim, Y. K., Kim, S. W., and Kim, Y. H. (2015). Efficacy of cumulative high-frequency rTMS on freezing of gait in Parkinson's disease. *Restorative Neurology and Neuroscience*, 33(4):521–530. [Cited on page 41]

Kim, Y. J., Ku, J., Kim, H. J., Im, D. J., Lee, H. S., Han, K. A., and Kang, Y. J. (2013). Randomized, sham controlled trial of transcranial direct current stimulation for painful diabetic polyneuropathy. *Annals of Rehabilitation Medicine*, 37(6):766–776. [Cited on page 25]

Klomjai, W., Lackmy-Vallée, A., Roche, N., Pradat-Diehl, P., Marchand-Pauvert, V., and Katz, R. (2015). Repetitive transcranial magnetic stimulation and transcranial direct current stimulation in motor rehabilitation after stroke: An update. [Cited on page 16]

Knotkova, H., Nitsche, M. A., Bikson, M., and Woods, A. J. (2019). *Practical Guide to Transcranial Direct Current Stimulation : Principles, Procedures and Applications*. [Cited on pages v, 14, 15, 62]

Kobayashi, M. and Pascual-Leone, A. (2003). Basic principles of magnetic stimulation. *The Lancet*, 2:145–156. [Cited on page 194]

Kohl, S., Hannah, R., Rocchi, L., Nord, C. L., Rothwell, J., and Voon, V. (2019). Cortical Paired Associative Stimulation Influences Response Inhibition: Cortico-cortical and Cortico-subcortical Networks. *Biological Psychiatry*, 85(4):355–363. [Cited on page 31]

Kon, T., Suzuki, C., Hotta, R., Funamizu, Y., Haga, R., Ueno, T., Nishijima, H., Arai, A., Nunomura, J., Nukada, H., Tomiyama, M., and Baba, M. (2017). Utility of nerve conduction studies for diagnosis of injury to the medial branch of the superficial radial nerve. *eNeurologicalSci*, 8:38–39. [Cited on page 179]

Koponen, L. M., Nieminen, J. O., and Ilmoniemi, R. J. (2015). Minimum-energy coils for transcranial magnetic stimulation: Application to focal stimulation. *Brain Stimulation*, 8(1):124–134. [Cited on page 167]

Koponen, L. M., Nieminen, J. O., and Ilmoniemi, R. J. (2018). Multi-locus transcranial magnetic stimulation-theory and implementation. *Brain Stimul*, 11(4):849–855. [Cited on page 172]

Koponen, L. M. and Peterchev, A. V. (2020). *Transcranial Magnetic Stimulation: Principles and Applications*, pages 245–270. Springer International Publishing, Cham. [Cited on pages 168, 169]

Krause, P., Förderreuther, S., and Straube, A. (2006). Tms motor cortical brain mapping in patients with complex regional pain syndrome type i. *Clinical neurophysiology*, 117(1):169–176. [Cited on page 172]

Kreis, P. G. and Fishman, S. M. (2009). *The Development of Spinal Cord Stimulation*, pages 1–9. Oxford University Press, New York. [Cited on page 16]

Krieg, S. M., Lioumis, P., Mäkelä, J. P., Wilenius, J., Karhu, J., Hannula, H., Savolainen, P., Lucas, C. W., Seidel, K., Laakso, A., Islam, M., Vaalto, S., Lehtinen, H., Vitikainen, A. M., Tarapore, P. E., and Picht, T. (2017). Protocol for motor and language mapping by navigated TMS in patients and healthy volunteers; workshop report. *Acta Neurochirurgica*, 159(7):1187–1195. [Cited on pages 63, 103, 165]

Kroenke, C. D. (2018). Using diffusion anisotropy to study cerebral cortical gray matter development. *Journal of Magnetic Resonance*, 292:106–116. [Cited on page 59]

Kujirai, T., Caramia, M. D., Rothwell, J. C., Day, B. L., Thompson, P. D., Ferbert, A., Wroe, S., Asselman, P., and Marsden, C. D. (1993). Corticocortical inhibition in human motor cortex. *The Journal of Physiology*, 471(1):501–519. [Cited on pages 30, 172]

Kumar, S., Singh, S., Parmar, A., Verma, R., and Kumar, N. (2018). Effect of high-frequency repetitive transcranial magnetic stimulation (rtms) in patients with comorbid panic disorder and major depression. *Australas Psychiatry*, 26(4):398–400. [Cited on pages 35, 62]

Kurokawa, Y., Nitta, H., Imai, H., and Kabuto, M. (2003). Can extremely low frequency alternating magnetic fields modulate heart rate or its variability in humans? *Autonomic Neuroscience: Basic and Clinical*, 105(1):53–61. [Cited on page 113]

Laakso, I. (2018). Alvar: Adult whole-body anatomic phantom for computational dosimetry, Project website: https://version.aalto.fi/gitlab/ilaakso/alvar/. [Cited on pages 56, 64]

Laakso, I. and Hirata, A. (2012). Reducing the staircasing error in computational dosimetry of low-frequency electromagnetic fields. *Physics in Medicine and Biology*. [Cited on page 68]

Laakso, I. and Hirata, A. (2013). Evaluation of the induced electric field and compliance procedure for a wireless power transfer system in an electrical vehicle. *Physics in Medicine and Biology*, 58(21):7583–7593. [Cited on page 58]

Laakso, I., Hirata, A., and Ugawa, Y. (2014). Effects of coil orientation on the electric field induced by TMS over the hand motor area. *Physics in Medicine and Biology*, 59(1):203–218. [Cited on pages 45, 52, 68, 72]

Laakso, I., Mikkonen, M., Koyama, S., Ito, D., Yamaguchi, T., Hirata, A., and Tanaka, S. (2018a). Electric field dependent effects of motor cortical TDCS. *bioRxiv*, 1:327361. [Cited on pages 63, 66, 67]

Laakso, I., Murakami, T., Hirata, A., and Ugawa, Y. (2018b). Where and what TMS activates: Experiments and modeling. *Brain Stimulation*, 11(1):166–174. [Cited on pages 44, 49, 57, 58, 63]

Laakso, I., Tanaka, S., Koyama, S., De Santis, V., and Hirata, A. (2015). Inter-subject Variability in Electric Fields of Motor Cortical tDCS. *Brain Stimulation*, 8(5):906–913. [Cited on pages 45, 48, 63, 65, 66, 67]

Lang, N., Sueske, E., Hasan, A., Paulus, W., and Tergau, F. (2006). Pregabalin exerts oppositional effects on different inhibitory circuits in human motor cortex: A double-blind, placebo-controlled transcranial magnetic stimulation study. *Epilepsia*, 47(5):813–819. [Cited on page 31]

Larsson, J. (2007). Electromagnetics from a quasistatic perspective. *American Journal of Physics*, 75(3):230–239. [Cited on page 48]

Lattari, E., Costa, S. S., Campos, C., de Oliveira, A. J., Machado, S., and Maranhao Neto, G. A. (2017). Can transcranial direct current stimulation on the dorsolateral prefrontal cortex improves balance and functional mobility in Parkinson's disease? *Neuroscience Letters*, 636:165–169. [Cited on pages 28, 63]

Lawson McLean, A. (2019). Publication trends in transcranial magnetic stimulation: a 30-year panorama. *Brain Stimul*, 12(3):619–627. [Cited on page 172]

Lee, B. C., Bing, G., Chunchon, W. K. J., Yoon, J. M., Kang, K. S., Shin, E. J., Kim, W. K., Ko, K. H., and Kim, H. C. (2001). Prenatal exposure to magnetic field increases dopamine levels in the striatum of offspring. *Clinical and Experimental Pharmacology and Physiology*, 28(11):884–886. [Cited on page 109]

Lee, H. K., Ahn, S. J., Shin, Y. M., Kang, N., and Cauraugh, J. H. (2019). Does transcranial direct current stimulation improve functional locomotion in people with Parkinson's disease? A systematic review and meta-analysis. *Journal of NeuroEngineering and Rehabilitation*, 16(1):84. [Cited on page 28]

Lee, J. Y., Kim, S. H., Ko, A. R., Lee, J. S., Yu, J. H., Seo, J. H., Cho, B. P., and Cho, S. R. (2013). Therapeutic effects of repetitive transcranial magnetic stimulation in an animal model of Parkinson's disease. *Brain Research*, 1537:290–302. [Cited on page 166]

Lee, M. B., Kim, Y. H., Kim, H. J., and Kwon, O. I. (2018). Anisotropic conductivity tensor by analyzing diffusion tensor for electrical brain stimulation (EBS). *Physics in Medicine and Biology*, 63(24). [Cited on page 91]

Lefaucheur, J., Drouot, X., Menard-Lefaucheur, I., Keravel, Y., and Nguyen, J. (2006). Motor cortex rtms restores defective intracortical inhibition in chronic neuropathic pain. *Neurology*, 67(9):1568–1574. [Cited on page 172]

Lefaucheur, J. P., Aleman, A., Baeken, C., Benninger, D. H., Brunelin, J., Di Lazzaro, V., Filipović, S. R., Grefkes, C., Hasan, A., Hummel, F. C., Jääskeläinen, S. K., Langguth, B., Leocani, L., Londero, A., Nardone, R., Nguyen, J. P., Nyffeler, T., Oliveira-Maia, A. J., Oliviero, A., Padberg, F., Palm, U., Paulus, W., Poulet, E., Quartarone, A., Rachid, F., Rektorová, I., Rossi, S., Sahlsten, H., Schecklmann, M., Szekely, D., and Ziemann, U. (2020). Evidence-based guidelines on the therapeutic use of repetitive transcranial magnetic stimulation (rTMS): An update (2014–2018). *Clinical Neurophysiology*, 131(2):474–528. [Cited on pages 35, 36, 37, 38, 39, 40, 41, 42, 43, 166]

Lefaucheur, J.-P., André-Obadia, N., Antal, A., Ayache, S. S., Baeken, C., Benninger, D. H., Cantello, R. M., Cincotta, M., de Carvalho, M., De Ridder, D., Devanne, H., Di Lazzaro, V., Filipović, S. R., Hummel, F. C., Jääskeläinen, S. K., Kimiskidis, V. K., Koch, G., Langguth, B., Nyffeler, T., Oliviero, A., Padberg, F., Poulet, E., Rossi, S., Rossini, P. M., Rothwell, J. C., Schönfeldt-Lecuona, C., Siebner, H. R., Slotema, C. W., Stagg, C. J., Valls-Sole, J., Ziemann, U., Paulus, W., and Garcia-Larrea, L. (2014). Evidence-based guidelines on the therapeutic use of repetitive transcranial magnetic stimulation (rTMS). *Clinical Neurophysiology*, 125(11):2150–2206. [Cited on pages 29, 30, 35, 37, 62, 76]

Lefaucheur, J. P., Antal, A., Ayache, S. S., Benninger, D. H., Brunelin, J., Cogiamanian, F., Cotelli, M., De Ridder, D., Ferrucci, R., Langguth, B., Marangolo, P., Mylius, V., Nitsche, M. A., Padberg, F., Palm, U., Poulet, E., Priori, A., Rossi, S., Schecklmann, M., Vanneste, S., Ziemann, U., Garcia-Larrea, L., and Paulus, W. (2017). Evidence-based guidelines on the therapeutic use of transcranial direct current stimulation (tDCS). *Clinical Neurophysiology*, 128(1):56–92. [Cited on pages 19, 24, 25, 26, 27, 28]

Lefaucheur, J. P., Ayache, S. S., Sorel, M., Farhat, W. H., Zouari, H. G., Ciampi De Andrade, D., Ahdab, R., Ménard-Lefaucheur, I., Brugières, P., and Goujon, C. (2012). Analgesic effects of repetitive transcranial magnetic stimulation of the motor cortex in neuropathic pain: Influence of theta burst stimulation priming. *European Journal of Pain (United Kingdom)*, 16(10):1403–1413. [Cited on page 172]

Legros, A. and Beuter, A. (2005). Effect of a low intensity magnetic field on human motor behavior. *Bioelectromagnetics*, 26(8):657–669. [Cited on page 113]

Legros, A., Corbacio, M., Beuter, A., Modolo, J., Goulet, D., Prato, F. S., and Thomas, A. W. (2012). Neurophysiological and behavioral effects of a 60 Hz, 1,800 lT magnetic field in humans. *European Journal of Applied Physiology*, 112(5):1751–1762. [Cited on page 113]

Legros, A., Modolo, J., Brown, S., Roberston, J., and Thomas, A. W. (2015). Effects of a 60 Hz magnetic field exposure up to 3000 μT on Human brain activation as measured by functional magnetic resonance imaging. *PLoS ONE*, 10(7):1–27. [Cited on page 113]

Lenoir, C., Algoet, M., and Mouraux, A. (2018). Deep continuous theta burst stimulation of the operculo-insular cortex selectively affects Aδ-fibre heat pain. *Journal of Physiology*, 596(19):4767–4787. [Cited on page 38]

Levkovitz, Y., Isserles, M., Padberg, F., Lisanby, S. H., Bystritsky, A., Xia, G., Tendler, A., Daskalakis, Z. J., Winston, J. L., Dannon, P., Hafez, H. M., Reti, I. M., Morales, O. G., Schlaepfer, T. E., Hollander, E., Berman, J. A., Husain, M. M., Sofer, U., Stein, A., Adler, S., Deutsch, L., Deutsch, F., Roth, Y., George, M. S., and Zangen, A. (2015). Efficacy and safety of deep transcranial magnetic stimulation for major depression: A prospective multicenter randomized controlled trial. *World Psychiatry*, 14(1):64–73. [Cited on page 36]

Lewis, P. M. and Rosenfeld, J. V. (2015). Electrical stimulation of the brain and the development of cortical visual prostheses: An historical perspective. *Brain Research*, 1630(December):208–224. [Cited on page 9]

Li, C. T., Hsieh, J. C., Huang, H. H., Chen, M. H., Juan, C. H., Tu, P. C., Lee, Y. C., Wang, S. J., Cheng, C. M., and Su, T. P. (2016a). Cognition-Modulated Frontal Activity in Prediction and Augmentation of Antidepressant Efficacy: A Randomized Controlled Pilot Study. *Cerebral Cortex*, 26(1):202–210. [Cited on page 35]

Li, J., Meng, X. M., Li, R. Y., Zhang, R., Zhang, Z., and Du, Y. F. (2016b). Effects of different frequencies of repetitive transcranial magnetic stimulation on the recovery of upper limb motor dysfunction in patients with subacute cerebral infarction. *Neural Regeneration Research*, 11(10):1584–1590. [Cited on page 40]

Lin, V. W. ., Hsiao, I. N., and Dhaka, V. (2000). Magnetic coil design considerations for functional magnetic stimulation. *IEEE Transactions on Biomedical Engineering*, 47(5):600–610. [Cited on page 169]

Lindholm, P., Lamusuo, S., Taiminen, T., Pesonen, U., Lahti, A., Virtanen, A., Forssell, H., Hietala, J., Hagelberg, N., Pertovaara, A., Parkkola, R., and Jääskeläinen, S. (2015). Right secondary somatosensory cortex-a promising novel target for the treatment of drug-resistant neuropathic orofacial pain with repetitive transcranial magnetic stimulation. *Pain*, 156(7):1276–1283. [Cited on pages 37, 38]

Lisanby, S. H., Luber, B., Schlaepfer, T. E., and Sackeim, H. A. (2003). Safety and Feasibility of Magnetic Seizure Therapy (MST) in Major Depression: Randomized Within-Subject Comparison with Electroconvulsive Therapy. 28(10):1852–1865. [Cited on page 18]

Liu, C., Ding, H., Fang, X., and Wang, Z. (2020). Optimal Design of Transcranial Magnetic Stimulation Thin Core Coil with Trade-Off between Stimulation Effect and Heat Energy. *IEEE Transactions on Applied Superconductivity*, 30(4). [Cited on page 167]

Long, H., Wang, H., Zhao, C., Duan, Q., Feng, F., Hui, N., Mao, L., Liu, H., Mou, X., and Yuan, H. (2018). Effects of combining high-and low-frequency repetitive transcranial

magnetic stimulation on upper limb hemiparesis in the early phase of stroke. *Restorative Neurology and Neuroscience*, 36(1):21–30. [Cited on page 40]

Lontis, E. R., Voigt, M., and Struijk, J. J. (2006). Focality assessment in transcranial magnetic stimulation with double and cone coils. *Journal of clinical neurophysiology : official publication of the American Electroencephalographic Society*, 23(5):462–471. [Cited on page 34]

Loo, C. K., Sachdev, P., Martin, D., Pigot, M., Alonzo, A., Malhi, G. S., Lagopoulos, J., and Mitchell, P. (2010). A double-blind, sham-controlled trial of transcranial direct current stimulation for the treatment of depression. *International Journal of Neuropsychopharmacology*, 13(1):61–69. [Cited on page 27]

Lozano, A. M., Lipsman, N., Bergman, H., Brown, P., Chabardes, S., Chang, J. W., Matthews, K., McIntyre, C. C., Schlaepfer, T. E., Schulder, M., Temel, Y., Volkmann, J., and Krauss, J. K. (2019). Deep brain stimulation: current challenges and future directions. *Nature Reviews Neurology*, 15(3):148–160. [Cited on page 15]

Lu, M. and Ueno, S. (2017). Comparison of the induced fields using different coil configurations during deep transcranial magnetic stimulation. *PloS one*, 12(6):e0178422. [Cited on pages 34, 52, 67]

Lu, M., Ueno, S., Thorlin, T., and Persson, M. (2008). Calculating the activating function in the human brain by transcranial magnetic stimulation. *IEEE Transactions on Magnetics*, 44(6):1438–1441. [Cited on page 167]

Lusicic, A., Schruers, K. R., Pallanti, S., and Castle, D. J. (2018). Transcranial magnetic stimulation in the treatment of obsessive–compulsive disorder: Current perspectives. *Neuropsychiatric Disease and Treatment*, 14:1721–1736. [Cited on pages 34, 40]

Ma, S. M., Ni, J. X., Li, X. Y., Yang, L. Q., Guo, Y. N., and Tang, Y. Z. (2015). High-Frequency Repetitive Transcranial Magnetic Stimulation Reduces Pain in Postherpetic Neuralgia. *Pain Medicine (United States)*, 16(11):2162–2170. [Cited on page 37]

Maeda, F., Gangitano, M., Thall, M., and Pascual-Leone, A. (2002). Inter- and intra-individual variability of paired-pulse curves with transcranial magnetic stimulation (TMS). *Clinical Neurophysiology*, 113(3):376–382. [Cited on page 32]

Mahmoudi, H., Haghighi, A. B., Petramfar, P., Jahanshahi, S., Salehi, Z., and Fregni, F. (2011). Transcranial direct current stimulation: Electrode montage in stroke. *Disability and Rehabilitation*, 33(15-16):1383–1388. [Cited on page 22]

Makarov, S. N., Noetscher, G. M., Raij, T., and Nummenmaa, A. (2018). A Quasi-Static Boundary Element Approach With Fast Multipole Acceleration for High-Resolution Bioelectromagnetic Models. *IEEE Transactions on Biomedical Engineering*, 65(12):2675–2683. [Cited on page 51]

Mäkelä, J. P. and Laakso, A. (2017). *nTMS Language Mapping: Basic Principles and Clinical Use*, pages 131–150. Springer International Publishing, Cham. [Cited on page 86]

Makris, N., Angelone, L., Tulloch, S., Sorg, S., Kaiser, J., Kennedy, D., and Bonmassar, G. (2008). MRI-based anatomical model of the human head for Specific Absorption Rate Mapping. *Medical & biological engineering & computing*, 46(12):1239–1251. [Cited on pages 56, 64]

Manoli, Z., Parazzini, M., Ravazzani, P., and Samaras, T. (2017). The electric field distributions in anatomical head models during transcranial direct current stimulation for post-stroke rehabilitation. *Medical Physics*, 44 (1):262–271. [Cited on pages 45, 48, 54, 55, 57, 58, 63, 136, 137]

Marceglia, S., Mrakic-Sposta, S., Rosa, M., Ferrucci, R., Mameli, F., Vergari, M., Arlotti, M., Ruggiero, F., Scarpini, E., Galimberti, D., Barbieri, S., and Priori, A. (2016). Transcranial direct current stimulation modulates cortical neuronal activity in alzheimer's disease. *Frontiers in Neuroscience*, 10:134. [Cited on page 28]

Martinez, M., Brezun, J. M., Zennou-Azogui, Y., Baril, N., and Xerri, C. (2009). Sensorimotor training promotes functional recovery and somatosensory cortical map reactivation following cervical spinal cord injury. *European Journal of Neuroscience*, 30(12):2356–2367. [Cited on pages 172, 194]

Massot, O., Grimaldi, B., Bailly, J. M., Kochanek, M., Deschamps, F., Lambrozo, J., and Fillion, G. (2000). Magnetic field desensitizes 5-HT1B receptor in brain: Pharmacological and functional studies. *Brain Research*, 858(1):143–150. [Cited on page 108]

Mayo-Yáñez, M., Corrás, T., and Méndez-Iglesias, R. (2018). Transcranial Direct Current Stimulation for Treatment of Alzheimer's Disease: A Systematic Review of Randomized Clinical Trial. *Current Psychiatry Reviews*, 14(4):211–214. [Cited on page 28]

McDonnell, M. N., Orekhov, Y., and Ziemann, U. (2007). Suppression of LTP-like plasticity in human motor cortex by the GABA B receptor agonist baclofen. *Experimental Brain Research*, 180(1):181–186. [Cited on page 31]

McFarlane, E. H., Dawe, G. S., Marks, M., and Campbell, I. C. (2000). Changes in neurite outgrowth but not in cell division induced by low emf exposure: influence of field strength and culture conditions on responses in rat pc12 pheochromocytoma cells. *Bioelectrochemistry*, 52:23–28. [Cited on page 120]

McIntyre, C. C. and Anderson, R. W. (2016). Deep brain stimulation mechanisms: the control of network activity via neurochemistry modulation. *Journal of Neurochemistry*, pages 338–345. [Cited on page 15]

McIntyre, C. C. and Grill, W. M. (2002). Extracellular stimulation of central neurons: Influence of stimulus waveform and frequency on neuronal output. *Journal of Neurophysiology*, 88(4):1592–1604. [Cited on pages 184, 186, 197]

McIntyre, C. C., Richardson, A. G., and Grill, W. M. (2002). Modeling the excitability of mammalian nerve fibers: Influence of afterpotentials on the recovery cycle. *Journal of Neurophysiology*, 87(2):995–1006. [Cited on pages 184, 186, 197]

McNab, J. A., Polimeni, J. R., Wang, R., Augustinack, J. C., Fujimoto, K., Stevens, A., Janssens, T., Farivar, R., Folkerth, R. D., Vanduffel, W., and Wald, L. L. (2013). Surface based analysis of diffusion orientation for identifying architectonic domains in the in vivo human cortex. *NeuroImage*, 69:87–100. [Cited on page 59]

Medeiros, L. F., Caumo, W., Dussán-Sarria, J., Deitos, A., Brietzke, A., Laste, G., Campos-Carraro, C., de Souza, A., Scarabelot, V. L., Cioato, S. G., Vercelino, R., de Castro, A. L., Araújo, A. S., Belló-Klein, A., Fregni, F., and Torres, I. L. (2016). Effect of deep intramuscular stimulation and transcranial magnetic stimulation on neurophysiological biomarkers in chronic myofascial pain syndrome. *Pain Medicine (United States)*, 17(1):122–135. [Cited on page 38]

Mendonca, M. E., Santana, M. B., Baptista, A. F., Datta, A., Bikson, M., Fregni, F., and Araujo, C. P. (2011). Transcranial DC stimulation in fibromyalgia: Optimized cortical target supported by high-resolution computational models. *Journal of Pain*, 12(5):610–617. [Cited on page 26]

Mendonca, M. E., Simis, M., Grecco, L. C., Battistella, L. R., Baptista, A. F., and Fregni, F. (2016). Transcranial direct current stimulation combined with aerobic exercise to optimize analgesic responses in fibromyalgia: A randomized placebo-controlled clinical trial. *Frontiers in Human Neuroscience*. [Cited on page 26]

Meng, Z. Y. and Song, W. Q. (2017). Low frequency repetitive transcranial magnetic stimulation improves motor dysfunction after cerebral infarction. *Neural Regeneration Research*, 12(4):610–613. [Cited on page 39]

Mikkonen, M., Laakso, I., Sumiya, M., Koyama, S., Hirata, A., and Tanaka, S. (2018). TMS motor thresholds correlate with TDCS electric field strengths in hand motor area. *Frontiers in Neuroscience*, 12(JUN). [Cited on pages 44, 49, 57, 58, 65]

Mikkonen, M., Laakso, I., Tanaka, S., and Hirata, A. (2020). Cost of focality in TDCS: Interindividual variability in electric fields. *Brain Stimulation*, 13(1):117–124. [Cited on page 24]

Minati, L. and Weglarz, W. P. (2007). Physical foundations, models, and methods of diffusion magnetic resonance imaging of the brain: A review. *Concepts in Magnetic Resonance Part A: Bridging Education and Research*, 30(5):278–307. [Cited on page 91]

Minhas, P., Bansal, V., Patel, J., Ho, J. S., Diaz, J., Datta, A., and Bikson, M. (2010). Electrodes for high-definition transcutaneous dc stimulation for applications in drug delivery and electrotherapy, including tdcs. *Journal of Neuroscience Methods*, 190(2):188 – 197. [Cited on page 23]

Minhas, P., Datta, A., and Bikson, M. (2011). Cutaneous perception during tDCS: Role of electrode shape and sponge salinity. [Cited on page 22]

Miranda, P. C., Hallett, M., and Basser, P. J. (2003). The electric field induced in the brain by magnetic stimulation: A 3-d finite-element analysis of the effect of tissue heterogeneity and anisotropy. *IEEE Transactions on Biomedical Engineering*, 50 (9):1074–1085. [Cited on pages 52, 63, 122]

Miranda, P. C., Lomarev, M., and Hallett, M. (2006). Modeling the current distribution during transcranial direct current stimulation. *Clinical Neurophysiology*, 117(7):1623–1629. [Cited on pages 55, 63]

Miranda, P. C., Mekonnen, A., Salvador, R., and Ruffini, G. (2013). The electric field in the cortex during transcranial current stimulation. *NeuroImage*, 70:48–58. [Cited on page 54]

Mirbagheri, A., Schneider, H., Zdunczyk, A., Vajkoczy, P., and Picht, T. (2020). NTMS mapping of non-primary motor areas in brain tumour patients and healthy volunteers. *Acta Neurochirurgica*, 162(2):407–416. [Cited on page 33]

Mishra, S. (2017). Electroceuticals in medicine – The brave new future. *Indian Heart Journal*, 69(5):685–686. [Cited on page 13]

Moffa, A. H., Brunoni, A. R., Nikolin, S., and Loo, C. K. (2018). Transcranial Direct Current Stimulation in Psychiatric Disorders: A Comprehensive Review. *Psychiatric Clinics of North America*, 41(3):447–463. [Cited on page 28]

Moisello, C., Blanco, D., Fontanesi, C., Lin, J., Biagioni, M., Kumar, P., Brys, M., Loggini, A., Marinelli, L., Abbruzzese, G., Quartarone, A., Tononi, G., Di Rocco, A., Ghilardi, M. F., and Sensory Motor Integration, L. (2015). Tms enhances retention of a motor skill in parkinson's disease. *Brain Stimul*, 8(2):224–30. [Cited on page 172]

Mondino, M., Brunelin, J., Palm, U., Brunoni, A., Poulet, E., and Fecteau, S. (2015). Transcranial direct current stimulation for the treatment of refractory symptoms of schizophrenia. current evidence and future directions. *Current pharmaceutical design*, 21. [Cited on pages 28, 63]

Morales-Quezada, L., Saavedra, L. C., Rozisky, J., Hadlington, L., and Fregni, F. (2014). Intensity-dependent effects of transcranial pulsed current stimulation on interhemispheric connectivity: A high-resolution qEEG, sham-controlled study. *NeuroReport*, 25(13):1054–1058. [Cited on page 17]

Moretti, A., Ferrari, F., and Villa, R. F. (2015). Neuroprotection for ischaemic stroke: Current status and challenges. *Pharmacology and Therapeutics*, 146:23–34. [Cited on pages 120, 161]

Moro, E., LeReun, C., Krauss, J. K., Albanese, A., Lin, J. P., Walleser Autiero, S., Brionne, T. C., and Vidailhet, M. (2017). Efficacy of pallidal stimulation in isolated dystonia: a systematic review and meta-analysis. *European Journal of Neurology*, 24(4):552–560. [Cited on page 15]

Motomura, K., Takeuchi, H., Nojima, I., Aoki, K., Chalise, L., Iijima, K., Wakabayashi, T., and Natsume, A. (2020). Navigated repetitive transcranial magnetic stimulation as preoperative assessment in patients with brain tumors. *Scientific Reports*, 10(1):1–14. [Cited on pages 85, 86]

Multanen, J., Häkkinen, A., Heikkinen, P., Kautiainen, H., Mustalampi, S., and Ylinen, J. (2018). Pulsed electromagnetic field therapy in the treatment of pain and other symptoms in fibromyalgia: A randomized controlled study. *Bioelectromagnetics*, 39(5):405–413. [Cited on page 114]

Nadeem, M., Thorlin, T., Gandhi, O. P., and Persson, M. (2003). Computation of electric and magnetic stimulation in human head using the 3-d impedance method. *IEEE Transactions on Biomedical Engineering*, 50 (7):900–907. [Cited on page 122]

Nagaoka, T., Watanabe, S., Sakurai, K., Kunieda, E., Watanabe, S., Taki, M., and Yamanaka, Y. (2004). Development of realistic high-resolution whole-body voxel models of Japanese adult males and females of average height and weight, and application of models to radio-frequency electromagnetic-field dosimetry. *Physics in Medicine and Biology*, 49(1):1–15. [Cited on pages 56, 64]

Najib, U., Bashir, S., Edwards, D., Rotenberg, A., and Pascual-Leone, A. (2011). Transcranial brain stimulation: Clinical applications and future directions. *Neurosurgery Clinics of North America*, 22(2):233–251. [Cited on pages 62, 172, 194]

Nardone, R., Höller, Y., Langthaler, P. B., Lochner, P., Golaszewski, S., Schwenker, K., Brigo, F., and Trinka, E. (2017). rTMS of the prefrontal cortex has analgesic effects on neuropathic pain in subjects with spinal cord injury. *Spinal Cord*, 55(1):20–25. [Cited on page 38]

Nardone, R., Versace, V., Brigo, F., Golaszewski, S., Carnicelli, L., Saltuari, L., Trinka, E., and Sebastianelli, L. (2020). Transcranial magnetic stimulation and gait disturbances in Parkinson's disease: A systematic review. *Neurophysiologie Clinique*, 50(3):213–225. [Cited on page 62]

Neuling, T., Wagner, S., Wolters, C. H., Zaehle, T., and Herrmann, C. S. (2012). Finite-element model predicts current density distribution for clinical applications of tDCS and tACS. *Frontiers in Psychiatry*, 3(SEP):1–10. [Cited on pages 54, 69]

Ni, Z., Charab, S., Gunraj, C., Nelson, A. J., Udupa, K., Yeh, I. J., and Chen, R. (2011). Transcranial magnetic stimulation in different current directions activates separate cortical circuits. *Journal of Neurophysiology*, 105(2):749–756. [Cited on page 31]

Nienow, T. M., MacDonald, A. W., and Lim, K. O. (2016). TDCS produces incremental gain when combined with working memory training in patients with schizophrenia: A proof of concept pilot study. [Cited on page 28]

Nitsche, M. A., Cohen, L. G., Wassermann, E. M., Priori, A., Lang, N., Antal, A., Paulus, W., Hummel, F., Boggio, P. S., Fregni, F., and Pascual-Leone, A. (2008). Transcranial direct current stimulation: State of the art 2008. [Cited on pages 19, 62, 63, 72]

Nitsche, M. A., Doemkes, S., Karaköse, T., Antal, A., Liebetanz, D., Lang, N., Tergau, F., and Paulus, W. (2007). Shaping the effects of transcranial direct current stimulation of the human motor cortex. *Journal of Neurophysiology.* [Cited on page 23]

Nitsche, M. A., Fricke, K., Henschke, U., Schlitterlau, A., Liebetanz, D., Lang, N., Henning, S., Tergau, F., and Paulus, W. (2003). Pharmacological modulation of cortical excitability shifts induced by transcranial direct current stimulation in humans. *Journal of Physiology.* [Cited on page 20]

Nitsche, M. A., Jaussi, W., Liebetanz, D., Lang, N., Tergau, F., and Paulus, W. (2004). Consolidation of human motor cortical neuroplasticity by D-cycloserine. *Neuropsychopharmacology*. [Cited on page 20]

Nitsche, M. A. and Paulus, W. (2001). Sustained excitability elevations induced by transcranial DC motor cortex stimulation in humans. *Neurology*, 57(10):1899–1901. [Cited on pages 19, 22, 62]

Nitsche, M. A. and Paulus, W. (2011). Transcranial direct current stimulation - Update 2011. *Restorative Neurology and Neuroscience*, 29(6):463–492. [Cited on page 21]

Nummenmaa, A., Stenroos, M., Ilmoniemi, R. J., Okada, Y. C., Hamalainen, M. S., and Raij, T. (2013). Comparison of spherical and realistically shaped boundary element head models for transcranial magnetic stimulation navigation. *Clinical Neurophysiology*, 124(10):1995–2007. [Cited on pages 63, 87]

Nurmikko, T., MacIver, K., Bresnahan, R., Hird, E., Nelson, A., and Sacco, P. (2016). Motor Cortex Reorganization and Repetitive Transcranial Magnetic Stimulation for Pain—A Methodological Study. *Neuromodulation*, 19(7):669–678. [Cited on page 37]

Oda, T. and Koike, T. (2004). Magnetic field exposure saves rat cerebellar granule neurons from apoptosis in vitro. *Neuroscience Letters*, 356:83–86. [Cited on page 120]

Odekerken, V. J., Boel, J. A., Schmand, B. A., De Haan, R. J., Figee, M., Van Den Munckhof, P., Schuurman, P. R., and De Bie, R. M. (2016). GPi vs STN deep brain stimulation for Parkinson disease. *Neurology*, 86(8):755–761. [Cited on page 15]

Olney, R. K., So, Y. T., Goodin, D. S., and Aminoff, M. J. (1990). A comparison of magnetic and electrical stimulation of peripheral nerves. *Muscle & Nerve*, 13(10):957–963. [Cited on page 187]

Opitz, A., Fox, M. D., Craddock, R. C., Colcombe, S., and Milham, M. P. (2016). An integrated framework for targeting functional networks via transcranial magnetic stimulation. *NeuroImage*, 127:86–96. [Cited on page 63]

Opitz, A., Legon, W., Rowlands, A., Bickel, W. K., Paulus, W., and Tyler, W. J. (2013). Physiological observations validate finite element models for estimating subject-specific electric field distributions induced by transcranial magnetic stimulation of the human motor cortex. *NeuroImage*, 81:253–264. [Cited on page 44]

Opitz, A., Windhoff, M., Heidemann, R. M., Turner, R., and Thielscher, A. (2011). How the brain tissue shapes the electric field induced by transcranial magnetic stimulation. *NeuroImage*, 58(3):849–859. [Cited on pages 55, 59, 70, 72, 103]

Opitz, A., Yeagle, E., Thielscher, A., Schroeder, C., Mehta, A. D., and Milham, M. P. (2018). On the importance of precise electrode placement for targeted transcranial electric stimulation. *NeuroImage*, 181:560–567. [Cited on page 63]

Opitz, A., Zafar, N., Bockermann, V., Rohde, V., and Paulus, W. (2014). Validating computationally predicted TMS stimulation areas using direct electrical stimulation in patients with brain tumors near precentral regions. *NeuroImage: Clinical*, 4:500–507. [Cited on pages 48, 58, 63, 64, 70]

O'Reardon, J. P., Solvason, H. B., Janicak, P. G., Sampson, S., Isenberg, K. E., Nahas, Z., McDonald, W. M., Avery, D., Fitzgerald, P. B., Loo, C., Demitrack, M. A., George, M. S., and Sackeim, H. A. (2007). Efficacy and safety of transcranial magnetic stimulation in the acute treatment of major depression: A multisite randomized controlled trial. *Biological Psychiatry*, 62(11):1208 – 1216. Depression: New Perspectives on Treatment and Etiology. [Cited on page 35]

Ozdemir, E., Demirkazik, A., Gursoy, S., Taskiran, A. S., Kilinc, O., and Arslan, G. (2017). Effects of extremely low frequency electromagnetic fields on morphine analgesia and tolerance in rats. *General Physiology and Biophysics*, 36(4):415–422. [Cited on page 110]

Ozdemir, E., Demirkazik, A., Taskıran, A. S., and Arslan, G. (2019). Effects of 5-HT1 and 5-HT 2 Receptor Agonists on Electromagnetic Field-Induced Analgesia in Rats. *Bioelectromagnetics*, 40(5):319–330. [Cited on page 110]

Paffi, A., Apollonio, F., D'Inzeo, G., and Liberti, M. (2013). Stochastic resonance induced by exogenous noise in a model of a neuronal network. *Network: Computation in Neural Systems*. [Cited on pages 62, 115]

Paffi, A., Camera, F., Apollonio, F., d'Inzeo, G., and Liberti, M. (2015a). Numerical characterization of intraoperative and chronic electrodes in deep brain stimulation. *Frontiers in Computational Neuroscience*, 9:2. [Cited on pages 62, 122]

Paffi, A., Camera, F., Carducci, F., Rubino, G., Tampieri, P., Liberti, M., and Apollonio, F. (2015b). A computational model for real-time calculation of electric field due to transcranial magnetic stimulation in clinics. *International Journal of Antennas and Propagation*, 2015(Article ID 976854):23–27. [Cited on pages vii, 52, 53, 63, 64, 67, 73, 78, 87, 88, 89, 90, 122, 206]

Paffi, A., Camera, F., Lucano, E., Apollonio, F., and Liberti, M. (2016). Time resolved dosimetry of human brain exposed to low frequency pulsed magnetic fields. *Physics in Medicine and Biology*, 61:4452–4465. [Cited on pages viii, 116, 122, 131, 139]

Paffi, A., Liberti, M., Apollonio, F., and Tampieri, P. (2018). Experimental Characterization of a Figure of Eight Coil for Transcranial Magnetic Stimulation. *MeMeA 2018 - 2018 IEEE International Symposium on Medical Measurements and Applications, Proceedings*, pages 1–5. [Cited on pages 33, 95]

Panebianco, M., Rigby, A., Weston, J., and Marson, A. G. (2015). Vagus nerve stimulation for partial seizures. *Cochrane Database of Systematic Reviews*, 2015(4). [Cited on page 15]

Paolucci, T., Piccinini, G., Iosa, M., Piermattei, C., de Angelis, S., Grasso, M. R., Zangrando, F., and Saracen, V. M. (2016). Efficacy of extremely low-frequency magnetic field in fibromyalgia pain: A pilot study. *Journal of Rehabilitation Research and Development*, 53(6):1023–1034. [Cited on page 114]

Papi, F., Ghione, S., Rosa, C., Seppia, C. D., and Luschi, P. (1995). Exposure to oscillating magnetic fields influences sensitivity to electrical stimuli. II. experiments on humans. *Bioelectromagnetics*, 16(5):295–300. [Cited on page 114]

Parazzini, M., Fiocchi, S., Liorni, I., and Ravazzani, P. (2015). Effect of the Interindividual Variability on Computational Modeling of Transcranial Direct Current Stimulation. *Computational Intelligence and Neuroscience*, 2015:1–9. [Cited on pages 48, 57, 63, 67]

Parazzini, M., Fiocchi, S., and Ravazzani, P. (2012). Electric field and current density distribution in an anatomical head model during transcranial direct current stimulation for tinnitus treatment. *Bioelectromagnetics*, 33(6):476–487. [Cited on pages 45, 67]

Parazzini, M., Fiocchi, S., Rossi, E., Paglialonga, A., and Ravazzani, P. (2011). Transcranial direct current stimulation: Estimation of the electric field and of the current density in an anatomical human head model. *IEEE Transactions on Biomedical Engineering*, 58(6):1773–1780. [Cited on pages 45, 63, 67, 74]

Parazzini, M., Rossi, E., Ferrucci, R., Liorni, I., Priori, A., and Ravazzani, P. (2014). Modelling the electric field and the current density generated by cerebellar transcranial DC stimulation in humans. *Clinical Neurophysiology*, 125(3):577–584. [Cited on pages 67, 75]

Parent, A. (2004). Giovanni aldini: From animal electricity to human brain stimulation. *Canadian Journal of Neurological Sciences*, 31(4):576–584. [Cited on page 10]

Park, H. J., Bonmassar, G., Kaltenbach, J. A., Machado, A. G., Manzoor, N. F., and Gale, J. T. (2013). Activation of the central nervous system induced by micro-magnetic stimulation. *Nature Communications*, 4:1–9. [Cited on pages 169, 173, 188, 195]

Pascual-Leone, A., Gates, J. R., and Dhuna, A. (1991). Induction of speech arrest and counting errors with rapid-rate transcranial magnetic stimulation. *Neurology*, 41(5):697–702. [Cited on page 32]

Pascual-Leone, A. and Wagner, T. (2007). A Brief Summary of the History of Noninvasive Brain Stimulation. Supplementary Appendix. *The Annual Review of Biomedical Engineering*, 9(Figure 1):1–7. [Cited on pages 9, 11, 12]

Pascual-Leone, A., Walsh, V., and Rothwell, J. (2000). Transcranial magnetic stimulation in cognitive neuroscience - Virtual lesion, chronometry, and functional connectivity. *Current Opinion in Neurobiology*, 10(2):232–237. [Cited on page 194]

Patel, R. and Madhavan, S. (2019). Comparison of transcranial direct current stimulation electrode montages for the lower limb motor cortex. *Brain Sciences*, 9(8):1–10. [Cited on page 22]

Pedata, P., Dettori, I., Coppi, E., Melani, A., Fusco, I., Corradetti, R., and Pugliese, A. M. (2015). Purinergic signalling in brain ischemia. *Neuropharmacology*, 104:105–130. [Cited on page 121]

Pellegrini, M., Zoghi, M., and Jaberzadeh, S. (2020). The effects of transcranial direct current stimulation on corticospinal and cortico-cortical excitability and response variability: Conventional versus high-definition montages. *Neuroscience Research*. [Cited on page 24]

Pena-Philippides, J., Yang, Y., Bragina, O., Hagberg, S., Nemoto, E., and Roitbak, T. (2014). Effect of pulsed electromagnetic field (pemf) on infarct size and inflammation after cerebral ischemia in mice. *Translational stroke research*, 5(4):491–500. [Cited on pages 111, 121, 147]

Perera, T., George, M. S., Grammer, G., Janicak, P. G., Pascual-Leone, A., and Wirecki, T. S. (2016). The clinical tms society consensus review and treatment recommendations for tms therapy for major depressive disorder. *Brain Stimul*, 9(3):336–346. [Cited on page 172]

Peterchev, A. V., Deng, Z. D., and Goetz, S. M. (2015). Advances in Transcranial Magnetic Stimulation Technology. *Brain Stimulation: Methodologies and Interventions*, pages 165–189. [Cited on page 33]

Peterchev, A. V., Dostilio, K., Rothwell, J. C., and Murphy, D. L. (2014). Controllable pulse parameter transcranial magnetic stimulator with enhanced circuit topology and pulse shaping. *Journal of Neural Engineering*, 11(5). [Cited on page 33]

Peterchev, A. V., Jalinous, R., and Lisanby, S. H. (2008). A transcranial magnetic stimulator inducing near-rectangular pulses with controllable pulse width (ctms). *IEEE Transactions on Biomedical Engineering*, 55(1):257–266. [Cited on page 174]

Peterchev, A. V., Wagner, T. A., Miranda, P. C., Nitsche, M. A., Paulus, W., Lisanby, S. H., Pascual-Leone, A., and Bikson, M. (2013). Fundamentals of transcranial electric and magnetic stimulation dose: definition, selection, and reporting practices. *Brain Stimulation*, 5(4):435–453. [Cited on pages 43, 44]

Petrov, P. I., Mandija, S., Sommer, I. E. C., van den Berg, C. A. T., and Neggers, S. F. W. (2017). How much detail is needed in modeling a transcranial magnetic stimulation figure-8 coil: Measurements and brain simulations. *PloS one*, 12(6):e0178952. [Cited on pages 52, 53, 57]

Picht, T. (2014). Current and potential utility of transcranial magnetic stimulation in the diagnostics before brain tumor surgery. *CNS oncology*, 3(4):299–310. [Cited on page 85]

Pierpaoli, C. and Basser, P. J. (1996). Toward a quantitative assessment of diffusion anisotropy. *Magnetic Resonance in Medicine*, 36(6):893–906. [Cited on page 59]

Pinto, C. B., Teixeira Costa, B., Duarte, D., and Fregni, F. (2018). Transcranial Direct Current Stimulation as a Therapeutic Tool for Chronic Pain. *Journal of ECT*, 34(3):e36–e50. [Cited on page 25]

Pisa, S., Apollonio, F., and D'Inzeo, G. (2014). A complete model for the evaluation of the magnetic stimulation of peripheral nerves. *The open biomedical engineering journal*, 8:1–12. [Cited on page 49]

Pitkänen, M., Kallioniemi, E., Järnefelt, G., Karhu, J., and Julkunen, P. (2018). Efficient Mapping of the Motor Cortex with Navigated Biphasic Paired-Pulse Transcranial Magnetic Stimulation. *Brain Topography*, 31(6):963–971. [Cited on page 85]

Polanía, R., Nitsche, M. A., and Ruff, C. C. (2018). Studying and modifying brain function with non-invasive brain stimulation. *Nature Neuroscience*, 21(2):174–187. [Cited on page 16]

Prasser, J., Schecklmann, M., Poeppl, T. B., Frank, E., Kreuzer, P. M., Hajak, G., Rupprecht, R., Landgrebe, M., and Langguth, B. (2015). Bilateral prefrontal rTMS and theta burst TMS as an add-on treatment for depression: A randomized placebo controlled trial. *World Journal of Biological Psychiatry*, 16(1):57–65. [Cited on page 36]

Prato, F. S. (2015). Non-thermal extremely low frequency magnetic field effects on opioid related behaviors: Snails to humans, mechanisms to therapy. *Bioelectromagnetics*, 36(5):333–348. [Cited on pages 107, 110]

Prato, F. S., Thomas, A. W., and Cook, C. M. (2001). Human standing balance is affected by exposure to pulsed ELF magnetic fields: Light intensity-dependent effects. *NeuroReport*, 12(7):1501–1505. [Cited on page 115]

Priori, A., Berardelli, A., Rona, S., Accornero, N., and Manfredi, M. (1998). Polarization of the human motor cortex through the scalp. 9(10):2257–2260. [Cited on pages 11, 19, 22, 62]

Puonti, O., Saturnino, G. B., Madsen, K. H., and Thielscher, A. (2019). Comparing and Validating Automated Tools for Individualized Electric Field Simulations in the Human Head. *bioRxiv*, page 611962. [Cited on page 63]

Radman, T., Ramos, R. L., Brumberg, J. C., and Bikson, M. (2009). Role of cortical cell type and morphology in subthreshold and suprathreshold uniform electric field stimulation in vitro. *Brain Stimulation*. [Cited on page 19]

Rahman, A., Reato, D., Arlotti, M., Gasca, F., Datta, A., Parra, L. C., and Bikson, M. (2013). Cellular effects of acute direct current stimulation: Somatic and synaptic terminal effects. *Journal of Physiology*, 591(10):2563–2578. [Cited on page 44]

Rashed, E. A., Gomez-Tames, J., and Hirata, A. (2019). Human Head Skin Thickness Modeling for Electromagnetic Dosimetry. *IEEE Access*, 7:46176–46186. [Cited on page 65]

Ravazzani, P., Ruohonen, J., Grandori, F., and Tognola, G. (1996). Magnetic stimulation of the nervous system: Induced electric field in unbounded, semi-infinite, spherical, and cylindrical media. *Annals of Biomedical Engineering*, 24(5):606–616. [Cited on pages 52, 53]

Ravnborg, M., Blinkenberg, M., and Dahl, K. (1990). Significance of magnetic coil position in peripheral motor nerve stimulation. *Muscle Nerve*, 13(8):681–686. [Cited on page 187]

Ray, P., Sinha, V. K., and Tikka, S. K. (2015). Adjuvant low-frequency rTMS in treating auditory hallucinations in recent-onset schizophrenia: a randomized controlled study investigating the effect of high-frequency priming stimulation. *Annals of General Psychiatry*, 14(1):8. [Cited on page 62]

Razza, L. B., Palumbo, P., Moffa, A. H., Carvalho, A. F., Solmi, M., Loo, C. K., and Brunoni, A. R. (2020). A systematic review and meta-analysis on the effects of transcranial direct current stimulation in depressive episodes. *Depression and Anxiety*, 37(7):594–608. [Cited on page 27]

Reed, T. and Cohen Kadosh, R. (2018). Transcranial electrical stimulation (tES) mechanisms and its effects on cortical excitability and connectivity. *Journal of Inherited Metabolic Disease*, 41(6):1123–1130. [Cited on pages 17, 19]

Reif-Acherman, S. (2017). Jacques Arsene d'Arsonval: His Life and Contributions to Electrical Instrumentation in Physics and Medicine. Part III: High-Frequency Experiences and the Beginnings of Diathermy. *Proceedings of the IEEE*, 105(2):394–404. [Cited on page 12]

Ren, C., Tarjan, P. P., and Popovic, D. B. (1995). A Novel Electric Design for Electromagnetic Stimulation—The Slinky Coil. *IEEE Transactions on Biomedical Engineering*, 42(9):918–925. [Cited on page 187]

Reti, I. M. (2013). A rational insurance coverage policy for repetitive transcranial magnetic stimulation for major depression. *J ECT*, 29(2):e27–8. [Cited on page 172]

Robertson, J. A., Juen, N., Théberge, J., Weller, J., Drost, D. J., Prato, F. S., and Thomas, A. W. (2010a). Evidence for a dose-dependent effect of pulsed magnetic fields on pain processing. *Neuroscience Letters*, 482(2):160–162. [Cited on page 114]

Robertson, J. A., Théberge, J., Weller, J., Drost, D. J., Prato, F. S., and Thomas, A. W. (2010b). Low-frequency pulsed electromagnetic field exposure can alter neuroprocessing in humans. *Journal of the Royal Society Interface*, 7(44):467–473. [Cited on page 114]

Roizenblatt, S., Fregni, F., Gimenez, R., Wetzel, T., Rigonatti, S. P., Tufik, S., Boggio, P. S., and Valle, A. C. (2007). Site-specific effects of transcranial direct current stimulation on sleep and pain in Fibromyalgia: A randomized, sham-controlled study. *Pain Practice*, 7(4):297–306. [Cited on page 26]

Rosler, J., Niraula, B., Strack, V., Zdunczyk, A., Schilt, S., Savolainen, P., Lioumis, P., Makela, J., Vajkoczy, P., Frey, D., and Picht, T. (2014). Language mapping in healthy volunteers and brain tumor patients with a novel navigated tms system: evidence of tumor-induced plasticity. *Clin Neurophysiol*, 125(3):526–36. [Cited on page 85]

Ross, C. L., Zhou, Y., McCall, C. E., Soker, S., and Criswell, T. L. (2019). The Use of Pulsed Electromagnetic Field to Modulate Inflammation and Improve Tissue Regeneration: A Review. *Bioelectricity*, 1(4):247–259. [Cited on page 111]

Rossi, M. and Besnerais, J. L. (2015). Vibration reduction of inductors under magnetostrictive and maxwell forces excitation. *IEEE Transactions on Magnetics*, 51(12):1–6. [Cited on page 176]

Rossi, S., Hallett, M., Rossini, P. M., Pascual-Leone, A., Avanzini, G., Bestmann, S., Berardelli, A., Brewer, C., Canli, T., Cantello, R., Chen, R., Classen, J., Demitrack, M., Di Lazzaro, V., Epstein, C. M., George, M. S., Fregni, F., Ilmoniemi, R., Jalinous, R., Karp, B.,

Lefaucheur, J. P., Lisanby, S., Meunier, S., Miniussi, C., Miranda, P., Padberg, F., Paulus, W., Peterchev, A., Porteri, C., Provost, M., Quartarone, A., Rotenberg, A., Rothwell, J., Ruohonen, J., Siebner, H., Thut, G., Valls-Solè, J., Walsh, V., Ugawa, Y., Zangen, A., and Ziemann, U. (2009). Safety, ethical considerations, and application guidelines for the use of transcranial magnetic stimulation in clinical practice and research. *Clinical Neurophysiology*, 120(12):2008–2039. [Cited on page 32]

Rossini, P. M., Burke, D., Chen, R., Cohen, L. G., Daskalakis, Z., Di Iorio, R., Di Lazzaro, V., Ferreri, F., Fitzgerald, P. B., George, M. S., Hallett, M., Lefaucheur, J. P., Langguth, B., Matsumoto, H., Miniussi, C., Nitsche, M. A., Pascual-Leone, A., Paulus, W., Rossi, S., Rothwell, J. C., Siebner, H. R., Ugawa, Y., Walsh, V., and Ziemann, U. (2015). Non-invasive electrical and magnetic stimulation of the brain, spinal cord, roots and peripheral nerves: Basic principles and procedures for routine clinical and research application: An updated report from an I.F.C.N. Committee. *Clinical Neurophysiology*, 126(6):1071–1107. [Cited on page 65]

Rotenberg, A. (2010). Prospects for clinical applications of transcranial magnetic stimulation and real-time EEG in epilepsy. *Brain Topography*, 22(4):257–266. [Cited on pages 62, 194]

Rotenberg, A., Horvath, J., and Pascual-Leone, A. (2014). *Transcranial Magnetic Stimulation Series Editor*. [Cited on pages 29, 35, 62, 76, 194]

Roth, B. J. and Basser, P. J. (1990). A Model of the Stimulation of a Nerve Fiber by Electromagnetic Induction. *IEEE Transactions on Biomedical Engineering*, 37(6):588–597. [Cited on page 187]

Roth, B. J., Saypol, J. M., Hallett, M., and Cohen, L. G. (1991). A theoretical calculation of the electric field induced in the cortex during magnetic stimulation. *Electroencephalography and Clinical Neurophysiology/Evoked Potentials Section*, 81(1):47 – 56. [Cited on page 48]

Rullmann, M., Anwander, A., Dannhauer, M., Warfield, S. K., Duffy, F. H., and Wolters, C. H. (2009). EEG source analysis of epileptiform activity using a 1 mm anisotropic hexahedra finite element head model. *NeuroImage*, 44(2):399–410. [Cited on page 92]

Ruohonen, J. and Karhu, J. (2010). Navigated transcranial magnetic stimulation. *Clinical Neurophysiology*, 40(1):7–17. [Cited on pages 63, 86, 87]

Saad, Y. and van der Vorst, H. A. (2000). Iterative solution of linear systems in the 20th century. *Journal of Computational and Applied Mathematics*, 123(1):1 – 33. [Cited on page 51]

Sack, A. T., Camprodon, J. A., Pascual-Leone, A., and Goebel, R. (2005). The dynamics of interhemispheric compensatory processes in mental imagery. *Science*, 308(5722):702–4. [Cited on page 172]

Sadleir, R. J., Vannorsdall, T. D., Schretlen, D. J., and Gordon, B. (2010). Transcranial direct current stimulation (tDCS) in a realistic head model. *NeuroImage*, 51(4):1310–1318. [Cited on pages 54, 69]

Sadleir, R. J., Vannorsdall, T. D., Schretlen, D. J., and Gordon, B. (2012). Target optimization in transcranial direct current stimulation. *Frontiers in Psychiatry*, 3(OCT):1–13. [Cited on page 69]

Sakreida, K., Lange, I., Willmes, K., Heim, S., Binkofski, F., Clusmann, H., and Neuloh, G. (2018). High-resolution language mapping of Broca's region with transcranial magnetic stimulation. *Brain Structure and Function*, 223(3):1297–1312. [Cited on pages 85, 165]

Salinas, F. S., Lancaster, J. L., and Fox, P. T. (2007). Detailed 3d models of the induced electric field of transcranial magnetic stimulation coils. *Physics in Medicine and Biology*, 52 (10):12879. [Cited on pages 53, 122]

Salinas, F. S., Lancaster, J. L., and Fox, P. T. (2009). 3d modeling of the total electric field induced by transcranial magnetic stimulation using the boundary element method. *Physics in Medicine and Biology*, 54 (12):3631–3647. [Cited on pages 63, 69, 122, 173, 188, 194]

Salomons, T. V., Dunlop, K., Kennedy, S. H., Flint, A., Geraci, J., Giacobbe, P., and Downar, J. (2014). Resting-state cortico-thalamic-striatal connectivity predicts response to dorsomedial prefrontal rTMS in major depressive disorder. *Neuropsychopharmacology*, 39(2):488–498. [Cited on page 40]

Salvador, R. and Miranda, P. C. (2009). Transcranial magnetic stimulation of small animals: A modeling study of the influence of coil geometry, size and orientation. *Proceedings of the 31st Annual International Conference of the IEEE Engineering in Medicine and Biology Society: Engineering the Future of Biomedicine, EMBC 2009*, pages 674–677. [Cited on page 167]

Salvador, R., Silva, S., Basser, P., and Miranda, P. (2011). Determining which mechanisms lead to activation in the motor cortex: a modeling study of transcranial magnetic stimulation using realistic stimulus waveforms and sulcal geometry. *Clin. Neurophysiol.*, 122:748–58. [Cited on page 122]

Sarmiento, C. I., San-Juan, D., and Prasath, V. B. (2016). Letter to the Editor: Brief history of transcranial direct current stimulation (tDCS): From electric fishes to microcontrollers. *Psychological Medicine*, 46(15):3259–3261. [Cited on page 11]

Sasaki, N., Abo, M., Hara, T., Yamada, N., Niimi, M., and Kakuda, W. (2017). High-frequency rTMS on leg motor area in the early phase of stroke. *Acta Neurologica Belgica*, 117(1):189–194. [Cited on page 40]

Sathappan, A. V., Luber, B. M., and Lisanby, S. H. (2019). The dynamic Duo: Combining noninvasive brain stimulation with cognitive interventions. 89:347–360. [Cited on page 27]

Saturnino, G. B., Antunes, A., and Thielscher, A. (2015). On the importance of electrode parameters for shaping electric field patterns generated by tDCS. *NeuroImage*, 120:25–35. [Cited on page 55]

Saturnino, G. B., Madsen, K. H., and Thielscher, A. (2019a). Electric field simulations for transcranial brain stimulation using FEM: An efficient implementation and error analysis. *Journal of Neural Engineering*, 16(6). [Cited on pages 48, 65, 87, 103]

Saturnino, G. B., Thielscher, A., Madsen, K. H., Knösche, T. R., and Weise, K. (2019b). A principled approach to conductivity uncertainty analysis in electric field calculations. *NeuroImage*, 188(October 2018):821–834. [Cited on page 78]

Schecklmann, M., Schmaußer, M., Klinger, F., Kreuzer, P. M., Krenkel, L., and Langguth, B. (2020). Resting motor threshold and magnetic field output of the figure-of-8 and the double-cone coil. *Scientific Reports*, 10(1):1–6. [Cited on page 34]

Schindler, K., Nyffeler, T., Wiest, R., Hauf, M., Mathis, J., Hess, C. W., and Müri, R. (2008). Theta burst transcranial magnetic stimulation is associated with increased EEG synchronization in the stimulated relative to unstimulated cerebral hemisphere. *Neuroscience Letters*, 436(1):31–34. [Cited on page 32]

Schmid, G., Cecil, S., and Überbacher, R. (2013). The role of skin conductivity in a low frequency exposure assessment for peripheral nerve tissue according to the ICNIRP 2010 guidelines. *Physics in Medicine and Biology*, 58(13):4703–4716. [Cited on page 64]

Schoisswohl, S., Agrawal, K., Simoes, J., Neff, P., Schlee, W., Langguth, B., and Schecklmann, M. (2019). RTMS parameters in tinnitus trials: a systematic review. *Scientific Reports*, 9(1):1–11. [Cited on page 62]

Schutter, D. J. (2009). Antidepressant efficacy of high-frequency transcranial magnetic stimulation over the left dorsolateral prefrontal cortex in double-blind sham-controlled designs: a meta-analysis. *Psychol Med*, 39(1):65–75. [Cited on page 35]

Schwenkreis, P., Scherens, A., Rönnau, A.-K., Höffken, O., Tegenthoff, M., and Maier, C. (2010). Cortical disinhibition occurs in chronic neuropathic, but not in chronic nociceptive pain. *BMC neuroscience*, 11(1):73. [Cited on page 172]

Segal, Y., Segal, L., Blumenfeld-Katzir, T., Sasson, E., Poliansky, V., Loeb, E., Levy, A., Alter, A., and Bregman, N. (2016). The effect of electromagnetic field treatment on recovery from ischemic stroke in a rat stroke model: Clinical, imaging, and pathological findings. *Stroke research and treatment*, 2016:6941946. [Cited on page 121]

Seynaeve, L., Haeck, T., Gramer, M., Maes, F., De Vleeschouwer, S., and Van Paesschen, W. (2019). Optimized preoperative motor cortex mapping in brain tumors using advanced processing of transcranial magnetic stimulation data. *NeuroImage: Clinical*, 21. [Cited on page 33]

Shahbazi-Gahrouei, D., Shiri, L., Alaei, H., and Naghdi, N. (2016). The effect of continuous ELF-MFs on the level of 5-HIAA in the raphe nucleus of the rat. *Journal of Radiation Research*, 57(2):127–132. [Cited on page 109]

Sharafi, E., Taghva, A., Arbabi, M., Dadarkhah, A., and Ghaderi, J. (2019). Transcranial Direct Current Stimulation for Treatment-Resistant Major Depression: A Double-Blind Randomized Sham-Controlled Trial. *Clinical EEG and Neuroscience*, 50(6):375–382. [Cited on page 27]

Shen, B., Yin, Y., Wang, J., Zhou, X., McClure, S. M., and Li, J. (2016). High-definition tDCS alters impulsivity in a baseline-dependent manner. *NeuroImage*. [Cited on page 24]

Shimony, J. S., McKinstry, R. C., Akbudak, E., Aronovitz, J. A., Snyder, A. Z., Lori, N. F., Cull, T. S., and Conturo, T. E. (1999). Quantitative diffusion-tensor anisotropy brain MR imaging: Normative human data and anatomic analysis. *Radiology*, 212(3):770–784. [Cited on pages 59, 92]

Shin, E. J., Ji, H. J., Hyun, J. K., Jang, C. G., Yamada, K., Nabeshima, T., and Kim, H. C. (2007). Exposure to extremely low frequency magnetic fields enhances locomotor activity via activation of dopamine D1-like receptors in mice. *Journal of Pharmacological Sciences*, 105(4):367–371. [Cited on page 109]

Shirahige, L., Melo, L., Nogueira, F., Rocha, S., and Monte-Silva, K. (2016). Efficacy of Noninvasive Brain Stimulation on Pain Control in Migraine Patients: A Systematic Review and Meta-Analysis. [Cited on page 25]

Shupak, N. M., Hensel, J. M., Cross-Mellor, S. K., Kavaliers, M., Prato, F. S., and Thomas, A. W. (2004a). Analgesic and behavioral effects of a 100 μT specific pulsed extremely low frequency magnetic field on control and morphine treated CF-1 mice. *Neuroscience Letters*, 354(1):30–33. [Cited on pages 107, 114]

Shupak, N. M., McKay, J. C., Nielson, W. R., Rollman, G. B., Prato, F. S., and Thomas, A. W. (2006). Exposure to a specific pulsed low-frequency magnetic field: A double-blind placebo-controlled study of effects on pain ratings in rheumatoid arthritis and fibromyalgia patients. *Pain Research and Management*, 11(2):85–90. [Cited on page 114]

Shupak, N. M., Prato, F. S., and Thomas, A. W. (2004b). Human exposure to a specific pulsed magnetic field: Effects on thermal sensory and pain thresholds. *Neuroscience Letters*, 363(2):157–162. [Cited on pages 110, 114]

Sieroń, A., Brus, R., Szkilnik, R., Plech, A., Kubański, N., and Cieślar, G. (2001). Influence of alternating low frequency magnetic fields on reactivity of central dopamine receptors in neonatal 6-hydroxydopamine treated rats. *Bioelectromagnetics*, 22(7):479–486. [Cited on page 109]

Sieroń, A., Labus, Ł., Nowak, P., Cieślar, G., Brus, H., Durczok, A., Zagził, T., Kostrzewa, R. M., and Brus, R. (2004). Alternating extremely low frequency magnetic field increases turnover of dopamine and serotonin in rat frontal cortex. *Bioelectromagnetics*, 25(6):426–430. [Cited on page 108]

Silva, A. F., Zortea, M., Carvalho, S., Leite, J., da Silva Torres, I. L., Fregni, F., and Caumo, W. (2017). Anodal transcranial direct current stimulation over the left dorsolateral prefrontal cortex modulates attention and pain in fibromyalgia: Randomized clinical trial. *Scientific Reports*, 7(1):1–11. [Cited on page 26]

Smith, R. C., Boules, S., Mattiuz, S., Youssef, M., Tobe, R. H., Sershen, H., Lajtha, A., Nolan, K., Amiaz, R., and Davis, J. M. (2015). Effects of transcranial direct current stimulation (tDCS) on cognition, symptoms, and smoking in schizophrenia: A randomized controlled study. *Schizophrenia Research*, 168(1-2):260–266. [Cited on page 28]

Soldati, M. and Laakso, I. (2020). Computational errors of the induced electric field in voxelized and tetrahedral anatomical head models exposed to spatially uniform and localized magnetic fields. *Physics in Medicine and Biology*, 65(1). [Cited on page 73]

Sollmann, N., Goblirsch-Kolb, M. F., Ille, S., Butenschoen, V. M., Boeckh-Behrens, T., Meyer, B., Ringel, F., and Krieg, S. M. (2016). Comparison between electric-field-navigated and line-navigated TMS for cortical motor mapping in patients with brain tumors. *Acta Neurochirurgica*, 158(12):2277–2289. [Cited on pages 86, 87]

Solomons, C. D. and Shanmugasundaram, V. (2020). Transcranial direct current stimulation: A review of electrode characteristics and materials. *Medical Engineering and Physics*, 85:63–74. [Cited on pages 21, 23]

Sonmez, A. I., Camsari, D. D., Nandakumar, A. L., Voort, J. L. V., Kung, S., Lewis, C. P., and Croarkin, P. E. (2019). Accelerated tms for depression: A systematic review and meta-analysis. *Psychiatry Res*, 273:770–781. [Cited on page 172]

Stagg, C. J., Antal, A., and Nitsche, M. A. (2018). Physiology of transcranial direct current stimulation. *The Journal of ECT*, 34(3):144–152. [Cited on pages 19, 20]

Stagg, C. J., Best, J. G., Stephenson, M. C., O'Shea, J., Wylezinska, M., Kineses, Z. T., Morris, P. G., Matthews, P. M., and Johansen-Berg, H. (2009). Polarity-sensitive modulation of cortical neurotransmitters by transcranial stimulation. *Journal of Neuroscience*. [Cited on page 20]

Starzynski, J., Sawicki, B., Wincenciak, S., Krawczyk, A., and Zyss, T. (2002). Simulation of magnetic stimulation of the brain. *IEEE Transactions on Magnetics*, 38 (2 I):1237–1240. [Cited on pages 63, 122]

Stodilka, R. Z., Modolo, J., Prato, F. S., Robertson, J. A., Cook, C., Patrick, J., Beuter, A., Thomas, A. W., and Legros, A. (2011). Pulsed magnetic field exposure induces lasting changes in neural network dynamics. *Neurocomputing*, 74(12-13):2164–2175. [Cited on page 115]

Stubbeman, W. F., Zarrabi, B., Bastea, S., Ragland, V., and Khairkhah, R. (2018). Bilateral neuronavigated 20hz theta burst tms for treatment refractory depression: An open label study. *Brain Stimul*, 11(4):953–955. [Cited on page 172]

Stultz, D. J., Osburn, S., Burns, T., Walton, R., and Pawlowska-Wajswol, S. (2019). Tms treatment in a patient with seizures and refractory depression. *Brain Stimul*, 12(6):1603–1604. [Cited on page 172]

Subbanna, N. K., Rajashekar, D., Cheng, B., Thomalla, G., Fiehler, J., Arbel, T., and Forkert, N. D. (2019). Stroke lesion segmentation in flair mri datasets using customized markov random fields. *Frontiers in Neurology*, 10:541. [Cited on page 150]

Tachas, N. J., Efthimiadis, K. G., and Samaras, T. (2013). The effect of coil modeling on the predicted induced electric field distribution during TMS. *IEEE Transactions on Magnetics*, 49(3):1096–1100. [Cited on page 52]

Talebinejad, M. and Musallam, S. (2010). Effects of TMS coil geometry on stimulation specificity. *2010 Annual International Conference of the IEEE Engineering in Medicine and Biology Society, EMBC'10*, pages 1507–1510. [Cited on pages 169, 173, 194, 195, 201]

Tang, A., Thickbroom, G., and Rodger, J. (2017). Repetitive Transcranial Magnetic Stimulation of the Brain: Mechanisms from Animal and Experimental Models. *Neuroscientist*, 23(1):82–94. [Cited on page 167]

Tang, A. D., Lowe, A. S., Garrett, A. R., Woodward, R., Bennett, W., Canty, A. J., Garry, M. I., Hinder, M. R., Summers, J. J., Gersner, R., Rotenberg, A., Thickbroom, G., Walton, J., and Rodger, J. (2016). Construction and evaluation of rodent-specific rTMS coils. *Frontiers in Neural Circuits*, 10(JUNE):1–10. [Cited on page 167]

Tarao, H., Kuisti, H., Korpinen, L., Hayashi, N., and Isaka, K. (2012). Effects of tissue conductivity and electrode area on internal electric fields in a numerical human model for ELF contact current exposures. *Physics in Medicine and Biology*. [Cited on pages 59, 64, 67, 68]

Tarapore, P. E., Picht, T., Bulubas, L., Shin, Y., Kulchytska, N., Meyer, B., Berger, M. S., Nagarajan, S. S., and Krieg, S. M. (2016). Safety and tolerability of navigated TMS for preoperative mapping in neurosurgical patients. *Clinical Neurophysiology*, 127(3):1895–1900. [Cited on page 165]

Tavakoli, A. V. and Yun, K. (2017). Transcranial alternating current stimulation (tacs) mechanisms and protocols. *Frontiers in Cellular Neuroscience*, 11:214. [Cited on page 17]

Tavares, D. F., Myczkowski, M. L., Alberto, R. L., Valiengo, L., Rios, R. M., Gordon, P., De Sampaio-Junior, B., Klein, I., Mansur, C. G., Marcolin, M. A., Lafer, B., Moreno, R. A., Gattaz, W., Daskalakis, Z. J., and Brunoni, A. R. (2017). Treatment of bipolar depression with deep TMS: Results from a double-blind, randomized, parallel group, sham-controlled clinical trial. *Neuropsychopharmacology*, 42(13):2593–2601. [Cited on page 36]

Teng, S., Guo, Z., Peng, H., Xing, G., Chen, H., He, B., McClure, M. A., and Mu, Q. (2017). High-frequency repetitive transcranial magnetic stimulation over the left DLPFC for major depression: Session-dependent efficacy: A meta-analysis. *European Psychiatry*, 41:75–84. [Cited on page 36]

Terney, D., Chaieb, L., Moliadze, V., Antal, A., and Paulus, W. (2008). Increasing Human Brain Excitability by Transcranial High-Frequency Random Noise Stimulation. *Journal of Neuroscience*, 28(52):14147–14155. [Cited on page 17]

Theleritis, C., Sakkas, P., Paparrigopoulos, T., Vitoratou, S., Tzavara, C., Bonaccorso, S., Politis, A., Soldatos, C. R., and Psarros, C. (2017). Two versus one high-frequency repetitive transcranial magnetic stimulation session per day for treatment-resistant depression. *Journal of ECT*, 33(3):190–197. [Cited on page 35]

Thickbroom, G. W. (2007). Transcranial magnetic stimulation and synaptic plasticity: Experimental framework and human models. *Experimental Brain Research*, 180(4):583–593. [Cited on page 31]

Thielscher, A. and Kammer, T. (2004). Electric field properties of two commercial figure-8 coils in tms: calculation of focality and efficiency. *Clinical Neurophysiology*, 115(7):1697 – 1708. [Cited on pages 52, 53, 173]

Thielscher, A., Opitz, A., and Windhoff, M. (2011). Impact of the gyral geometry on the electric field induced by transcranial magnetic stimulation. *NeuroImage*, 54(1):234–243. [Cited on pages 64, 70, 72]

Thomas, A. W., Drost, D. J., and Prato, F. S. (2001a). Human subjects exposed to a specific pulsed (200 μT) magnetic field: Effects on normal standing balance. *Neuroscience Letters*, 297(2):121–124. [Cited on page 115]

Thomas, A. W., Kavaliers, M., Prato, F. S., and Ossenkopp, K. P. (1997). Antinociceptive effects of a pulsed magnetic field in the land snail, Cepaea nemoralis. *Neuroscience Letters*, 222(2):107–110. [Cited on pages 110, 114]

Thomas, A. W., Prato, F. S., Kavaliers, M. I., and Persinger, M. A. (2001b). U. S. Patent No. 6,234,953. [Cited on page 114]

Thomas, C., Ghodratitoostani, I., Delbem, A. C., Ali, A., and Datta, A. (2019). Influence of gender-related differences in transcranial direct current stimulation: A Computational Study. *Proceedings of the Annual International Conference of the IEEE Engineering in Medicine and Biology Society, EMBS*, pages 5196–5199. [Cited on page 45]

Thompson, S. P. (1910). A physiological effect of an alternating magnetic field. *Proceedings of the Royal Society of London. Series B, Containing Papers of a Biological Character*, 82(557):396–398. [Cited on page 12]

Thut, G. and Pascual-Leone, A. (2010). A review of combined TMS-EEG studies to characterize lasting effects of repetitive TMS and assess their usefulness in cognitive and clinical neuroscience. [Cited on page 32]

Tischler, H., Wolfus, S., Friedman, A., Perel, E., Pashut, T., Lavidor, M., Korngreen, A., Yeshurun, Y., and Bar-Gad, I. (2011). Mini-coil for magnetic stimulation in the behaving primate. *Journal of Neuroscience Methods*, 194(2):242–251. [Cited on pages 173, 187, 194, 195, 201]

To, W. T., James, E., Ost, J., Hart, J., De Ridder, D., and Vanneste, S. (2017). Differential effects of bifrontal and occipital nerve stimulation on pain and fatigue using transcranial direct current stimulation in fibromyalgia patients. *Journal of Neural Transmission*, 124(7):799–808. [Cited on page 26]

Tringali, S., Perrot, X., Collet, L., and Moulin, A. (2012). Repetitive transcranial magnetic stimulation: hearing safety considerations. *Brain Stimul*, 5(3):354–363. [Cited on pages 176, 177]

Truong, D. Q., Magerowski, G., Blackburn, G. L., Bikson, M., and Alonso-Alonso, M. (2013). Computational modeling of transcranial direct current stimulation (tDCS) in obesity: Impact of head fat and dose guidelines. *NeuroImage: Clinical*, 2(1):759–766. [Cited on pages 54, 63, 68, 74]

Tsai, B., Xue, H., Birgersson, E., Ollmar, S., and Birgersson, U. (2019). Dielectrical properties of living epidermis and dermis in the frequency range from 1 kHz to 1 MHz. *Journal of Electrical Bioimpedance*, 10(1):14–23. [Cited on pages xv, 71, 79, 81, 82, 83, 84]

Tsai, P. Y., Wang, C. P., Ko, J. S., Chung, Y. M., Chang, Y. W., and Wang, J. X. (2014). The persistent and broadly modulating effect of inhibitory rTMS in nonfluent aphasic patients: A sham-controlled, double-blind study. *Neurorehabilitation and Neural Repair*, 28(8):779–787. [Cited on page 40]

Tuch, D. S., Wedeen, V. J., Dale, A. M., George, J. S., and Belliveau, J. W. (2001). Conductivity tensor mapping of the human brain using diffusion tensor MRI. *Proceedings of the National Academy of Sciences of the United States of America*, 98(20):11697–11701. [Cited on pages 59, 92]

Ueno, S., Tashiro, T., and Harada, K. (1988). Localized stimulation of neural tissues in the brain by means of a paired configuration of time-varying magnetic fields. *Journal of Applied Physics*, 64(10):5862–5864. [Cited on pages 33, 167]

Urnukhsaikhan, E., Mishig-Ochir, T., Kim, S., Park, J., and Seo, Y. (2017). Neuroprotective effect of low frequency-pulsed electromagnetic fields in ischemic stroke. *Applied Biochemestry and Biotechnology*, 181(4):1360–1371. [Cited on pages 112, 120]

Vahabzadeh-Hagh, A. M., Muller, P. A., Gersner, R., Zangen, A., and Rotenberg, A. (2012). Translational neuromodulation: Approximating human transcranial magnetic stimulation protocols in rats. *Neuromodulation*, 15(4):296–305. [Cited on page 167]

Valero-Cabré, A., Amengual, J. L., Stengel, C., Pascual-Leone, A., and Coubard, O. A. (2017). Transcranial magnetic stimulation in basic and clinical neuroscience: A comprehensive review of fundamental principles and novel insights. *Neuroscience and Biobehavioral Reviews*, 83(September):381–404. [Cited on pages 29, 31, 32, 33, 35]

Valero-Cabré, A., Pascual-Leone, A., and Coubard, O. A. (2011). Transcranial magnetic stimulation (TMS) in basic and clinical neuroscience research. *Revue Neurologique*, 167(4):291–316. [Cited on pages 62, 194]

Valiengo, L. C., Goulart, A. C., De Oliveira, J. F., Benseñor, I. M., Lotufo, P. A., and Brunoni, A. R. (2017). Transcranial direct current stimulation for the treatment of post-stroke depression: Results from a randomised, sham-controlled, double-blinded trial. *Journal of Neurology, Neurosurgery and Psychiatry*, 88(2):170–175. [Cited on page 27]

Valle, A., Roizenblatt, S., Botte, S., Zaghi, S., Riberto, M., Tufik, S., Boggio, P. S., and Fregni, F. (2009). Efficacy of anodal transcranial direct current stimulation (tdcs) for the treatment of fibromyalgia: results of a randomized, sham-controlled longitudinal clinical trial. *J Pain Manag*, 2(3):353–361. [Cited on page 26]

van der Vorst, H. A. (2002). Efficient and reliable iterative methods for linear systems. *Journal of Computational and Applied Mathematics*, 149(1):251 – 265. [Cited on page 51]

Van Nierop, L. E., Slottje, P., Van Zandvoort, M., and Kromhout, H. (2015). Simultaneous exposure to MRI-related static and low-frequency movement-induced time-varying magnetic fields affects neurocognitive performance: A double-blind randomized crossover study. *Magnetic Resonance in Medicine*, 74(3):840–849. [Cited on page 113]

Vanhaerents, S., Chang, B., Rotenberg, A., Pascual-Leone, A., and Shafi, M. (2020). Noninvasive brain stimulation in epilepsy. *Journal of Clinical Neurophysiology*, 37(2):118–130. [Cited on page 62]

Varani, K., Gessi, S., Merighi, S., Iannotta, V., Cattabriga, E., Pancaldi, C., Cadossi, R., and Borea, P. A. (2003). Alteration of A3adenosine receptors in human neutrophils and low frequency electromagnetic fields. *Biochemical Pharmacology*, 66(10):1897–1906. [Cited on page 111]

Varani, K., Gessi, S., Merighi, S., Iannotta, V., Cattabriga, E., Spisani, S., Cadossi, R., and Borea, P. A. (2002). Effect of low frequency electromagnetic fields on A_{2A} adenosine receptors in human neutrophils. *British Journal of Pharmacology*, 136:57–66. [Cited on pages 111, 121, 138, 147]

Varani, K., Vincenzi, F., Cadossi, M., Setti, S., Borea, P. A., and Cadossi, R. (2018). *Role of Adenosine Receptors in Clinical Biophysics Based on Pulsed Electromagnetic Fields*, pages 557–580. Springer International Publishing, Cham. [Cited on page 111]

Varani, K., Vincenzi, F., Ravani, A., Pasquini, S., Merighi, S., Gessi, S., Setti, S., Cadossi, M., Borea, P. A., and Cadossi, R. (2017). Adenosine receptors as a biological pathway for the anti-inflammatory and beneficial effects of low frequency low energy pulsed electromagnetic fields. *Mediators of Inflammation*. [Cited on pages 111, 120]

Varani, K., Vincenzi, F., Targa, M., Corciulo, C., Fini, M., Setti, S., Cadossi, R., and Borea, P. A. (2012). Effect of pulsed electromagnetic field exposure on adenosine receptors in rat brain. *Bioelectromagnetics*, 33:279–287. [Cited on pages 111, 121, 138]

Vekrellis, K., Xilouri, M., Emmanouilidou, E., and Stefanis, L. (2009). Inducible over-expression of wild type $\alpha-$synuclein in human neuronal cells leads to caspase-dependent non-apoptotic death. *Journal of Neurochemestry*, 109:1348–1362. [Cited on pages 121, 131]

Verheyden, G., Purdey, J., Burnett, M., Cole, J., and Ashburn, A. (2013). Immediate effect of transcranial direct current stimulation on postural stability and functional mobility in parkinson's disease. *Movement Disorders*, 28(14):2040–2041. [Cited on page 28]

Veronesi, F., Torricelli, P., Giavaresi, G., Sartori, M., Cavani, F., Setti, S., Cadossi, M., Ongaro, A., and Fini, M. (2014). In vivo effect of two different pulsed electromagnetic field frequencies on osteoarthritis. *Journal of Orthopaedic Research*, 32(5):677–685. [Cited on page 116]

Villard, S., Allen, A., Bouisset, N., Corbacio, M., Thomas, A., Guerraz, M., and Legros, A. (2019). Impact of extremely low-frequency magnetic fields on human postural control. *Experimental Brain Research*, 237(3):611–623. [Cited on page 113]

Vincenzi, F., Ravani, A., Pasquini, S., Merighi, S., Gessi, S., Setti, S., Cadossi, R., Borea, P. A., and Varani, K. (2017). Pulsed electromagnetic field exposure reduces hypoxia and inflammation damage in neuron-like and microglial cells. *Journal of Cell Physiol.,*, 232 (5):1200–1208. [Cited on pages 111, 112, 121]

Vincenzi, F., Targa, M., Corciulo, C., Gessi, S., Merighi, S., Setti, S., Cadossi, R., Borea, P. A., and Varani, K. (2012). The anti-tumor effect of A_3 adenosine receptors is potentiated by pulsed electromagnetic fields in cultured neural cancer cells. *Plos One*, 7 (6). [Cited on pages 112, 121, 131]

Volz, M. S., Farmer, A., and Siegmund, B. (2016). Reduction of chronic abdominal pain in patients with inflammatory bowel disease through transcranial direct current stimulation: A randomized controlled trial. *Pain*, 157(2):429–437. [Cited on page 25]

Wagner, S., Rampersad, S. M., Aydin, Ü., Vorwerk, J., Oostendorp, T. F., Neuling, T., Herrmann, C. S., Stegeman, D. F., and Wolters, C. H. (2014). Investigation of tDCS volume conduction effects in a highly realistic head model. *Journal of Neural Engineering*, 11(1). [Cited on page 69]

Wagner, T., Fregni, F., Eden, U., Ramos-Estebanez, C., Grodzinsky, A., Zahn, M., and Pascual-Leone, A. (2006). Transcranial magnetic stimulation and stroke: a computer based human model study. *NeuroImage*, 30:857–870. [Cited on pages 45, 135]

Wagner, T., Fregni, F., Fecteau, S., Grodzinsky, A., Zahn, M., and Pascual-Leone, A. (2007a). Transcranial direct current stimulation: A computer-based human model study. *NeuroImage*, 35(3):1113–1124. [Cited on pages 54, 55]

Wagner, T., Rushmore, J., Eden, U., and Valero-Cabre, A. (2009). Biophysical foundations underlying TMS: Setting the stage for an effective use of neurostimulation in the cognitive neurosciences. *Cortex*, 45(9):1025–1034. [Cited on page 166]

Wagner, T., Valero-Cabre, A., and Pascual-Leone, A. (2007b). Noninvasive Human Brain Stimulation. *Annual Review of Biomedical Engineering*, 9(1):527–565. [Cited on page 33]

Wagner, T. A., Zahn, M., Grodzinsky, A. J., and Pascual-Leone, A. (2004). Three-dimensional head model simulation of transcranial magnetic stimulation. *IEEE Transactions on Biomedical Engineering*, 51(9):1586–1598. [Cited on pages 66, 70]

Wake, K., Sasaki, K., and Watanabe, S. (2016). Conductivities of epidermis, dermis, and subcutaneous tissue at intermediate frequencies. *Physics in Medicine and Biology*, 61(12):4376–4389. [Cited on page 82]

Wang, C. P., Tsai, P. Y., Yang, T. F., Yang, K. Y., and Wang, C. C. (2014). Differential Effect of Conditioning Sequences in Coupling Inhibitory/Facilitatory Repetitive Transcranial Magnetic Stimulation for PostStroke Motor Recovery. *CNS Neuroscience and Therapeutics*, 20(4):355–363. [Cited on page 40]

Wang, Y., Zhou, H., Li, Y., and Liu, W. (2018). Impact of electrode number on the performance of high-definition transcranial direct current stimulation (hd-tdcs). In *2018 40th Annual*

International Conference of the IEEE Engineering in Medicine and Biology Society (EMBC), pages 4182–4185. [Cited on page 24]

Wassermann, E. M., Blaxton, T. A., Hoffman, E. A., Berry, C. D., Oletsky, H., Pascual-Leone, A., and Theodore, W. H. (1999). Repetitive transcranial magnetic stimulation of the dominant hemisphere can disrupt visual naming in temporal lobe epilepsy patients. *Neuropsychologia*. [Cited on pages 172, 194]

Wassermann, E. M., McShane, L. M., Hallett, M., and Cohen, L. G. (1992). Noninvasive mapping of muscle representations in human motor cortex. *Electroencephalography and Clinical Neurophysiology/ Evoked Potentials*, 85(1):1–8. [Cited on page 194]

Watanabe, K., Kudo, Y., Sugawara, E., Nakamizo, T., Amari, K., Takahashi, K., Tanaka, O., Endo, M., Hayakawa, Y., and Johkura, K. (2018). Comparative study of ipsilesional and contralesional repetitive transcranial magnetic stimulations for acute infarction. *Journal of the Neurological Sciences*, 384(October 2017):10–14. [Cited on page 62]

Weber, M. and Eisen, A. A. (2002). Magnetic stimulation of the central and peripheral nervous systems. *Muscle and Nerve*, 25(2):160–175. [Cited on page 76]

Weise, D., Mann, J., Ridding, M., Eskandar, K., Huss, M., Rumpf, J. J., Di Lazzaro, V., Mazzone, P., Ranieri, F., and Classen, J. (2013). Microcircuit mechanisms involved in paired associative stimulation-induced depression of corticospinal excitability. *Journal of Physiology*, 591(19):4903–4920. [Cited on page 31]

Weise, K., Numssen, O., Thielscher, A., Hartwigsen, G., and Knösche, T. R. (2020). A novel approach to localize cortical TMS effects. *NeuroImage*, 209(December 2019). [Cited on pages 43, 44, 48, 52, 53, 57, 63, 64]

Weissman-Fogel, I. and Granovsky, Y. (2019). The "virtual lesion" approach to transcranial magnetic stimulation. *PAIN Reports*, 4(4):e760. [Cited on page 165]

Wheeler, H. M., Mlynash, M., Inoue, M., Tipirneni, A., Liggins, J., Zaharchuk, G., Straka, M., Kemp, S., Bammer, R., Lansberg, M. G., and Albers, G. W. (2013). Early diffusion-weighted imaging and perfusion-weighted imaging lesion volumes forecast final infarct size in DEFUSE 2. *Stroke*, 44(3):681–685. [Cited on page 150]

Wheless, J. W., Gienapp, A. J., and Ryvlin, P. (2018). Vagus nerve stimulation (vns) therapy update. *Epilepsy & Behavior*, 88:2 – 10. Neurostimulation for Epilepsy. [Cited on page 15]

Williams, N. R., Sudheimer, K. D., Bentzley, B. S., Pannu, J., Stimpson, K. H., Duvio, D., Cherian, K., Hawkins, J., Scherrer, K. H., Vyssoki, B., DeSouza, D., Raj, K. S., Keller, J., and Schatzberg, A. F. (2018). High-dose spaced theta-burst tms as a rapid-acting antidepressant in highly refractory depression. *Brain*, 141(3):e18. [Cited on page 172]

Windhoff, M., Opitz, A., and Thielscher, A. (2013). Electric field calculations in brain stimulation based on finite elements: An optimized processing pipeline for the generation and usage of accurate individual head models. *Human Brain Mapping*, 34(4):923–935. [Cited on pages 59, 70]

Wolters, C. H., Anwander, A., Tricoche, X., Weinstein, D., Koch, M. A., and MacLeod, R. S. (2006). Influence of tissue conductivity anisotropy on EEG/MEG field and return current computation in a realistic head model: A simulation and visualization study using high-resolution finite element modeling. *NeuroImage*, 30(3):813–826. [Cited on page 92]

Woods, A. J., Antal, A., Bikson, M., Boggio, P. S., Brunoni, A. R., Celnik, P., Cohen, L. G., Fregni, F., Herrmann, C. S., Kappenman, E. S., Knotkova, H., Liebetanz, D., Miniussi, C., Miranda, P. C., Paulus, W., Priori, A., Reato, D., Stagg, C., Wenderoth, N., and Nitsche, M. A. (2016). A technical guide to tDCS, and related non-invasive brain stimulation tools. [Cited on pages 21, 22]

Wörsching, J., Padberg, F., Goerigk, S., Heinz, I., Bauer, C., Plewnia, C., Hasan, A., Ertl-Wagner, B., and Keeser, D. (2018). Testing assumptions on prefrontal transcranial direct current stimulation: Comparison of electrode montages using multimodal fMRI. *Brain Stimulation*, 11(5):998–1007. [Cited on page 22]

Wright, C. W., Bu, L., Jones, A., and Calder Green, N. (2017). *VNS Therapy for the Treatment of Epilepsy*, pages 181–204. Springer International Publishing, Cham. [Cited on page 15]

Wrigley, P. J., Gustin, S. M., McIndoe, L. N., Chakiath, R. J., Henderson, L. A., and Siddall, P. J. (2013). Longstanding neuropathic pain after spinal cord injury is refractory to transcranial direct current stimulation: A randomized controlled trial. *Pain*. [Cited on page 26]

Wu, Z., Liu, Y., Hong, M., and Yu, X. (2018). A review of anisotropic conductivity models of brain white matter based on diffusion tensor imaging. *Medical and Biological Engineering and Computing*, 56(8):1325–1332. [Cited on page 91]

Xu, H. and Mandal, M. (2015). Epidermis segmentation in skin histopathological images based on thickness measurement and k-means algorithm. *Eurasip Journal on Image and Video Processing*, 2015(1):1–14. [Cited on page 71]

Yamamoto, T. and Yamamoto, Y. (1976). Electrical properties of the epidermal stratum corneum. *Medical & Biological Engineering*, 14(2):151–158. [Cited on pages 66, 68]

Yang, C., Guo, Z., Peng, H., Xing, G., Chen, H., McClure, M. A., He, B., He, L., Du, F., Xiong, L., and Mu, Q. (2018). Repetitive transcranial magnetic stimulation therapy for motor recovery in Parkinson's disease: A Meta-analysis. *Brain and Behavior*, 8(11):1–17. [Cited on page 41]

Yang, S. and Chang, M. C. (2020). Effect of Repetitive Transcranial Magnetic Stimulation on Pain Management: A Systematic Narrative Review. *Frontiers in Neurology*, 11(February). [Cited on pages 37, 38, 62]

Yokoe, M., Mano, T., Maruo, T., Hosomi, K., Shimokawa, T., Kishima, H., Oshino, S., Morris, S., Kageyama, Y., Goto, Y., Shimizu, T., Mochizuki, H., Yoshimine, T., and Saitoh, Y. (2018). The optimal stimulation site for high-frequency repetitive transcranial magnetic stimulation in Parkinson's disease: A double-blind crossover pilot study. *Journal of Clinical Neuroscience*, 47:72–78. [Cited on page 41]

Yoo, H. B., Ost, J., Joos, W., Van Havenbergh, T., De Ridder, D., and Vanneste, S. (2018). Adding Prefrontal Transcranial Direct Current Stimulation before Occipital Nerve Stimulation in Fibromyalgia. *Clinical Journal of Pain*, 34(5):421–427. [Cited on page 26]

Yoon, T. H., Han, S. J., Yoon, T. S., Kim, J. S., and Yi, T. I. (2015). Therapeutic effect of repetitive magnetic stimulation combined with speech and language therapy in post-stroke non-fluent aphasia. *NeuroRehabilitation*, 36(1):107–114. [Cited on page 40]

Yrondi, A., Sporer, M., Péran, P., Schmitt, L., Arbus, C., and Sauvaget, A. (2018). Electroconvulsive therapy, depression, the immune system and inflammation: A systematic review. *Brain Stimulation*, 11(1):29–51. [Cited on page 17]

Yuan, T., Yadollahpour, A., Salgado-Ramírez, J., Robles-Camarillo, D., and Ortega-Palacios, R. (2018). Transcranial direct current stimulation for the treatment of tinnitus: A review of clinical trials and mechanisms of action 11 Medical and Health Sciences 1103 Clinical Sciences. *BMC Neuroscience*, 19(1):1–9. [Cited on page 28]

Zago, S., Ferrucci, R., Fregni, F., and Priori, A. (2008). Bartholow, sciamanna, alberti: Pioneers in the electrical stimulation of the exposed human cerebral cortex. *The Neuroscientist*, 14(5):521–528. [Cited on page 10]

Zewdie, E. and Kirton, A. (2016). *TMS Basics: Single and Paired Pulse Neurophysiology.* Elsevier Inc. [Cited on pages 31, 33]

Zhao, N., Zhang, J., Qiu, M., Wang, C., Xiang, Y., Wang, H., Xie, J., Liu, S., and Wu, J. (2018). Scalp acupuncture plus low-frequency rTMS promotes repair of brain white matter tracts in stroke patients: A DTI study. *Journal of integrative neuroscience*, 17(1):125–139. [Cited on page 62]

Zhou, D.-D., Wang, W., Wang, G.-M., Li, D.-Q., and Kuang, L. (2017). An updated meta-analysis: Short-term therapeutic effects of repeated transcranial magnetic stimulation in treating obsessive-compulsive disorder. *Journal of Affective Disorders*, 215:187–196. [Cited on page 62]

Zhu, C. E., Yu, B., Zhang, W., Chen, W. H., Qi, Q., and Miao, Y. (2017). Effectiveness and safety of transcranial direct current stimulation in fibromyalgia: A systematic review and meta-analysis. *Journal of Rehabilitation Medicine*, 49(1):2–9. [Cited on pages 25, 26]

Ziegelberger, G., van Rongen, E., Croft, R., Feychting, M., Green, A. C., Hirata, A., D'Inzeo, G., Marino, C., Miller, S., Oftedal, G., Okuno, T., Röösli, M., Sienkiewicz, Z., and Watanabe, S. (2020). Principles for non-ionizing radiation protection. *Health Physics*, 118(5):477–482. [Cited on pages 18, 112]

Zienkiewicz, O., Taylor, R., and Zhu, J. (2005). *The Finite Element Method: Its Basis and Fundamentals.* Butterworth-Heinemann, Canada, 6th edition. [Cited on page 49]

Zimmermann, K. P. and Simpson, R. K. (1996). "Slinky" coils for neuromagnetic stimulation. *Electroencephalography and Clinical Neurophysiology - Electromyography and Motor Control*, 101(2):145–152. [Cited on page 169]

Zschorlich, V. R., Hillebrecht, M., Tanjour, T., Qi, F., Behrendt, F., Kirschstein, T., and Köhling, R. (2019). Repetitive peripheral magnetic nerve stimulation (Rpms) as adjuvant therapy reduces skeletal muscle reflex activity. *Frontiers in Neurology*, 10(AUG):1–8. [Cited on page 172]